

## PDF hosted at the Radboud Repository of the Radboud University Nijmegen

The following full text is a publisher's version.

For additional information about this publication click this link.

<http://hdl.handle.net/2066/114098>

Please be advised that this information was generated on 2017-12-06 and may be subject to change.

**Single-electron charging, tunneling  
spectroscopy and quantum resistance  
in mesoscopic systems**

**Richard Smokers**



**Single-electron charging, tunneling spectroscopy  
and quantum resistance in mesoscopic systems**

**Richard Smokers**

Smokers, Richard Teunis Mathijs

Single-electron charging, tunneling spectroscopy and  
quantum resistance in mesoscopic systems / Richard Teunis  
Mathijs Smokers. – [S.l. : s.n.]. – Ill.

Thesis Nijmegen. – With ref. – With summary in Dutch.

ISBN 90-9005016-7

Subject headings: single-electron charging / tunneling.

# Single-electron charging, tunneling spectroscopy and quantum resistance in mesoscopic systems

een wetenschappelijke proeve op het gebied van  
de natuurwetenschappen

Proefschrift

ter verkrijging van de graad van doctor aan  
de Katholieke Universiteit Nijmegen,  
volgens besluit van het College van Decanen  
in het openbaar te verdedigen op  
woensdag 24 juni 1992  
des namiddags om 3.30 uur

door

Richard Teunis Mathijs Smokers

geboren op 22 september 1964  
te Eindhoven

Promotor: Prof. Dr. H. van Kempen  
Copromoter: Dr. P.J.M. van Bentum

*"Is this love ...  
... or just confusion?"*

Jimi Hendrix  
*Are you experienced?*



Dit werk maakt deel uit van het onderzoeksprogramma van de Stichting voor Fundamenteel Onderzoek der Materie (FOM) en is mede mogelijk gemaakt door financiële steun van de Nederlandse Organisatie voor Wetenschappelijk Onderzoek (NWO).

# Voorwoord

"*I act the role in classic style ...*", citeerde ik Marillion's *Script for a jester's tear* in het motto van mijn afstudeerscriptie. Niet om in herhaling te vallen, maar zozeer als dit citaat daar al van toepassing was, des te meer nog is dat het geval met betrekking tot het nu voor U liggende script. Ondanks zijn zes bedrijven is ook dit proefschrift een drama in klassieke zin. Klassiek niet alleen omdat het, zoals te doen gebruikelijk, verslag doet van vier jaren promotie-onderzoek, maar bovenal door het feit dat die vier jaren, zoals het geval bij vrijwel alle promovendi, gekenmerkt werden door afwisselende perioden van euforische roes maar vooral ook ultieme frustratie.

"*of a martyr carved with twisted smile ...*", want al is het beroep natuurkundige soms verre van leuk ("Hierna nooit meer!", heb ik meer dan eens verzucht), het vak natuurkunde blijft fantastisch, opwindend en boeiend.

"*to bleed the lyric for this song ...*", omdat na vier jaar onderzoek aan de grenzen der menselijke kennis een half jaar schrijven mij dicht bij de grenzen der menselijke energie heeft gebracht.

"*to write the rites to right my wrongs.*", daar het proefschrift noodde tot grondige overpeinzing van alle resultaten die niet waren wat ik zocht, en zodoende één en ander toch nog aardig op zijn pootjes terecht is gekomen.

Het zal niemand verbazen dat in een toneelstuk van deze omvang veel medespelers een belangrijke rol hebben gehad. De belangrijkste wil ik graag op deze plaats voor hun respectievelijke bijdragen bedanken:

Regie en productie:	Jan van Bentum en Herman van Kempen
Acteurs:	Michel Nelissen, Frank Nolden en Edwin Boon
Figuranten:	De vakgroep Vaste Stof Fysica 2
Decor en requisieten:	Cees Beers, Jan Hermsen, Jan Gerritsen, Rob Kasman, Eef Jansen en Riki Gommers
Muziek:	Het Micro-Canoniek Ensemble
Belichting:	Henk Hoervers, Jérôme Dubois, Urs Wyder, Bart Nelissen, Menno Prins en Dan Abraham
Special effects:	Henk Hoervers

Speciale loges in het publiek waren gereserveerd voor mijn ouders, vrienden en huisgenoten. Bedankt voor kritiek, applaus en nimmer aflatende belangstelling.

Sonja, bedankt voor al zeven jaar alles en meer dan dat. "*'Cause when I'm sad she comes to me, with a thousand smiles she gives to me free!*"



# Contents

<b>General introduction</b>	<b>13</b>
<b>1 Basic aspects of tunneling in solid-state configurations</b>	<b>17</b>
1.1 Introduction	18
1.1.1 The principle of tunneling	18
1.1.2 Brief historical overview	19
1.2 Some experimental realizations of electron tunneling geometries	19
1.2.1 Thin film tunnel junctions	19
1.2.2 Point-contact tunnel junctions	21
1.2.3 Tunneling spectroscopy	21
1.3 Tunneling theory	22
1.3.1 Tunneling between normal metals	23
1.3.2 Tunneling into superconductors	28
1.4 General considerations on tunneling spectroscopy in STM-like geometries	34
References	36
<b>2 Charging effects in tunnel junctions: a general introduction</b>	<b>39</b>
2.1 A short history of charging effects	40
2.2 Single junctions: Coulomb blockade and Single-Electron Tunneling	41
2.2.1 Intuitive introduction to SET-effects	41
2.2.2 Quantitative analysis of SET: the orthodox theory	44
2.2.3 Quantitative analysis of SET: Monte Carlo simulations	47
2.2.4 Influence of the electromagnetic environment on the Coulomb blockade	51
2.2.5 Josephson junctions: Bloch oscillations	58
2.3 Multiple junction geometries	59
2.3.1 Double junctions: incremental charging and Coulomb staircase	59
2.3.2 Monte Carlo simulations	65
2.3.3 Analytic expression	66
2.3.4 Modulation of the potential of the central electrode	66
2.3.5 Multiple junction arrays	68
2.4 Experimental status	68
2.4.1 Metal-insulator-metal systems	68
2.4.2 Non-metal systems	70
2.4.3 Conclusion	70
2.5 Practical applications	70
References	72

<b>3</b>	<b>Charging effects in single point-contact tunnel junctions</b>	<b>75</b>
3.1	Introduction . . . . .	76
3.2	Circumstantial evidence for charging effects in point-contact tunnel junctions . . . . .	76
3.2.1	"Dirty" materials . . . . .	77
3.2.2	"Clean" junctions . . . . .	79
3.2.3	Charging effects and gap-spectroscopy . . . . .	81
3.3	A conceptual view of charging effects in point-contact tunneling . . .	82
3.4	Point-contact junctions on surface-doped Si samples . . . . .	85
3.4.1	Sample properties and experimental set-up . . . . .	85
3.4.2	Experimental results . . . . .	88
3.4.3	Conclusions . . . . .	92
3.5	Surface-doped Si with Al islands . . . . .	92
3.5.1	Sample preparation . . . . .	93
3.5.2	Preliminary results . . . . .	94
3.5.3	Discussion . . . . .	94
3.6	Conclusions . . . . .	95
	Appendix: the experimental set-up . . . . .	96
	3.6.1 Electronics . . . . .	98
	References . . . . .	98
<b>4</b>	<b>Incremental charging of single small particles: point-contact tunneling experiments</b>	<b>101</b>
4.1	Granular aluminum films . . . . .	102
4.1.1	Sample preparation and experimental set-up . . . . .	102
4.1.2	Results . . . . .	103
4.2	High- $T_c$ superconductors . . . . .	108
4.3	Ligand-stabilized clusters . . . . .	111
4.3.1	Introduction . . . . .	111
4.3.2	Preliminary results . . . . .	114
4.4	Discussion . . . . .	115
	References . . . . .	117
<b>5</b>	<b>Tunneling spectroscopy on high temperature superconductors</b>	<b>119</b>
5.1	Introduction . . . . .	120
5.2	Material parameters . . . . .	121
5.3	Gap spectroscopy . . . . .	123
5.3.1	General considerations . . . . .	123
5.3.2	Results on $\text{YBa}_2\text{Cu}_3\text{O}_{7-\delta}$ . . . . .	124
5.3.3	Results on $(\text{Pb}_x\text{Bi}_{1-x})_2\text{Sr}_2\text{CaCu}_2\text{O}_8$ . . . . .	128
5.4	Josephson effects . . . . .	132
5.5	Charging effects . . . . .	135
5.6	Negative differential resistance . . . . .	136
5.7	Conclusions . . . . .	137

---

References . . . . .	138
<b>6 Quantum resistance and localization in one-dimensional systems</b>	<b>141</b>
6.1 Introduction . . . . .	142
6.2 Theory of nonlinear quantum tunneling resistance in one-dimensional disordered systems . . . . .	145
6.2.1 Introduction . . . . .	146
6.2.2 Derivation of the resistance formula . . . . .	147
6.2.3 Numerical results for a Kronig-Penney-type potential . . . . .	151
6.2.4 Scaling behaviour of the resistance . . . . .	155
6.2.5 Summary and conclusions . . . . .	158
6.3 Carrier dynamics in a ring, Landauer resistance and localization in a periodic system . . . . .	161
References . . . . .	169
<b>Summary</b>	<b>171</b>
<b>Samenvatting</b>	<b>175</b>
<b>List of publications</b>	<b>179</b>
<b>Curriculum Vitae</b>	<b>181</b>



## General introduction

Two technical developments in the past decades have opened completely new possibilities for the study of the solid state at the so-called mesoscopic and even atomic scale. Nanolithography allows the production of extremely small devices such as quasi-one-dimensional wires, quantum wells and ultrasmall tunnel junctions with typical lengthscales of the order of 10 – 100 nm. These devices are elegant test-cases for the experimental verification of quantum-mechanics text-book problems, but also display a variety of completely new and fascinating quantum phenomena. The invention of the Scanning Tunneling Microscope (STM) provided a tool for topographic as well as spectroscopic characterization of materials at the sub-nanometer scale, allowing e.g. the visualization of individual atoms and molecules under a wide range of experimental conditions. The STM, however, also offers, in combination with specific samples, the possibility to create mesoscopic tunneling geometries.

The dimensions of nanolithographically defined structures can, especially in semiconductor structures, be of the order of the de-Broglie wave length of the conduction electrons, and can certainly be made smaller than the inelastic scattering length at low temperatures. Electrical conduction in such devices is completely governed by coherent wave propagation, leading to interference effects of arbitrary complexity depending on the elastic scattering potential. These effects are quantum-mechanical in the sense that they bring the fundamental constant  $\hbar$  into the formulas describing charge transport in these systems.

Although commonly taken for granted the quantization of charge in units of  $e$  is also an essential part of the quantum nature of matter. While in macroscopic systems the charge  $Q$  may be treated as a continuous variable, this need no longer be the case in systems at the mesoscopic scale. The electrostatic capacitance of e.g. sub-micron tunnel junctions and isolated metallic islands may be so small that the charging energy  $e^2/2C$ , associated with a single electron charge, becomes larger than the thermal energy  $k_B T$ . As an example: the presence of a single electron charge  $e$  on a junction with an overlap area of  $(0.1 \mu\text{m})^2$  already produces a voltage of order 1 mV ( $\propto 10$  K). The tunneling of single electrons in such a system will have a significant influence on the potential difference across the junction and will consequently alter the probability of subsequent tunnel events. The STM and point-contact geometries in general also define small tunnel junctions in which single-electron charging effects may play a role.

With the progressive miniaturization in the microfabrication of electronic devices the above mentioned mesoscopic phenomena will sooner or later become a significant factor in the device operation. In the current silicon- and transistor-based technology they will mainly be a disturbing factor, but the effects themselves can also be used to design entirely new types of small and fast switching devices.



Especially charging effects are believed to be a very promising candidate for a future generation of both analog and digital electronics (single-electron logics).

This thesis presents both theoretical and experimental investigations of a number of effects associated with tunneling in solid-state devices. Tunneling is generally recognized as a versatile tool for obtaining spectroscopic information on e.g. the electronic structure of normal metals, semi-conductors and superconductors. To this end both evaporated planar junctions and STM- or point-contact tunnel junctions can be used. The latter have the advantage of being less demanding where it concerns the tractability of the sample material, and it is this type of junction that is employed in all the experiments presented in this thesis.

The smallness of STM- and point-contact junctions, however, makes that these junctions create conditions which may go beyond the limits of validity of widely applied tunneling theories such as the Bardeen formalism. The interpretation of spectroscopic data in terms of the densities of states of tip and sample requires better insight in the special properties of this type of tunnel geometries. As a general theory of STM-tunneling is not yet available, chapter 1 introduces the basic concepts of electron tunneling along the lines of the exact wave-matching formalism and the transfer-Hamiltonian approach. The results of these methods are placed in a wider perspective by comparison with both experience from STM-experiments and insight gained from recent tentative approaches towards a more general concept of tunneling in point-contact geometries.

Chapter 2 of this thesis sets out the theoretical framework of charging effects in small tunnel junctions, with the main attention focussed on junctions between two normal metals. A distinction is made between single junctions and multiple junction arrays. Single junctions are shown to display charging effects only if they are properly decoupled from stray capacitances caused by the leads to which the junctions are attached. The strength of the decoupling depends on the electromagnetic impedance of the junction environment. In arrays the decoupling is provided by the presence of other tunnel junctions. The so-called double-junction system, a series connection of two small junctions, is extensively analyzed. Furthermore a brief overview will be given of the present experimental status regarding nanolithographic junctions, as well as of practical applications in the fields of metrology and electronics.

Experimental evidence for the occurrence of charging effects in single point-contact tunnel junctions, established with the aid of a low temperature STM-like set-up, will be presented in chapter 3. As these junctions do not meet the above described decoupling conditions a novel decoupling mechanism will be proposed and qualitatively analyzed.

The double junction system can be realized in a point-contact configuration by sandwiching a small insulated metallic grain between the tip and a second electrode. Chapter 4 shows the results of measurements at low temperatures on point-contact tunnel junctions established on several granular samples. Furthermore some speculations are presented concerning the possibility of observing the discrete density of states of extremely small organometallic clusters.

Another major break-through in the recent history of solid-state physics concerns the discovery of the high- $T_c$  superconducting oxides, in the beginning of 1987. Despite tremendous scientific effort still no satisfactory explanation for the unprecedentedly high critical temperatures has been found. In chapter 5 the point-contact geometry is used to study the quasi-particle density of states of two species of high- $T_c$  superconductors,  $\text{YBa}_2\text{Cu}_3\text{O}_{7-\delta}$  and  $(\text{Pb}_x\text{Bi}_{1-x})_2\text{Sr}_2\text{CaCu}_2\text{O}_8$ . Besides gap-characteristics the current-voltage curves of point-contact tunnel junctions on these materials display a rich pageant of other effects, not necessarily associated with superconductivity. Striking examples will be presented and discussed.

Finally, chapter 6 is devoted to a theoretical investigation of quantum interference effects, such as localization, in one-dimensional systems. The first part concerns the behaviour of the quantum resistance of one-dimensional wires with a disordered potential as a function of the applied voltage and the length of the wire. In the second part a connection will be laid between the carrier dynamics in a ring and the stationary quantum tunneling through a one-dimensional wire with a periodic potential which is connected to thermalizing reservoirs. From these considerations a new conception will emerge regarding the role of dissipation in the definition of quantum resistance.



## **Chapter 1**

# **Basic aspects of tunneling in solid-state configurations**

## 1.1 Introduction

In this chapter I will attempt to summarize the basic theoretical and experimental concepts of tunneling phenomena in solid-state devices. This chapter is intended to provide a basis for further theoretical considerations made in subsequent chapters, as well as a frame of reference for the interpretation of experimental observations presented in this thesis. For extensive reviews the reader is referred to Refs. [1, 2, 3].

The first two sections give a layman-level introduction to the concept of tunneling and its possible realizations in solid-state devices. Section 1.3 is devoted to the general theory of electron tunneling. Tunneling characteristics of junctions with normal-metal and/or superconducting electrodes will be analyzed with the aid of the wave-matching approach and the transfer-Hamiltonian formalism. While it has been proven that these theories apply well to tunneling in "macroscopic" planar junctions, section 1.4 comments on the difficulties in applying these formalisms to the more complicated geometries as encountered in point-contact experiments and Scanning Tunneling Microscopy (STM). Several recent attempts towards a more general tunneling theory will be briefly discussed.

### 1.1.1 The principle of tunneling

Within the framework of classical mechanics a region of space where the local potential  $U(\mathbf{x})$  surmounts the total energy  $E$  of a particle, with  $E$  equal to the sum of the particle's potential and kinetic energy, is a forbidden region. The particle is not allowed to enter that region, but instead will be reflected at the so-called classical turning point where its kinetic energy is zero and its potential energy equals the local potential.

Quantum mechanics (see e.g. Ref. [4]) describes particles in terms of wave functions, which are a function of time and the spatial coordinates. The amplitude  $|\Psi(\mathbf{x}, t)|^2$  of a wave function  $\Psi(\mathbf{x}, t)$  gives the probability of finding the particle at a given time  $t$  at a given position  $\mathbf{x}$  in space. As both  $\Psi$  and  $\nabla\Psi$  are continuous functions of the spatial coordinates, the wave function will have a finite amplitude even beyond a classical turning point, except for regions in space where the potential is infinite. This essentially means that there is a finite probability of finding a particle in a classically forbidden region. In the forbidden region the amplitude of the wave function is predicted to decay exponentially with the distance from the classical boundary.

If the width of a forbidden region is finite it is called a potential barrier. For widths of the order of a few decay lengths or less the wave function will still have a finite amplitude at the opposite side of the barrier where the particle with energy  $E$  is again free to propagate, as the local potential on that side is lower than the particle's total energy. This means that a particle initially residing on one side of a barrier has a finite probability of finally finding itself on the other side. This essentially quantum-mechanical effect is commonly denoted as tunneling. In fact, the tunneling phenomenon is indissolubly connected to the wave-mechanical nature

of the quantum theory of matter.

A major consequence of the tunneling phenomenon is the fact that a current can flow from one conductor to another even though the materials are not physically touching, but separated by an insulating barrier (e.g. vacuum or an oxide layer), presumed that this barrier is not too thick. The electrical resistance of such a tunneling contact will scale roughly exponentially with both the thickness and the height of the barrier.

### 1.1.2 Brief historical overview

The concept of tunneling has been developed as early as in 1928 by Oppenheimer [5] in his treatment of ionization of the hydrogen atom under the influence of a static electric field. Some thirty years later the development of metal evaporation techniques for the preparation of thin metal films allowed Giaever [6] to produce stable devices, in which the current transfer was dominated by tunneling of electrons through an oxide barrier separating two electrodes. Subsequently it was observed [7, 8] that the differential conductance of a tunnel junction between a normal metal and a superconductor is directly proportional to the density of quasi-particle states, as described by the theory of superconductivity formulated by Bardeen, Cooper and Schrieffer (further referred to as BCS-theory) [9, 10, 11, 12, 13]. Around the same time Esaki [14] demonstrated the occurrence of interband tunneling in narrow semiconductor p-n junctions. These developments triggered theorists in the early 60's to develop the basic theoretical concepts of tunneling in solid-state devices. The current-voltage dependence can be calculated taking into account the influences of barrier shape, electrode composition and density of states, inelastic tunneling processes, etcetera.

Over the years electron tunneling has become recognized as a very versatile and sensitive tool for spectroscopic investigation of various properties of among others normal metals, superconductors, and semiconductors on the energy scale of millivolts to a few volts, and even of e.g. vibration spectra of chemical species which can be artificially incorporated in a tunneling barrier [1, 2, 3, 15].

More recently the development of the Scanning Tunneling Microscope (STM) [16] opened an entirely new field for application of the tunneling phenomenon, as with this technique topographic and spectroscopic information can be obtained and combined on the scale of individual atoms on the surface of the conductors under investigation.

## 1.2 Some experimental realizations of electron tunneling geometries

### 1.2.1 Thin film tunnel junctions

A very convenient tunneling configuration is the one pioneered by Giaever [6], which basically consists of two metal electrodes separated by an insulating layer

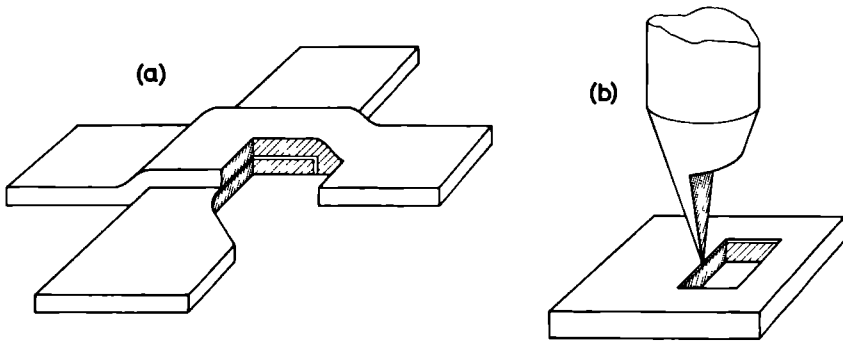


**Figure 1.1** Schematic drawings of (a) an evaporated thin film junction, and (b) a point-contact tunnel junction, both with cut-away views of the tunneling area. The electrodes (hatched regions) are separated by a thin oxide layer (white region).

with a thickness of only a few nanometers. Generally the electrodes are two crossed thin metal strips, separated at the overlap by a thin insulating barrier, which are deposited on some substrate using evaporation or sputtering techniques. This configuration is illustrated in Fig. 1.1(a). Substrates have to be insulating and, depending on demands considering e.g. the crystallinity or homogeneity of the films, can be glass, quartz, sapphire, undoped silicon, etc..

Using evaporation or sputtering it is relatively easy to make films of metals (single elements or simple alloys), and some semiconductors. More elaborate state of the art technology is required to deposit more complex compounds like the high- $T_c$  superconducting oxides. Due to the deposition technique the films are amorphous, polycrystalline, or at best polycrystalline with some preferential orientation. With the use of Molecular Beam Epitaxy (MBE) or Metal-Organic Chemical Vapour Deposition (MOCVD) however the epitaxial growth of crystalline films is also feasible. Single crystals, grown by other means can only be applied if they are used as substrate for the deposition of the counter electrode, but it generally proves more difficult to obtain useful junctions in this way.

Film thicknesses generally range from a few nanometers to a few microns. The width of the thin film strips determines the overlap area of the junction, and is controlled by masks which are placed between the sample and the evaporation source. For most simple experimental purposes widths of the order of a few tenths of a millimeter will suffice. The observation of charging effects as described in chapter 2 of this thesis requires tunneling areas less than  $0.1 \mu\text{m}^2$ . These can be achieved by using masks which are defined by electron-beam lithography. Shadowing techniques as developed by Dolan [17] can be applied to further minimize the overlap area.

As a tunneling barrier a native oxide of one of the electrode materials can be used. This is achieved by exposing the base electrode, before deposition of the top electrode, to oxygen inside the evaporation system, or to air. Instead of this, deposi-

tion of an artificial barrier is also possible. For instance aluminum oxide ( $\text{Al}_2\text{O}_3$ ) or silicon oxide can be evaporated or sputtered, or some organic insulating compound can be spun onto the base electrode.

### 1.2.2 Point-contact tunnel junctions

The tunneling geometry that will be predominantly dealt with in this thesis is the point-contact configuration, which is schematically depicted in Fig. 1.1(b). The development of this technique dates back to 1966 [18].

The simplest point-contact junction is achieved by gently bringing a sharp tip of some conducting material in mechanical contact with the sample, a piece of conducting material of in principle arbitrary shape and size. A true tunneling contact is established when at least one of the electrodes is covered by an oxide or other non-conducting layer which is strong enough to withstand some mechanical force but thin or deformable enough to allow for an electrode separation of 100 down to some 10 Å.

The subtle approach of the tip is carried out with the use of a differential screw mechanism, a piezo-electric device or, even better, a combination of both. This type of tunnel junction is employed in most of the experiments presented in this thesis.

The development of the STM by Binnig and Rohrer [16] invoked a more sophisticated approach towards point-contact tunneling. In combination with minimization of the influence of external vibrations through system design and damped suspension, the application of a feedback system, which keeps the current constant, permits the tip-sample separation to be stabilized without the presence of a solid tunneling barrier. In fact the STM is able to operate not only in vacuum, but also in gaseous and liquid environments. If the tip is scanned over the sample, surface corrugations will tend to alter the tunnel current. The feedback system compensates for this either by retracting the tip or by pushing it forward. A topographic image can be obtained by plotting the feedback signal as a function of the tip position. The exponential dependence of the tunnel current on tip-sample separation and a small size of the tunnel area provide the possibility of atomic resolution.

In most modern STM's a single segmented piezo tube is used to move the tip in  $x$ -,  $y$ -, and  $z$ -directions. Tunnel microscopes can be designed and built for operation at room temperature or at low temperatures, in vacuum, air and other gasses, or liquids, and under the application of a magnetic field. For extensive reviews on the field of STM-applications I refer to Refs. [19, 20].

### 1.2.3 Tunneling spectroscopy

As will be further elucidated in the next section of this chapter the voltage dependence of the tunnel current is determined by various intrinsic and extrinsic parameters of the tunnel junction and elastic as well as inelastic processes which interfere with the tunneling process. These factors are generally dependent on the energy of the tunneling electrons. This means that from the current-voltage ( $I(V)$ )



characteristics spectroscopic information can be obtained concerning material properties of the electrodes, the energy dependence of the tunneling probability, etcetera

In most cases where the energy dependence of the parameters or processes under consideration is not dominating the overall shape of the  $I(V)$  characteristics clear information can only be obtained from the first derivative (the differential conductance  $\partial I/\partial V(V)$  or differential resistance  $\partial V/\partial I(V)$ ) or the second derivative ( $\partial^2 I/\partial V^2(V)$  or  $\partial^2 V/\partial I^2(V)$ ) of the characteristics

Experimentally these derivatives can easily be measured by modulating the dc-voltage (or equivalently the current, depending on the bias configuration) with a small sinusoidal modulation signal  $dV \sin(\omega t)$  (or  $dI \sin(\omega t)$ ) and measuring the response in the current (voltage) at the first or second harmonic ( $\omega$  and  $2\omega$  resp.) of the modulation frequency  $\omega$ , using phase locked detection techniques (lock-in amplifier) These harmonic responses are directly proportional to respectively the first and second derivative

$I(V)$  characteristics can be recorded using either a voltage or a current bias Depending on the junction resistance and the contact resistances a two-probe or a four-probe configuration is used For thin film junctions, which have a large junction area and therefore a small resistance of the order of  $10 \Omega$  to  $10 \text{ k}\Omega$ , a four-probe configuration is commonly used For junctions with predominantly linear characteristics a bridge circuit can be employed to increase the sensitivity of derivative measurements In the case of point-contact junctions, which have tunnel resistances in the  $\text{M}\Omega$  regime, a two-terminal configuration will suffice

### 1.3 Tunneling theory

This section will review the basic theoretical descriptions of those junction configurations which we will encounter in this thesis Essential formulae will be summarized and discussed For exact derivations the reader will be referred to the original papers More extensive reviews on theoretical (as well as experimental) aspects of the tunneling phenomenon can be found in Refs [1, 2, 3]

There are two widely applied approaches to the calculation of tunneling characteristics The first and probably most insightful one is a steady-state approach based on the time-independent Schrodinger equation and matching of wave functions at the barrier The exact wave matching problem is only solvable in one-dimensional or otherwise separable single-particle models, but has the advantage that arbitrary barrier shapes can be treated in an exact manner The second method is generally referred to as transfer-Hamiltonian approach It employs a time-dependent Schrodinger equation in the second-quantization formalism, in which, besides the Hamiltonians of the unperturbed electrodes, a so-called transfer or tunneling Hamiltonian is incorporated, which describes the transfer of electrons between both electrodes This method is less rigorous in the sense that it is a first-order perturbation approach, with validity limited to opaque barriers Within this limitation, however, it is more powerful than the steady-state approach as it enables the incorporation of many-particle and inelastic effects in three-dimensional geometries

Both methods have proven to be successful in the interpretation of tunneling measurements on evaporated planar junctions, which are effectively one-dimensional. Point-contact geometries and especially STM-junctions, however, may provide circumstances which go beyond the limits of validity of the above mentioned theories (see e.g. Ref. [21]). Thin barriers in these small junctions will induce significant coupling between the electronic states of tip and sample, whereas the wave functions in the tip will be heavily dependent on the exact tip shape if the radius of curvature becomes of atomic dimensions. For the rather blunt type of mechanically touching point contacts employed in the experiments presented in chapters 3, 4 and 5 the effects will in most cases not be dramatic, but for the interpretation of spectroscopic STM-measurements a more general tunneling theory is certainly required. Various promising attempts in this direction are being made at the moment, but none of these have reached a level of maturity to become of importance for a quantitative interpretation of the type of experimental results described in this thesis.

In the discussion of the formalisms used in this section attention will be paid to assumptions limiting their applicability. A qualitative overview and discussion of some more general theories of STM-tunneling will be presented in section 1.4.

### 1.3.1 Tunneling between normal metals

I will start the description of tunneling between normal-metal electrodes using the wave-matching approach, as this formalism is most convenient for the introduction of the pictorial representation which is used to visualize the tunneling problem.

#### Calculation of the current-voltage characteristics using the wave-matching approach

Most theoretical considerations restrict themselves to the effectively one-dimensional situation of a tunnel junction between two parallel planar electrodes. In this system the Schrödinger equation for motion in the tunneling direction is

$$-\frac{\hbar^2}{2m} \frac{\partial^2 \psi(x)}{\partial x^2} + U(x)\psi(x) = E_x \psi(x), \quad (1.1)$$

with three-dimensional solutions of the general form:

$$\Psi = \psi(x) \exp(ik_y y + ik_z z), \quad (1.2)$$

where  $U(x)$  is the one-dimensional potential, and  $k_y$  and  $k_z$  are the momenta in the transverse directions. A simple model approximation for this potential is shown in Fig. 1.2. For the moment we restrict ourselves to the generally employed idealization in which the electrodes are assumed to be nearly-free electron metals so that  $U(x)$  is flat on both sides of the barrier, which has a thickness  $d$ . The metals have Fermi energies  $\mu_l$  and  $\mu_r$  respectively.  $U(x)$  has a trapezoidal shape inside the barrier region. In general a more realistic potential will be rounded due to e.g. the image potential experienced by electrons in the barrier region [1, 2, 3]. If the electrodes

are non-identical metals their Fermi levels will tend to line up when the metals are brought in (tunneling) contact. This is realized by a net charge transfer causing a surface charge on the electrodes, and consequently a static electric field inside the barrier. An applied potential difference shifts the Fermi level of the right hand side electrode by  $eV$  with respect to that of the left hand side electrode. In case the electrodes are separated by a vacuum the height of the barrier on both sides equals the work functions  $\phi_l$  and  $\phi_r$  of the respective metals. If the barrier is an insulator, the top of the barrier corresponds to the energy of the bottom of the empty conduction band of the insulator. The effective masses of the electrons in the three regions will in general be different, but this is not taken into account here.

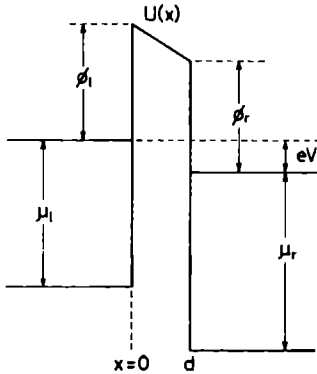


**Figure 1.2**

Effectively one-dimensional model of a tunnel junction with planar parallel electrodes. The quantities and variables are defined in the text.

Solutions of the Schrödinger equation can be obtained in each of the three regions independently. Inside the nearly-free electron metals the wave functions can be described by plane waves. In the barrier region the wave function is exponentially decaying like  $e^{\pm|\kappa(x)|x}$  due to its imaginary wave number  $\kappa(x)$ , which will in general vary with the local potential. In fact there are two independent solutions, starting from plane waves with unity amplitude incident on the barrier from the left and the right respectively:

$$\begin{aligned} \psi^{(1)}(x) &= e^{ikx} + R_{ll}e^{-ikx}, & x < 0 \\ &= T_{lr}e^{iqx}, & x > d \\ \psi^{(2)}(x) &= T_{rl}e^{-ikx}, & x < 0 \\ &= e^{-iqx} + R_{rr}e^{iqx}, & x > d. \end{aligned} \quad (1.3)$$

The amplitudes  $|T_{ij}|^2$  and  $|R_{ii}|^2$  can be related to the probability of transmission and reflection respectively. The transmission probability  $D(E_x, V)$  is defined as the ratio of transmitted over incident current density carried by states at energy  $E_x$ . Current conservation demands that applying the current density operator

$$j = \frac{i\hbar}{2m} \left( \psi \frac{\partial \psi^*}{\partial x} - \psi^* \frac{\partial \psi}{\partial x} \right) \quad (1.4)$$

to the wave functions inside the metals and the barrier yields the same value. For our plane wave approximation this gives the following relationship between the trans-

mission and reflection amplitudes of solution  $\psi^{(1)}$ :

$$k(1 - |R_{ll}|^2) = q|T_{lr}|^2, \quad (1.5)$$

and a similar expression for solution  $\psi^{(2)}$ .

Detailed balance arguments demand that the elastic transition rates from left to right and vice versa between equally filled states are equal, so that

$$D(E_x, V) \equiv |T_{lr}(E_x)|^2(q/k) = |T_{rl}(E_x)|^2(k/q). \quad (1.6)$$

Using the above relations the total wave function and the corresponding probabilities of transmission and reflection can now be calculated by matching the solutions of the Schrödinger equations for the three regions at the boundaries under the condition that  $\psi(x)$  and  $\partial\psi(x)/\partial x$  are continuous.

The total current density  $j$  is then evaluated by either summing the net contributions of all available  $k$ -states on one side of the barrier, or by subtracting the transmitted currents from left to right and vice versa. Both electrodes are assumed in thermal equilibrium so that their electronic states are occupied with a probability described by the Fermi-Dirac distributions  $f_l(E) = f(E) = [1 + \exp(E/k_B T)]^{-1}$  and  $f_r(E) = f(E + eV)$ , with  $\mu_l - \mu_r = eV$  the applied voltage across the barrier, and  $E$  measured from the Fermi level of the left-hand side electrode.  $T$  is the temperature and  $k_B$  is the Boltzmann constant. By integrating over all directions for the incoming plane waves one finally arrives at [1, 2, 22]:

$$j_{lr} = 2e \int \frac{d^3 k_l}{(2\pi)^3} v_{xl} D(E, V) f(E) [1 - f(E + eV)] \quad (1.7a)$$

$$j_{rl} = 2e \int \frac{d^3 k_r}{(2\pi)^3} v_{xr} D(E, V) f(E + eV) [1 - f(E)]. \quad (1.7b)$$

The prefactor 2 accounts for spin degeneracy. In the independent particle approximation (see Harrison [23]) the velocity  $v_x$  equals  $\hbar^{-1} \partial E / \partial k_x$ , in other words, the velocity is inversely proportional to the density of states. Using  $v_{x_i} dk_{x_i} = \hbar^{-1} dE_{x_i}$  it is possible to separate the integral over  $k$ -space in an integral over the energy  $E_x$  and an integral over transverse states  $k_t$ , yielding [1, 2, 24])

$$j = \frac{2e}{h} \int \frac{d^2 k_t}{(2\pi)^2} \int_{-\infty}^{\infty} D(E_x, V) [f(E) - f(E + eV)] dE_x, \quad (1.8)$$

where the first integration is over all transverse states obeying  $E_t = E - E_x$ . At zero temperature the Fermi distributions sharply define an energy window of width  $eV$ , and the integration over  $k_t$  can be carried out explicitly as shown by Floyd and Walmsley [25]. Other explicit expressions for  $j(V)$ , derived under different restricting assumptions, are given by Simmons [26, 27].

If  $D(E_x, V)$  is known from wave matching at the boundaries of the barrier, the  $I(V)$  characteristic can be calculated. For simple cases, like the rectangular or trapezoidal barrier, analytic expressions are readily available, while more realistic

barriers can be evaluated numerically. A general expression for the transmission factor  $D(E_x, V)$  of barriers with arbitrary shape, is commonly calculated using a Wentzel-Kramers-Brillouin (WKB) approximation method. The solutions  $\psi(x) = C e^{\pm i u^o(x)}$  of the Schrödinger equation, with  $u^o = \int_{x_1}^x \kappa(x') dx'$ , are expressed in terms of the "local" wave number  $\kappa(x) = (2m/\hbar^2 [E - U(x)])^{1/2}$ , where  $U(x)$  describes the in principal arbitrary shape of the potential barrier. This results in [23, 24]:

$$D(E_x, V) = g \exp\left(-\frac{2}{\hbar} \int_0^d (2m[U(x, V) - E_x])^{1/2} dx\right). \quad (1.9)$$

In the WKB-approximation the prefactor  $g$  equals 1. Equation 1.9 generally gives the right order of magnitude of the dependence of  $D(E_x, V)$  on the various barrier parameters, provided that  $E_x$  is not too close to the top of the barrier.

As a comparison the transmission of a rectangular barrier, calculated using exact wave matching at the sharp boundaries, is given by Harrison [23], who finds Eq. 1.9 with prefactor

$$g = \frac{16kq\kappa^2}{(k^2 + \kappa^2)(q^2 + \kappa^2)}. \quad (1.10)$$

The WKB-approximation is valid only if  $U(x)$ , and the corresponding bandstructure, vary slowly over lengthscales of the electron wave length in the vicinity of the turning points. In realistic barriers, especially if e.g. the effect of the image potential is taken into account, this condition is generally fulfilled.

For tunnel junctions with well defined oxide-layer barriers the barrier height is usually of the order of several eV, which is much larger than the tunnel voltages, and corresponding electron energies, of interest. If the barrier is not too thin ( $d > 10 \text{ \AA}$ ) the applied voltage will not noticeably deform the barrier shape and the transmission factor can be assumed constant. For the case of thin or low barriers, however, the explicit incorporation of an energy and voltage dependent transmission factor, obtained from Eq. 1.9 or from numerically or analytically evaluated exact wave matching, is essential.

In deriving Eq. 1.8 we have seen that the velocity and the density of states cancel each other. Therefore the current as a function of voltage contains no explicit information on the densities of states of the normal-metal electrodes. Only through the incorporation of the exact transmission probability (e.g. Eq. 1.10), or through the summation over transverse  $k$  states in case of a non-parabolic  $E(k)$  or non-spherical Fermi surface, might the  $I(V)$  characteristic reveal spectroscopic information on the densities of states. These energy dependences are generally weak and very indirect. Only in the vicinity of e.g. band edges and gaps, and in systems which in one or more directions exhibit a discrete density of states, like for example tunneling perpendicularly into a two-dimensional electron gas, will the  $I(V)$  characteristics, calculated within the context of this planar junction model, depend strongly on the density of available states.

## The transfer-Hamiltonian approach

The transfer-Hamiltonian approach applies to the situation where the reflection probability of the barrier is near unity. In such a situation the electrodes can be treated as nearly independent systems with unperturbed Hamiltonians  $H_L$  and  $H_R$  respectively. A weak residual coupling is modelled by a perturbing transfer Hamiltonian  $H_T$ , such that the total Hamiltonian  $H$  reads

$$H = H_L + H_R + H_T. \quad (1.11)$$

$H_T$  describes the tunneling of electrons from one electrode to the other. Using the second-quantization formalism it can be expressed as

$$H_T = \sum_{k,q} (T_{kq} a_k^* a_q + T_{qk} a_q a_k^*), \quad (1.12)$$

with  $a_k^*$  and  $a_{k,q}$  operators respectively creating or annihilating an electron in state  $k$  in the left electrode or state  $q$  in the right electrode. Following Bardeen [28] the transition rate is usually calculated using the Fermi Golden Rule,

$$w_{ab} = \left(\frac{2\pi}{\hbar}\right) |\langle \psi_a | H_T | \psi_b \rangle|^2 \rho(E_b) f_a (1 - f_b) \delta(E_b - E_a), \quad (1.13)$$

where  $\rho(E_b)$  is the density of final states in the right hand electrode, and  $f_a$  and  $f_b$  are the probabilities of occupation of states  $a$  and  $b$ .

The states in both electrodes are now taken as standing waves [23], which are matched to exponentially decaying tails in the barrier. The states are constructed to continue to decay exponentially in the opposite electrode, this in contrast to the stationary state approach where the decaying tails are again matched to oscillatory wave functions. The overlap of the wave functions in the barrier region now determines the transition rate.

Bardeen [28] shows that the matrix element  $M_{ab} = \langle \psi_a | H_T | \psi_b \rangle$  can be expressed in terms of the matrix element  $J_{ab}$  of the current operator like  $M_{ab} = -i\hbar J_{ab}$ , which is evaluated on a plane inside the barrier:  $M_{ab} = (\hbar^2/2m) \int d\mathbf{S} (\psi_a^* \nabla \psi_b - \psi_b \nabla \psi_a^*)$ .  $M_{ab}$  vanishes unless the transverse wave number  $k_t$  of initial and final state is the same (i.e. specular transmission). The net current can now be written as a summation over transverse  $k$ -states of an integral over the total energy  $E$ , in which  $k_t$  is kept constant:

$$J = \frac{4\pi e}{\hbar} \sum_{k_t} \int_{-\infty}^{\infty} |M_{ab}|^2 \rho_a(E - eV) \rho_b(E) (f_a - f_b) dE. \quad (1.14)$$

Using its relation to the current density matrix element and the explicit wave functions  $\psi_a$  and  $\psi_b$ , the matrix element can be calculated in a WKB-approximation:

$$|M_{ab}|^2 = \exp\left(-\frac{2}{\hbar} \int_0^d (2m[U(x, V) - E_x])^{1/2} dx\right) (4\pi^2 \rho_a \rho_b)^{-1}. \quad (1.15)$$

Combining Eq. 1.15 with Eq. 1.14 now yields an expression for the current which is identical to the stationary state result. The power of the transfer-Hamiltonian approach is not evident from this simple calculation of the characteristics of a normal-metal tunnel junction. However, if we want to describe inelastic tunneling processes (e.g. photon-assisted tunneling, interaction with barrier impurities), this method proves to be very convenient. In the description of tunnel junctions with superconducting electrodes, which goes beyond the realm of the independent particle approximation, the transfer-Hamiltonian approach has also been applied successfully.

### 1.3.2 Tunneling into superconductors

In a superconductor the electrons near the Fermi level experience an attractive interaction, which is phonon-mediated for the case of the classical superconductors whose behaviour is described by the BCS-theory [9]. As a result of this they will be bound into so-called Cooper pairs, which are pairs consisting of two interacting electrons with opposite spin and momentum. These  $(\mathbf{k}\uparrow, -\mathbf{k}\downarrow)$  pairs are condensed in a macroscopic ground state, and are bosons, in contrast to the fermionic individual electrons. The interaction energy of a Cooper pair is  $2\Delta$ . This binding energy is temperature dependent and becomes zero when the temperature rises above the critical temperature  $T_c$ , where the superconductor becomes a normal metal. The BCS theory [9, 10, 11, 12] predicts a linear relation between a superconductor's critical temperature and its binding energy at zero temperature:

$$\frac{2\Delta(0)}{k_B T_c} = 3.53. \quad (1.16)$$

The temperature dependence of  $\Delta(T)$  is depicted in Fig. 1.3.

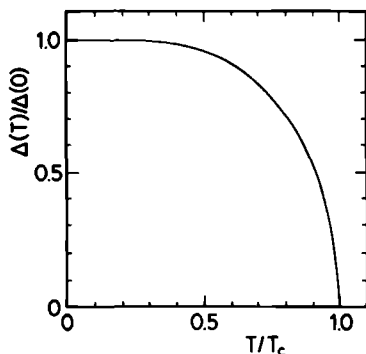


**Figure 1.3** Temperature dependence of  $\Delta(T)$  according to the BCS-theory.

Excitations out of the ground state can be generated by transferring an amount of energy larger than  $2\Delta$  to a Cooper pair. The excitations are described in terms of quasi-particles, which are of partly electron-like and partly hole-like nature. The ratio of electron- and hole-like nature depends on the quasi-particle's energy with

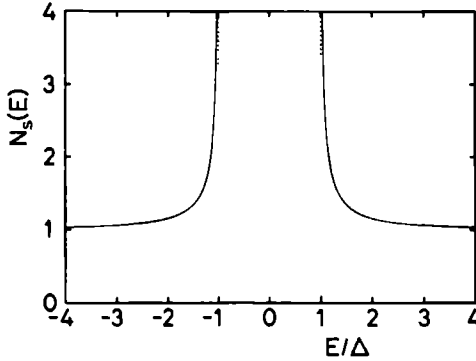


**Figure 1.4** Quasi-particle density of states  $N_s(E)$  of a superconductor.

respect to the Fermi level. Far above the Fermi energy quasi-particles behave like normal-metal electrons, and far below they resemble the holes in the normal metal. The quasi-particle density of states is drawn in Fig. 1.4, and can be expressed as:

$$\rho_s(E) = N_n(E)N_s(E) \equiv N_n(E) \operatorname{Re}\left(\frac{|E|}{\sqrt{E^2 - \Delta^2}}\right), \quad (1.17)$$

with  $N_n(E)$  the density of states of the metal in the normal state. The density of quasi-particle states is zero in the interval  $(-\Delta, \Delta)$  around the Fermi level. This is the so-called energy gap of the superconductor. At the gap edges  $\rho_s(E)$  displays sharp singularities.

If a single electron is to tunnel into a superconductor it can not be accommodated in the condensate ground state, as it is unpaired. It can only enter as an excitation and is as such to be accommodated in a quasi-particle state, meaning that the electron is not allowed to enter the superconductor if its energy is inside the gap region. The operators  $a_{k\sigma}^*$  and  $a_{k\sigma}$ , which describe the creation and annihilation of a "real" electron in or out of a state with momentum  $k$  and spin  $\sigma$ , are related to the creation and annihilation operators  $\alpha_{k\sigma}^*$  and  $\alpha_{k\sigma}$  of quasi-particles through the Bogoliubov transformation [28, 29, 30, 31], as follows:

$$a_{k\uparrow}^* = u_k \alpha_{k\uparrow}^* + v_k \alpha_{-k\downarrow} \quad (1.18a)$$

$$a_{-k\downarrow}^* = u_k \alpha_{-k\downarrow}^* - v_k \alpha_{k\uparrow}. \quad (1.18b)$$

The prefactors  $u_k$  and  $v_k$  are related through

$$|u_k|^2 = 1 - |v_k|^2 = \frac{1}{2} \left[ 1 + \frac{(E^2 - \Delta^2)^{1/2}}{E} \right], \quad (1.19)$$

where  $|u_k|^2$  and  $|v_k|^2$  give the respective amplitudes of the electron- and hole-like contributions to the quasi-particle state the electron is accommodated in or taken out of.



Through the Bogoliubov transformations the transfer Hamiltonian (Eq. 1.12) is coupled to the macroscopic ground state of the superconductor. This means that the problem of tunneling into a superconductor has to be treated from a many-particle point of view [28], in contrast to the normal-metal case to which the independent-particle approximation [23] was applied.

In the calculation of the  $I(V)$  characteristics we have to discriminate between two different situations. The simplest case concerns tunnel junctions between a normal-metal electrode and a superconductor (NIS: I stands for "insulator"). The behaviour of such a junction is completely described by quasi-particle tunneling. The case of tunneling between two superconducting electrodes (SIS) proves to be more complex as in this configuration more quasi-particle tunneling channels open up, and also tunneling of Cooper pairs is possible.

### Normal-metal–superconductor junctions

Cohen, Falicov, and Phillips [32] have calculated the tunnel current in the transfer-Hamiltonian approach. The Hamiltonian of the total system is again given by Eq. 1.11. The Hamiltonian of the normal electrode is simply:

$$H_n = \sum_{k\sigma} \epsilon_k a_{k\sigma}^* a_{k\sigma}. \quad (1.20)$$

The Hamiltonian of the superconductor can be written as:

$$H_s = \sum_q E_q (\alpha_{q\uparrow}^* \alpha_{q\uparrow} + \alpha_{-q\downarrow}^* \alpha_{-q\downarrow}) + H_0, \quad (1.21)$$

where the condensate and the interaction terms are comprised in  $H_0$ . The tunnel Hamiltonian takes the form

$$H_T = \sum_{kq\sigma} (T_{kq} a_{k\sigma}^* a_{q\sigma} + T_{qk} a_{k\sigma} a_{q\sigma}^*), \quad (1.22)$$

with  $a_{q\sigma}^*$  and  $a_{q\sigma}$  given by Eq. 1.18.

From these premises Ref. [32] calculates the current as the expectation value of the time derivative of the number operator applied to the superconductor ( $\dot{\mathcal{N}}_s$ ), whose equation of motion is given by

$$i\hbar \dot{\mathcal{N}}_s = [\mathcal{N}_s, H] = [\mathcal{N}_s, H_T]. \quad (1.23)$$

This procedure is a more formal alternative for the use of the Fermi Golden Rule as sketched in Eqs. 1.13 and 1.14 of section 1.3.1, and explicitly proves the absence of the coherence factors  $u_k$  and  $v_k$  in the final expression for the quasi-particle current. Both approaches yield the following expression for the current-voltage dependence:

$$j(V) = \frac{4\pi e}{\hbar} \sum_{k_t} \int_{-\infty}^{\infty} |T|^2 [f_n(E - eV) - f_s(E)] \rho_n(E - eV) \rho_s(E) dE_x. \quad (1.24)$$

The matrix element  $|T|^2$  is again evaluated on a plane inside the barrier, and is therefore determined by the overlap of the exponentially decaying tails of the electrodes' wave functions in the barrier. Using the Gor'kov equations [33] Bardeen [28] shows that, for a low transparency barrier (an assumption already governing the applicability of the transfer Hamiltonian approach), the position-dependent energy gap  $\Delta(x)$  drops rapidly to zero inside the barrier. Therefore the electrons of the superconducting electrode are essentially unpaired in the barrier region, and the exponential tail of the wave function is basically equal to that of the normal-state wave function. For this reason the tunnel matrix element can be assumed equal in both the superconducting and normal case. As a result  $|T|^2$  can be calculated by applying Eq. 1.15, in which  $\rho_a$  and  $\rho_b$  are the normal-metal densities of states of both electrodes.

Based on Eqs. 1.14 and 1.24 we now arrive at our final expression for the tunnel current between a normal metal and a superconductor:

$$j = \frac{4\pi m_{\parallel} q}{h^3} \int_{-\infty}^{\infty} dE_x D(E_x, V) \int_{-\infty}^{\infty} dE_{\parallel} (f(E - qV) - f(E)) N_s(E). \quad (1.25)$$

In this equation  $q$  is the charge of the carrier type (electrons or holes), and the barrier transmission probability  $D(E_x, V)$  is given by Eq. 1.9. The explicit use of  $m_{\parallel}$  allows for an anisotropy in the effective masses for normal and transverse motion. Eq. 1.25 is used by Kirtley [34] in his review on tunneling measurements on high- $T_c$  superconductors.

A general expression that is often used [1, 11, 12, 13], and which circumvents the above sketched delicate treatment of densities of states by simply neglecting it, is given by

$$j(V) = \frac{G_{\text{nn}}}{e} \int_{-\infty}^{\infty} N_s(E) [f(E - eV) - f(E)] dE. \quad (1.26)$$

As also the integration over transverse  $k$ -states is ignored, this is a truly one-dimensional approximation. The normal state conductance  $G_{\text{nn}}$  expressed as

$$G_{\text{nn}} = A \cdot N_{n1}(0) N_{n2}(0) |T|^2, \quad (1.27)$$

with  $A$  a constant. The normal state densities of states, as well as the tunnel matrix element, are explicitly assumed constant and hence replaced by their value at the Fermi level. These assumptions are generally allowed for the Giaever-type tunnel junctions between nearly free electron metals and classical superconductors. The resulting  $I(V)$  characteristic is depicted in Fig. 1.5. At  $T = 0$  K the differential conductance is directly proportional to the effective superconductive density of states as defined in Eq. 1.17.

For junctions with a large barrier transparency the applicability of the transfer Hamiltonian approach breaks down, due to the coupling between the wave functions in the normal metal and those in the superconductor. Using the Bogoliubov-equation formalism Blonder, Tinkham and Klapwijk [35] have been able to describe the transition from metallic to tunneling conduction in NIS-junctions. This method (see

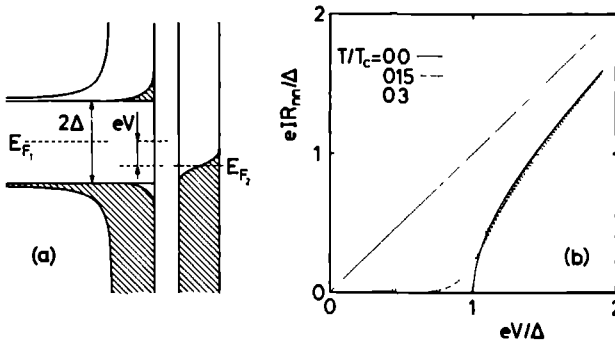


**Figure 1.5** Energy diagram (a) and  $I(V)$  characteristic (b) of a NIS tunnel junction at  $T/T_c = 0, 0.15$  and  $0.3$ .

also Ref. [36]) is again based on exact wave matching involving the proper quasi-particle wave functions, and can in principle be extended to deal with arbitrary barrier shapes. The main result for large transparencies is the occurrence of an excess current, resulting from Andreev reflection of charge carriers incident on the interface with energies within the gap.

### Superconductor–superconductor tunnel junctions

For the case of junctions between two superconductors one can follow essentially the same procedure after inserting two superconductor Hamiltonians  $H_{s1}$  and  $H_{s2}$  into the Hamiltonian of the total system (Eq. 1.11). For opaque barriers ( $T \ll 1$ ) the  $I(V)$  dependence of quasi-particle tunneling [1, 11, 12, 13] can be written in a form similar to Eq. 1.26:

$$\begin{aligned}
 j(V) &= \frac{G_{nn}}{e} \int_{-\infty}^{\infty} N_{s1}(E - eV) N_{s2}(E) [f(E - eV) - f(E)] dE \\
 &= \frac{G_{nn}}{e} \int_{-\infty}^{\infty} \frac{|E - eV|}{[(E - eV)^2 - \Delta_1^2]^{1/2}} \frac{|E|}{[E^2 - \Delta_2^2]^{1/2}} \\
 &\quad \times [f(E - eV) - f(E)] dE,
 \end{aligned} \tag{1.28}$$

with  $G_{nn}$  again given by Eq. 1.27. The results are shown in Fig. 1.6. At  $T = 0$  K all states above the Fermi level are empty, and the current is zero until  $eV = \Delta_1 + \Delta_2$ . The current jump at this voltage is in principle infinitely sharp, even at finite temperatures, due to the crossing of two singularities in the densities of states (Fig. 1.6 (a)). At finite temperatures a junction between dissimilar electrodes will display a blunt peak in the current at  $eV = |\Delta_1 - \Delta_2|$ , which is a consequence of the occupation of quasi-particle states above the gap (Fig. 1.6 (b)).

In the case of more transparent barriers, as well as for metallic shorts and other types of weak links between superconductors, a coupling between the phase coherent ground states of both superconductors will result in tunneling of Cooper pairs, the

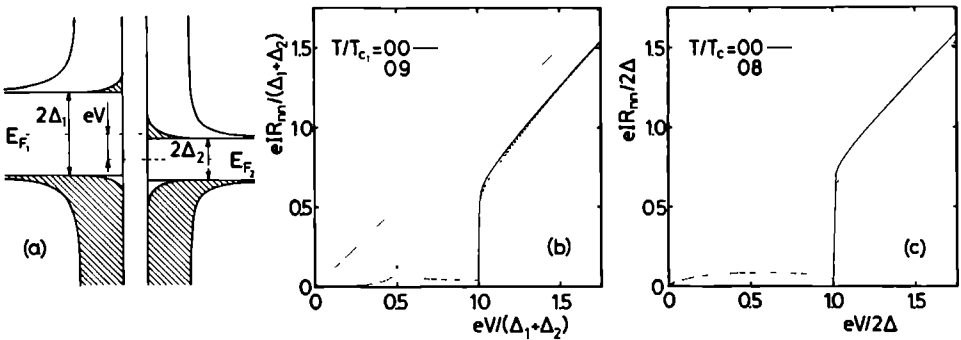


**Figure 1.6** (a) Energy diagram of a SIS tunnel junction at  $T \neq 0$ . (b)  $I(V)$ -curves of a junction with  $\Delta_1 \neq \Delta_2$  for  $T/T_{c1} = 0$  and  $0.9$ . (c)  $I(V)$ -curves of a junction between identical superconductors ( $\Delta_1 = \Delta_2$ ) for  $T/T_c = 0$  and  $0.8$ .

so-called Josephson current [31, 37]. Due to the phase coherence the tunnel matrix element of a Cooper pair is of the same order as that of a single quasi-particle. The dc-Josephson effect constitutes a finite supercurrent at zero voltage, as depicted in Fig. 1.7 (a). The occurrence of the effect depends on the amplitude of the Josephson coupling energy  $E_J \cos \Delta\phi = (\hbar I_0/2e) \cos \Delta\phi$ , in which  $\Delta\phi$  is the ground state phase difference across the junction.  $I_0$  is the maximum zero voltage current, which, for the case of a tunnel junction between identical superconductors, is calculated by Ambegaokar and Baratoff [38]:

$$I_0 = \frac{\pi \Delta(T)}{2eR_{nn}} \tanh \frac{\Delta(T)}{2k_B T}. \tag{1.29}$$

In this equation  $R_{nn}$  is the normal-state junction resistance per unit area. The voltage dependence of the Josephson effect will depend on the impedance of the

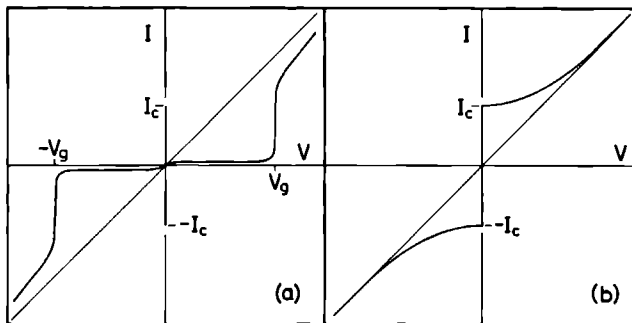


**Figure 1.7** (a)  $I(V)$  characteristic of a SIS tunnel junction with significant Josephson coupling. (b)  $I(V)$  characteristic of a weak-link type Josephson junction.

specific junction geometry For extensive reviews on the Josephson effect I refer to Refs [39, 40] Fig 1 7 (b) shows the a possible  $I(V)$  curve for a weak-link type of Josephson junction

## 1.4 General considerations on tunneling spectroscopy in STM-like geometries

The above given expressions for the voltage dependence of the tunnel current all strictly apply to planparallel junction geometries For such systems the energies for normal and transverse motion are easily separable The problem becomes essentially one-dimensional, and can conveniently be described in a basis of plane waves Obviously this description must be revised for tunneling in three dimensional STM-geometries, where the current flows between a sharp tip, with a radius of curvature down to atomic dimensions, and a possibly corrugated sample [41, 42] The interpretation of STM-spectroscopy (STS) measurements requires more insight in the microscopic properties of the tunnel process

For STM-junctions with blunt tips the effects may not be dramatic The small size of the tunneling area and the tip curvature will mainly result in an uncertainty in the momentum of electrons tunneling with a fixed energy, causing some "wave vector smearing" of sharp spectroscopic features, as stated by Kaiser and Jaklevic in Ref [43] Most of the measurements in this thesis are performed with tunneling point contacts, which are mechanically touching, so that the tip will always be more or less blunt compared to atomic dimensions

The problem of tunneling from an atomically sharp tip can again be approached along two paths described above, i e stationary calculations and the transfer Hamiltonian method Both treatments require the calculation of realistic wave functions of tip and sample at finite voltage The tip wave functions will be of atomic rather than plane wave nature Also the true potential for small tunneling distances is not known (see e g Ref [44]) Attempts to refine the transfer Hamiltonian method of Bardeen [28] have been undertaken by Tersoff and Haman [45], Lang [46] and Chen [47]

Calculating the tunnel matrix element  $|M_{ab}|^2$  in the transfer-Hamiltonian approach one encounters the problem that the result depends on the position of the plane of integration on which the matrix element  $J_{ab}$  is evaluated In the model of Lang [46], which describes the tunnel current between two atoms adsorbed on opposite free electron electrodes, the error appears to be of second order in the voltage if the plane is chosen halfway between the electrodes The transfer-Hamiltonian method can therefore still be applied quite reliably to STM-junctions with not too small tunnel distance (see also Ref [42])

The results of calculations in this approach so far [42, 45, 46, 47, 48] suggest a qualitative generalization of the form

$$I(V) \propto \int \rho_t(E - eV) \rho_s(E) D(E, V) dE, \quad (1 30)$$

in which  $\rho_t(E)$  and  $\rho_s(E)$  are the local densities of states of tip and sample. Such local density of states will in general be due to a combination of surface states and manifestations of the bulk states. For small voltages the transmission factor  $D(E, V)$  will be more or less constant, and the differential conductance will be proportional to the density of states. This conclusion is confirmed experimentally [43, 49] in STS-measurements of the surface states of Au(111).

For large voltages  $D(E, V)$  becomes exponentially voltage dependent and will thus tend to distort the  $I(V)$  characteristic. In order to be able to extract information on the density of states in this regime, Refs. [50, 51] propose to normalize  $\partial I/\partial V(V)$  by division by  $I/V$ , yielding  $\partial \ln I/\partial \ln V$ . This expression effectively cancels the exponential voltage dependence of  $D(E, V)$ , and is again a reasonable measure of the density of states, as pointed out by the calculations of Ref. [46].

Although the above conclusions may seem rather appealing in view of the correspondence with experimental results, there are some serious doubts concerning the applicability of the Bardeen formalism in the STM-geometry. First of all the transfer-Hamiltonian method is a first-order perturbation approach, which obviously requires a large barrier width so that the tip and sample states can be assumed independent and unperturbed [52]. In STM-measurements this condition may often not be satisfied. At tunnel distances less than 10 Å, the tip and sample states are thought to experience a significant mutual influence, which may e.g. even lead to tip-induced surface states on the sample surface [53].

A more severe problem is posed by the possible contribution of surface states to the tunnel current. In Eq. 1.30 as well as in the interpretation of experimental results in e.g. Refs. [43, 49] the local density of states is regarded as due to both bulk and surface states. Strictly speaking however, it is not justified to apply the transfer-Hamiltonian expression to surface states. This is due to the fact that application of the Fermi Golden Rule (Eq. 1.13) in determining the tunnel rate implicitly assumes that electrons incident on the barrier have no phase memory of previous encounters with that barrier. This is equivalent to demanding that all electrons that have tunneled undergo inelastic scattering before they are able to reflect from the other boundary of the electrode and again reach the barrier. In principle this means that the inelastic scattering length has to be smaller than the thickness of the electrode. If this is not the case, multiple reflections inside both electrodes will lead to coherent contributions to the tunnel current, the rate of which will be governed by  $|M_{ab}|$  rather than  $|M_{ab}|^2$ . Surface states are standing waves in the direction perpendicular to the surface, thus obviously violating the above assumption underlying the use of the Golden Rule argument [52, 54].

These difficulties may be overcome by the use of more sophisticated approaches to the tunnel problem. Noguera [52] and Sacks and Noguera [54] have employed the Keldysh formalism to derive an expression for the tunnel current (see also Caroli *et al.* [55]). This formalism allows exact determination of the systems out-of-equilibrium Green's functions to infinite order of perturbation. In the limit of weak coupling their result coincides with the result of Refs. [45, 46, 47] based on the Bardeen approach. Taking a simplified model for the tip but arbitrary sample they

find the tunnel conductance proportional to the density of surface states evaluated at the tip position, divided by a renormalization factor, which takes account of multiple reflections and changes in the local density of states due to the presence of the tip.

Another promising alternative is given by Molotkov *et al.* [53]. They evaluate the tunnel current by describing the tip-sample wave functions in terms of quasi-stationary states subject to complex boundary conditions. These boundary conditions provide sources and drains which maintain the quasi-stationary current. For weak coupling their result also formally reduces to that of Refs. [45, 46, 47]. Practical geometries are calculated in a tight-binding formalism.

The general conclusion remains that the  $I(V)$  characteristics in STS-measurements are strongly dependent on the presence of surface states and impurity states in tip or sample contamination, and will in general strongly vary with position if the sample is not homogeneous. The influence of contamination is explicitly shown by Refs. [56, 57, 58]. Experiments with tungsten tips on superconducting films only revealed the superconducting density of states after the tip was cleaned with e.g. a field emission discharge. In the same type of experiment [59] also the strong position dependence has been observed.

"The" theory of tunneling in STM-geometries does not yet exist. From the various attempts in establishing such theory it is nevertheless clear that STM-geometries define conditions outside the scope of the treatment sketched in section 1.3 of this chapter.

## References

1. E.L. Wolf, *Principles of Electron Tunneling Spectroscopy*, (Oxford University Press, N.Y. 1985).
2. E. Burnstein and S. Lundqvist, eds., *Tunneling Phenomena in Solids*, (Plenum Press, N.Y., 1969).
3. C.B. Duke, *Tunneling in Solids*, (Academic Press, N.Y., 1969).
4. C. Cohen-Tannoudji, B. Diu, and F. Laloë, *Quantum Mechanics*, (Wiley-Interscience, N.Y., 1977).
5. J.R. Oppenheimer, *Phys. Rev.* **31** (1928) 66.
6. I. Giaever, *Science* **183** (1974) 1253; J.C. Fisher and I. Giaever, *J. Appl. Phys.* **32** (1961) 172.
7. I. Giaever, *Phys. Rev. Lett.* **5** (1960) 147, 464.
8. J. Nicol, S. Shapiro, and P.H. Smith, *Phys. Rev. Lett.* **5** (1960) 461.
9. J. Bardeen, L.N. Cooper, and J.R. Schrieffer, *Phys. Rev.* **108** (1957) 1175.
10. R.D. Parks, ed., *Superconductivity*, Vols. 1 and 2, (Marcel Dekker, N.Y., 1969).
11. M. Tinkham, *Introduction to Superconductivity*, (Krieger Publ. Comp., 1975).
12. J.R. Schrieffer, *Theory of Superconductivity*, (Addison-Wesley, 1964).
13. A.A. Abrikosov, *Fundamentals of the Theory of Metals*, (North-Holland, 1988).
14. L. Esaki, *Phys. Rev.* **109** (1958) 603; *Science* **183** (1974) 1149.
15. P.K. Hansma, ed., *Tunneling Spectroscopy*, (Plenum Press, N.Y., 1982).

- 16 G Binnig, H Rohrer, Ch Gerber, and E Weibel, *Appl Phys Lett* **40** (1982) 178, *Phys Rev Lett* **49** (1982) 57
- 17 G J Dolan, *Appl Phys Lett* **31** (1977) 337
- 18 H J Levinstein and J E Kunzler, *Phys Lett* **20** (1966) 581
- 19 L L Soethout and H van Kempen, *Advances in Electronics and Electron Physics* **79** (1990) 155, see also L L Soethout, Ph D thesis (1991), University of Nijmegen, the Netherlands
- 20 L E C van de Leemput and H van Kempen, to be published in *Reports on Progress in Physics*, see also L E C van de Leemput, Ph D thesis (1991), University of Nijmegen, the Netherlands
- 21 T E Feuchtwang and P H Cutler, *Phys Scr* **35** (1987) 132
- 22 C R Leavens and G C Aers, in *Scanning Tunneling Microscopy and Related Methods*, eds R J Behm, N Garcia and H Rohrer, (Kluwer Academic Publ, Dordrecht, 1990), proceedings of the NATO Advanced Study Institute, 1989, Erice, Italy
- 23 W A Harrison, *Phys Rev* **123** (1961) 85
- 24 W F Brinkman, R C Dynes, and J M Rowell, *J Appl Phys* **41** (1970) 1915
- 25 R B Floyd and D G Walmsley, *J Phys C* **11** (1978) 4601
- 26 J G Simmons, *J Appl Phys* **34** (1963) 1793
- 27 J G Simmons, *J Appl Phys* **34** (1963) 2581
- 28 J Bardeen, *Phys Rev Lett* **6** (1961) 57
- 29 N N Bogolubov, *Nuevo Cimento* **7** (1958) 794, *Sov Phys JETP* **7** (1958) 41
- 30 J G Valatin, *Nuevo Cimento* **7** (1958) 843
- 31 B D Josephson, *Phys Lett* **1** (1962) 251
- 32 M H Cohen, L M Falicov, and J C Phillips, *Phys Rev Lett* **8** (1962) 316
- 33 L P Gor'kov, *Sov Phys JETP* **34** (1958) 505
- 34 J R Kirtley, *Int J Mod Phys B* **4** (1990) 201
- 35 G E Blonder, M Tinkham, and T M Klapwijk, *Phys Rev B* **25** (1982) 4515
- 36 H F C Hoovers, Ph D thesis (1992), University of Nijmegen, the Netherlands
- 37 B D Josephson, *Advan Phys* **14** (1965) 419, *Rev Mod Phys* **46** (1974) 251
- 38 V Ambegaokar and A Baratoff, *Phys Rev Lett* **10** (1963) 486, erratum **11** (1963) 104
- 39 A Barone and G P Paterno, *Physics and Applications of the Josephson Effect*, (Wiley & Sons, N Y, 1982)
- 40 K K Likharev, *Dynamics of Josephson Junctions and Circuits*, (Gordon & Breach, N Y, 1986)
- 41 J Tersoff, in *Scanning Tunneling Microscopy and Related Methods*, eds R J Behm, N Garcia and H Rohrer, (Kluwer Academic Publ, Dordrecht, 1990), proceedings of the NATO Advanced Study Institute, 1989, Erice, Italy
- 42 C J Chen, *Scanning Tunneling Microscopy*, to be published
- 43 W J Kaiser and R C Jaklevic, *IBM J Res Dev* **30** (1986) 411
- 44 R Garcia, *Phys Rev B* **42** (1990) 5476
- 45 J Tersoff and D R Hamann, *Phys Rev B* **31** (1985) 805, *Phys Rev Lett* **50** (1983) 1998
- 46 N D Lang, *Phys Rev Lett* **55** (1985) 230, *Phys Rev B* **34** (1986) 5947, *Phys Rev Lett* **58** (1987) 45
- 47 C J Chen, *J Vac Sci Technol A* **6** (1988) 319,
- 48 A Selloni, P Carnevali, E Tossati, and C D Chen, *Phys Rev B* **31** (1985) 2602



49. M.P. Everson, L.C. Davis, R.C. Jaklevic, and W. Shen, *J. Vac. Sci. Technol. B* **9** (1991) 891.
50. J.A. Stroschio, R.M. Feenstra, and A.P. Fein, *Phys. Rev. Lett.* **57** (1986) 2579.
51. R.M. Feenstra and P. Mårtensson, *Phys. Rev. Lett.* **61** (1988) 447.
52. C. Noguera, *J. Microscopy* **152** (1988) 3.
53. S.N. Molotkov, S.S. Nazin, I.S. Smirnova, and V.V. Tatarskii, *Surface Science* **259** (1991) 339.
54. W. Sacks and C. Noguera, *J. Microscopy* **152** (1988) 23; *J. Vac. Sci. Technol. B* **9** (1991) 488; *Phys. Rev. B* **43** (1991) 11612.
55. C. Caroli, R. Combescot, P. Nozieres, and D. Saint-James, *J. Phys. C* **4** (1971) 2598.
56. S.A. Elrod, A. Bryant, A.L. de Lozanne, S. Park, D. Smith, and C.F. Quate, *IBM J. Res. Dev.* **30** (1986) 387.
57. R. Wilkins, M. Amman, E. Ben-Jacob, and R.C. Jaklevic, *J. Vac. Sci. Technol. B* **9** (1991) 996.
58. M.A. Ramos, S. Viera, A. Buendia, and A.M. Baro, *J. Microsc.* **152** (1988) 137.
59. T. Chen, S. Tessmer, J.R. Tucker, J.W. Lyding, and D.J. van Harlingen, *J. Vac. Sci. Technol. B* **9** (1991) 1000.

## **Chapter 2**

### **Charging effects in tunnel junctions: a general introduction**

## 2.1 A short history of charging effects

The influence of the electrostatic charging energy on tunneling into small metal particles was already studied in 1968. Shortly after the development of the evaporated planar junction technology, Zeller and Giaever [1] made tunnel junctions which contained small Sn particles in the oxide barrier. These particles were produced by evaporating a granular Sn film in between two oxidation steps. In the current-voltage characteristics of these junctions they observed a strongly reduced conductance at low bias voltages (Coulomb blockade). In their model, tunneling through a Sn particle was described in terms of a series connection of two small tunnel junctions, where the electrostatic energy required for charging the particle was to be supplied by the applied voltage. As their junction basically consisted of many of these systems in parallel, all with different capacitances due to a spread in the particle size, they averaged the single particle low-voltage characteristics over an adequate distribution of junction capacitances.

Around the same time Lambe and Jaklevic [2] developed a similar system, in which the oxide layer between the granular film and one of the electrodes was so thick that tunneling through the system became impossible. Using ac-techniques for capacitance measurements they studied tunneling between the grains and the other electrode. The results were also explained in terms of incremental charging of the small particles. Their system even exhibited memory effects. By maintaining a fixed voltage over the junction for some time, the static charges in the oxide layer were allowed to rearrange themselves according to the electric fields present around the islands. When subsequently the voltage was swept and the capacitance measured, reproducing features were observed around the prefixed voltage, which only disappeared after considerable time or thermal cycling.

In the modelling of these experiments the basic ingredients of the theory described in this chapter were already present. Nevertheless it took almost twenty years before revived theoretical interest in the problem triggered new experimental efforts. In 1975 Kulik and Shekter [3] already formulated a concept of a new type of voltage oscillations that might occur in small capacitance Josephson junctions, but general interest was first focused on the fascinating new possibilities of these mesoscopic systems in 1985, when several authors [4, 5, 6, 7] further analyzed the influence of charging effects due to a small intrinsic capacitance in both normal-metal and Josephson tunnel junctions. Two types of the new voltage oscillations were predicted for the two different junction types. A solid foundation for the so-called orthodox theory of charging effects was laid by Averin and Likharev, and Likharev and Zorin [8, 9, 10]. After these publications an extensive experimental search was started for the verification of the predicted effects. Several groups approached the problem with the aid of small junctions produced with nanolithographic techniques. Our group, followed by others, pioneered in applying the versatility of the STM-technique. For an extensive review of both the theoretical and experimental aspects of the field the reader is referred to Ref. [11] and references therein.

In this chapter I will first outline the theoretical basis of the charging effects for

as far as they are of relevance to the experiments described in chapters 3 and 4, followed by a brief review of the experimental status of the field, and some indications for the possible application of charging effects.

## 2.2 Single junctions: Coulomb blockade and Single-Electron Tunneling

### 2.2.1 Intuitive introduction to SET-effects

The principle of Single-Electron Tunneling (SET) is easily explained using the idealized model evaluated by Averin and Likharev in Refs. [8, 10, 11]. In this model (see Fig. 2.1(a)) a tunnel junction with capacitance  $C$  and tunnel resistance  $R_T$ , with electrodes consisting of free-electron metals, is connected to an ideal current source, which is defined to be a device of infinite impedance, providing continuous current at a fixed rate.  $R_T$  is assumed to be larger than the quantum resistance  $R_Q \equiv \pi \hbar / 2e^2 \simeq 6.5 \text{ k}\Omega$ , so that quantum fluctuations can be ignored. The potential difference  $V$  across the junction is proportional to the net charge  $Q$  accommodated on the junction through the simple relation  $Q = VC$ . The charging energy  $E_c$  associated with the charge  $Q$  is  $E_c = Q^2 / 2C$ , as defined in classical electrostatics. The tunneling process transfers electrons between the junction electrodes in a discrete way. Starting from a situation with charge  $Q$  a tunneling event changes the charge by  $\pm e$ , where the sign depends on the direction of tunneling. The charging energy changes by  $\Delta E_{\pm}$ :

$$\begin{aligned} \Delta E_{\pm} = E(Q \pm e) - E(Q) &= \frac{(Q \pm e)^2}{2C} - \frac{Q^2}{2C} \\ &= \pm eV + \frac{e^2}{2C}. \end{aligned} \quad (2.1)$$

As we see this energy change is always positive for voltages  $|V| < e/2C$ . This means that within this voltage range tunneling is energetically unfavourable, if the temperature of the system is such that the thermal energy  $k_B T \ll e^2/2C$ . For simplicity we will assume zero temperature in this section, so that tunneling is completely prohibited if  $|V| < e/2C$ . This is the so-called Coulomb blockade of tunneling. The energy diagram is depicted in Fig. 2.1(b). The solid arrow indicates an allowed tunnel transition, while the dashed arrows indicates a forbidden transition.

In the current biased situation, a tunnel event changes the junction voltage, i.e. it shifts the Fermi levels of both electrodes with respect to each other, by an amount  $e/C$ . If, however, the junction is connected to a voltage source, the situation is completely different. The voltage source can be viewed as an infinitely large capacitor which is able to supply charge infinitely fast. The change in junction charge due to a tunnel event will be compensated for immediately and the difference between Fermi levels is essentially fixed. Tunneling will be allowed at any junction voltage, as long as the tunneling electron gains a non-negative amount of energy. The source takes care of the required charging energy.

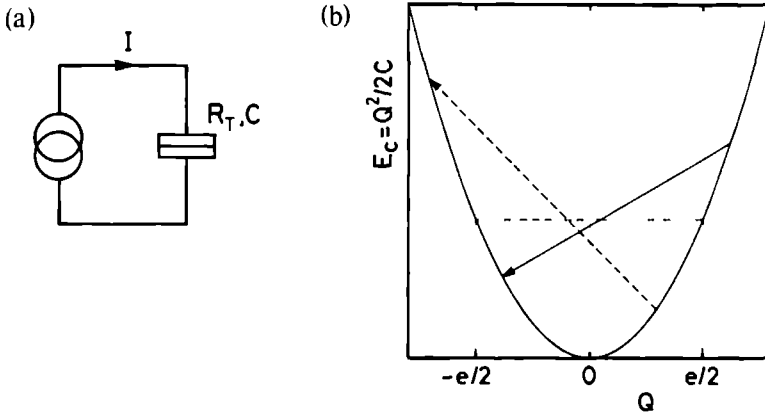


**Figure 2.1** (a) Model system of a current biased tunnel junction with capacitance  $C$  and tunnel resistance  $R_T$  (b) Charging energy  $E_c$  as a function of charge  $Q$  for a single junction with capacitance  $C$  The solid arrow indicates a tunnel transition that reduces  $E_c$ , and therefore is always allowed The dashed arrow indicates a transition which increases  $E_c$  and for this reason is not possible at low temperatures

The time-development of the charge (or equivalently voltage) of a junction in the current biased configuration, is illustrated in Fig 2.2 Starting from a situation  $Q = 0$  at  $t = 0$ , the current source imposes a constant (and in this example positive)  $Q$  on the junction so that the charge will increase linearly in time unless a tunneling event takes place While the charge is inside the blockade region  $|Q| < e/2$  no tunneling events occur Once  $Q$  exceeds  $e/2$ , tunnel transitions are in principle allowed However, tunneling is a stochastic process, and there is a constant probability  $P(V)$  per unit time for a tunneling event to take place

$$P(V)dt = R_T^{-1} (V - e/2C)dt \quad (2.2)$$

This means that after surpassing the Coulomb blockade it will generally take a finite though random amount of time before an electron actually tunnels The ratio between this delay time and the time needed to charge the junction above the Coulomb blockade region is determined by the magnitude of  $Q$

A tunnel event will decrease the charge by  $e$  If the initial charge was smaller than  $3e/2$  the junction will end up inside the blockade range again, and the junction will have to be charged before a second tunneling event can take place The voltage change due to tunneling of one electron thus blocks all subsequent tunneling events until the external circuit again overcomes the Coulomb blockade For small currents (trace (a) in Fig 2.2) the junction spends most of its time inside the blockade region The voltage across the junction will oscillate almost periodically in a sawtooth-like manner, with an average frequency which is trivially equal to  $f_{\text{SET}} = I/e$  In other words, electrons tunnel one by one after equal time intervals

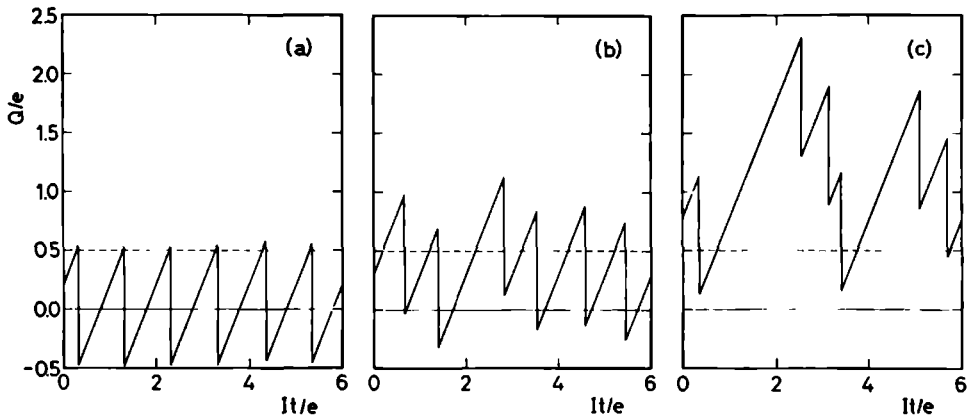


**Figure 2.2** Time-development of the junction charge for three different values of the current imposed by the current source: (a)  $I = I_0$ , (b)  $I = 160 I_0$ , (c)  $I = 1280 I_0$ .  $I_0$  is close to zero.

These are the so-called Single-Electron Tunneling (SET-) oscillations. The current source, by fixing  $\dot{Q}$ , provides an external clock for the synchronisation of the oscillations. The average voltage will be smaller than  $e/2C$ . The smaller the current, the more regular the SET-oscillations are, but there will always be a noise component due to the stochastic nature of the tunneling process. This means that the oscillations are never really coherent in the strict sense of the word. This denomination is nevertheless often used to make a distinction between the regular SET-oscillations and more random voltage fluctuations that occur in less ideal systems subject to charging effects. For larger currents the average voltage will be above the Coulomb blockade and the coherence of the oscillations will be gradually lost with increasing current. This situation is illustrated by curves (b) and (c) in Fig. 2.2.

As already stated above, the essential condition for the SET-oscillations to be observable is that the charging energy  $e^2/2C$  has to be larger than the thermal energy  $k_B T$ . Estimated with a parallel plate approximation the conventional Giaever-type tunnel junctions, with tunnel areas of the order of  $0.1 \text{ mm}^2$  to  $1 \text{ mm}^2$  (see chapter 1, section 1.2.1), have a capacitance in the  $10^{-9} \text{ F}$  regime or larger. Coulomb blockade effects will therefore only manifest themselves at temperatures below  $1 \mu\text{K}$ , with a typical blockade region in the  $I(V)$  characteristic smaller than  $10^{-9} \text{ V}$ , a voltage range hardly measurable with available technology. Thus it is clear that charging effects will play no role whatsoever in so-called macroscopic tunnel junctions. Instead, we will have to go to the mesoscopic regime, i.e. sub-micron dimensions, to have some chance of encountering these charging effects, and even then low temperatures will often be needed to observe them. Table 2.1 gives an overview of accessible junction sizes and their subsequent capacitances, and the temperature below which charging effects start interfering with the tunneling process.

After this qualitative introduction of concepts it is time to tackle the charging

size ( $\mu\text{m}^2$ )	$C$ (F)	$E_c$ (eV)	$T$ (K)
$10^4$	$3 \times 10^{-10}$	$10^{-9}$	$10^{-5}$
10	$3 \times 10^{-13}$	$10^{-6}$	$10^{-2}$
$10^{-2}$	$3 \times 10^{-16}$	$10^{-3}$	10
$10^{-5}$	$3 \times 10^{-19}$	1	$10^4$

**Table 2.1** Estimate of the charging energy and corresponding temperature below which charging effects may become apparent, as a function of junction size. In all cases the thickness of the barrier is assumed to be  $20 \text{ \AA}$ , and  $\epsilon_r = 7$ .

phenomena in a more quantitative way. The situation can be approached in two different ways. Starting from the intuitive picture sketched above it is possible to simulate the time-dependence of the junction charge (or voltage) on a computer using a Monte Carlo technique. By generating random numbers the stochastic nature of the tunneling process is simulated and after equal time intervals the computer decides whether an electron tunnels, or whether the junction is charged by the external circuit. Before discussing this technique, which is applicable to both single and multiple junctions, I will now proceed with a summary of the more rigorous treatment of ideally current biased single junctions as formulated by Averin and Likharev [8].

### 2.2.2 Quantitative analysis of SET: the orthodox theory

Averin and Likharev [8] start their calculations by investigating the properties of the system Hamiltonian  $H$ . Disregarding the influence of a shunt resistance in this summary, the Hamiltonian of the system is written as

$$\begin{aligned} H &= H_0 + H_T - I(t)\Phi \\ H_0 &= H_1 + H_2 + Q^2/2C. \end{aligned} \quad (2.3)$$

$H_1$  and  $H_2$  describe the internal degrees of freedom of the electrodes,  $H_T$  is a transfer Hamiltonian as defined in Eq. 1.12 of chapter 1, the term  $I(t)\Phi$  with  $\Phi = \int_{-\infty}^t V dt'$  accounts for the work done on the system by the current source, and  $Q$ , the charge operator, is defined as

$$Q = -\frac{e}{2} \left( \sum_{k_1} a_{k_1}^* a_{k_1} - \sum_{k_2} a_{k_2}^* a_{k_2} \right) + \text{const.} \quad (2.4)$$

The operators  $\Phi$  and  $Q$  are related as  $[\Phi, Q] = i\hbar$ . Also  $H_T$  does not commute with  $Q$  as a tunnel event changes the expectation value of  $Q$  by  $\pm e$ .  $[H_{1,2}, Q] \approx 0$  as the number of electron states in each electrode is always much larger than  $Q/e$ , and  $H_1, H_2$  can thus be assumed to commute with  $Q$ , meaning that tunnel events or charging of the junction do not alter the internal states of the electrodes.

Using only Eq. 2.3 and the above stated basic relations between the operators, disregarding their explicit expressions (Eqs. 1.12 and 2.4), Averin and Likharev are able to express the problem in terms of a density matrix  $\rho$ , and its time dependence given by the von Neumann equation. Treating all terms in the Hamiltonian except  $H_0$  as perturbations they derive a differential master equation for the probability density  $\sigma(Q, t)$  of the junction being in a state with charge  $Q$ . From this the expectation values of  $Q(t)$  and  $V(t)$  can be calculated, as well as their dependence on the driving current and temperature.

Figures 2.3, 2.4 and 2.5 show the basic predictions calculated in Ref. [8]. Around the origin the  $I(V)$  characteristic at  $T = 0$  K (Fig. 2.3) displays a horizontal branch  $[-e/2C, e/2C]$ , indicating that at zero current bias the junction can be in any state within the Coulomb blockade range. For finite but small currents the  $I(V)$  curve is parabolic

$$I = \frac{2C}{\pi R_T e} V^2 \quad \text{for } |I| \leq \frac{0.1e}{R_T C}, \quad (2.5)$$

as the Coulomb blockade actually suppresses the current below the Ohmic value  $I = V/R_T$ . For larger currents the characteristic approaches a linear asymptote

$$I = R_T^{-1} (V - e/2C) \quad \text{for } |I| \rightarrow \infty, \quad (2.6)$$

which is shifted from the origin by  $e/2C$  due to the Coulomb blockade. Apart from the zero current branch, the predicted  $I(V)$  characteristic is free of sharp and decisive features, making it difficult to distinguish from the influence of possible other effects on the  $I(V)$  curve of single junctions. However, if we look at Eqs. 2.5 and 2.6, we see that both the parabolic dependence near the origin and the asymptotic behaviour at high current values are described by the same two parameters  $C$  and  $R_T$ . Reading these from the offset and the slope of the asymptote it should be possible to fit the low current part of the  $I(V)$  curve with the same parameter values.

Figure 2.4 shows the frequency spectrum of  $V(t)$ . The infinitely sharp equidistant peaks can be attributed to the Fourier transform of the sawtooth-like wave form of the SET-oscillations, while the noise background is due to the stochastic nature of the tunneling process. For increasing current the effective amplitude of the SET-oscillations decreases, meaning that the tunnel events become uncorrelated, and the peaks disappear into the rising noise pedestal.

SET-oscillations can be locked to an externally applied modulation, as it will be energetically favourable for electrons to tunnel in phase with an oscillating field. Using an oscillation frequency  $f$ , harmonic and subharmonic phase locking occurs at dc-current values

$$I_{n,m} = \frac{n}{m} e f, \quad (2.7)$$

with  $n$  and  $m$  integers. At these resonant current levels, the  $I(V)$  characteristic of the ideal system will display infinitely sharp horizontal branches as depicted in Fig. 2.5. The position on a branch depends on the phase difference between the



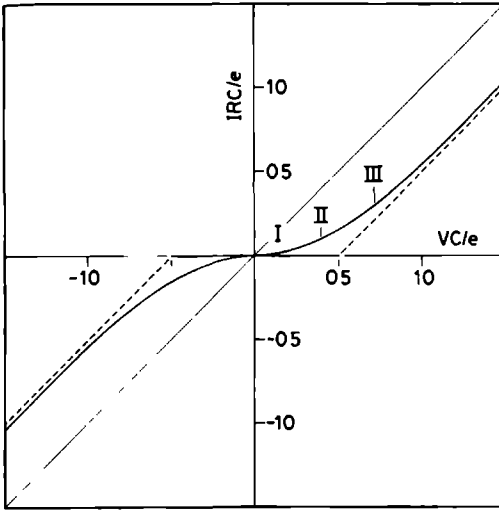


**Figure 2.3**  $I(V)$  characteristic of a perfectly current biased single junction, according to the calculations of Ref. [8].

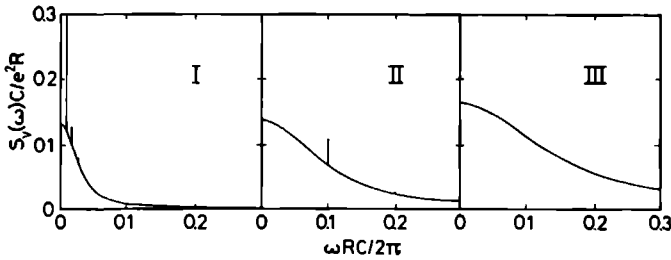


**Figure 2.4** Frequency spectrum of the SET-oscillations [8] for three values of the applied current, corresponding to the positions indicated in Fig. 2.3.

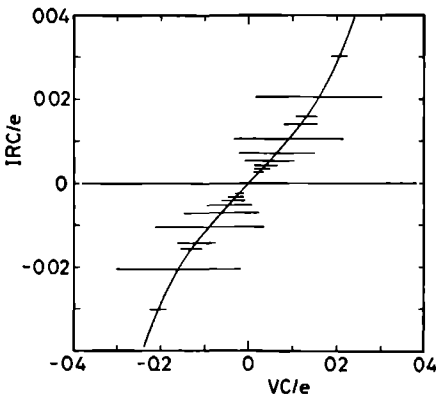


**Figure 2.5** The influence of externally applied ac-modulation on the  $I(V)$  characteristic [8].

SET-oscillations and the externally applied modulation. In any practical geometry, however, charge fluctuations will cause this phase difference to jump, and the branch will average out to the regular point on the  $I(V)$  characteristic. If the junction is shunted by a weak ohmic conductance, the branches will develop a finite width and become single-valued [12], i.e. the position on the branch no longer unphysically depends on the initial phase condition. The plateau will be slightly tilted with a slope equal to the shunt conductance (Fig. 2.6). Just to get a feeling for the frequencies that we are talking about: For mesoscopic tunnel junctions with resistances in the  $100\text{ k}\Omega$  to  $10\text{ M}\Omega$  regime the SET-effects play a role at current levels of the order of nA's, corresponding to frequencies in or below the microwave regime (10 MHz tot 1 GHz). The observation of these resonances provides the only true proof of the existence of Single-Electron Tunneling.

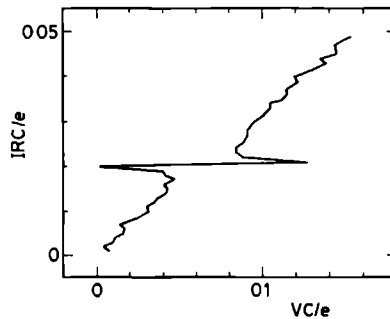


**Figure 2.6** Tilting of a resonant plateau in the  $I(V)$  curve of an ac-modulated junction, according to Ref. [12], due to the presence of a small shunt conductance.

### 2.2.3 Quantitative analysis of SET: Monte Carlo simulations

As already mentioned, the time dependence of the junction voltage can be easily simulated on a computer. The advantages of this method are that it requires little mathematics, and that it gives direct insight in the dynamics of the tunneling process. The method is not restricted to single current biased junctions, but can be applied to arbitrary bias conditions, and also to systems consisting of several tunnel junctions connected in series and/or parallel, as we will see in section 2.3. The effects of finite temperature can easily be incorporated in the calculation of the tunneling rate involved in this approach. A drawback of the method is that it is very complicated to treat in a proper way the effects of quantum fluctuations of the charge, which influence the tunneling rate and reduce the Coulomb blockade when the impedance of the bias circuit attached to the junction is smaller than the quantum resistance  $R_Q$  (see section 2.2.4). The Monte Carlo method has been developed independently by us (i.e. van Bentum and Smokers, see Refs. [13, 14, 15]), and several other groups [16, 17, 18].

The Monte Carlo simulation evaluates the junction state at times  $t$ , separated by equal time intervals  $\Delta t$ . The charge on the junction at time  $t$ , being  $Q(t)$ , there are in general three possibilities for the charge at time  $t_{i+1}$ :

$$Q(t_{i+1}) = \begin{cases} Q(t_i) + \dot{Q}(t_i)\Delta t + e, & \text{with probability } l(Q)\Delta t; \\ Q(t_i) + \dot{Q}(t_i)\Delta t - e, & \text{with probability } r(Q)\Delta t; \\ Q(t_i) + \dot{Q}(t_i)\Delta t, & \text{with probability} \\ & 1 - (r(Q) + l(Q))\Delta t. \end{cases} \quad (2.8)$$

In this equation  $l(Q)$  and  $r(Q)$  are the respective instantaneous rates for tunneling in the bias direction or vice versa (let's assume for simplicity that in case of a positive voltage the Fermi level of the right hand side electrode is lowered with respect to that of the left hand side electrode).  $\dot{Q}(t_i)$  is determined by the complex impedance and corresponding effective charging (e.g.  $RC$ -) time of the bias circuit. In the ideally current biased situation we simply have  $\dot{Q}(t_i) = I$ .

Incorporating the effects of finite temperature the tunneling rates of Eq. 2.8 can be calculated according to the Fermi Golden Rule argument, discussed in section 1.3.1. For simplicity we will actually use a one-dimensional variant of Eq. 1.14. However, we have to take into account that for the case of low capacitance junctions, as considered here, the tunneling of an electron changes the voltage across the junction by  $\pm e/C$ , thus shifting the electrodes' Fermi levels. In determining the possibility of occupation of the final state of a tunneling event we have to take this shift into account. "In gedanken" we first bring the charge of an electron, that is about to tunnel, to the opposite electrode and establish the shift in Fermi levels. If the resulting final state, i.e. the state of equal energy in the opposite electrode, is with some probability unoccupied then tunneling will be allowed with corresponding probability. If the voltage difference before tunneling was in the Coulomb blockade region ( $|V| < e/2C$ ) the tunneling electron will, after tunneling, end up in a state below the Fermi level of the counter electrode, meaning that at zero temperature the tunnel event could not have taken place. In formulae:

$$\begin{aligned} r(Q) &= \frac{2\pi}{\hbar} \int_{-\infty}^{+\infty} \rho_l(E) \rho_r(E + eV - \frac{e^2}{2C}) |T(E)|^2 f(E) \\ &\quad \times (1 - f(E + eV - \frac{e^2}{2C})) dE, \end{aligned} \quad (2.9a)$$

$$\begin{aligned} l(Q) &= \frac{2\pi}{\hbar} \int_{-\infty}^{+\infty} \rho_r(E) \rho_l(E - eV - \frac{e^2}{2C}) |T(E)|^2 f(E) \\ &\quad \times (1 - f(E - eV - \frac{e^2}{2C})) dE, \end{aligned} \quad (2.9b)$$

$\rho_l(E)$  and  $\rho_r(E)$  denote the densities of states of the electrodes, and  $f(E)$  is the Fermi distribution. All arguments of  $\rho_l(E)$ ,  $\rho_r(E)$  and  $f(E)$  are defined relative to the Fermi levels of the left and right hand side electrodes respectively. The shift of Fermi levels after charge transfer is distributed symmetrically over both electrodes, so that the effective energy shift in one electrode amounts  $e^2/2C$ .

The time dependence of the junction charge is simulated by computer. At each time  $t_i$  it calculates the tunneling rates based on the actual junction charge  $Q(t_i)$ , and decides whether tunneling is allowed. If so, a random number is generated and compared with an interval proportional to the tunneling rate, in order to determine whether or not a tunnel event takes place in the time interval under consideration.  $Q(t_{i+1})$  is then calculated, taking into account the charging by the external bias circuit. This process is repeated as long as necessary for a significant number of tunnel events to have taken place. In case of a current biased junction, where the current value is preset, the average junction voltage is determined. When dealing with other bias configurations, generally described by a voltage source with an arbitrary series impedance so that the external voltage is preset, the average current is determined by simply dividing the total number of tunnel events by the simulated time interval.

For a comparison with the results of Averin and Likharev [8], we must take  $T = 0$  K, so that the Fermi distribution function  $f(E)$  is a step function, and furthermore assume perfect current biasing. The electrodes are assumed free electron metals, and the barrier much higher than the Fermi energy and voltages of interest, and therefore the densities of states as well as the tunnel matrix element are approximately constant in the relevant energy regime (in so far as their energy dependences do not already cancel anyway (see section 1.3.1)). Equations 2.8 and 2.9 now can be greatly simplified, as in this case  $l(Q)$  is zero and the tunneling rate is completely determined by the applied voltage and the Coulomb blockade.

$$\begin{aligned} \text{if } |Q| \leq e/2: \quad & Q_{i+1} = Q_i + I\Delta t; \\ \text{if } |Q| > e/2: \quad & \left\{ \begin{array}{l} Q_{i+1} = Q_i + I\Delta t - e \\ \text{with probability } P(V)\Delta t = R_T^{-1}(V - e/2C)\Delta t; \\ Q_{i+1} = Q_i + I\Delta t \\ \text{with probability } P'(V)\Delta t = 1 - P(V)\Delta t. \end{array} \right. \end{aligned} \quad (2.10)$$

The densities of states and the tunnel matrix element are incorporated in the tunnel resistance  $R_T$ . The results are in perfect agreement with those of the "orthodox theory" [8].

The Monte Carlo approach can also be applied to bias conditions other than the perfect current biasing studied so far. As will become clear in section 2.2.4 the applicability is restricted to bias circuit impedances much larger than the quantum resistance  $R_Q$ . Figure 2.7 shows the frequency spectra of a junction connected to a voltage source via a large series resistance  $R_S$ . For  $R_S \gg R_T$  the junction is essentially current biased and the SET-oscillations manifest themselves in a sharp peak. Upon decreasing  $R_S$  the SET-peak broadens and gradually drowns in the noise background. For  $R_Q \ll R_S < R_T$  the junction voltage is still subject to fluctuations due to electron tunneling and subsequent recharging, but the fluctuations are no longer coherent as in the case of the SET-oscillations.

The influence of an externally applied modulation can be easily implemented by taking  $\dot{Q} = I_{dc} + I_{ac} \sin(\omega t + \phi)$ , in the case of perfect current biasing, or by e.g. setting  $V = V_{dc} + V_{ac} \sin(2\pi f_0 t)$  when the junction is connected to a voltage source

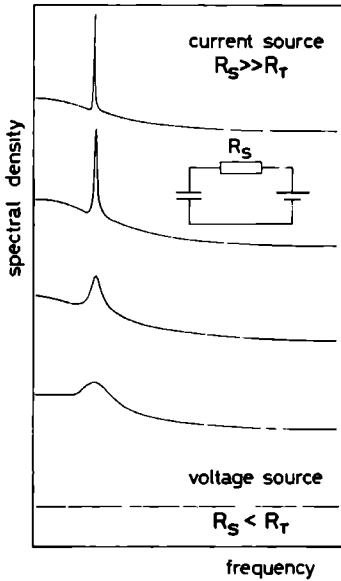


**Figure 2.7** Frequency spectrum of a small capacitance junction biased by a voltage source in series with a large resistance  $R_S$ , as a function of decreasing series resistance.

via a large series resistance  $R_S$ . A result is shown in Fig. 2.8.

As can be seen from Eq. 2.9 it is also possible to incorporate non-trivial densities of states into the simulation. Figure 2.9 shows the results for a tunnel junction between a normal metal and a superconductor [13]. With decreasing junction capacitance the  $I(V)$  characteristic is seen to deviate from the familiar BCS-curve (see section 1.3.2). The offset of the asymptote in trace (c) is  $\Delta/e + e/2C$ . In general we can state that energy dependent features in the  $I(V)$  curve of small capacitance

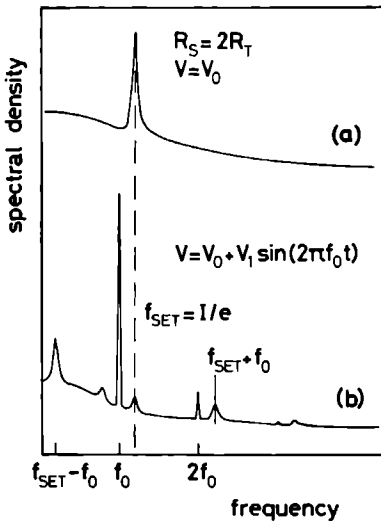


**Figure 2.8** Frequency spectrum of the SET-oscillations in a junction biased by a voltage source in series with a resistance  $R_S = 2R_T$  (a) without modulation, and (b) influenced by a non-resonant ac-modulation.

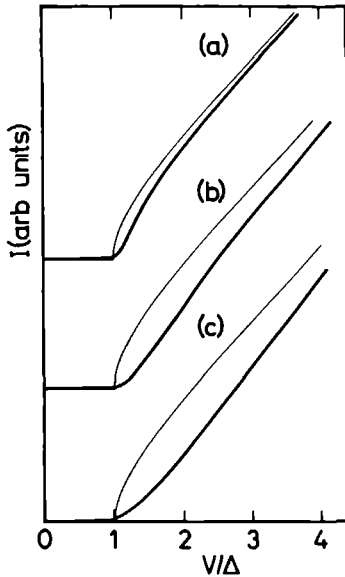


**Figure 2.9**  $I(V)$  characteristics of a small capacitance tunnel junction between a normal metal and a superconductor, as a function of decreasing junction capacitance  $\Delta/(e^2/2C) = 6, 2$  and  $1$  for traces (a), (b) and (c) respectively

tunnel junctions will be shifted to higher voltages by an amount of order  $e/2C$  due to the Coulomb blockade. Furthermore the presence of SET-oscillations with an amplitude  $e/2C$  will induce a broadening of all features in  $I(V)$  or its derivatives to  $V$ . Jaklevic *et al* [19] have applied this concept to inelastic tunneling processes.

### 2.2.4 Influence of the electromagnetic environment on the Coulomb blockade

In relation to the possibilities of practical realization, the condition of perfect current biasing, as employed in Ref [8], is a vast overidealization. In any physical situation the leads attached to the junction provide a stray capacitance that is generally much larger than the intrinsic junction capacitance. This stray capacitance constitutes a charge buffer, washing out all variations of the junction voltage. Therefore, in terms of the microscopical dynamics, all single junctions tend to behave as if they are voltage biased, independent of the externally connected source. The Coulomb blockade does not exist in a voltage biased junction, and SET-effects will be absent. For the observation of the Coulomb blockade it is therefore essential to establish some sort of effective current biasing on a local, i.e. mesoscopic scale. The key idea is that the junction can in principle be decoupled from stray capacitances by insertion of a large series impedance in the leads close to the junction.

But even then questions can be raised about how much of the environment is actually seen by a tunneling electron or one that is about to tunnel. At first this "electromagnetic horizon" was generally thought to be determined by  $c\tau_{tr}$ , i.e. the speed of light times the traversal time of tunneling. This traversal time has been studied by Buttiker and Landauer [20], and for conventional junctions with an oxide barrier width of some tens of Ångstroms it is estimated to be of the order of  $10^{-15}$  s.

Experiments [21, 22] however show that this concept gives far too optimistic predictions of the effective junction capacitance. In this section I will review recent theoretical work, pioneered especially by Nazarov [23, 24, 25], in which the main influence of the environment on the dc tunnel current is shown to originate from the impedance at frequencies much lower than  $\tau_{tr}^{-1}$ , namely  $\omega \sim \Delta E/\hbar \approx \max(eV, k_B T)/\hbar$ . The quantum nature of the tunneling process is expressed in something like an uncertainty relation, stating that a tunneling electron spends a time  $\Delta t$  "probing" whether or not the maximally available energy  $\Delta E$  really exists. During this time virtual tunneling processes are thought to create virtual photons which are able to spread into the environment up to distances of order  $ch/\Delta E$ , thus setting the electromagnetic horizon of the tunneling electron.

For studying the influence of the impedance of the environment on the junction characteristics it is necessary to incorporate the electrodynamic behaviour of the environment into the system Hamiltonian. The interaction between electrons is generally described in terms of photon exchange. The Coulomb interaction between a tunneling electron and its environment can therefore in principle be treated as an interaction of the electron with the photon modes of the environment. In a general representation of a single junction embedded in an environment with arbitrary impedance, the leads which connect the junction to a voltage source can be viewed as a transmission line with a characteristic, frequency dependent, impedance  $Z(\omega)$  and a corresponding characteristic spectrum of harmonic oscillator excitation modes (see Ref. [26] for a fundamental treatment).

Tunneling of an electron causes a charge imbalance in the leads, i.e. a displacement of the harmonic oscillators. It can be shown that the oscillator frequencies involved are in general smaller than  $\tau_{tr}^{-1}$ , for the oxide barrier junction types studied in this thesis, so that it can be assumed that the oscillators are displaced suddenly. Comparison of the amount of energy taken up by the environment as a consequence of the transfer of one electron charge across the junction – irrespective of whether or not the electron can be accommodated in an empty state of the opposite electrode – with the available energy supplied by the voltage source determines the possibility of a tunnel event [23, 24, 27, 28, 29]. If the probabilities of emission or absorption of an electromagnetic excitation of the junction environment are known, the  $I(V)$  characteristics can be calculated.

General treatments for arbitrary  $Z(\omega)$  are given by Refs. [23, 24, 28, 29, 30, 31, 32]. I will show that the validity of the results is restricted to series impedances much smaller than the tunnel resistance of the junction, which in turn is assumed much larger than  $R_Q$ . This limitation is not explicitly stated in the above references. Different groups basically treat the same model along different, though probably largely equivalent approaches and all arrive at comparable results. I will summarize the main concepts along the lines of Refs. [28, 29, 30, 31], being in my view the most insightful ones of the above mentioned approaches.

The model of the single junction connected to a voltage source by leads with characteristic impedance  $Z(\omega)$  is depicted in Fig. 2.10. The total impedance, including the junction capacitance, is  $Z_t(\omega) = (i\omega C + Z^{-1}(\omega))^{-1}$ . For the moment we

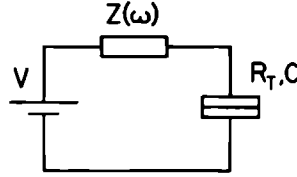


**Figure 2.10** Single junction connected to a voltage source by leads with arbitrary impedance  $Z(\omega)$ .

restrict ourselves to low pass environments for which  $\lim_{\omega \rightarrow 0} \omega Z(\omega) = 0$ . This means that there are no capacitors in series with the junction, so that the effects of charge quantization on the charging of isolated islands do not have to be considered. The latter situation mainly applies to the multiple junction geometries described in the section 2.3.

Devoret *et al.* [28] (see also Refs. [29, 30, 31]) start from a system Hamiltonian  $H = H_0 + H_{em} + H_T$ , where  $H_0$  describes the electronic degrees of freedom of the junction electrodes,  $H_{em}$  represents the electromagnetic environment and  $H_T$  is the conventional tunneling Hamiltonian. The system wave function is a product of the electronic wave function of the electrodes, the total wave function of the harmonic oscillators and the source wave function. Through a unitary transformation  $H \rightarrow UHU^{-1}$ , with  $U = e^{i\epsilon n_t \Phi/\hbar}$  in which  $n_t$  is the total number of electrons that has tunneled through the junction and  $\Phi = \int_{-\infty}^t V dt'$  is the phase coordinate as introduced in Eq. 2.3, it is possible to incorporate the coupling to the environment into the tunnel Hamiltonian, which can now be written as

$$H_T = \sum_{\sigma k q} T_{kq} a_{k\sigma}^* a_{q\sigma} \Lambda_e + \text{H.c.} \quad (2.11)$$

The operator  $\Lambda_e = e^{ie\Phi/\hbar}$  changes the charge coordinate of the source and the harmonic oscillators in the environment by  $e$ :  $\Lambda_e Q \Lambda_e^* = Q - e$ . At  $T = 0$  K the environment can be assumed to be in a ground state just before every tunneling event as long as the average time between tunnel events  $e/I$  is much larger than the relaxation time of the environment. This in turn is only true as long as  $|Z(\omega)| \ll R_T$ . At finite temperatures the environment is assumed to be in thermal equilibrium.

A tunnel event forces the system from a given initial state into a final state in which a number of oscillator modes has been excited, and in which the almost infinite charge buffer representing the voltage source has changed by one electron charge. If for example  $Z(\omega) = i\omega L$ , the system has one eigen mode with energy  $\hbar\omega_1 = \hbar/\sqrt{LC}$ . During a tunnel event the oscillator absorbs  $N$  photons with a probability given by  $r^N \exp(-r)/N!$ . The constant  $r$  is basically determined by the ratio between the effective impedance and the quantum resistance  $r = \pi Z/4R_Q = (e^2/2C)/(\hbar\omega_1)$ . The energy difference between the initial and final system state is given by  $E_f - E_i = \Delta E_{el} + N\hbar\omega_1 - eV$ , with  $\Delta E_{el}$  the energy gained by the tunneling electron which has to be positive or zero at  $T = 0$  K. Transitions are only



allowed if they conserve the total energy of the system. Transitions to a state with  $N$  photons are therefore only allowed when  $eV \geq N\hbar\omega_1$ . If  $r \ll 1$ , meaning that the environment impedance is much smaller than the quantum resistance, the elastic transition with  $N$  remaining zero is most probable and tunneling is allowed for any finite voltage  $V$ . As a result the  $I(V)$  characteristic is linear and does not display a Coulomb blockade. In the opposite case, with  $r \gg 1$ , i.e. a very large series impedance, inelastic transitions to states with  $N\hbar\omega_1 \approx e^2/2C$  are most probable, meaning that the dominant tunnel channels open up at voltages around  $e/2C$ . At lower voltages the current is strongly suppressed by the Coulomb blockade. Every time the voltage is increased by  $\hbar\omega_1/e$ , a new inelastic channel opens up, resulting in a stepwise increment of the conductance.

In general a junction environment will have a continuous spectrum of modes. Inelastic tunnel processes have to be considered in which the tunneling electron creates or absorbs an electromagnetic excitation with energy  $E$ . The probability for such tunnel events to happen is calculated to be [28, 29]

$$P(E) = (2\pi\hbar)^{-1} \int_{-\infty}^{+\infty} dt \exp[J(t) + iEt/\hbar], \quad (2.12)$$

in which the equilibrium phase correlation function  $J(t)$  is given by

$$J(t) = \int_0^\infty \frac{d\omega}{\omega} \frac{\text{Re}(Z_t(\omega))}{2R_Q} \left\{ \coth\left(\frac{\hbar\omega}{2k_B T}\right) [\cos(\omega t) - 1] - i \sin(\omega t) \right\}. \quad (2.13)$$

$P(E)$  is normalized ( $\int_{-\infty}^{+\infty} P(E) dE = 1$ ), and satisfies a sum rule  $\int_{-\infty}^{+\infty} E P(E) dE = e^2/2C$ , which states that for an allowed tunnel event on the average an energy  $e^2/2C$  is required by the environment.

If  $|Z(\omega)|$  is small,  $P(E)$  is strongly peaked around  $E = 0$ . For increasing  $|Z(\omega)|$  the peak gradually shifts towards  $E = e^2/2C$ , sharpening to a delta function when the series impedance is very much larger than  $R_Q$  [33]. Figure 2.11 illustrates this behaviour.

For the tunnel geometries of interest, i.e. junctions between two normal metals separated by an oxide or vacuum barrier, we can assume the densities of states as well as the tunnel matrix element to be constant on the relevant energy scale  $eV \ll E_F, \phi$ , with  $\phi$  the height of the tunneling barrier. The  $I(V)$  characteristic can now be calculated by plugging in an explicit expression for the total impedance, and numerically integrating the following analytical expression for the current (in first order perturbation approximation):

$$I(V) = \frac{1}{eR_T} \int_{-\infty}^{+\infty} dE \int_{-\infty}^{+\infty} dE' \{ f(E)[1 - f(E')]P(E + eV - E') - [1 - f(E)]f(E')P(E' - E - eV) \}. \quad (2.14)$$

In a conventional treatment without coupling  $P(E) = \delta(E)$ , meaning that the energy of the tunneling electron is conserved, which results in a linear  $I(V)$  characteristic.

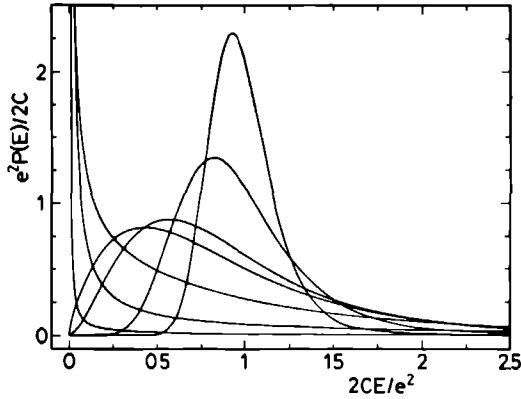


**Figure 2.11** The probability  $P(E)$  that a tunneling electron transfers an energy  $E$  to the oscillators in the electromagnetic environment of the junction for increasing values of the impedance of the environment (from Ref. [33]).

From the normalization of  $P(E)$  and  $EP(E)$  it can be deduced that for sufficiently large voltages the  $I(V)$  curve will always have linear asymptotes displaced from the origin by  $\Delta V = e/2C$ .

In a different approach of the same system (Fig. 2.10) Nazarov [23] presents his results in terms of two contributions to a deviation from the Ohmic  $I(V)$  dependence. The first term originates from the emission and absorption of real photons, and resembles Eqs. 2.12 to 2.14. with this exception that  $I(V)$  only depends linearly on  $J(t)$  instead of exponentially. This may be a matter of a first order approximation introduced somewhere along the way in his derivation, but on the other hand this would be surprising as Nazarov derives his results using the Keldysh diagram technique, which is exact to infinite order of perturbation. The first contribution is voltage dependent as  $\max(eV, k_B T)$  sets a limit to the energy of the photons involved. The second term, however, accounts for elastic tunneling due to processes involving virtual photons for which all frequencies are allowed. This term therefore follows the voltage dependence of the total current so that its contribution to the  $I(V)$  curve can not readily be distinguished, even though both contributions appear to be of the same order of magnitude. At the moment it is unclear to me to what extent these virtual processes are missed in the other approaches, and whether they are essential in quantitative fits of measurements.

For all models it is found that in general the mode spectrum of  $Z(\omega)$  will reflect itself in the shape of the  $I(V)$  characteristic. A spectrum containing discrete modes, resulting e.g. from interference effects due to the finite length of the leads, will cause steps in the conductance at positions  $V_{i,n} = n\hbar\omega_i/e$  corresponding to the energy of the modes and their harmonics.

Fig. 2.12 shows the results from Refs. [28, 29] for the situation  $Z(\omega) = R$ , i.e. a completely resistive environment. For small series resistances the  $I(V)$  curve

is almost linear as the Coulomb blockade is smeared out by quantum fluctuations of the junction charge. Finite temperatures will enhance this smearing [31]. Only for large series resistances ( $R \gg R_Q$ ) a suppression of the current at low voltages is observable, which can be attributed to the presence of a Coulomb blockade. Trace (e) in Fig. 2.12 shows the  $I(V)$  curve in case  $R = \infty$ . The current in Fig. 2.12 is calculated as a function of the externally applied bias voltage which is equal to the sum of the voltage drops over both the series resistance and the tunnel junction. The fact that the slope of trace (e) is still equal to  $R_T^{-1}$  reflects, in accordance with the already mentioned restriction, that the case  $R = \infty$  pertains to a situation in which  $R$ , although being much larger than the quantum resistance  $R_Q$ , is still very much smaller than the tunnel resistance  $R_T$ . This means that the junction is still not effectively current biased, so that the presence of a fully developed Coulomb blockade does not imply the occurrence of SET-oscillations, and that the impedance regime covered by the above described calculations differs fundamentally from the scope of Ref. [8], of which the results have been summarized in section 2.2.2 of this chapter.

This discrepancy can be understood in the following way: In the calculations described in this section it is explicitly assumed that each tunnel event starts from a situation where the system is in an equilibrium state regarding both the energy and charge distribution. This can only be the case when the discharge ( $RC$ -) time of the system is much shorter than  $e/I$ , or equivalently  $R_S \ll R_T$ . The charge imbalance caused by one tunnel event is already damped out long before a following transition takes place, and tunnel events are therefore strictly uncorrelated. The above described calculations solely account for the work done on the environment

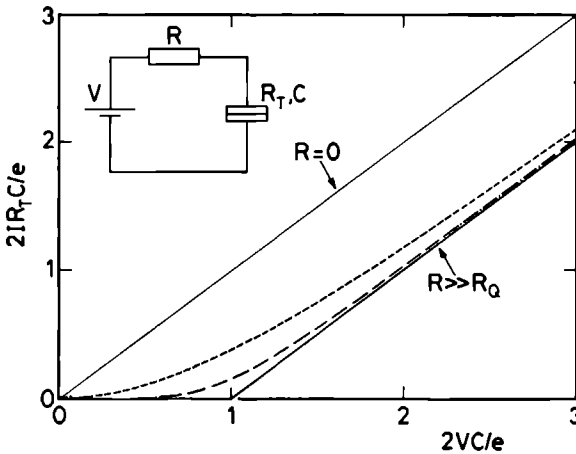


**Figure 2.12**  $I(V)$  characteristics of a junction in a purely resistive environment, for different values of the series resistance ( $R/R_Q = 0, 0.1, 1, 10, \infty$ ), according to the calculations of Ref. [28, 29].

during a single tunnel event. This energy, paid at the expense of the energy gain of the tunneling electron, happens to increase with decreasing junction capacitance.

In the current biased situation, ranging from  $R_S \approx R_T$  to  $R_S \gg R_T$  [8], the  $RC$ -time of the system is comparable to, or larger than, the average time interval between tunneling events, meaning that a tunneling electron still senses the charge imbalance caused by a preceding tunnel event. In the regime of small voltages one tunneling electron is even able to completely block the possibility of a following event during a finite amount of time. This induces time correlation of the tunnel events, resulting, at low current levels, in almost coherent SET-oscillations.

Strictly speaking therefore, the two regimes involve different conceptions of the word Coulomb blockade, which more or less accidentally happen to coincide regarding their dominant energy scale  $e^2/2C$ . The crossover between both regimes has not yet been described explicitly in the literature.

Part the chasm is bridged by the Monte Carlo simulations of section 2.2.3. That formalism is able to deal with bias conditions ranging from  $R_S \gg R_T$  to  $R_Q \ll R_S < R_T$ , but obviously fails for lower  $R_S$  values as it neglects the above described electrodynamic interaction with the environment. Although it may be possible to include  $P(E)$  into the evaluation of the tunnel probability in the Monte Carlo method, a better approach towards a theory describing the full range of possible series impedances would be a generalization of the above described analytical method. For this to be realized one has to drop the assumption that all tunnel events start from the same equilibrium situation. In that case Eq. 2.14 can no longer be used to calculate the current. Instead, one may employ a master equation approach similar to the one used in Ref. [8], but extended to include both the differential equation governing the time development of the junction charge and the probability  $P(E)$  for energy transfer to the electromagnetic modes of the environment.

Cleland *et al.* [22] also study the influence of quantum and thermal fluctuations on the Coulomb blockade in small-capacitance junctions, both for small and large series resistances. In contrast to Refs. [28, 29, 32] however they still take the junction to be current biased, and perform Monte Carlo simulations of the type described in section 2.2.3. That means that they intrinsically introduce SET-oscillations, which in turn are disturbed by the charge fluctuations. In the case of small series resistance the application of this method is probably not correct, as the above given fundamental calculation does not result in an oscillatory junction voltage. Fitting their experimental results with the theoretical prediction does not justify the method, as broadening due to whatever kind of fluctuations does not yield any discriminative features in an  $I(V)$  characteristic as featureless as an ideal SET-curve.

The situation where the lead impedance is small and the Coulomb interaction does not significantly change the in principle ohmic  $I(V)$  characteristic, is considered in more detail by Averin and Nazarov in Ref. [27]. In this regime there will be offset asymptotes, but these will be reached at much higher voltages. The offset is determined by both the junction capacitance and the capacitance of the leads close to the junction. Interference effects due to reflections in finite leads will still display themselves as steps in the derivative of the  $I(V)$  characteristics.

An analysis of the influence of the electromagnetic environment on quasi-particle and Cooper pair tunneling in junctions with superconducting electrodes has been made by Falci *et al.* [33]. Also in this limit where  $R_Q < R_S \ll R_T$  (the opposite limit has already been discussed in section 2.2.3) the Coulomb blockade is found to shift the superconducting gap features in the  $I(V)$  characteristics by  $e/2C$ . This shift is accompanied by a strong smearing of the features, which in this case is not due to voltage fluctuations but to the finite width of the probability spectrum  $P(E)$  (see Fig. 2.11).

### 2.2.5 Josephson junctions: Bloch oscillations

In the Hamiltonian description of the current biased single junction (see Eq. 2.3) the part  $Q^2/2C - I\Phi$  is similar to the Hamiltonian of the mechanical system of a free particle moving along the  $\Phi$  coordinate, with mass  $(\hbar/2e)^2C$ , momentum  $(\hbar/2e)Q$ , and subject to a generalized force  $I$ .  $\Phi$  and  $Q$  are related through  $[\Phi, Q] = i\hbar$ , so that in the same analogy  $Q$  can be expressed as  $Q = (\hbar/i) \partial/\partial\Phi$ . Apart from the tunneling events, therefore, the behaviour of the single junction system as a quantum mechanic entity is equivalent to that of a classical particle in a field, propagating according to a parabolic dispersion relation.

In case of a tunnel junction between two superconducting electrodes [9] a Josephson coupling energy  $U_J = -E_J \cos\phi$  has to be added to the Hamiltonian. Here  $\phi$  is the condensates phase difference across the junction, which is related to  $\Phi$  as  $\phi = (2e/\hbar)\Phi$ . In the above described analogy the Josephson coupling adds a periodic potential to the mechanical single particle Hamiltonian. This Hamiltonian is well known in solid state physics. The corresponding Schrödinger equation is to be solved in terms of Bloch waves (see e.g. [34, 35])  $\psi_k = u_k(\phi) \exp(iq\phi/2e)$ , with  $u_k(\phi)$  obeying  $u_k(\phi + 2\pi) = u_k(\phi)$ , and  $q$  the quasi-momentum replacing the real momentum  $Q$ . The corresponding dispersion relation takes the form of an energy band spectrum. Figure 2.13(a) illustrates the situation in which  $E_Q = Q^2/2C \gg E_J$ , meaning that Coulomb repulsion dominates over the Josephson coupling. Quasi-particle effects are ignored for the moment.

Under influence of a small and constant generalized force  $I = \dot{q}$  the system will move through the band, undergoing Bragg-reflections whenever it crosses a zone boundary ( $q = (2n + 1)e$  with  $n = 0, \pm 1, \pm 2, \dots$ ). It can be proven [9], that these Bragg-reflections correspond to the tunneling of a Cooper pair through the junction. If the current  $I$  is constant, Cooper pairs will tunnel after exactly equal time intervals. As a result the junction voltage ( $V = Q/C$ ) will oscillate with a frequency  $f_{\text{Bloch}} = I/2e$ . These so-called Bloch oscillations are truly coherent quantum oscillations, in contrast to the SET-oscillations which always suffer from stochastic noise. If the current is small enough the system stays inside a single band. For higher currents interband transitions (Zener tunneling) will tend to destroy the coherence of the Bloch-oscillations. The corresponding  $I(V)$  characteristics are depicted in Fig. 2.13(b). If  $E_Q$  and  $E_J$  are of the same order of magnitude, the Bloch oscillations will be in competition with the well-known Josephson oscillations. In

superconducting junctions with significant quasi-particle tunneling the Bloch- and SET-oscillations can coexist.

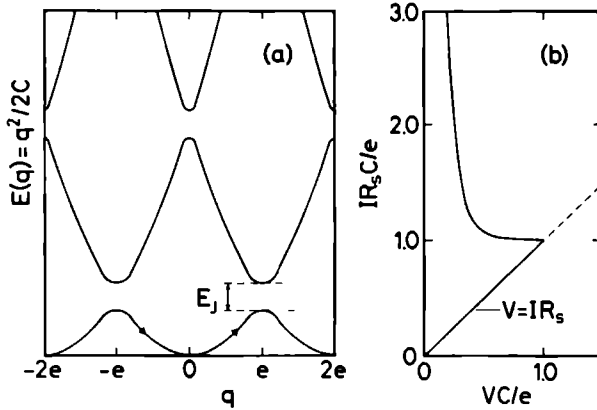


**Figure 2.13** (a) Energy band spectrum for a small capacitance Josephson junction with  $E_Q \gg E_J$ . (b) Typical  $I(V)$  curves of a Josephson junction with small capacitance (from Ref. [9]).

### 2.3 Multiple junction geometries

In geometries of serially connected tunnel junctions the impedance  $Z(\omega)$  of the environment of a single junction is infinite at zero frequency, due to the capacitance of the other junctions. This system therefore constitutes a high-pass environment with charging properties different from the single junction case. The presence of a Coulomb blockade in a system consisting of a series connection of two small capacitance tunnel junctions (which we will call from now on: the double junction system) was already established both theoretically and experimentally in 1969 by Zeller and Giaever [1]. As they applied their theory to a system of many double junction systems acting in parallel, with a wide distribution of junction sizes, they unfortunately missed the notion of more dramatic consequences such as the Coulomb staircase, which is observed in the isolated double junction systems that can nowadays be produced with the help of nanolithography or STM-techniques.

#### 2.3.1 Double junctions: incremental charging and Coulomb staircase

In case of a single small capacitance tunnel junction connected to low resistance leads the charging of the junction is determined by the parallel connection of the intrinsic junction capacitance, proportional to the size of the tunneling area, and the generally much larger stray capacitance of the leads connecting the junction to a source. As we have seen in the previous section this stray capacitance suppresses the Coulomb blockade. Let us now focus on the situation depicted in Fig. 2.14, in

which we have two small capacitance junctions connected in series. The junctions are characterized by capacitances  $C_1$  and  $C_2$  and tunnel resistances  $R_1$  and  $R_2$ . The impedance of the environment of a single junction in this array is now determined by the impedance of the series connection of the small capacitance of the second junction and the stray capacitance  $C_s$  of the leads. For junction 1 this impedance equals  $(C_2 + C_s)/j\omega C_2 C_s$ , the value of which is obviously completely determined by the small size of  $C_2$ . This means that in a double junction system like this each individual junction effectively sees a high impedance environment, independent of the impedance of the leads or the nature of the bias source. Therefore, at low enough temperatures, conduction in the double junction system will be fully dominated by charging effects.

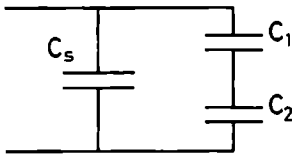


**Figure 2.14** Schematics of a double junction system  $C_1, C_2$  connected to leads with stray capacitance  $C_s$

The same conclusion can be reached by looking at the system from another point of view. The central electrode connecting the two tunnel junctions essentially is an isolated island that can be charged by tunnel events through either one of the two junctions. The capacitance  $C_{\text{eff}} = C_1 + C_2$  of this island with respect to its environment is limited in a natural way as a consequence of the finite size of the island. This effective capacitance now determines the change in the central electrodes potential due to charging of the electrode. In the system under consideration charging can only take place in units of  $e$ , as the charge is transferred to the central electrode by tunneling through the junctions it is connecting (so-called incremental charging).

Knowing that the smallness of junction capacitances in a double junction system will affect the conductance of the system in a fashion that is irrespective of the lead impedance and bias condition, we can conveniently model the system as two junctions in series connected to a voltage source. This model system is sketched in Fig. 2.15. As we will see later on, from an experimental point of view this also greatly relaxes the constraints for the actual observation of charging effects. The potential differences across both junctions can now be expressed in terms of the externally applied potential difference  $V$  and the excess charge on the central electrode.

$$V_1 = \frac{VC_2}{C_1 + C_2} - \frac{ne - Q_0}{C_1 + C_2} \quad (2.15a)$$

$$V_2 = \frac{VC_1}{C_1 + C_2} + \frac{ne - Q_0}{C_1 + C_2} \quad (2.15b)$$

In this expression  $ne$ , with  $n$  an integer, is the excess charge as a result of tunneling processes, and  $Q_0$  is a phenomenological parameter accounting for the possible

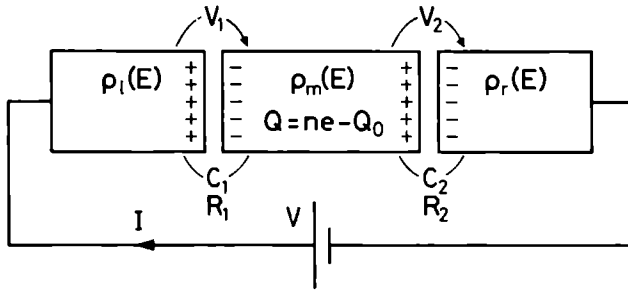


**Figure 2.15** The model system of two small capacitance tunnel junctions in series, biased by a voltage source. The indicated quantities and variables are explained in the text.

misalignment of Fermi levels as a consequence of the restriction of discrete charge transfer, and the inductive effects of static charges in the physical environment of the middle electrode. The absolute value of this residual charge is always smaller than  $e/2$ .

The  $I(V)$  characteristics of the system can be calculated by considering the time evolution of  $n$ , i.e.  $n(t)$ , in a way similar to the one used in the Monte Carlo simulations of section 2.2.3. This time evolution is governed by the forward and backward tunneling rates  $r_1, l_1$  and  $r_2, l_2$  of junctions 1 and 2 respectively:

$$n(t + \Delta t) = \begin{cases} n(t) + 1, & \text{with probability } [r_1(V_1) + l_2(V_2)]\Delta t \\ n(t) - 1, & \text{with probability } [l_1(V_1) + r_2(V_2)]\Delta t \\ n(t), & \text{with probability} \\ & 1 - [r_1(V_1) + l_1(V_1) + r_2(V_2) + l_2(V_2)]\Delta t. \end{cases} \quad (2.16)$$

The transition rates are calculated in a general way according to the tunneling theory described in chapter 1, including the effects of the energy dependence of the tunnel matrix elements and the densities of states of the electrodes for as far as they do not cancel, as well as the effects of finite temperature. With  $E_l, E_m$  and  $E_r$  being the Fermi energies of the left, middle and right electrode we find (similar to e.g. Refs. [36, 37]):

$$r_1(V_1) = \frac{2\pi}{\hbar} \int_{-\infty}^{\infty} |T_1(E)|^2 \rho_l(E - E_l) \rho_m(E - E'_m) \times f(E - E_r) [1 - f(E - E'_m)] dE, \quad (2.17a)$$

$$l_1(V_1) = \frac{2\pi}{\hbar} \int_{-\infty}^{\infty} |T_1(E)|^2 \rho_m(E - E_m) \rho_l(E - E'_r) \times f(E - E_m) [1 - f(E - E'_r)] dE, \quad (2.17b)$$

$$r_2(V_2) = \frac{2\pi}{\hbar} \int_{-\infty}^{\infty} |T_2(E)|^2 \rho_m(E - E_m) \rho_r(E - E'_r) \times f(E - E_m) [1 - f(E - E'_r)] dE, \quad (2.17c)$$



$$l_2(V_2) = \frac{2\pi}{\hbar} \int_{-\infty}^{\infty} |T_2(E)|^2 \rho_r(E - E_r) \rho_m(E - E'_m) \times f(E - E_r) [1 - f(E - E'_m)] dE. \quad (2.17d)$$

Primes denote final values of the Fermi levels after tunneling and consequent charge redistribution.  $|T_1(E)|^2$  and  $|T_2(E)|^2$  are the tunnel matrix elements of junctions 1 and 2.  $\rho_l(E)$ ,  $\rho_m(E)$  and  $\rho_r(E)$  are the densities of states of the left, right and middle electrode, the arguments of which are defined with respect to the Fermi levels of the electrodes, and  $f(E)$  is the Fermi-Dirac distribution.

The explicit incorporation of the density of states is necessary if we want to apply the analysis to e.g. a system with superconducting electrodes [18, 38] or a central electrode which is so small that its discrete electronic structure becomes noticeable (see e.g. section 4.3 of chapter 4, and Refs. [36, 39]). For the case that all three electrodes are normal metals with continuous densities of states the expressions of Eq. 2.17 can be greatly simplified by taking the transmission probability and the densities of states out of the integral and writing them as a constant prefactor  $1/(e^2 R_{1,2})$ . The remaining expressions then integrate to

$$r_1(V_1) = \frac{1}{e^2 R_1} \frac{1}{1 - \exp[-(E_l - E'_m)/k_B T]} \quad (2.18a)$$

$$l_1(V_1) = \frac{1}{e^2 R_1} \frac{1}{1 - \exp[-(E_m - E'_l)/k_B T]} \quad (2.18b)$$

$$r_2(V_2) = \frac{1}{e^2 R_2} \frac{1}{1 - \exp[-(E_m - E'_r)/k_B T]} \quad (2.18c)$$

$$l_2(V_2) = \frac{1}{e^2 R_2} \frac{1}{1 - \exp[-(E_r - E'_m)/k_B T]} \quad (2.18d)$$

For all practical cases of interest in this thesis we may assume that the charge redistribution on the central electrode is instantaneous, which is true if the charge relaxation time is much shorter than the tunneling time. This assumption expresses that we are only considering what is called the non-local limit. The electron tunneling through one of the junctions interacts with the charges on both. The charging energy involved is thus, as we will see, determined by the sum of both capacitances in series. In the opposite local limit [40] the junctions are assumed so far apart that the energy change upon tunneling is determined by the individual Coulomb blockades of the junctions. This may be the case when the charge relaxation time is larger than the tunnel time, due to e.g. the resistivity of the central electrode, or the fact that the central electrode is large so that its capacitance with respect to the environment (the substrate, back gates, etc.) is much larger than the junction capacitances.

An intermediate case where the charge redistribution time is comparable to the tunneling time  $\tau_{tr}$  [20] may be found in non-metallic systems, such as e.g. can be created in the two-dimensional electron gas (see section 2.4.2), for which  $\tau_{tr}$  can be several orders of magnitude larger than the value of  $10^{-14}$ – $10^{-15}$  s which is assumed for the case of an oxide barrier between two metallic electrodes. It would

be interesting to realize this intermediate situation also in metallic systems as the dependence on charge redistribution parameters may yield quantitative information on the traversal time in well defined oxide barriers.

Furthermore it is assumed (see Amman *et al.* [36]) that the redistribution responds linearly to the charge transfer, so that the energy effectively gained by the tunneling electron can be calculated by an integration over  $n$  of the potential difference across the junction from  $n$  to  $n \pm 1$ . One then finds for the energies in Eq. 2.18:

$$E_l - E'_m = e \int_n^{n+1} V_1(n', V) dn' = eV_1(n, V) - E_c \quad (2.19a)$$

$$E_m - E'_l = -e \int_{n-1}^n V_1(n', V) dn' = -eV_1(n, V) - E_c \quad (2.19b)$$

$$E_m - E'_r = e \int_{n-1}^n V_2(n', V) dn' = eV_2(n, V) - E_c \quad (2.19c)$$

$$E_r - E'_m = -e \int_n^{n+1} V_2(n', V) dn' = -eV_2(n, V) - E_c. \quad (2.19d)$$

$E_c = e^2/2(C_1 + C_2)$  is the energy associated with charging the central island with one excess electron.

In the above energy considerations it is also assumed that the energy relaxation time in the central electrode is much shorter than the time between successive tunnel events, so that every event starts from a thermal equilibrium situation. Also the tunneling time has to be much smaller than the time between tunnel events, which is correct as long as  $I \ll e/\tau_{tr} \approx e/(10^{-15}\text{s}) \approx 10^{-4}$  A. This condition is satisfied for all junctions of interest in this thesis.

Before we proceed to calculate the complete  $I(V)$  characteristics for the double junction system, we will have a closer look at Eqs. 2.18 and 2.19, as already from these some basic predictions can be extracted, especially concerning the behaviour near the origin. This will give insight in the interpretation of further calculations.

From the zero temperature limit of Eq. 2.18 we can derive the following conditions under which the respective tunnel rates are non-zero:

$$r_1 \neq 0 \quad \text{if} \quad C_2V - ne + Q_0 - e/2 > 0 \quad (2.20a)$$

$$l_1 \neq 0 \quad \text{if} \quad -C_2V + ne - Q_0 - e/2 > 0 \quad (2.20b)$$

$$r_2 \neq 0 \quad \text{if} \quad C_1V + ne - Q_0 - e/2 > 0 \quad (2.20c)$$

$$l_2 \neq 0 \quad \text{if} \quad -C_1V - ne + Q_0 - e/2 > 0. \quad (2.20d)$$

Setting  $Q_0 = 0$  for the moment, we start from a situation with  $n = 0$  and  $V$  increasing from zero. At  $T = 0$  K the backward rates  $l_1$  and  $l_2$  are always zero for positive bias and corresponding  $n$ -values. From Eqs. 2.20a and 2.20c we see that the ratio  $C_2/C_1$  determines which junction opens up first. If  $C_2 > C_1$  the tunnel rate  $r_1$  becomes finite at  $V = e/2C_2$ . A resulting tunnel event will change  $n$  from 0 to 1, which immediately sets  $r_2 > 0$  and  $r_1 = 0$ , allowing tunneling through the second junction, which again changes  $n$  to zero. In this way electrons can be

transferred through the complete system one by one. A similar reasoning applies to the situation  $C_2 < C_1$ . The effective Coulomb blockade is thus determined by the largest of the two capacitances in the system and the threshold voltage equals  $V = e/2\max(C_1, C_2)$ .

Supposing that  $R_2 \gg R_1$ , junction 2 determines the net current through the system, while junction 1 simply acts as a quick supply of electrons, recharging the central electrode immediately after a tunnel event through junction 2. If also  $C_2 > C_1$ , we can expect a jump in the current at  $V = e/2C_2$ . The jump has a height  $\Delta I = e/2C_2R_2$ , and is followed by a plateau with slope  $C_1/R_2(C_1 + C_2)$ . As we can see from Eq. 2.20a,  $r_1 = 0$  for  $n = 1$  until  $V = 3e/2C_2$ . At this voltage we therefore again expect a current step, this time to a value  $I = 3e/2C_2R_2$ , followed by a plateau with the same slope as the first one. The same reasoning can be repeated for higher voltages as well as for negative bias, in which case we have to consider  $l_1$  and  $l_2$ . In this way we can predict that the  $I(V)$  characteristic of a double junction system with  $R_2 \gg R_1$  and  $C_2 > C_1$  will display sharp current steps at voltages  $V_n = \pm(e + 2|n|)/2C_2$  for which the maximally allowed number of excess charges  $n$  on the central electrode changes by one to  $n \pm 1$ . Such a characteristic is called a Coulomb staircase. The plateaus will be almost horizontal if  $C_2 \gg C_1$ . In this situation a finite value of the residual charge  $Q_0$  will mainly result in a shift of the step positions by  $\Delta V_n = -Q_0/C_2$ , as can again be seen from Eq. 2.20.

In the opposite situation, i.e.  $R_2 \gg R_1$  but  $C_2 < C_1$ , junction 2 will first allow tunneling at  $V = e/2C_1$ , thus changing  $n$  to  $n - 1$ , which immediately sets  $r_1 \neq 0$ . Again junction 2 determines the effective rate of the total system, and junction 1 quickly resupplies charge to the central electrode. At  $V = e/2C_1$  we thus expect the onset of current with a rate equal to  $I = (C_1V - e/2)/[R_2(C_1 + C_2)]$ , i.e. a linearly increasing current starting at the threshold voltage. Above this voltage the charge  $ne$  on the central electrode is either 0 or  $-e$ , with  $r_1 = 0$  if  $n = 0$ . At  $V = e/2C_2$  however junction 1 will allow a finite  $r_1$  even for  $n = 1$ . This certainly does cause a step in the current to a value  $I = e/2C_2R_2$ . This step is followed by a linear increase with the same slope as before the step. The steps will again repeat themselves with a period  $\Delta V = e/C_2$ , where each step corresponds to a sudden increase of the maximally allowed number of excess electrons on the central electrode. In this situation a finite value of  $Q_0$  will shift the Coulomb blockade voltages ( $\pm e/2C_1$ ) and the step positions in opposite directions by  $Q_0/C_1$  and  $-Q_0/C_2$  respectively.

The complete  $I(V)$  characteristics for all possible values of  $R_2/R_1$  and  $C_2/C_1$  and finite temperature can now be derived from Eqs. 2.15–2.19 along two different approaches. The first developed method is an extension of the Monte Carlo technique which is also applied to the single junction case [15, 16, 17]. Later the authors of Refs. [17, 36, 41] were able to derive an analytic expression for  $I(V)$  by rewriting the problem in a master equation and finding its stationary solution.

### 2.3.2 Monte Carlo simulations

A numerical evaluation of the time development of the state of the double junction system can be carried out along the lines sketched in section 2.2.3. Given the externally applied voltage  $V$ , and starting from some initial value for  $n(t=0)$ , the individual junction voltages and corresponding forward and backward tunneling rates are calculated after each time interval  $\Delta t$ . By generating random numbers, and comparing these with intervals proportional to each of the tunneling rates, it is decided whether or not a tunneling event takes place. If so, the excess charge  $n(t)$  is adjusted, and the procedure is repeated at the next point in time  $t + \Delta t$ . The current is calculated by counting the net amount of electrons that passed through either one of the junctions, and dividing that amount by the evaluated time span, which must be sufficiently long in order to eliminate noise in the calculated  $I(V)$  characteristic.

From the simulated time development we find that the tunnel events through each individual junction are completely uncorrelated. The subsequent tunnel events through junctions 1 and 2, however, prove to be strongly correlated, i.e. the time interval between tunneling to the central electrode through one junction and subsequent tunneling from the central electrode through the other is more or less constant. This involves a correlation of tunnel events in space domain, in contrast to the correlation in the time domain found in current-biased single junctions (SET-oscillations). This correlation was of course foreseen in the previous section where we noted that tunnel events through one junction immediately set the tunnel rate of the second junction from zero to a finite value.

Figure 2.15 shows the results of Monte Carlo simulations for different values of the resistance and capacitance ratios at zero temperature.

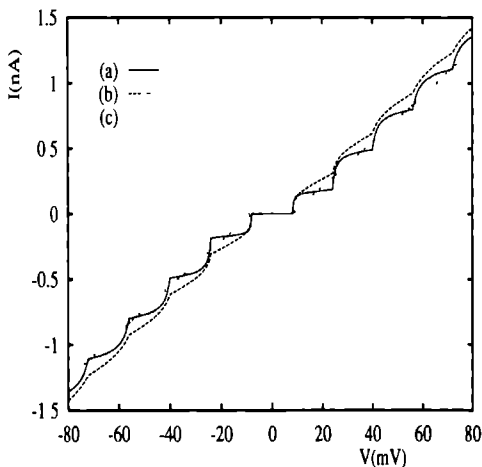


**Figure 2.16**

Monte Carlo simulation of the  $I(V)$  characteristics of the double junction system at  $T = 0$  K for the ratios  $(R_1/R_2, C_1/C_2)$  equal to (a) (25, 10), (b) (25, 1), (c) (25, 0.1).

### 2.3.3 Analytic expression

In Refs. [17, 36, 41] the ensemble averaged dynamics of the two junction system is calculated on the basis of a master equation approach. To this end  $\rho(n, V, t)$  is defined to be the probability that  $n$  excess electrons are present on the middle electrode at time  $t$ , while an external voltage  $V$  is applied. The time development of  $\rho(n, V, t)$  is given by the following master equation:

$$\begin{aligned} \partial\rho(n, V, t)/\partial t = & [r_1(n-1, V) + l_2(n-1, V)]\rho(n-1, V, t) \\ & + [l_1(n+1, V) + r_2(n+1, V)]\rho(n+1, V, t) \\ & - [r_1(n, V) + l_1(n, V) + r_2(n, V) + l_2(n, V)]\rho(n, V, t). \end{aligned} \quad (2.21)$$

The tunneling rates  $r_{1,2}(n, V)$  and  $l_{1,2}(n, V)$  are defined in Eq. 2.17. The potential differences  $V_1$  and  $V_2$  are defined in terms of the independent variables  $n$  and  $V$ . A stationary solution can be found by simply demanding that  $\partial\rho(n, V, t)/\partial t = 0$ , which is equivalent to demanding that the net probability of making a transition between any two states (say  $n$  and  $n+1$ ) is zero. If  $\rho(n, V)$  is known, the current can be calculated by summing the net transition rates through either one of the junctions over all states  $n$ . The result comes down to [36]:

$$I = \sum_{n=-\infty}^{+\infty} e[r_2(n, V) - l_2(n, V)]\rho(n, V) \quad (2.22)$$

with

$$\rho(n, V) = \frac{[\prod_{i=-\infty}^{n-1} x(i, V)][\prod_{i=n+1}^{+\infty} y(i, V)]}{\sum_{j=-\infty}^{+\infty} [\prod_{i=-\infty}^{j-1} x(i, V)][\prod_{i=j+1}^{+\infty} y(i, V)]}, \quad (2.23)$$

in which  $x(n, V) \equiv r_1(n, V) + l_2(n, V)$  and  $y(n, V) \equiv l_1(n, V) + r_2(n, V)$ .

The analytic approach basically gives the same results as obtained from Monte Carlo simulations, and is drastically less time consuming for the evaluation of the sensitivity of the  $I(V)$  characteristic to changes in the system parameters.

### 2.3.4 Modulation of the potential of the central electrode

In Eq. 2.16 we introduced the residual charge  $Q_0$  to account for a possible induced potential shift of the central electrode as a consequence of the presence of static charges in the electrodes environment. The effect of  $Q_0$  on the  $I(V)$  characteristics has already been analyzed in section 2.3.1 for two extreme limits of the involved parameter values. As can be seen from Fig. 2.17 (a), changing  $Q_0$  in a system with a well-developed Coulomb staircase ( $R_2 > R_1, C_2 > C_1$ ) mainly results in a collective shift of the positions of the steps, keeping the voltage spacing constant. Fig. 2.17 (b) shows the opposite shifts of steps and kinks in the  $I(V)$  curve of a

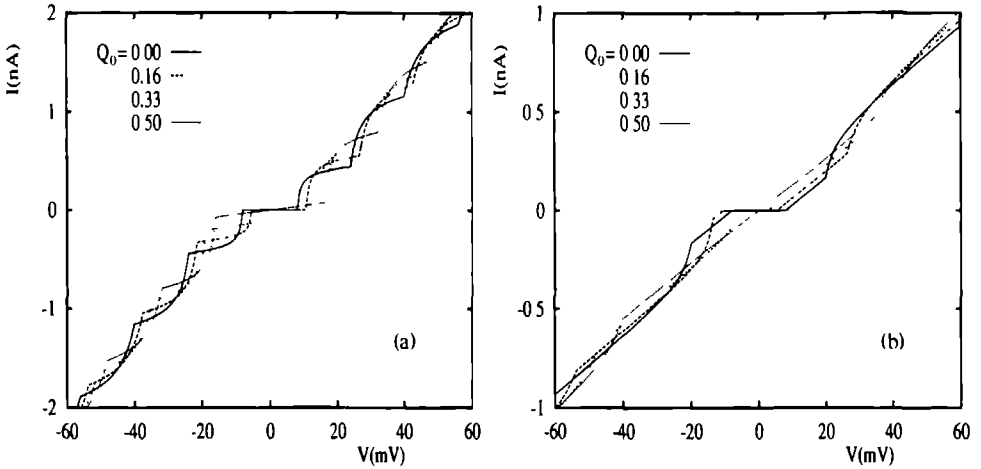


**Figure 2.17** The influence of different values of the residual charge  $Q_0$  on the  $I(V)$  curve of the double junction system for two different parameter sets, calculated with the analytic expression of Ref. [36]. (a)  $R_1 = 20 \text{ M}\Omega, R_2 = 2 \text{ M}\Omega, C_1 = 10 \times 10^{-18} \text{ F}, C_2 = 1 \times 10^{-18} \text{ F}$ ; (b)  $R_1 = 50 \text{ M}\Omega, R_2 = 2 \text{ M}\Omega, C_1 = 4 \times 10^{-18} \text{ F}, C_2 = 10 \times 10^{-18} \text{ F}$ , and  $T = 0 \text{ K}$ .

system with  $R_2 > R_1, C_2 < C_1$ .

Hanna and Tinkham [37] use the above formalism to show that, given  $R_2/R_1 \gg 1$ , the  $I(V)$  curves can be separated into four distinct cases depending on the ratio of capacitance  $C_2/C_1$  and the size of  $Q_0$ . Supported by fits of experimental data, the theory allows determination of the parameters  $C_1, C_2$  and  $Q_0$  from the position of steps and kinks in the central region of the  $I(V)$  characteristic. In experimental situations  $Q_0$  is thought to be the result of the ionization of impurities or other localized states in the oxide or possible surface contamination near the central electrode. Such a localized charge changes the electric field and induces a shift in the charge distribution on the central electrode, thus causing a change in the distribution of the applied potential difference over both junctions in the system.

Another way of influencing the central electrode's potential is established by the use of an extra, non-tunneling, capacitive coupling  $C_{\text{mod}}$ , as drawn in Fig. 2.18 [8, 11, 18, 36, 42]. By changing the voltage  $V_{\text{mod}}$  on the modulation capacitor the central electrodes' potential can be changed continuously. This system is called the Single-Electron Transistor. For a bias voltage  $V$  inside the Coulomb blockade region the system can be switched continuously between a zero-current state and a state with finite current. The influence of the electromagnetic environment, as discussed for single junctions in section 2.2.4, on the case of the Single-Electron Transistor has recently been analyzed in Ref. [43].

### 2.3.5 Multiple junction arrays

A series connection of more than two tunnel junctions can be used to increase the apparent Coulomb blockade. For a one-dimensional array with  $N$  identical junctions with capacitance  $C$  the  $I(V)$  characteristic will, for large voltages, approach an asymptote which is offset from the origin by  $Ne/2C$  [44, 45]. An analytic approach is given by Ref. [46].

The behaviour of large arrays is strongly influenced by the parasitic capacitance  $C_0$  between the islands (the electrodes interconnecting the junctions) and the substrate. This capacitance reduces the coupling between junction capacitors, as it absorbs a part of the excess charge on the island. If  $C_0 \ll C$  an excess electron charge on island  $i$  will polarize its neighbouring islands, causing an exponentially decaying potential  $\propto \exp(-|i-k|M)$ , with a decay constant of order  $M \approx (C/C_0)^{1/2}$  [40, 47]. The excess electron plus its polarized environment is called a charge soliton, and the conduction of the array has to be described in terms of the motion of these solitons. Solitons with equal charge repel each other and will tend to form a Wigner lattice with constant spacing between the solitons. Translation of the lattice under the influence of an applied electric field causes current flow. As a result of the passage of a soliton train (moving Wigner lattice) the potential of a single island is predicted [40, 47] to display periodic oscillations, strongly resembling the SET-oscillations described in section 2.2. These oscillations can also be locked to an external ac-modulation.

## 2.4 Experimental status

In this section I will very briefly review the present experimental status of the field, with emphasis on the results obtained with nanolithographic junctions. The results obtained with the STM-technique will be further discussed in chapters 3 and 4.

### 2.4.1 Metal-insulator-metal systems

Modern electron-beam lithography techniques are able to define metallic structures with widths between a few hundred and 50 nanometers. Using shadow evaporation in combination with a suspended bridge mask – a technique developed by Dolan [48, 49] – junction areas of order  $0.01 \mu\text{m}^2$  (with corresponding capacitances

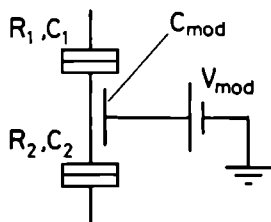


**Figure 2.18** Single-Electron Transistor with a third terminal capacitively coupled to the central electrode

in the  $10^{-15}$  to  $10^{-16}$  F regime) are routinely attainable. In tunnel junctions established with the STM-technique the capacitance can be made even smaller.

### Single junctions

Observation of the Coulomb blockade in single junctions has proven to be extremely difficult. There are several papers on STM-measurements claiming the observation, but a discussion of these result has to be postponed to the next chapter. Delsing *et al.* [21] report that the characteristics of single nanolithographic junctions, for which no care has been taken to decouple them from stray capacitances, are in reasonable agreement with the predictions of Nazarov [23, 24, 25, 27], in the sense that they only show a faint trace of the Coulomb blockade. The same authors report the observation of a clear Coulomb blockade in a junction connected to current and voltage leads consisting of multiple junction arrays. Cleland *et al.* [22] have succeeded in connecting resistive leads to a single junction and observed characteristics in accordance with the theory of Refs. [28, 29, 32]. So far no SET-oscillations have been observed. Charging effects have also been investigated in systems with superconducting electrodes. Kuzmin and coworkers [50] have recently reported the observation of phase-locking of Bloch-oscillations to external microwave irradiation in single junctions connected to resistive leads.

### Double junctions

As in the early work of Refs. [1, 2], the first more recent observations of the Coulomb blockade were made in double junction systems. Fulton and Dolan [42] observed the blockade in a nanolithographic system, and were able to modulate the  $I(V)$  with a back-gate. Barner and Ruggiero [51] observed the Coulomb staircase in a junction, similar to that of Ref. [1], with a granular film in the oxide barrier. They assume this to be the result of uniform grain size, so that all small double junctions acting in parallel effectively have the same capacitance. Kuzmin and Likharev [52] report observation of the staircase in a similar system, for which they claim that, due to a special way of evaporating a silicon oxide barrier, the current is carried by one or at most a few of the larger grains in the junction.

At the moment several groups master the technology of producing nanolithographic junctions in almost arbitrarily complex circuits. Results on double junctions can in general be perfectly fitted with the theory of section 2.3 [18, 44, 53]. The effects of quasi-particle and Josephson tunneling in case of superconducting electrodes are also very well understood (see e.g. Ref. [18]).

In the STM-approach (see chapter 4) double junctions can be realized by tunneling through an individual grain in a granular metal film. Grain diameters can be as small as 50 Å, yielding capacitance values as small as  $5 \times 10^{-18}$  F [15, 36, 37, 38]. These systems show clear Coulomb staircases, including the effects of non-zero residual charge  $Q_0$ .



## Multiple junction arrays

Junction arrays have been used as a means of magnifying the effective system Coulomb blockade [44, 45, 54], thus simplifying its observation. More important is the observation of coherent soliton motion in arrays designed to have a small  $C_0/C$  ratio [21, 49, 53]. The voltage oscillations could be locked to external ac-modulation, and appeared not to be very sensitive to non-uniformity of the junction parameters by some 10%. In two-dimensional arrays of small normal metal and Josephson junctions interesting collective effects concerning charge and flux motion are predicted and observed (see e.g. Refs. [55, 56]).

### 2.4.2 Non-metal systems

Using metal gate electrodes on a GaAs-AlGaAs heterojunction, it is possible to squeeze the two-dimensional electron gas (2DEG) at the GaAs-AlGaAs interface into various structures such as channels, point contacts, quantum wires and quantum dots. In a narrow constriction the potential barrier can be tuned by changing the electrode voltage. If two such constrictions connect an isolated area of the 2DEG to larger 2DEG reservoirs, one essentially establishes a double junction system as described in section 2.3. The main differences with the metallic junction systems are the two dimensional density of states, the large electron wave length and the wider and lower potential barriers.

References [57, 58, 59, 60] report the observation of conductance oscillations of these double junction systems in response to incremental charging of the central region. Kouwenhoven *et al.* [59] have been able to observe Coulomb staircases which could be modulated by the voltage on an extra gate electrode.

Similar effects can be observed in laterally confined resonant tunneling structures. In this case the  $I(V)$  characteristic will also be influenced by the discrete density of states of the quantum dot [61, 62].

### 2.4.3 Conclusion

As a general conclusion it can be stated that the basic concepts of the "orthodox theory" of charging effects have been verified experimentally, even though SET-oscillations in single junctions are still to be observed. These concepts are now being applied to a much wider range of systems outside the scope of intermetal tunneling.

## 2.5 Practical applications

Both SET- and Bloch-oscillations can be used in practice for metrological purposes. The resonances of these oscillations to an externally applied modulation (e.g. microwave irradiation) allow the definition of a dc-current standard based on frequency measurement. As frequency measurement is in essence a counting problem, it can be carried out with extreme accuracy. This application is analogous to the

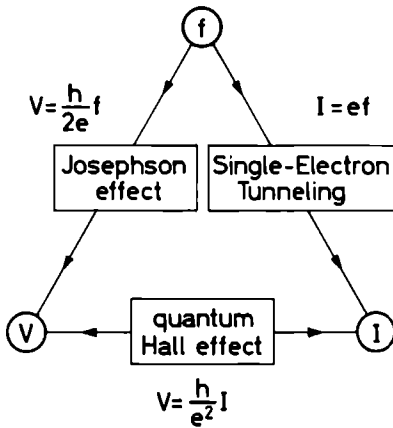


**Figure 2.19** The metrological triangle connecting standards for the measurement of current, voltage and resistance.

dc-voltage standard based on the ac-Josephson effect, in which the  $I(V)$  curve displays so-called Shapiro steps when the Josephson voltage oscillations resonate with irradiated microwaves. Combination of the current and voltage standards with the resistance standard based on the Quantum Hall effect results in a "quantum metrological triangle", as shown in Fig. 2.19. A connection of the three effects in a single experiment provides a possibility for testing the consistency of our definition of the quantum constants  $e$  and  $\hbar$ .

In a slightly different approach a current standard has already been developed experimentally by Geerligns *et al.* [63]. Their device is called "Single Electron Turnstile" and operates like a shift register by transferring electrons one by one through an array of four or possibly more junctions, with a frequency determined by the ac-modulation voltage which is applied to a capacitive coupling to the central island. The accuracy of the device is limited by the occurrence of missing tunnel events due to the stochastic nature of tunneling, thermally activated tunneling, and second order tunnel events across more than one junction. Both effects can be minimized by proper system design, and the estimated attainable accuracy with present day technology is of order  $10^{-6}$ .

Furthermore, multiple junction configurations like the Single-Electron Transistor can be used as fast and small analog and digital switching devices with low dissipation and possible finite amplification. An extrapolation of the current trend in circuit miniaturization will inevitably result in systems in which transport is dominated by charging effects, regardless of whether we are dealing with semiconductor devices based on present-day Si-technology, or devices based on other more sophisticated physical effects which are investigated nowadays, for at the atomic scale there isn't much beyond Coulomb interaction. Proposed candidates for application in a future generation of electronic devices are based on the physical properties of systems at mesoscopic or atomic lengthscales such as quantum wires (coherent wave propagation, interference devices), quantum dots, resonant tunneling devices, biological and molecular structures, etcetera. For all these devices charging effects

come into play as soon as the systems become small enough, and the system design will have to take these effects into account, or, even better, take advantage of them. From a comparison of all possible candidates at the NATO-ASI on "granular nanoelectronics" in 1990 [64] it became clear that only the charging effects provide promising perspectives for a future generation of solid state electronics, while some of the other effects may be useful in specialized applications.

## References

1. H.R. Zeller and I. Giaever, *Phys. Rev.* **181** (1969) 789; I. Giaever and H.R. Zeller, *Phys. Rev. Lett.* **20** (1968) 1504.
2. J. Lambe and R.C. Jaklevic, *Phys. Rev. Lett.* **22** (1969) 1371.
3. I.O. Kulik and R.I. Shekter, *Sov. Phys. JETP* **41** (1975) 308.
4. E. Ben-Jacob and Y. Gefen, *Phys. Lett. A* **108** (1985) 289.
5. E. Ben-Jacob, Y. Gefen, K. Mullen, and Z. Schuss, in: *SQUID 85*, eds. H.D. Hahlbohm and H. Lübbig, (Walter de Gruyter, Berlin, 1985).
6. D.V. Averin and K.K. Likharev, in: *SQUID 85*, eds. H.D. Hahlbohm and H. Lübbig, (Walter de Gruyter, Berlin, 1985).
7. F. Guinea and G. Schön, *Europhys. Lett.* **1** (1986) 585.
8. D.V. Averin and K.K. Likharev, *J. Low Temp. Phys.* **62** (1986) 345.
9. K.K. Likharev and A.B. Zorin, *J. Low. Temp. Phys.* **59** (1985) 347.
10. K.K. Likharev, *Dynamics of Josephson Junctions and Circuits*, (Gordon & Breach, N.Y., 1986), chapter 16.
11. D.V. Averin and K.K. Likharev, in: *Quantum Effects in Small Disordered Systems*, eds. B.L. Altshuler, P.A. Lee and R.A Webb, (Elsevier, Amsterdam, 1991) p.169.
12. U. Geigenmüller and G. Schön, *Physica B* **152** (1988) 186.
13. P.J.M. van Bentum, L.E.C. van de Leemput, R.T.M. Smokers, and H. van Kempen, *J. Microscopy* **152** (1988) 11.
14. P.J.M. van Bentum, L.E.C. van de Leemput, R.T.M. Smokers, and H. van Kempen, *Phys. Scr.* **T25** (1989) 122.
15. P.J.M. van Bentum, R.T.M. Smokers, and H. van Kempen, *Phys. Rev. Lett.* **60** (1988) 2543.
16. K. Mullen, E. Ben-Jacob, R.C. Jaklevic, and Z. Schuss, *Phys. Rev. B* **37** (1988) 98.
17. K. Mullen, Yu. Gefen, and E. Ben-Jacob, *Physica B* **152** (1988) 172.
18. T.A. Fulton, P.L. Gammel, D.J. Bishop, L.N. Dunkleberger, and G.J. Dolan, *Phys. Rev. Lett.* **63** (1989) 1307.
19. R.C. Jaklevic, R. Wilkins, M. Amman, and E. Ben-Jacob, *Phys. Rev. B* **44** (1991) 1407.
20. M. Büttiker and R. Landauer, *Phys. Rev. Lett.* **49** (1982) 1739, *IBM J. Res. Dev.* **30** (1986) 451.
21. P. Delsing, K.K. Likharev, L.S. Kuzmin, and T. Claeson, *Phys. Rev. Lett.* **63** (1989) 1180.
22. A.N. Cleland, J.M. Schmidt, and J. Clarke, *Phys. Rev. Lett.* **64** (1990) 1565.
23. Yu.V. Nazarov, preprint.
24. Yu.V. Nazarov, *Sov. Phys. JETP Lett.* **49** (1989) 126.
25. Yu.V. Nazarov, *Sov. Phys. JETP* **68** (1989) 561.

26. A.O. Caldeira and A.J. Leggett, *Ann. Phys.* **149** (1983) 374.
27. D.V. Averin and Yu.V. Nazarov, *Physica B* **162** (1990) 309.
28. M.H. Devoret, D. Esteve, H. Grabert, G.-L. Ingold, H. Pothier, and C. Urbina, *Phys. Rev. Lett.* **64** (1990) 1824.
29. H. Pothier, Ph.D. thesis (1991), Université Paris 6, France.
30. H. Grabert, G.-L. Ingold, M.H. Devoret, D. Esteve, H. Pothier, and C. Urbina, preprint, to appear in Proceedings of the Adriatico Research Conference "Quantum Fluctuations in Mesoscopic and Macroscopic Systems", ICTP Trieste, 1990.
31. G.-L. Ingold and H. Grabert, preprint, to appear in *Europhys. Lett.*
32. S.M. Girvin, L.I. Glazman, M. Jonson, D.R. Penn, and M.D. Stiles, *Phys. Rev. Lett.* **64** (1990) 3183.
33. G. Falci, V. Babunja, and G. Schön, *Z. Phys. B* **85** (1991) 451.
34. N.W. Ashcroft and N.D. Mermin, *Solid State Physics*, (Holt-Saunders International Editions, 1976).
35. A.A. Abrikosov, *Fundamentals of the Theory of Metals*, (North-Holland, 1988).
36. M. Amman, R. Wilkins, E. Ben-Jacob, P.D. Maker, and R.C. Jaklevic, *Phys. Rev. B* **43** (1991) 1146.
37. A.E. Hanna and M. Tinkham, *Phys. Rev. B* **44** (1991) 5919.
38. K.A. McGreer, J.-C. Wan, N. Anand, and A.M. Goldman, *Phys. Rev. B* **39** (1989) 12260.
39. D.V. Averin and A.N. Korotkov, *J. Low Temp. Phys.* **80** (1990) 173.
40. M. Amman, E. Ben-Jacob, and K. Mullen, *Phys. Lett. A* **142** (1989) 431.
41. K. Mullen, E. Ben-Jacob, and S. Ruggiero, *Phys. Rev. B* **38** (1988) 5150.
42. T.A. Fulton and G.J. Dolan, *Phys. Rev. Lett.* **59** (1987) 109.
43. G.-L. Ingold, P. Wyrowski, and H. Grabert, *Z. Phys. B* **85** (1991) 443.
44. L.J. Geerligs, V.F. Vandereg, C.A. van der Jeugd, J. Romijn, and J.E. Mooij, *Europhys. Lett.* **10** (1989) 79.
45. L.J. Geerligs and J.E. Mooij, *Physica B* **152** (1988) 212.
46. B. Laikhtman, *Phys. Rev. B* **41** (1990) 138.
47. K.K. Likharev, N.S. Bakhvalov, G.S. Kazacha, and S.I. Serdyukova, *IEEE Trans. Mag.* **25** (1989) 1436.
48. G.J. Dolan, *Appl. Phys. Lett.* **31** (1977) 337.
49. P. Delsing, K.K. Likharev, L.S. Kuzmin, and T. Claeson, *Phys. Rev. Lett.* **63** (1989) 1861.
50. L.S. Kuzmin and D.B. Haviland, *Phys. Rev. Lett.* **67** (1991) 2890.
51. J.B. Barner and S.T. Ruggiero, *Phys. Rev. Lett.* **59** (1987) 807.
52. L.S. Kuzmin and K.K. Likharev, *JETP Lett.* **45** (1987) 495, *Jap. J. Appl. Phys.* **26** (1987) 1389.
53. P. Delsing, T. Claeson, K.K. Likharev, and L.S. Kuzmin, *Phys. Rev. B* **42** (1990) 7439.
54. L.S. Kuzmin, P.A. Delsing, T. Claeson, and K.K. Likharev, *Phys. Rev. Lett.* **62** (1989) 2539.
55. N.S. Bakhvalov, G.S. Kazacha, K.K. Likharev, and S.I. Serdyukova, *Physica B* **173** (1991) 319.
56. L.J. Geerligs, M. Peters, L.E.M. de Groot, A. Verbruggen, and J.E. Mooij, *Phys. Rev. Lett.* **63** (1989) 326.
57. U. Meirav, M.A. Kastner, and S.J. Wind, *Phys. Rev. Lett.* **65** (1990) 771.

- 58 U Meirav, P L McEuen, M A Kastner, E B Foxman, A Kumar, and S J Wind, *Z Phys B* **85** (1991) 357
- 59 L P Kouwenhoven, N C van der Vaart, A T Johnson, W Kool, C J P M Harmans, J G Williamson, A A M Staring, and C T Foxon, *Z Phys B* **85** (1991) 367
- 60 D C Glatth, C Pasquier, U Meirav, F I B Williams, Y Jin, and B Etienne, *Z Phys B* **85** (1991) 375
- 61 M A Reed, J H Randall, R J Aggarwal, R J Matyi, T M Moore, and A E Wetsel, *Phys Rev Lett* **60** (1988) 535
- 62 A Groshev, *Phys Rev B* **42** (1990) 5895
- 63 L J Geerligs, V F Anderegg, P A M Holweg, J E Mooij, H Pothier, D Esteve, C Urbina, and M H Devoret, *Phys Rev Lett* **64** (1990) 2691
- 64 *Granular Nanoelectronics*, eds D K Ferry, J R Barker, and C Jacoboni, (Plenum, N Y, 1991), proceedings of NATO Advanced Study Institute, 1990, Il Ciocco, Italy

## **Chapter 3**

# **Charging effects in single point-contact tunnel junctions**

### 3.1 Introduction

The ideal model system of the current biased single junction, as described by Averin and Likharev [1], cannot be realized in practice by simply connecting a small tunnel junction to a current source. The stray capacitance of the leads connecting such mesoscopic junction to the macroscopic world of bias sources and voltmeters will mask the small intrinsic junction capacitance, and make the junction effectively voltage biased on the local scale, irrespective of the nominal bias conditions.

In section 2.2.4 of the preceding chapter I already stressed the need for an effective local current biasing, which essentially implies a large series impedance close to the junction so that charge imbalances caused by tunneling electrons can only slowly move away from the tunneling area. Without such series impedance any fluctuation of the junction charge will immediately be compensated from the large charge buffer constituted by the stray capacitance of the junction environment.

From this point of view therefore it is obvious that, without special precautions, single junctions will not be subject to charging effects. They may at best be in the limiting situation described by Averin and Nazarov [2], but they will not display a measurable Coulomb blockade, let alone that they would produce SET-oscillations. For the well defined evaporated tunnel junctions, as studied in Refs. [3, 4] these predictions have been verified experimentally (see section 2.4.1).

A priori point-contact tunnel junctions are not expected to behave deviantly. In this chapter I will nevertheless claim to have strong indications for the interference of charging effects in point-contact tunneling, and a mechanism will be proposed that may be responsible for this effect. In the next section I will first present some circumstantial evidence obtained in measurements on various sample materials. In section 3.3 the concepts of the hypothetical mechanism will be enunciated. A test of this hypothesis on a controllable system is provided by point-contact measurements involving surface-doped silicon samples. The results of these experiments are shown and discussed in section 3.4. In the measurements presented in section 3.5 the samples of section 3.4 have been modified to yield experimental conditions which may approach the ideal current-biased model system of Ref. [1]. Some preliminary results are shown and possibilities for future attempts in this direction are indicated. Section 3.6 ends this chapter with some general conclusions.

### 3.2 Circumstantial evidence for charging effects in point-contact tunnel junctions

In this section results will be discussed of point-contact tunneling experiments on a range of quite different samples, which are thought to give some indication that charging effects (such as the Coulomb blockade) may even play a role in nominally voltage biased point-contact tunnel junctions. In order to be able to select these examples one of course first has to define what can be considered as indicative of charging effects. From the discussion of chapter 2, sections 2.2.2 to 2.2.4, we have learned that all distinguishable regimes, as determined by the respective ratios of the

tunnel resistance  $R_T$  and the series impedance  $Z(\omega)$  with respect to the quantum resistance  $R_Q$ , have one characteristic in common. This universal hallmark is the occurrence of linear asymptotes, offset from the origin by  $e/2C$ . When the series impedance is of the order of the quantum resistance or larger, the current will be significantly suppressed around zero bias, but the exact shape of the  $I(V)$  curve is determined by the specific environmental impedance and bias conditions.

The linearity of the asymptotes is of course the self-evident consequence of the explicit presumption, made in the theory of chapter 2, that the tunnel probabilities in the studied junctions are determined by a rate which is linear in the energy gained by the tunneling electron. Charging effects in junctions with intrinsic non-linear characteristics, e.g. due to non-ideal barrier effects or inelastic contributions, are therefore structurally missed when the above hallmark is used as a discriminative feature. This however only makes the definition stronger, as it is extremely unlikely for any combination of possible interfering non-linear effects to restore the initially linear behaviour of a tunnel junction. The occurrence of linear asymptotes, or equivalently the saturation of the differential conductance at larger voltages, can thus be considered as a characteristic of ideal tunneling behaviour, while the offset of the asymptotes implies the possible presence of a Coulomb blockade.

The intrinsic capacitance of a point-contact tunnel junction will, at least to first order, be inversely proportional to the tunnel distance, if this capacitance is indeed only determined by parts of the tip-sample configuration in the vicinity of the tunneling area. As the tunnel resistance scales roughly exponentially with the tunnel distance, this implies a linear relation between  $C^{-1}$  and  $\ln(R_T)$  [5, 6]. The influence of tip movement in the  $z$ -direction (by convention the  $z$ -coordinate in STM is along the direction of the tip axis, see appendix) on the offset value may thus provide additional proof for the presence of charging effects.

The single junction characteristics to be shown in this section have all been measured with the set-up described in the appendix of this chapter. The examples can be divided into three categories. The first one contains measurements on "dirty" materials with ill-defined surface and oxide properties in which, in a manner of speaking, anything can happen. The second category pertains to in principle relatively clean junctions such as NIN point-contacts on evaporated thin films, while in the third category the possible influence of charging effects on gap spectroscopy in NIS-junctions is considered.

### 3.2.1 "Dirty" materials

In Ref. [5] van Bentum *et al.* claimed the first observation of SET-characteristics in experiments with point-contact tunnel junctions between a tungsten tip and stainless steel and  $\text{YBa}_2\text{Cu}_3\text{O}_{7-\delta}$  samples. However, the measurement on stainless steel, which was in fact a test run with the sample holder itself serving as a sample, is an unfortunate example as the material and its oxide layer are thought to contain various magnetic impurities giving rise to not very well understood tunneling anomalies [8]. The experiments with  $\text{YBa}_2\text{Cu}_3\text{O}_{7-\delta}$  samples had the aim to measure



the energy gap of this high- $T_c$  superconductor. Tunneling measurements on these samples only revealed the expected NIS or SIS characteristics (see sections 1.3.2 and 5.3.2) in a minority of cases, while most junction characteristics were dominated by non-superconducting effects. Chapter 5 will expatiate on these observations in more detail.

At the time of the above measurements, the idealized theory of Averin and Likharev [1] was the only one available. In this theory the junction environment is treated as static with no stray capacitance. In Ref. [5] the relevance of a dynamic treatment of the environment was stipulated. In fact, from the more general understanding as expounded in section 2.2, one must conclude that the interpretation of the characteristics of any real junction in terms of the ideally current biased model of Ref. [1] is strictly speaking incorrect. The observed tunnel characteristics nevertheless do meet the criteria set above, and may thus still be considered as indicative of the occurrence of some form of charging effects. Both experiments of Ref. [5] (see also Refs. [6, 7]) revealed linear asymptotes, and at least for the stainless steel measurements the linear relation between  $C^{-1}$  and  $\ln(R_T)$  was confirmed. Offset values generally ranged between 10 and 60 mV, indicating junction capacitances of order  $5 \times 10^{-18}$  F.

Figure 3.1 shows another example of charging characteristics measured on the high- $T_c$  superconductor  $\text{YBa}_2\text{Cu}_3\text{O}_{7-\delta}$ . The current suppression can not be connected to a gap in the quasi-particle density of states of the superconductor, as the width of this suppressed-current region was often seen to exceed the gap value  $\Delta$  as inferred from more BCS-like characteristics (see chapter 5), and could be tuned by  $z$ -displacement of the tip. A non-superconducting origin therefore seems more plausible. Results of point-contact and STM-junctions on high- $T_c$  materials, similar to the ones presented here, have also been reported by Takeuchi *et al.* [9].

Devyatov and Kupriyanov [10] propose an alternative explanation for the observed current deficiency and corresponding displaced asymptotes observed in our

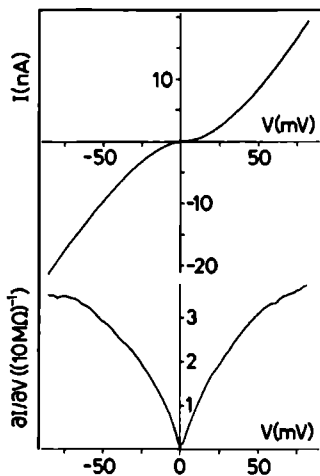


**Figure 3.1**  $I(V)$  and  $\partial I/\partial V(V)$  characteristics of a point-contact tunnel junction between a tungsten tip and ceramic  $\text{YBa}_2\text{Cu}_3\text{O}_{7-\delta}$ .

measurements on  $\text{YBa}_2\text{Cu}_3\text{O}_{7-\delta}$ . In their calculation they assume that all charge transport through the junction is by resonant tunneling via impurity states in the barrier. The expression for the current through a single localized state is averaged over a uniform distribution of impurity positions and energies, resulting in a severely rounded NIS  $I(V)$  relation with asymptotes offset from the origin by approximately  $0.60(\Delta/e)$ . The calculated curves however only qualitatively resemble the measurements of Fig. 3.1 if the temperature is taken larger than  $0.2T_c$ , which surely is not the case in our measurements. Although the principle of tunneling through localized impurity states fits very well in the conceptual view that will be sketched in section 3.3, there are a number of questionable aspects concerning this specific interpretation.

First of all it is explicitly assumed that all tunneling processes are indirect. This obviously guarantees that the studied effect will dominate the  $I(V)$  characteristic, but it does not necessarily apply to the experimental situation. Furthermore Devyatov and Kupriyanov average over a large ensemble of positions and energies of the impurity states in the barrier. This may apply very well to large planar junction geometries, but in the extremely small point-contact junctions studied here one expects only one or a few impurity states to be close enough to the tunnel area to have a significant contribution by indirect tunneling. In the calculations of Ref. [10] the Coulomb repulsion of electrons at the impurity sites [11] is explicitly taken into account. Nevertheless the effect is found to be solely determined by  $\Delta$ , and thus depends crucially on the superconducting nature of one of the electrodes. All in all one may conclude that the suggestion of Ref. [10] has to be taken serious from the conceptual point of view, although the concrete calculation probably bears no direct significance to the situation described here.

### 3.2.2 "Clean" junctions

Figure 3.2 displays the  $I(V)$  and  $\partial I/\partial V(V)$  characteristics of a point-contact tunnel junction between an etched tungsten tip and an aluminum thin-film sample. The sample had a film thickness of 200 Å, and was oxidized in air. The  $I(V)$  characteristic shows significant current suppression near the origin and saturating differential conductance at higher voltages, implying (almost) linear asymptotes. The offset of the asymptotes is of order 1 mV, which in the Coulomb blockade interpretation corresponds to a capacitance value of a few times  $10^{-17}$  F. Similar curves have been observed on other Al films.

Figure 3.3(a) shows some examples which exhibit current suppression over a much wider voltage range. The upper trace was measured on the same sample as Fig. 3.2. The lower trace of Fig. 3.3(a) shows an example of a type of  $I(V)$  curve with extreme current suppression, which is frequently encountered on a wide range of samples. The width of the zero current region could in most cases be tuned by z-movement of the tip.

The oxide layer of aluminum consists mainly of  $\text{Al}_2\text{O}_3$ , and is considered one of most reliable barrier materials for tunnel junctions. Native oxide layers are generally

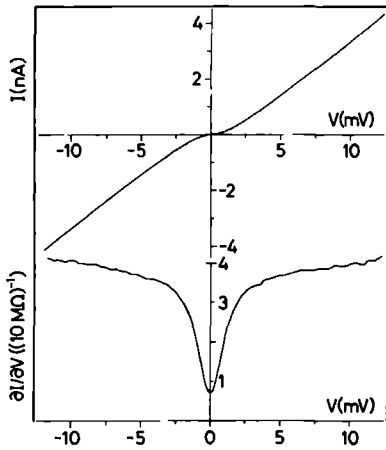


**Figure 3.2**  $I(V)$  and  $dI/dV(V)$  characteristics of a tunnel junction between a W tip and a Al thin-film sample, measured at  $T = 4.2$  K.

some 20 Å thick, and the barrier height is some 2.5 eV [12, 13]. Barrier effects are therefore not expected to play a role in the above measurements, provided at least that the barrier is thick enough.

Observations of a Coulomb blockade and accompanying linear asymptotes in STM-type junction between a tungsten tip and niobium and gold samples have been made by Hartmann *et al.* [14]. The results also confirm the linear dependence between  $\ln(R_T)$  and  $C^{-1}$ . Similar results on STM-junctions between tungsten or gold tips and HOPG (Highly Oriented Pure Graphite) samples, measured at room

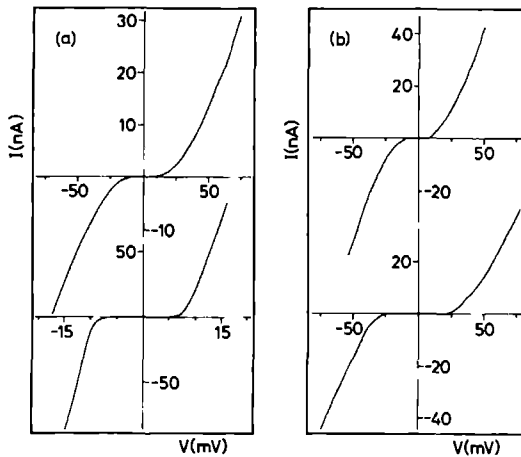


**Figure 3.3** (a) Some more extreme examples of possible Coulomb blockades measured with a W tip on Al samples, both at  $T = 4.2$  K. (b)  $I(V)$  characteristics measured at  $T = 4.2$  K on a HOPG sample with a tungsten tip.

temperature, are reported by Valdes and Choleva [15]. Point-contact measurements by ourselves, performed at  $T = 4.2$  K on both HOPG and resistive graphite from an Allen and Bradley carbon thermometer, also display characteristics obeying the above described criteria for possible charging effects (see Fig. 3.3(b) and Ref. [6] respectively). Coulomb-blockade features in tunnel junctions between two gold coated wires, measured at  $T = 4.2$  K, are reported by Gregory [16].

### 3.2.3 Charging effects and gap-spectroscopy

The open circles in Fig. 3.4 [17, 18] are data points taken from the  $I(V)$  characteristic of a point-contact tunnel junction between a tungsten tip and a 3000 Å thick Sn film, measured at  $T = 1.2$  K. This Sn film was part of a planar tunnel junction with a 150 Å thick Al counter electrode. The  $I(V)$  characteristic of the planar junction, shown in the inset of Fig. 3.4, allows us to infer the gaps of both superconducting electrodes with high accuracy. From the positions of the features associated with the sum gap and the difference of both gaps respectively we find  $\Delta_{\text{Sn}} = 0.59$  meV and  $\Delta_{\text{Al}} = 0.19$  meV.

The thin line in Fig. 3.4 now represents the  $T = 1.2$  K BCS tunneling curve calculated from the theory of section 1.3.2 using the above value for  $\Delta_{\text{Sn}}$ . It is clear that the point-contact measurement indicates an apparently larger gap.

Although it can not be proven from this measurement alone, we suggest a possible explanation based on the interference of charging effects. The Monte Carlo

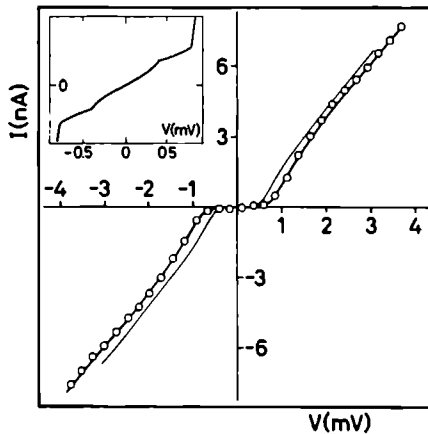


**Figure 3.4**  $I(V)$  characteristic (represented by the open dots) of a point-contact junction between a W tip and a 2000 Å thick Sn film, which was part of a planar junction with a 150 Å thick Al counter electrode. The inset shows the  $I(V)$  characteristic of the planar junction. The thin line is the calculated BCS-curve for this temperature with  $\Delta_{\text{Sn}}$  inferred from the planar junction characteristics, while the thick line represents a fit including the interference of charging effects.

simulations of Fig. 2.9 showed that the Coulomb blockade effectively shifts the characteristic energy of spectroscopic features by  $e/2C$ . The thick line in Fig. 3.4 is a Monte Carlo calculation of the  $I(V)$  curve including charging effects and a BCS density of states for one of the electrodes, with the capacitance  $C$  as a single fitting parameter. With  $C = 3.2 \times 10^{-16}$  F we find clear correspondence between the fit and the measurement. An explanation along the lines of Ref. [10] is rejected for the same reasons as explained previously.

### 3.3 A conceptual view of charging effects in point-contact tunneling

For all the measurements presented in the preceding section it can be stated that they can not be unambiguously interpreted as manifestations of the Coulomb blockade associated with a small intrinsic capacitance of the tunnel junction. In fact, the nominal circumstances in the above measurements are, at least at first sight, certainly not meeting the requirement of a large environmental impedance, which is thought to be crucial for the observation of a Coulomb blockade in single junctions. In all cases the tip and sample materials are good conductors or even superconductors, so that it can not be the resistivity of the bulk material that is impeding the neutralization of the charge imbalances resulting from the tunneling of single electrons through the junction. Nevertheless the strong resemblance between the above characteristics and the theoretical predictions of chapter 2 has led us to believe that charging effects can influence the tunneling behaviour of single, nominally voltage biased, point-contact junctions. The key question now converges to finding a mechanism that can be held responsible for the apparent decoupling of the intrinsic junction capacitance from stray capacitances in the junction environment.

In section 1.4 I discussed the differences of electron tunneling in STM-like geometries with respect to the planar junction model system for which the generally accepted tunnel formulae (e.g. Eqs. 1.8, 1.14, 1.26, and 1.28) have been derived. The main conclusion, summarized by Eq. 1.30, concerned the increased sensitivity of the tunnel current to the local densities of states of both tip and sample. These densities of states may differ significantly from the spatially and angularly averaged densities sensed in planar junctions.

It is from the above point of view that one can envisage a possible mechanism that might be able to decouple an STM-like junction from its low impedance environment. Let us consider the case in which localized states are involved in the tunneling process. Suppose an electron tunnels from the tip to a localized surface state of the sample or to e.g. an impurity state in the oxide layer covering the sample. The presence of an electron in such a state will alter the potential distribution in the junction area and will thus influence the probability of subsequent tunnel events. The electron can move away from the tunneling area by hopping to other localized states on the sample surface or by eventually tunneling into an extended bulk state. Hopping is a stochastic process, which can be thermally activated at

higher temperatures, but becomes very slow at low temperatures when the probability is solely determined by the average distance between the localized states and the height of the barrier separating them. In this way one can imagine that the time needed to remove charge from the tunneling area becomes comparable to the average time interval between tunnel events, resulting in an effective Coulomb blockade, and significant potential fluctuations across the junction. The same reasoning of course applies to electrons tunneling through the junction out of localized states, and is not depending on whether these localized states are residing on either tip or sample surface.

The principle of charge trapping in localized surface states has been experimentally verified by Cahill and Hamers [19] in STM-measurements on the clean Si(001) surface under Ultra-High Vacuum (UHV) conditions. Photovoltage measurements revealed decay times of the order of  $10^{-10}$  s. The presence of surface defects was found to enhance the local charge trapping. In fact Cahill and Hamers also mention the possibility of a Coulomb blockade energy associated with this trapping mechanism.

The role of localized states in the oxide barrier of planar metal-insulator-metal junctions has been extensively studied by Beasley and coworkers [20, 21, 22]. Most of their work concerns localized states which are naturally present in  $\text{SiO}_x$  barriers grown by oxidation of amorphous Si. In the experiments a clear distinction can be made between direct and indirect tunneling processes. The latter are either coherent (resonant tunneling, see also Ref. [10]) or incoherent (hopping). The nature of neutral and Coulombic trapping sites in As-ion-implanted Si-oxide is studied experimentally and theoretically in Ref. [23]. An important feature of these sites is the presence of a broad continuum of localized states close to the top of the potential well, allowing charging without too stringent energy requirements.

The above sketched charging and hopping mechanism is similar in a way to the decoupling procedure used by Delsing *et al.* [3]. Instead of using resistive leads they connected their single junction to current and voltage leads consisting of one-dimensional arrays of small capacitance tunnel junctions. The localized states on the tip or sample surface can be viewed as constituting a random two-dimensional network of small tunnel junctions. This network, while connecting the tip-sample junction to the bulk states of both junction electrodes, at the same time decouples the junction from stray capacitances.

Also without truly localized surface or impurity states a decoupling scheme seems feasible, as long as the group velocity of the non-localized surface states is small enough to effectively impede charge redistribution on the junction capacitor.

The proposed decoupling mechanism depends heavily on the local properties of tip and sample. The required localized states may result from the presence of oxide impurities, doping or adsorbates, or may be induced by structural defects. It is thus expected that the influence of charging effects on the junction characteristics will vary for different sample and tip materials and that it will depend on the surface treatment of both. Given a tip-sample combination the effect will also vary from position to position on the sample and is possibly depending on whether or not the

tip touches the sample.

For STM-junctions on clean and flat metal samples in a UHV environment decoupling through the above described mechanisms is obviously out of the question, and charging effects are thus unlikely to influence spectroscopy in such junctions. In the voltage range of interest in this context, i.e. up to a few hundred mV, this type of STM-junctions is known to display linear  $I(V)$  characteristics. However, for the mechanically touching point-contact junctions, as used throughout this thesis, this is certainly not the case. In almost all cases both tip and sample are covered with an oxide layer. The tip is electrochemically sharpened and its surface may, despite cleaning, still contain impurities from the etching solution. Due to exposure to air the outer layers of tip and sample will be covered by at least a monolayer of adsorbed gas molecules. Mechanical contact between tip and sample is bound to induce structural deformations. All this promotes the occurrence of localized surface or impurity states.

Experimental experience presented in the previous section is in support of this view of the microscopic properties of point-contact tunnel junctions. Measurements on continuous aluminum films with clean oxide layers only yield non-linear characteristics incidentally, while the major part of the sample area displays ohmic  $I(V)$  curves. For junctions on "dirty" materials such as the ceramic high- $T_c$  superconductors the situation is reversed in the sense that on these materials ohmic behaviour is only rarely encountered. In all cases we find, in the course of the measurement session, that the non-linearities tend to be washed out when the tip has repeatedly been brought in not too gentle contact with the sample. This is thought to blunt the tip, thus enlarging the tunneling area and reducing the atomic scale sensitivity of the contact.

The above sketched concept, inspired on experimental experience, thus clearly indicates, albeit in a for the time being rather qualitative fashion, possible mechanisms which are able to provide a decoupling of the intrinsic capacitance of a point-contact tunnel junction from stray capacitances associated with the leads connecting the mesoscopic junction to the macroscopic outside world. This decoupling mechanism gives rise to a Coulomb blockade and consequently induces charge fluctuations on the junction capacitor with amplitude of order  $e/2C$ . As the redistribution of charge on the junction is governed by a stochastic transport mechanism one does however not expect the occurrence of coherent SET-oscillations in the junction voltage. The combination of a Coulomb blockade and incoherent voltage fluctuations nevertheless also leads to a shifting and smearing of spectroscopic features, similar to what was described in section 2.2.3 for a small junction between a normal metal and a superconductor. In fact, the Monte Carlo fit of Fig. 3.4 was made using the perfectly current biased model, which for small currents produces coherent oscillations. The frequency spectrum of Fig. 2.4 however shows that the power associated with these oscillations is, for all finite current values, much smaller than the integrated power of the incoherent noise background. As long as  $e^2/2C < \Delta$  one can thus expect a more sophisticated model, properly incorporating stochastic charge transport, to have the same overall influence on the NIS tunneling characteristic.

In order to test this hypothetical concept experiments have been performed on samples in which the charge transport is completely governed by hopping conductivity. The next two sections will present results which not only support the here developed conceptual view of the possible mechanism for charging effects in single point-contact tunnel junctions in general, but which also point out a serious option for an experimental configuration allowing the observation of SET-oscillations.

### 3.4 Point-contact junctions on surface-doped Si samples

The surface-doped Si samples, used for the experiments presented in this section, not only provide the localized states, which in the above proposed mechanism are essential for decoupling of the junction capacitance, but also allow, by changing the temperature, a variation of the macroscopic series resistance of the junction such that the macroscopic bias condition can be continuously changed from voltage biased to current biased. Most of the results in this section have previously been published in Refs. [17, 18, 24].

#### 3.4.1 Sample properties and experimental set-up

##### Sample fabrication

The samples were fabricated by the EFFIC chips-lab of the Eindhoven Technical University, according to design parameters similar to the ones used by Chen Gang *et al.* [25, 26] for the production of microthermometers. The samples were made by As-ion implantation of standard p-type Si wafers with background acceptor density approximately  $10^{15} \text{ cm}^{-3}$ . Two subsequent implants at different energies were used to optimize the density profile. After implantation the wafers were annealed for 20 minutes in a  $\text{N}_2$  atmosphere at  $900^\circ\text{C}$ , and protected by a 10 nm oxide layer grown in an  $\text{O}_2$  atmosphere at  $900^\circ\text{C}$ . Finally the wafers were exposed to  $1000^\circ\text{C}$  in a  $\text{N}_2$  atmosphere allowing diffusion of the As doping to establish the desired density profile. Two different sets of fabrication parameters were used to obtain samples with different final donor concentrations. The first batch (hereafter referred to as batch I) was implanted with a first dose of  $11.4 \times 10^{13} \text{ cm}^{-2}$  at an energy of 160 keV, and a second dose of  $4.3 \times 10^{13} \text{ cm}^{-2}$  at 60 keV, and was given a diffusion treatment of 240 minutes. The second batch (batch II) received a first implantation dose of  $8.8 \times 10^{13} \text{ cm}^{-2}$  at 160 keV, and a second dose of  $3.9 \times 10^{13} \text{ cm}^{-2}$  at 60 keV. The implantation was allowed to diffuse for 100 minutes. Density profiles were estimated using a computer simulation model. Batch I is expected to have an almost constant dopant density of  $8.4 \times 10^{18} \text{ cm}^{-3}$  up to about  $0.1 \mu\text{m}$  below the sample surface. This concentration gradually drops to zero in the next  $0.2 \mu\text{m}$ . Batch II has a peak density of  $8.1 \times 10^{18} \text{ cm}^{-3}$  at  $0.1 \mu\text{m}$  below the surface, while the concentration at the surface is approximately  $5.7 \times 10^{18} \text{ cm}^{-3}$ . Deeper into the wafer the concentration falls off similarly to the profile in batch I.

The active regions were patterned into various small structures using photolithographic techniques, standard for IC-technology. The two structures that were



used as samples for the tunneling experiments described in this chapter are shown in Fig 3 5(a) and (b). The square structure (Fig 3 5(a)) has dimensions  $190 \times 190 \mu\text{m}^2$ , and is on all four corners connected to contact pads. These ohmic contacts are regions of the wafer which are degenerately doped with P ions ( $n^+ \approx 10^{21} \text{ cm}^{-3}$ ) and are covered by a sputtered Al film to allow wire bonding. A schematic cross section is drawn in Fig 3 5(c). A point-contact junction on the square will see a series impedance to each contact of roughly one sheet resistance  $R_{\square}$ . The meandering pattern of Fig 3 5(b) has the advantage that a contact on this structure will see a series impedance of several times  $R_{\square}$  depending on the exact position on the meander. Establishing a contact on this structure however is slightly more difficult as the width of the structure is only  $30 \mu\text{m}$ .

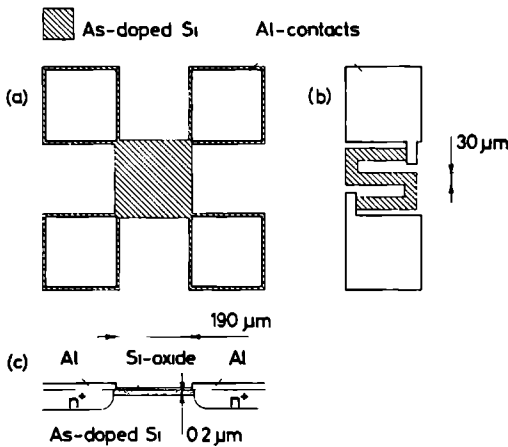


**Figure 3.5** Two As-doped structures ((a) square, and (b) "meander") patterned on Si wafers, as described in the text. (c) Schematic drawing of the cross section of the active region and connected contact pads

### Hopping conductivity

In the above described samples the doping concentration is definitely below the critical density associated with the metal-insulator (MI) transition, which for Si As is about  $8.5 \times 10^{18} \text{ cm}^{-3}$ . This means that the resistivity will diverge if  $T$  goes to zero. In Ref [25] it was proven that the temperature dependence can be well described by a variable range hopping model incorporating the Coulomb interaction of neighbouring hopping sites [27], resulting in a modified Mott-formula  $\rho(T) = \rho_0 \exp(T_0/T)^m$ , with  $m \approx 1/2$ .

This exponential temperature dependence of the sample resistivity enables variation of the series resistance of point-contact tunnel junctions on these samples by some three orders of magnitude, simply by changing the measurement temperature between 4.2 K and 1.2 K. The current-voltage characteristics of the samples

were found to be as good as linear in the voltage regime  $[-150 \text{ mV}, 150 \text{ mV}]$ . At  $T = 4.2 \text{ K}$  the square resistance  $R_{\square}$  of the samples was generally of order  $50 \text{ k}\Omega$  for batch I and  $150 \text{ k}\Omega$  for batch II, while at  $T = 1.2 \text{ K}$  this increased to  $\approx 30 \text{ M}\Omega$  and  $\approx 300 \text{ M}\Omega$  respectively.

The intrinsic p-doping of the Si surrounding the As-doped active regions is a factor of 1000 below that of the active regions, so that the wafer itself is completely insulating at the measurement temperatures of  $4.2 \text{ K}$  or lower.

### Expected point-contact behaviour

For the above described samples with high donor concentration the Fermi level will, at the measurement temperatures of  $4.2 \text{ K}$  and below, be pinned on the donor band. The average distance between donor sites is of the order of  $80 \text{ \AA}$ , while the Bohr radius of the hydrogen-like donor state is estimated to be about  $20 \text{ \AA}$ . In point-contact junctions the tunnel area is estimated to be of the order of  $25 \times 25 \text{ \AA}^2$ . This means that in this type of junctions on the surface-doped Si samples the tunneling will take place between the tip and one or a few donor sites directly below the contact.

The properties of metal-semiconductor contacts are extensively discussed in Refs. [28, 29, 30]. For our experimental conditions no significant Schottky-barrier is expected. Given  $n_D \approx 8 \times 10^{18} \text{ cm}^{-3}$  a planar junction without oxide layer would have a depletion width of some  $80 \text{ \AA}$ . The presence of a  $10 \text{ \AA}$  oxide layer separating metal and semiconductor will significantly decrease this value. When the expected depletion width is smaller than the distance between dopant sites, the whole concept of a depletion region becomes meaningless, especially in the context of our nanometer-scale junctions.

### Sample preparation

In the fabrication process the samples have been etched just before the deposition of the Al contacts, in order to remove the protective oxide layer grown before the diffusion stage. After this Al deposition the Si surface has been oxidized at room temperature by exposure to air. This generally yields a uniform oxide layer of some ten or twenty Ångstrom thickness. Tunneling measurements on fresh samples were generally performed on this native oxide layer. This oxide layer could be renewed by etching in dilute HF ( $\approx 5\%$ ) for some 20 seconds and subsequent oxidation in air. Contacts to the samples were made by bonding gold wires to the Al contact pads.

### Experimental set-up

Measurements have been performed using the insert and electronics described in the appendix of this chapter (Figs. 3.12 and 3.13). Stable junctions were established by bringing a tungsten tip in mechanical contact with the oxide layer on the sample.  $I(V)$  characteristics were recorded in either a two-terminal or a

three-terminal configuration, using the home-built voltage source with integrated current-to-voltage converter shown in Fig. 3.13 (b). With tunnel resistances in the  $M\Omega$  regime the junctions established at  $T = 4.2$  K can be considered effectively voltage biased, and a two terminal measurement suffices for these cases. At temperatures below 2 K the sample resistance is generally comparable to or larger than the junction resistance, so that the voltage drop over the junction is much smaller than the externally applied voltage, and the junction becomes essentially current biased. In these cases a three-terminal configuration, as shown in Fig. 3.6, is to be employed.

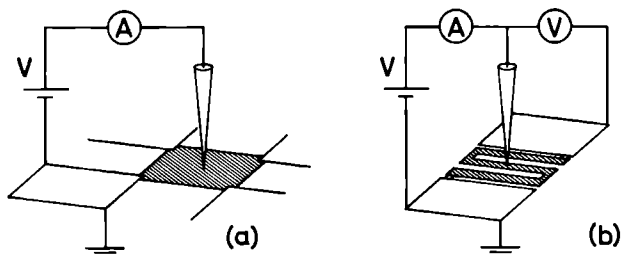


**Figure 3.6** (a) Two- and (b) three-terminal configurations used to record the  $I(V)$  characteristics of tunnel junctions on highly resistive surface-doped Si samples.

The differential conductance was measured by phase-sensitive detection of the current response to a small ac-modulation superimposed on the externally applied dc-voltage. The lock-in signal was not corrected for changes of the modulation amplitude over the junction due to variation of the  $R_T/R_S$  ratio. This means that the shape of  $\partial I/\partial V(V)$  is only correct if  $R_T/R_S \gg 1$ , which only is the case for the measurements performed at  $T = 4.2$  K. At lower temperatures the  $\partial I/\partial V(V)$  measurement will respond superlinearly to decreases in the real differential conductance. Correction of the data presented in the following is possible using information from  $I(V)$  and the measured constant series resistance, but in the present stage of the experiments this is not expected to yield any important information.

### 3.4.2 Experimental results

Figure 3.7(a) shows an example of the  $I(V)$  characteristics of a point-contact tunnel junction, measured in a two terminal configuration at  $T=4.2$  K on a square structure (Fig. 3.5(b)) from batch II. The contact had a series resistance  $R_S = 0.55$   $M\Omega$ . The tunnel resistance is  $R_T = 7.2$   $M\Omega$ . A clear Coulomb-gap structure is observed. The linear asymptotes are offset from the origin by 1.4 mV, implying a junction capacitance  $C = 5.7 \times 10^{-17}$  F. At lower voltages the characteristic is clearly parabolic as can be seen from the linear parts in the  $\partial I/\partial V(V)$  curve.  $C$  and  $R_T^{-1}$  could be increased by pushing the tip further into the sample, as is illustrated in Fig. 3.7(b) by a set of characteristics recorded on the same contact.

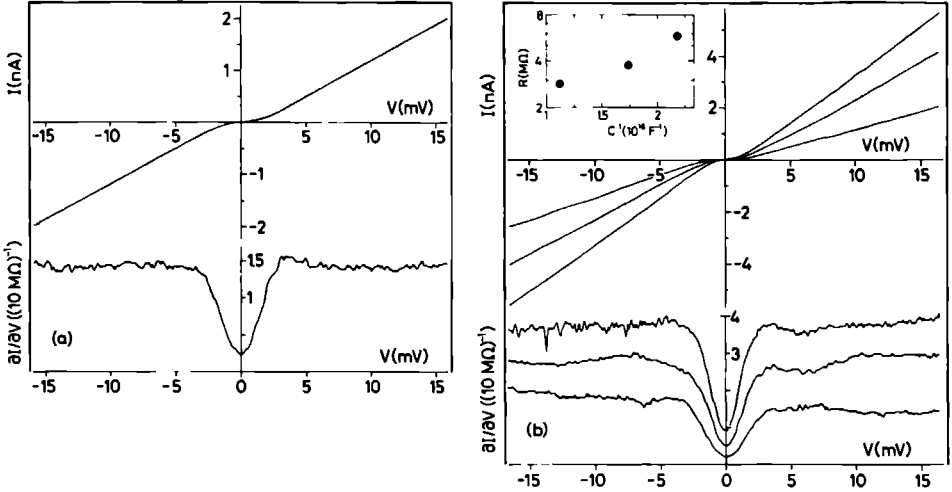


**Figure 3.7** (a)  $I(V)$  and  $\partial I/\partial V(V)$  characteristics of a point contact on a square structure of batch II. (b) Set of  $I(V)$  characteristics measured on the same contact, with the tip pushed deeper into the sample for each successive curve. The inset shows the shifting asymptotes characterized by  $C^{-1}$  and  $\ln(R_T)$ . The measurement was performed in a two-terminal configuration at  $T = 4.2$  K.

Similar characteristics have been observed on the meander structure. An example measured on a structure from batch I is shown in Fig. 3.8(a). The point-contact junction with  $R_T = 34$  M $\Omega$  was backed by a series resistance  $R_S \approx 4$  M $\Omega$ . The apparent Coulomb blockade corresponds with a junction capacitance  $C = 6.2 \times 10^{-17}$  F.

The results of a measurement at  $T = 1.8$  K, on a different position on the same sample, are depicted in Fig. 3.8(b). From the asymptote we can deduce  $C = 6.4 \times 10^{-17}$  F and  $R_T = 41$  M $\Omega$ . The series resistance in this case is 53 M $\Omega$  so that the junction is halfway between voltage and current bias. The current suppression around the origin is pronounced more strongly than in the case of Fig. 3.8(a). This is however not connected to the lower temperature or higher series resistance, as is exemplified by the  $I(V)$  characteristics of Fig. 3.9. In this measurement on a square structure from batch II the conductance dip is sharper and less deep. The  $I(V)$  curve depicted in Fig. 3.9(a) was recorded at  $T = 4.2$  K. With this junction the temperature of the helium bath could be varied continuously between 4.2 and 1.5 K without disturbing the contact. This temperature variation however did not significantly alter the  $I(V)$  characteristics except for a small increase in the junction resistance, as illustrated by Fig. 3.9(b). Although the asymptotes in this case are not completely linear, one can estimate  $C \approx 2.5 \times 10^{-17}$  F and  $R_T = 25$  M $\Omega$  and 30 M $\Omega$  for cases (a) and (b) respectively. The series resistance changed from  $\approx 100$  k $\Omega$  at 4.2 K, to  $\approx 80$  M $\Omega$  at  $T = 1.5$  K.

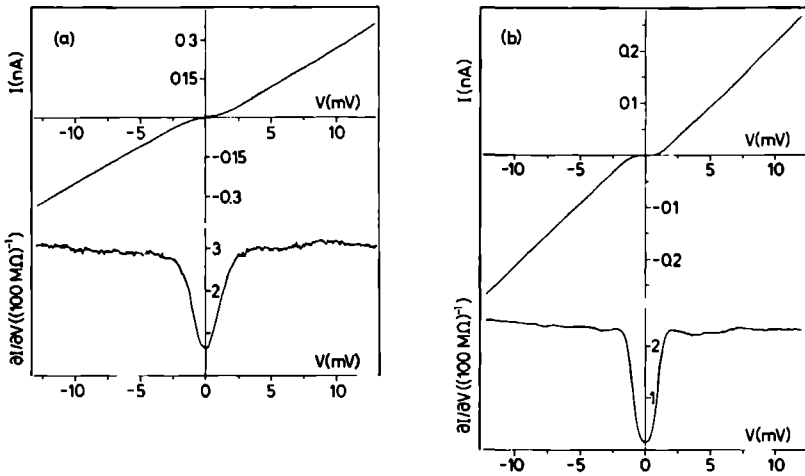


**Figure 3.8**  $I(V)$  and  $\partial I / \partial V(V)$  characteristics of two different point-contact junctions on the same surface-doped Si sample (batch I, meander structure), measured at (a)  $T = 4.2 \text{ K}$  and (b)  $T = 1.8 \text{ K}$  respectively.

A possible Coulomb gap like the ones displayed above was observed on most point contacts on samples of both batches and both structures. Not all characteristics displayed the desired linear asymptotes, but these could always be found after some probing around. In the above examples the asymptotic offset was generally

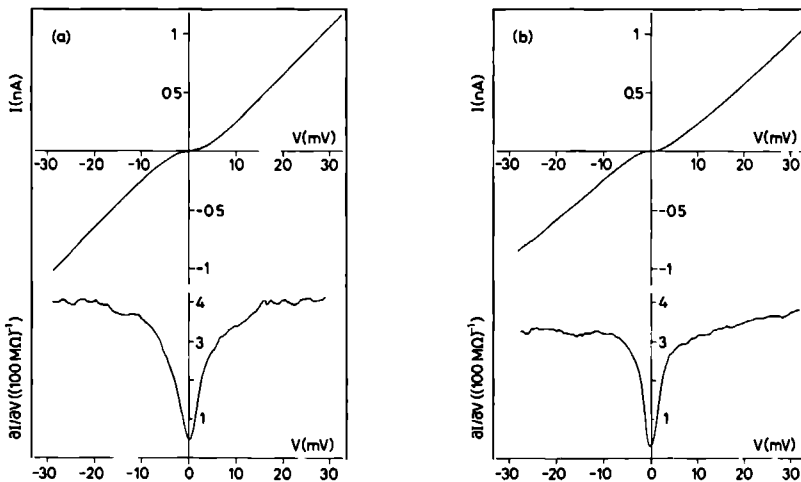


**Figure 3.9**  $I(V)$  and  $\partial I / \partial V(V)$  characteristics of a point-contact junction on a surface-doped Si sample (batch II, square structure), measured at  $T = 4.2 \text{ K}$  (a) and  $1.5 \text{ K}$  (b).

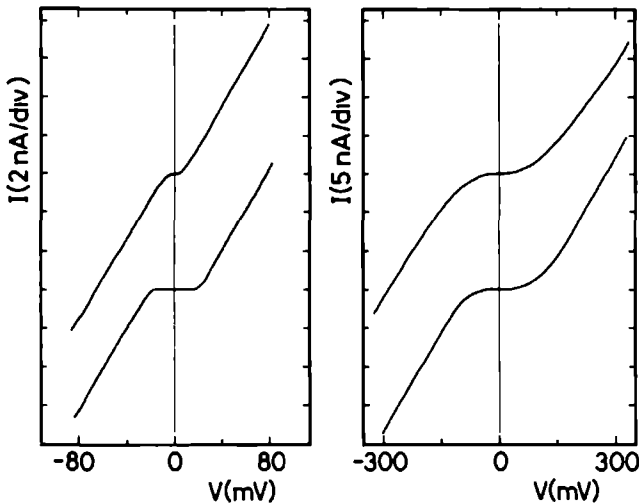


**Figure 3.10** A collection of  $I(V)$  characteristics recorded at  $T = 4.2$  K (a) and  $1.2$  K (b) on a Si sample of which the surface had been damaged by a voltage pulse

one or a few mV, but also values of the order of 25 mV have been observed, which correspond to junction capacitances in the  $10^{-18}$  F range

As a more eccentric example Fig. 3.10 shows a set of  $I(V)$  characteristics displaying extreme Coulomb gap features. The curves were measured at  $T = 4.2$  K and  $1.2$  K on the same sample (batch II, meander structure). During cool-down the tip had crashed the surface but could be retracted. No Coulomb gaps were observed on the first subtly established contacts. In an attempt to resharpen the tip a 10 V pulse was applied over the contact. After this rough treatment strong gap structure could be observed over the whole scan reach of the  $xy$ -piezo. The voltage pulse treatment is often used in STM-experiments, and from these it is known that the discharge caused by the pulse can run the sample surface over such a large area as encountered here. Apparently the surface change has strengthened the decoupling conditions in a way similar to what was found for the point contacts on so-called "dirty" materials (section 3.2.1).

Surface treatment by HF etching was on some occasions seen to improve the quality and reproducibility of the characteristics, but on other occasions had a negative effect in the sense that it promoted irregular and often unstable characteristics, probably due to the interference of e.g. inelastic processes induced by the presence of deposited residue from the etching solution.

Almost all junctions displaying charging characteristics like the ones presented above were examined for the possible presence of coherent voltage oscillations. To this end an rf-modulation between 100 kHz and 1 GHz could be capacitively coupled in to the tip lead (see Fig. 3.13). Resonances of the SET-oscillations with the external modulation will display themselves as horizontal branches or plateaus in the

$I(V)$  characteristic at positions where  $I/e$  equals a harmonic ( $n/m \times f_{\text{mod}}$  with  $n$  and  $m$  integers) of the applied frequency  $f_{\text{mod}}$ . Subtle influences of the modulation could be examined by phase sensitive detection of the current or voltage response to AM-modulation of the radiation amplitude ( $\partial I/\partial S$  or  $\partial V/\partial S$ )

In general only a smooth rectifying response to external modulation has been observed. Only one contact was found to display regular and reproducible arrays of peaks in  $\partial I/\partial S$ . The distance between the peaks even scaled linearly with the applied frequency. The peak positions themselves could, however, by no means be matched with reasonable ( $n/m$ ) values for the harmonics of the modulation frequency, so that we have to conclude that the peaks were probably the result of some, as yet not understood, geometrical resonance.

### 3.4.3 Conclusions

Clear and reproducible Coulomb blockade features are observed in the  $I(V)$  characteristics of point contacts on As-doped Si samples in which the conductance is completely governed by hopping transport. The mechanism responsible for the apparent decoupling of the junction capacitance from stray capacitances in the environment does not involve a series impedance in the sense of the theory of chapter 2. This can be concluded from the fact that similar characteristics are observed on both the square and the meander structure at  $T = 4.2$  K, where  $R_S \ll R_T$ , as well as at  $T < 2$  K, where the series resistance  $R_S$  is comparable to or larger than the tunnel resistance  $R_T$ . This, in combination with the absence of phase-locked resonances to externally applied rf-modulation, supports our interpretation in terms of the concept of decoupling involving hopping through localized states as sketched in section 3.3.

## 3.5 Surface-doped Si with Al islands

Although the above presented measurements clearly indicate a mechanism capable of introducing a Coulomb blockade in nominally voltage biased point-contact tunnel junctions, the resulting charging effects will not lead to coherent SET-oscillations. This is due to the stochastic nature of the underlying hopping mechanism. To produce SET-oscillations junction electrodes are required in which the charge redistribution is governed by a continuous and deterministic process involving a well-defined characteristic  $RC$ -time. This essentially comes down to a need for metallic electrodes. With such electrodes it is unfortunately very difficult to realize the large series impedance needed for the decoupling of the junction capacitance. The junction electrodes themselves however do not necessarily have to be highly resistive. It is the ratio of the intrinsic junction capacitance and the characteristic capacitance of the lead geometry that determines the maximum distance that a large impedance in the leads might be removed from the junction area. In practice this means that the electrodes themselves may be manufactured of well conducting metals provided they are correctly interfaced to a large resistance within, say, less than one tenth of

a micron from the junction. Here it is that the surface-doped Si samples may again be useful.

If it is possible to deposit small metallic islands on surface-doped Si without the presence of an oxide layer, and if it is also possible to establish a point contact tunnel junction on such a metallic island, then the desired current biased geometry with continuous charge redistribution may be realized. The islands must be small enough to restrict the intrinsic junction capacitance and at the same time large enough to cover at least some tens or hundred dopant sites in the Si, so that charge transport to and from the island is carried by many hopping channels in parallel. Diffusion of metal atoms into the Si might even give the contact more or less ohmic properties. Care should be taken to avoid any oxide layer between Si and metal island, as this would essentially create a double junction system instead of a single junction with large series impedance. Double junction systems display brilliant charging effects (see section 2.3 and chapter 4) but not the ones we are interested in here.

### 3.5.1 Sample preparation

The deposition of metal islands on the Si surface can be done in a simple and straightforward way by evaporation of a thin granular metal film. We chose Al as evaporation material, not only because it is easy to use in the evaporator but also because it forms a well defined oxide layer which is to serve as a barrier for the tip-island junction. The difficult part of the sample preparation concerns the surface treatment prior to the evaporation stage.

First the surface is cleaned by subsequent rinsing with a detergent and with alcohol, whereafter remaining organic contamination is removed by chemical oxidation in a 4:1:1 solution of  $\text{H}_2\text{O}_2$  (30%),  $\text{H}_2\text{O}$  and  $\text{H}_2\text{SO}_4$  (conc.). As already mentioned in section 3.4.1, the native oxide layer can be removed by etching with dilute HF for about 30 s. Renewed oxide growth can now be prevented by hydrogen termination of the dangling bonds on the clean Si surface, a treatment for which various recipes are available [31, 32, 33]. For our samples we employed a second etching process ( $\approx 1$  min) with a HF solution, containing 40% HF buffered to  $\text{pH} \approx 5$  by adding  $\text{NH}_4\text{F}$ . This passivates the surface and is supposed to prevent oxidation for at least an hour or so, giving us ample time to mount the clean sample into the High Vacuum (HV) bell jar of the evaporator.

To prevent the sample area surrounding the structures (especially the Al contact pads) from contaminating the etching procedure, the samples were carefully covered by thermoplastic resin, leaving only the relevant structures unprotected. After the etching this protective layer was removed with acetone.

A 75 Å thick granular Al film is now deposited using a sample temperature of 220 °C, a base pressure of  $2 \times 10^{-6}$  Torr and an evaporation rate of  $1.5 \text{ \AA s}^{-1}$ . This film is subsequently oxidized by a glow discharge in a 100  $\mu\text{Torr}$   $\text{O}_2$  atmosphere. In this way Al islands have been deposited on both the square and the meander structure.



### 3.5.2 Preliminary results

Finding the Al islands on these samples is a matter of trial and error, especially as the overall shape of the  $I(V)$  characteristics of the contacts we are looking for is not expected to differ significantly from what was found in the previous section on the bare Si samples. Using a tungsten tip, the samples were therefore probed on different positions, and promising  $I(V)$  characteristics were tested by their response to a rf-modulation, capacitively coupled in to the tip lead.

In the attempts so far we again encountered  $I(V)$  characteristics with displaced asymptotes and current suppression at low voltages. Unfortunately none of the probed contacts displayed any pronounced response to rf-modulation other than the regular rectification behaviour. Some contacts were found to display a so-called Coulomb staircase (see section 2.3.1 and chapter 4), indicating the presence of an oxide layer between the island under the tip and the surface-doped Si substrate.

On one occasion an  $I(V)$  curve (see Fig. 3.11) was seen which appears to possess a zero-current branch. This feature is essential to junctions in the current biased limit described by Averin and Likharev [1] (see chapter 2, Fig. 2.3) and has never been observed to date. In the measurement of Fig. 3.11 the tip was positioned above a square structure. The resulting point contact, examined in a three terminal configuration at  $T = 1.2$  K, experienced a series resistance of  $50 \text{ M}\Omega$ . The width of the zero current branch is seen to vary between curve (a) to (b). This is not surprising as the junction is in a bistable state for  $|V| < e/2C$  and, when on the zero-current branch, is known to be highly sensitive to voltage fluctuations like rf-noise. The maximum width of  $8 \text{ mV}$  indicates a junction capacitance at least smaller than  $10^{-17} \text{ F}$ .

Ill fate kept us from careful investigation of the complete  $I(V)$  characteristic, and its response to rf-modulation, as, presumably due to vibrations or a voltage spike, the contact was broken immediately after the traces of Fig. 3.11 had been recorded. Numerous attempts to restore the contact failed to reproduce the zero-current branch.

### 3.5.3 Discussion

The above described experiment is only a provisional and tentative endeavour to realize a microscopically current biased single junction geometry. Surface treatment is not well controlled and only a few grains on the sample may be expected to possess the required qualities concerning grain size, isolation from other grains and non-tunneling contact to the surface-doped Si. The concept nevertheless seems very promising.

The use of nanolithographic techniques in a controlled UHV environment will be highly advantageous in defining high quality islands, especially when the sample areas underneath the islands could be provided with extra doping to establish true ohmic contact to the resistive substrate. A really well-defined and controllable configuration can be achieved if a low temperature STM is employed to establish vacuum-barrier tunnel junctions to the islands.

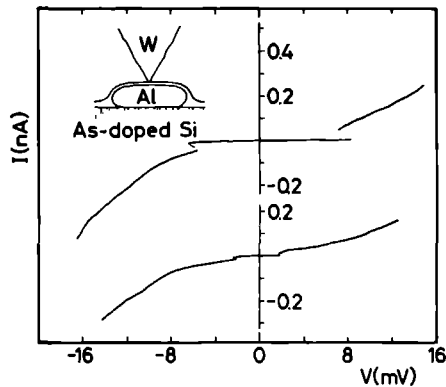


**Figure 3.11** Two  $I(V)$  characteristics measured on the same contact on the surface-doped Si sample covered with Al islands. The measurement temperature was 1.2 K and the contact had a series resistance of about 50 M $\Omega$ . This possibly represents the first observation of a zero-current branch, characteristic for a current-biased single junction.

### 3.6 Conclusions

Point-contact tunnel junctions on surface-doped Si samples, in which charge transport is completely governed by hopping conductance, reproducibly display  $I(V)$  characteristics with displaced linear asymptotes and strong current suppression near the origin. In our view these features have to be regarded as strong indications for the occurrence of charging effects associated with a small junction capacitance.  $I(V)$  characteristics meeting the same criteria are frequently observed in point-contact measurements on a wide the variety of sample materials, as discussed in section 3.2. Taken together this builds up consistent experimental evidence in support of the proposed decoupling mechanism involving hopping transport through localized surface, impurity or dopant states.

The absence of phase-locked resonances in the response of all examined junctions to externally applied rf-modulation, suggests the absence of coherent voltage oscillations. This is to be expected from the stochastic nature of the hopping mechanism, which is proposed to be responsible for the decoupling of the junction capacitance from stray capacitances in the environment.

Other mechanisms, known to induce non-linearities in tunneling characteristics, are thought unable to produce this particular shape of  $I(V)$  characteristics on such a wide range of sample materials.

At the moment our understanding of the proposed decoupling mechanism still has a very qualitative character. More insight may be gained by incorporating the theoretical concepts of tunneling transport in the presence of localized states, as expounded e.g. in Refs. [10, 11, 19, 20, 21, 22, 23], into a model describing tunneling between two metallic electrodes via an appropriate random network of hopping

sites. This model will probably have to take into account the special tunneling properties of point-contact and STM-type tunnel junctions which have been discussed in section 1.4.

From the experimental point of view very interesting future prospects can be found outside the scope of the present hunt for charging effects and SET-oscillations. Spatially resolved STS-measurements on e.g. the As-doped Si samples may reveal important information on the microscopic nature of hopping conductivity. Also the very origin of localized states in oxide layers or on more or less clean sample surfaces may be studied with STM.

The above results have general consequences for the performance and interpretation of point-contact and STM-measurements especially at low temperatures. Spectroscopy on oxidized or contaminated samples or on materials which for intrinsic reasons have localized surface or dopant states, may be severely influenced if not dominated by charging effects. These are expected to produce a shift of intrinsic spectroscopic features by the charging energy  $e^2/2C$ , and accompanying voltage fluctuations with amplitude  $e/2C$  will smear the junction characteristics.

The surface-doped Si samples have the advantage of their high and tunable resistance at low temperatures, and can be employed to establish a junction geometry approaching the ideal conditions of the theory of Ref. [1], if small metallic islands are deposited on the oxide-free sample surface. Tunnel junctions have been made by positioning a tip above such islands and establishing mechanical contact with the oxide layer of the deposited metal. The observation on one occasion of a possible zero-current branch gives funded hope that the desired conditions can be met reproducibly on samples produced under better controlled circumstances than in the provisional attempt presented here.

## Appendix: the experimental set-up

In this appendix some mechanical and electronic details of the set-up used in the experiments presented in chapters 3, 4 and 5 are described.

### The point-contact insert

The lower part of the insert (see Fig. 3.12) is essentially a low-temperature STM, although it is not used as such in the experiments presented here. Instead, tunnel junctions are made by subtly bringing a tip in mechanical contact with a sample. Coarse approach is established by bending a rigid cantilever via a worm-wheel construction. The tip (in most cases a sharpened  $50\ \mu\text{m}$  thick tungsten wire) is mounted on a piezo tube which in turn is connected to the cantilever. The piezo tube allows precise tip movement perpendicular to the sample (in STM commonly defined as the  $z$ -direction) as well as parallel to the sample surface ( $x$ - and  $y$ -direction).

The point-contact device is mounted in a brass pot, which for the most part is covered by a lead foil, to provide shielding from rf-noise. The insert is submersed in a liquid helium dewar. Vibration isolation is achieved by suspending the cryostat

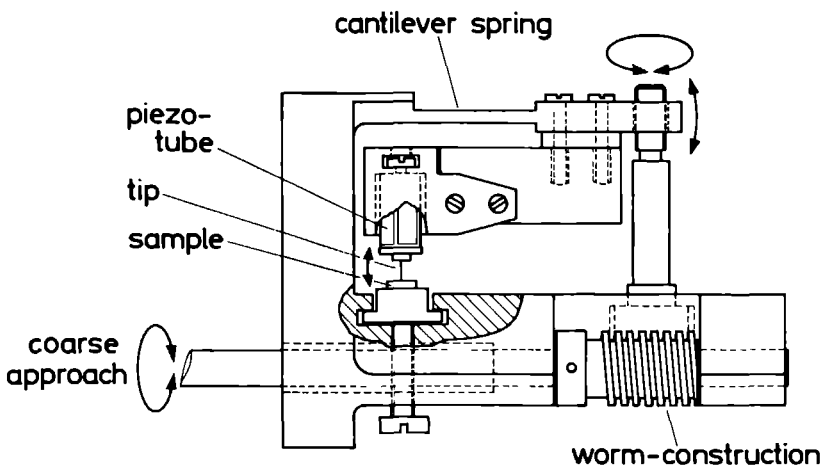


**Figure 3.12** Schematic drawing of the mechanics of the lower part of the point-contact insert, used in the experiments of chapter 3, 4 and 5 of this thesis.

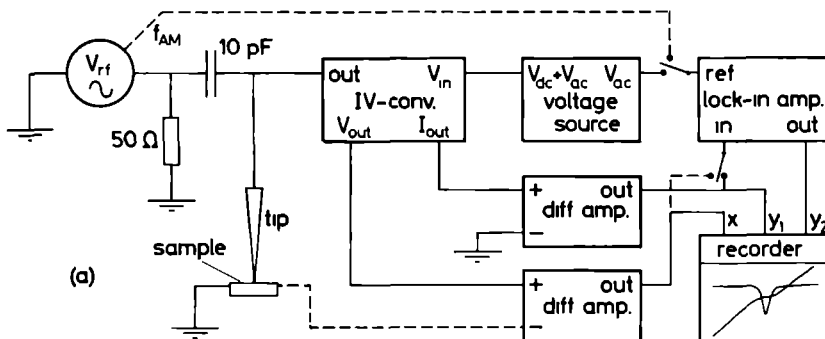


**Figure 3.13**

Electronic set-up used to record the  $I(V)$  and  $\partial I/\partial V(V)$  characteristics presented in chapters 3, 4 and 5 of this thesis: (a) general scheme; (b) simplified scheme of the home-built current-to-voltage converter.

from the ceiling with elastic rubber bands. The whole set-up is operated inside a Faraday cage, although for most measurements it did not matter whether or not the door was closed.

### 3.6.1 Electronics

The heart of the electronic part of the set-up (see Fig. 3.13) is a home-built current to voltage converter, which is essentially similar to the ones used in the STM-measurements of our group. In the general scheme the capacitive coupling of rf-modulation to the tip wire is optional, and only employed in the measurements described in this chapter.

## References

1. D.V. Averin and K.K. Likharev, *J. Low Temp. Phys.* **62** (1986) 345.
2. D.V. Averin and Yu.V. Nazarov, *Physica B* **162** (1990) 309.
3. P. Delsing, K.K. Likharev, L.S. Kuzmin, and T. Claeson, *Phys. Rev. Lett.* **63** (1989) 1180.
4. A.N. Cleland, J.M. Schmidt, and J. Clarke, *Phys. Rev. Lett.* **64** (1990) 1565.
5. P.J.M. van Bentum, H. van Kempen, L.E.C. van de Leemput, and P.A.A. Teunissen, *Phys. Rev. Lett.* **60** (1988) 369.
6. P.J.M. van Bentum, L.E.C. van de Leemput, R.T.M. Smokers, and H. van Kempen, *Phys. Scr.* **T25** (1989) 122.
7. P.J.M. van Bentum, L.E.C. van de Leemput, R.T.M. Smokers, and H. van Kempen, *J. Microscopy* **152** (1988) 11.
8. R.C. Jaklevic, private communication.
9. I. Takeuchi, J.S. Tsai, S. Ishizaka, T. Yoshitake, S. Satoh, and J. Fujita, preprint (1991).
10. I.A. Devyatov and M.Yu. Kupriyanov, *JETP Lett.* **52** (1990) 311 (*Pis'ma Zh. Eksp. Teor. Fiz.* **52** (1990) 929).
11. L.I. Glazman and K.A. Matveev, *JETP Lett.* **48** (1988) 445 (*Pis'ma Zh. Eksp. Teor. Fiz.* **48** (1988) 403).
12. D. McBride and G. Rochlin, *J. Appl. Phys.* **45** (1974) 2305.
13. J.B. Barner and S.T. Ruggiero, *IEEE Trans. Magn.* **23** (1987) 854.
14. U. Hartmann, R. Berthe, and C. Heiden, preprint (1988); R. Berthe, U. Hartmann, C. Heiden, and J. Halbritter, preprint (1988).
15. J. Valdes and E. Choleva, preprint (1989/1990).
16. S. Gregory, *Phys. Rev. Lett.* **64** (1990) 689.
17. R.T.M. Smokers, P.J.M. van Bentum, and H. van Kempen, *Physica B* **165&166** (1990) 63.
18. H. van Kempen, P.J.M. van Bentum, and R.T.M. Smokers, in *Scanned Probe Microscopy*, ed. H. Kumar Wickramasinghe, AIP conf. proc. **241** (1991) 101.
19. D.G. Cahill and R.J. Hamers, preprint (1991).
20. S.J. Bending and M.R. Beasley, *Phys. Rev. Lett.* **55** (1985) 324.
21. M. Naito and M.R. Beasley, *Phys. Rev. B* **35** (1987) 2548.
22. Y.Xu.A. Matsuda and M.R. Beasley, *Phys. Rev. B* **42** (1990) 1492.

23. D.A. Buchanan, M.V. Fischetti, and D.J. DiMaria, *Phys. Rev. B* **43** (1991) 1471.
24. R.T.M. Smokers, P.J.M. van Bentum, and H. van Kempen, in: *Granular Nanoelectronics*, eds. D.K. Ferry, J.R. Barker, and C. Jacoboni, (Plenum, N.Y., 1991), proceedings of NATO Advanced Study Institute, 1990, Il Ciocco, Italy.
25. Chen Gang, H.D. Koppen, R.W. van der Heijden, A.T.A.M. de Waele, H.M. Gijsman, and F.P.B. Tielen, *Solid State Comm.* **72** (1989) 173.
26. Chen Gang, H.D. Koppen, R.W. van der Heijden, A.T.A.M. de Waele, H.M. Gijsman, C.M. van Es, and F.P.B. Tielen, preprint (1989).
27. A.L. Efros and B.I. Shklovskii, *J. Phys. C: Solid State Phys.*
28. S.M. Sze, *Physics of Semiconductor Devices*, (John Wiley & Sons, N.Y., 1981).
29. E.H. Rhoderick and R.H. Williams, *Metal-Semiconductor Contacts*, (Clarendon Press, Oxford, 1988).
30. L.J. Brillson, *Surface Science Reports* **2** (1982) 123. **8** (1975) L49.
31. D.B. Fenner, D.K. Biegelsen and R.D. Bringans, *J. Appl. Phys.* **66** (1989) 419.
32. N. Hirashita, M. Kinoshita, I. Aikawa, and T. Ajioka, *Appl. Phys. Lett.* **56** (1990) 451.
33. G.S. Higashi, Y.J. Chabal, G.W. Trucks, and K. Raghavachari, *Appl. Phys. Lett.* **56** (1990) 656.



## Chapter 4

### **Incremental charging of single small particles: point-contact tunneling experiments**



The double junction system, i.e. two tunnel junctions connected in series by a small common electrode, is most convenient for the observation of charging effects, as each junction effectively decouples the other from the stray capacitance of the leads (see section 2.3). The first observations of the Coulomb blockade and the Coulomb staircase have been made in a configuration consisting of many double junction systems in parallel. In the classical experiment of Zeller and Giaever [1], as well as in the more recent experiments by Barner and Ruggiero [2] and Kuzmin and Likharev [3] granular films were employed to establish the small common electrode. These granular films were embedded in an oxide layer, and sandwiched between two continuous films. Observation of a Coulomb staircase in these systems is troubled by the spread in grain size. In 1987 Jan van Bentum and I employed an STM-like set-up in order to accomplish a double junction system in which all current really flows through a single isolated grain [4]. To this end we used a granular film deposited on an oxidized continuous base electrode. This experiment is described in section 4.1. Later STM-measurements by other groups [5–11] essentially confirmed and extended these observations on a range of similar systems.

Around the same time we also observed the Coulomb staircase in several systems of more or less granular nature which were not specially prepared for the purpose. In section 4.2 I present some results on both ceramic and supposedly crystalline high- $T_c$  superconductors.

Another interesting double junction system can be formed by depositing small organometallic clusters, such as the  $\text{Pd}_{561}(\text{phen})_{38\pm 2}\text{O}_{\approx 200}$  molecule, on a conducting substrate. With the STM the clusters can in principle be visualized and spectroscopy can be performed. In this type of experiment we expect to see the influence of the discrete density of electronic states inside the particle superimposed on the step structure due to the Coulomb staircase. Some preliminary results are presented in section 4.3.

## 4.1 Granular aluminum films

### 4.1.1 Sample preparation and experimental set-up

The samples used in these experiments consisted of a 35-40 Å thick granular Al film deposited on top of a thick (500 Å) oxidized continuous Al film. This continuous base electrode was evaporated on a glass substrate at a pressure  $2 \times 10^{-6}$  Torr using an evaporation rate of  $2 \text{ \AA s}^{-1}$ . The substrate temperature was approximately 80 °C throughout the preparation run. Without opening the evaporator system this film was then oxidized using a glow discharge in a pure oxygen atmosphere at a pressure of 0.15 Torr. On top of this oxide layer the granular film was evaporated. Granularity is achieved by slow evaporation ( $1 \text{ \AA s}^{-1}$ ) of a thin layer (35 Å) at a relatively high base pressure ( $2 \times 10^{-6}$  Torr), while keeping the substrate warm. Oxidation of the granular film was simply established by exposure to room air after removal of the sample from the evaporator.

Measurements were performed using the set-up described in the appendix of

chapter 3. At the time of the measurements STM-operation of the set-up was not possible. The oxide layer on the film would have made scanning very difficult anyway. The grains could therefore not be imaged, and could only be identified on the basis of the shape of the  $I(V)$  characteristics. The insert was submersed in a liquid helium bath, which was pumped to a temperature of 1.2 K in order to minimize thermal smearing of the  $I(V)$  characteristics. As a tip we used a  $50\ \mu\text{m}$  thick tungsten wire, sharpened by electrochemical etching in a 5M KOH solution while applying an ac voltage of 25 V. Using the piezo-drive, the tip is gently brought in mechanical contact with the sample. If the tip is positioned above a grain, a double junction system is established. In the tunnel junction between tip and grain the barrier is formed by the oxide layers of both the tip and the grain, while in the junction between grain and base electrode the barrier is formed by the oxide layer of the continuous film. A schematic drawing of the configuration is shown in Fig. 4.1. Using a parallel plate approximation  $C = \epsilon_0 \epsilon_r A/d$ , with  $A$  the cross-sectional area of the grain and  $d$  the barrier thickness, the capacitance  $C$  between the grain and the base electrode can be estimated. Taking  $\epsilon_r = 8$ ,  $A = (100\ \text{\AA})^2$  and  $d = 10\ \text{\AA}$ , one calculates a capacitance of order  $7 \times 10^{-18}$  F. The capacitance between tip and grain will be of the same order of magnitude.

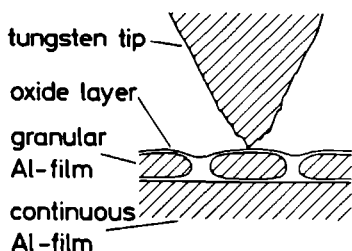


**Figure 4.1** Schematic drawing of the double junction system, constituted by tip, grain and base electrode.

The tip-sample system was voltage biased using the electronics as already shown in Fig. 3.13. The differential conductance  $\partial I/\partial V(V)$  was measured by superimposing a small ac-modulation signal on the ramped dc-voltage and recording the harmonic response in the current with a lock-in amplifier.

#### 4.1.2 Results

Figure 4.2(a) (also presented in Ref. [4]) shows the  $I(V)$  and corresponding  $\partial I/\partial V(V)$  characteristics of a point contact on the granular-Al/oxide/Al double layer. The equidistant peaks in  $\partial I/\partial V(V)$  correspond to clearly observable stepwise increments of the current in the  $I(V)$  curve. In other words, the  $I(V)$  characteristic displays a well developed Coulomb staircase. The peaks show up in a periodic pattern with a period  $\langle \Delta V \rangle = 15.0 \pm 1.6$  mV. According to the theory of chapter 2, section 2.3, this spacing corresponds to a capacitance  $C_2 = e/\Delta V = 1.1 \times 10^{-17}$  F.

The  $I(V)$  and corresponding  $\partial I/\partial V(V)$  characteristics depicted in Fig 4.2(b) were recorded on the same spot of the sample immediately after the trace of Fig. 4.2(a). We again observe equidistant peaks with the same average periodicity as

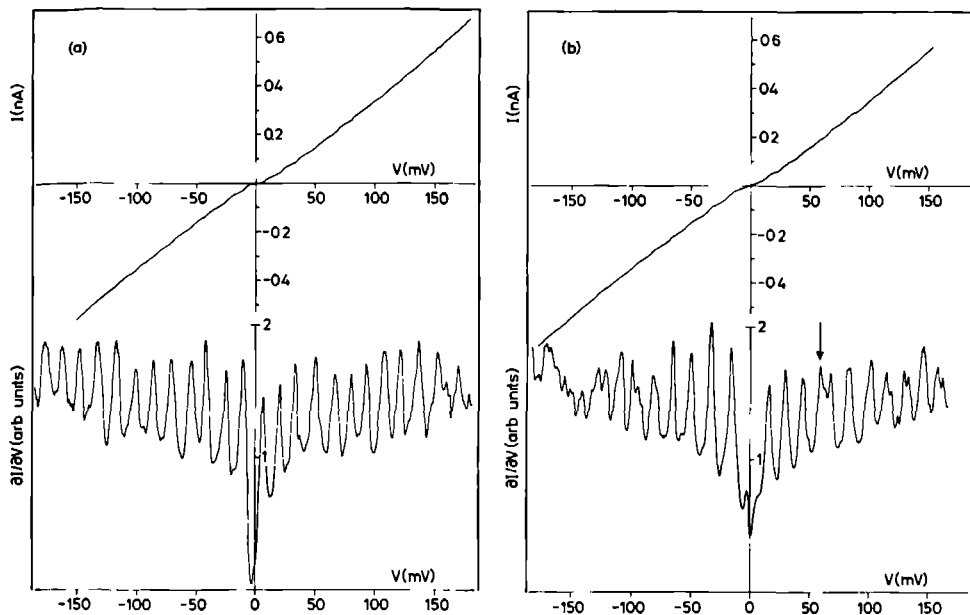


**Figure 4.2** (a)  $I(V)$  and  $dI/dV(V)$  characteristics of a point-contact tunnel junction on a sample consisting of a granular Al film (35 Å) deposited on an oxidized continuous Al film (500 Å), showing a well developed Coulomb staircase. (b)  $I(V)$  and  $dI/dV(V)$  characteristics of the same point-contact tunnel junction, recorded immediately after trace (a). The measurements were performed at  $T = 1.2$  K.

those in Fig. 4.2(a). This time, however, the peaks around zero bias are separated by twice this period. Also the current suppression near the origin, due to the Coulomb blockade, is much less pronounced. This "switching" behaviour between subsequently measured traces is observed on all contacts on the same and similar samples. Another remarkable difference with respect to Fig. 4.2(a) concerns the occurrence of discrete shifts in the "phase" of the periodicity, as indicated by the arrow in Fig. 4.2(b). As a matter of fact the absence of these shifts in Fig. 4.2(a) is accidental, as the shifts occur in almost all curves.

All the effects illustrated in Figs. 4.2(a) and 4.2(b) were also present in several point-contact junctions on other spots on the same sample, as well as on other similar samples. The characteristics show no sign of possible superconductivity in the aluminum. The bulk critical temperature ( $T_c$ ) of aluminum is 1.196 K, slightly lower than the measurement temperature. The corresponding energy gap equals 0.2 meV. The critical temperature of the grains might be increased due to their small size. However, regarding the size of the Coulomb gap observed in these measurements, a superconducting energy gap of the order of one mV is needed to produce a distinct shift in the staircase structure. For this a  $T_c$  of order 6 K is needed, which is

very improbable for the system under consideration. Therefore we can conveniently neglect the effects of superconductivity in the interpretation of the measurements.

The differences between the two figures can now be explained in terms of the theory of section 2.3 (see also Refs. [10, 11]). This is illustrated in Fig. 4.3 in which the low voltage parts of the  $I(V)$  curves of Figs. 4.2(a) and 4.2(b) are compared with fits calculated with the help of the analytical expression derived in Refs. [10, 11]. The capacitance values  $C_1$  and  $C_2$ , as well as the residual charge  $Q_0$  can be calculated from the positions of the steps and kinks in the  $I(V)$  curve (see chapter 2, section 2.3.1). The order of magnitude of the resistance of the junction with the largest capacitance can be estimated from the slope of the steps, or the slope of the high voltage asymptote. Apart from a small trade-off between  $Q_0$  and the two capacitance values, this leaves only the second resistance as a free fitting parameter. The ratio  $R_2/R_1$  mainly determines the observability of the steps. The exact values of the slopes of the linear part and the steps are determined by a complex combination of all resistance and capacitance values.

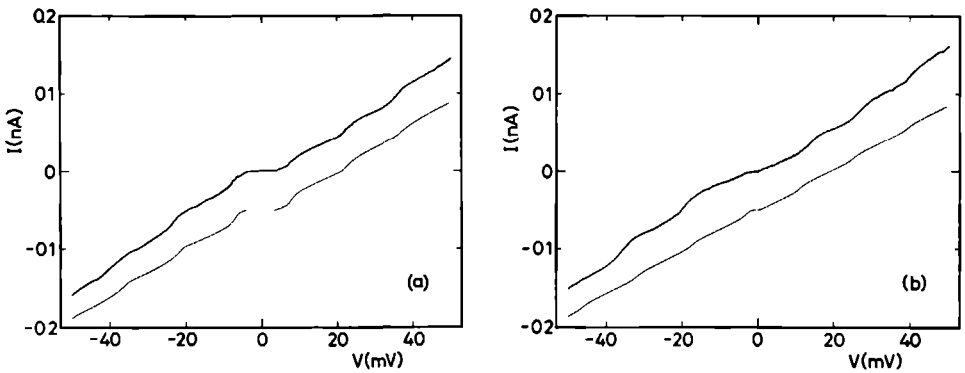


**Figure 4.3** (a) The low voltage part of the  $I(V)$  characteristic of Fig. 4.2(a). The thin line, offset for clarity, represents a fit with the theory of section 2.3, using  $C_1 = 19.9 \times 10^{-18}$  F,  $C_2 = 11.3 \times 10^{-18}$  F,  $R_1 = 15$  M $\Omega$ ,  $R_2 = 310$  M $\Omega$ ,  $Q_0 = -0.022e$  and  $T = 1.2$  K. (b) The low voltage part of the  $I(V)$  characteristic of Fig. 4.2(b). The thin line again represents a fit with the theory of section 2.3, using  $C_1 = 69.8 \times 10^{-18}$  F,  $C_2 = 11.3 \times 10^{-18}$  F,  $R_1 \approx 0.5$  M $\Omega$ ,  $R_2 = 390$  M $\Omega$ ,  $Q_0 = -0.274e$  and  $T = 1.2$  K.

The  $I(V)$  characteristics as calculated from the theory of section 2.3 are symmetric under reversal of the indices  $i, j$  in the parameters  $C_{i,j}$  and  $R_{i,j}$  and simultaneous reversal of the sign of  $Q_0$ . This leaves us with the freedom to assign the capacitance which dominates the step structure to either the tip-grain or the grain-base junction. In the above measurement the step width could not be influenced by changing the tip sample distance, which suggests that the fixed grain-base capacitance determines the step width of the Coulomb staircase. In the fits of traces (a) and (b) of Fig. 4.3, which were recorded on the same position, we have therefore kept  $C_2$  constant and equal to  $e/(\Delta V)$ . By definition of the bias direction,  $C_2$  is to

be identified with the grain-base junction

As one can see, the fits are quite satisfactory. The inferred capacitance values are in good agreement with the estimate given in the section 4.1.1. In the fit of Fig. 4.3 (b) the steps are not so pronounced as in the measurement. This is due to the reversed  $C_2/C_1$  ratio, and may only be repaired somewhat by assuming an unrealistically low value for the tip-grain resistance  $R_1$ .

The main differences between the curves (a) and (b) in Fig. 4.3 now reduce to a change of  $Q_0$  from  $-0.022e$  to  $-0.274e$ , a change of  $C_1$  from  $19.9 \times 10^{-18}$  F to  $69.8 \times 10^{-18}$  F, and a not too accurately determinable decrease of  $R_1$ , by about one and a half orders of magnitude. If we associate junctions 1 and 2 in the model with the junction between tip and grain and the one between grain and base electrode respectively, this change is consistent with an explanation in terms of a decrease of the tunnel distance in the tip-grain junction, in combination with the assumption that  $Q_0$  is induced by a localized charge located in the oxide on the tip. Decreasing the tunnel distance increases the capacitance linearly, meanwhile exponentially decreasing the resistance. Moving the localized charge with respect to the grain causes a redistribution of the excess charge on the grain, resulting in a different value of the effective residual charge  $Q_0$ . A change in the workfunction due to the change in tunnel distance can also induce a different  $Q_0$ . As one can see especially from Fig. 4.2(b), the  $I(V)$  and  $\partial I/\partial V(V)$  curves are somewhat shaky. The change in point-contact configuration causing the transition from trace 4.2(a) to 4.2(b) may therefore very well be induced by external vibrations.

The change in  $Q_0$  may also (partly) result from the ionization or neutralization of localized impurity or surface states, a process that becomes more probable at higher voltages. This may explain the fact that the "phase" shifts, which of course have the same origin as the switching behaviour, are mainly observed at higher voltages ( $\approx 50$  mV or more). However, this effect can not explain the differences in the  $C_1$  value needed to fit the two subsequent traces. Therefore the explanation in terms of a slightly unstable point contact suffering from external vibrations is most probable for this particular set of data. On the whole, however, the junctions established on the granular film were quite stable. Some of them could even be monitored for several hours.

The parameters used to fit trace (a) of Fig. 4.3 differ significantly from the ones used in Ref. [4]. At the time of that publication the theory of section 2.3 was still in development, and especially the influence of the residual charge was not yet incorporated quantitatively. From the difference it may be clear that for the correct fitting of parameters, other than the capacitance dominating the staircase, proper incorporation of the residual charge  $Q_0$  is essential. Because of that also the shifting of peak positions between subsequent traces could not be analyzed quantitatively, and was only understood in a rather intuitive way. Nevertheless the interpretation of Ref. [4] in terms of essential physical principles was appropriate.

Figure 4.4 shows two more examples of  $I(V)$  curves measured on other spots on the same sample. The thin lines again represent fits with the theory of section 2.3. For both cases the curves can be fitted quite accurately in the interval

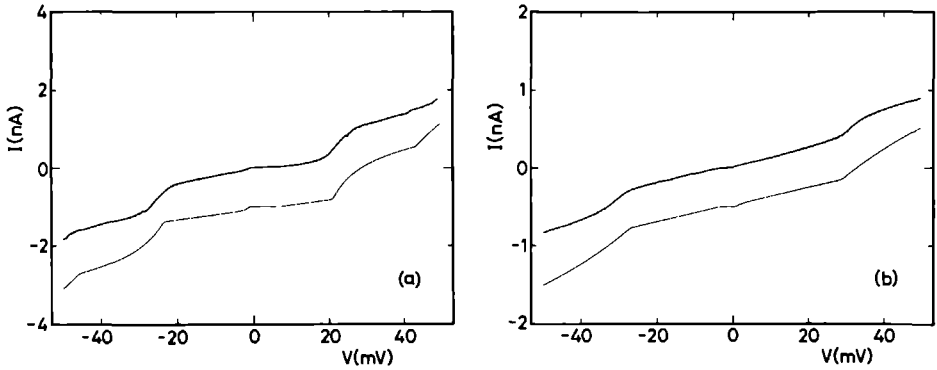


**Figure 4.4** Two more examples of  $I(V)$  characteristics on a granular-Al/oxide/Al double layer sample. The thin lines, offset for clarity, again represent fits to the theory of section 2.3, with the following parameters: (a)  $C_1 = 1.41 \times 10^{-18}$  F,  $C_2 = 7.2 \times 10^{-18}$  F,  $R_1 = 4.0$  M $\Omega$ ,  $R_2 = 12.0$  M $\Omega$ ,  $Q_0 = -0.44e$  and  $T = 1.2$  K. (b)  $C_1 = 1.47 \times 10^{-18}$  F,  $C_2 = 5.72 \times 10^{-18}$  F,  $R_1 = 16.5$  M $\Omega$ ,  $R_2 = 14$  M $\Omega$ ,  $Q_0 = 0.467e$  and  $T = 1.2$  K.

$[-e/C_2, e/C_2]$ . Outside this range, however, it appears difficult to properly fit the slopes and asymptotic heights of the steps. This may be due to non-linearities in the tunnel rates of the junctions. In the expression used to fit these measurements the rate is explicitly assumed linear in the applied voltage.

In the measurements presented above the samples were specifically designed to produce the double junction system. The Coulomb staircase can however also be observed on metal film samples, which may be supposed to be continuous, but nevertheless often contain some isolated grains. This is e.g. illustrated by the results of McGreer *et al.* [5, 6] of STM and STS measurements on a Pb film. Here I will show a point-contact measurement on a 150 Å thick Al film, which was part of an Al/oxide/Al planar tunnel junction. The characteristics of the planar junction itself exhibited a zero voltage Josephson current branch, indicating that the films were in principle superconducting at the measurement temperature of 1.2 K. The thin film strips themselves however showed basically ohmic behaviour with critical current effects in the nA-regime, implying that the films were only locally superconducting and that the junction characteristics were probably dominated by a small superconducting region short-circuiting the normal tunnel channels.

The  $I(V)$  curves measured on one spot of the sample show a very peculiar Coulomb staircase, as exemplified in Fig. 4.5. Superimposed on a Coulomb staircase with a periodicity of  $\Delta V = 18.6 \pm 0.7$  mV a weaker step structure can be discerned, which has about the same periodicity but markedly different phase. A jump in the phase of the weaker staircase, indicated by the arrows in Fig. 4.5 does not noticeably alter the phase of the dominant staircase structure (the trace was recorded from right to left).

Although I will not attempt to prove this quantitatively, the above data seem

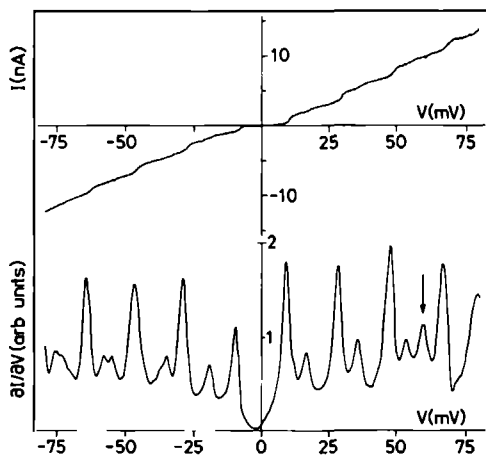


**Figure 4.5**  $I(V)$  and  $\partial I/\partial V(V)$  characteristics of a point-contact tunnel junction on a supposedly continuous Al film (150 Å). Apparently the film contained some isolated grains. The measurement was performed at  $T = 1.2$  K.

adequately explained by assuming for this case a triple junction geometry, consisting of a single small junction connected in series to a parallel configuration of two junctions. As the two entangled staircases have equal step width, the single junction must have the largest capacitance. Charged impurities in the barriers of the two parallel junctions can then influence the phase of the individual staircases. The parallel junction may be the result of a double tip effect, as is often encountered in topographic STM-measurements, or can be attributed to two separated weak spots in the oxide of the grain that constitutes the central electrode.

## 4.2 High- $T_c$ superconductors

In 1986 the high- $T_c$  superconducting oxides were discovered by Bednorz and Müller [12]. The extremely high critical temperatures of these, in the normal state, very poor conductors raised questions to the extent in which these superconductors could still be described in a BCS-like framework. Tunneling spectroscopy of the effective superconducting density of states (see chapter 1, section 1.3.2) might be helpful in answering these questions. The first samples of  $\text{La}_{1.85}\text{Sr}_{0.15}\text{CuO}_4$  and  $\text{YBa}_2\text{Cu}_3\text{O}_{7-\delta}$  and related species were sintered ceramics with a lot of off-stoichiometric residue, and were therefore completely unfit for application in evaporated planar junctions. Point-contact tunnel junctions provided a convenient alternative, with the extra advantage of yielding information on the local variation of the material properties. The results of this type of spectroscopic measurements are described in chapter 5.

The reason why we pay attention to these materials here, lies in the fact that

the granular nature of the ceramic material often resulted in double junction configurations in which the tunneling behaviour is completely dominated by charging effects. For several reasons the grains on the surface of the samples were often not superconducting, so that Coulomb staircases were observed without the interference of superconductivity. In the beginning these staircases were mistakenly interpreted by several authors as being multiple superconducting energy gap structures. As we can see from the calculations of chapter 2, section 2.3, the low voltage part ( $|V| < 3e/2C_2$ ) of the Coulomb staircase strongly resembles the  $I(V)$  characteristics of NIS and SIS tunnel junctions as described in chapter 1, section 1.3.2. And, even more confusingly, also the magnitudes of the observed charging energy and the gap energy expected on the basis of the BCS-relation between the gap and the critical temperature (chapter 1, Eq. 1.16) are of the same order. Therefore the distinction between the two effects can only be made unambiguously if the  $I(V)$  characteristics are measured up to a voltage of at least three times the apparent gap. A similar warning is also expressed in Refs. [13, 14].

Figure 4.6 depicts the  $I(V)$  characteristics of a tunneling point contact between a tungsten tip and a ceramic  $\text{YBa}_2\text{Cu}_3\text{O}_{7-\delta}$  sample. Experiments were performed at  $T = 1.2$  K in the same set-up as described in the previous section. The average step width is about 10.5 mV, corresponding to a capacitance of  $1.5 \times 10^{-17}$  F. The three curves have been recorded immediately after each other. Again the switching behaviour is observed. The curves are asymmetric with regard to the, non-linear, background conductance. This is often observed in tunneling on high- $T_c$  superconductors, and is probably the result of low barrier heights or inelastic processes in the barrier. I will come back to this point in chapter 5.

In the measurement shown in Figs. 4.7(a) and 4.7(b) the sample was a tiny single crystal (area  $< 1 \text{ mm}^2$ ) of  $\text{YBa}_2\text{Cu}_3\text{O}_{7-\delta}$  material. Spectroscopic measurements with a tungsten tip revealed no trace of superconductivity on most parts of the surface, apart from some weak Josephson-like behaviour on a few spots. Also, some negative differential resistance (NDR: see chapter 5) features were observed.

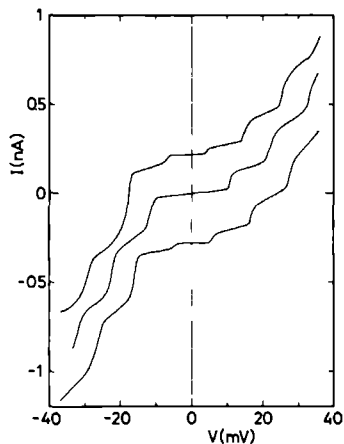


**Figure 4.6** Three subsequently recorded  $I(V)$  characteristics of a tunnel junction between a W tip and a ceramic  $\text{YBa}_2\text{Cu}_3\text{O}_{7-\delta}$  sample.



All this indicates that the top layer of the sample was for the largest part not superconducting, and probably off-stoichiometric. On some positions on the surface, however, we did observe clear Coulomb staircases. The traces of Figs. 4.7(a) and 4.7(b), recorded immediately after each other, again display the switching behaviour, due to a change in the residual charge, which was also observed on the Al samples described in the previous section. The curves have the same average step width equal to  $\langle \Delta V \rangle = 10.9 \pm 0.7$  mV. From the symmetric position of the peaks in both figures it is clear that  $Q_0$  this time changed from approximately zero in Fig. 4.7(a) to almost  $\pm e/2$  in Fig. 4.7(b). Furthermore the arrows in the figures indicate the occurrence of discrete phase shifts in the step structure at higher voltages, as also reported for the experiments on granular aluminum.

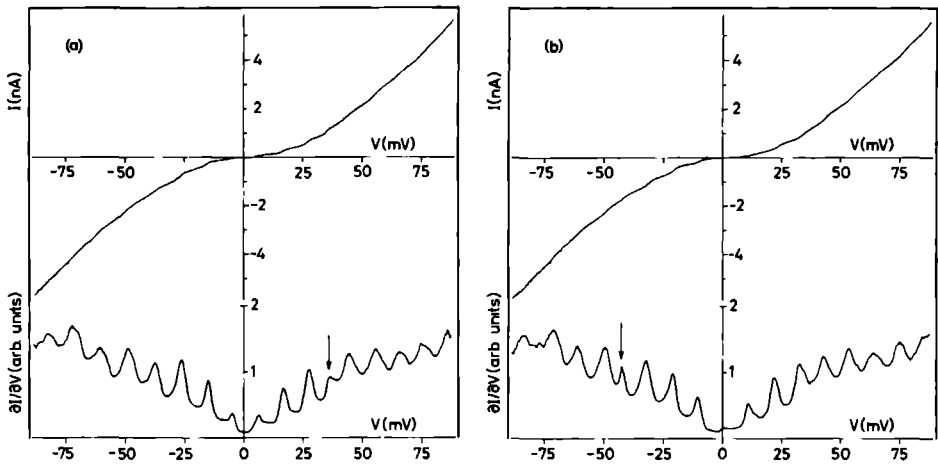


**Figure 4.7** (a)  $I(V)$  and  $\partial I/\partial V(V)$  characteristics of a point-contact tunnel junction on a single-crystal  $\text{YBa}_2\text{Cu}_3\text{O}_{7-\delta}$  sample. The measurement was performed at  $T = 1.2$  K. (b)  $I(V)$  and  $\partial I/\partial V(V)$  characteristics of the same point-contact tunnel junction, recorded immediately after trace (a).

The grain that constitutes the central electrode in this experiment is possibly a small particle, left on the surface when the crystal was taken from the melt. The parabolic background of the  $I(V)$  characteristics is more or less symmetric in this case, and can therefore be accounted for in the model calculations quite easily by adding a cubic term to the linear tunnel rates as defined in Eq. 2.18 of chapter 2. The rates are thereto written as  $r_i(E, V) \propto (\Delta E + \alpha_i(\Delta E)^2)/R_i$ . The weight  $\alpha_i$  of the correction can be estimated from the overall shape of the  $I(V)$  characteristics. The result of a fit to the curve of Fig. 4.7(a) is shown in Fig. 4.8.

The contact on which the measurements were performed could be kept stable for almost seven hours. This allowed careful investigation of the effect of changing the tunnel distance in the tip-grain junction by changing the voltage on the  $z$ -piezo. Figure 4.9 shows the peak positions of the contact at two different values of the

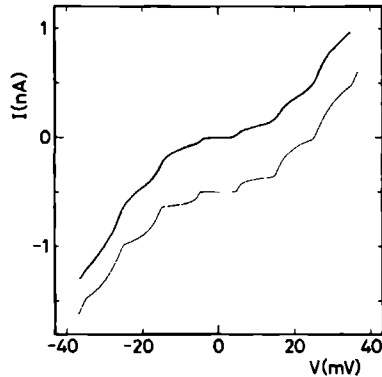


**Figure 4.8** Fit to the  $I(V)$  curve of Fig. 4.7, including a cubic term in the tunnel rates. Used parameters are:  $C_1 = 2.4 \times 10^{-18}$  F,  $R_1 = 6$  M $\Omega$ ,  $C_2 = 16 \times 10^{-18}$  F,  $R_2 = 58$  M $\Omega$ ,  $Q_0 = 0$ ,  $\alpha_1 = 160$  (eV) $^{-1}$ , and  $\alpha_2 = 55$  (eV) $^{-1}$ .

$z$ -piezo voltage. The step width is changed by about 50%, proving that in this case the capacitance dominating the staircase is the one between tip and grain. The mere fact that the tunnel distance influences the step width, proves that the step structure is the result of incremental charging, and rules out all other explanations in terms of e.g. multiple superconducting energy gaps or quantum size effects.

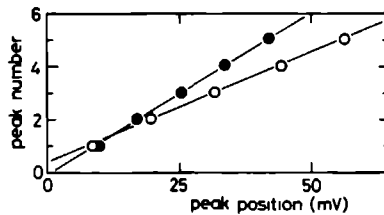


**Figure 4.9** Peak positions in  $\partial I/\partial V(V)$  of the same contact at two different tip-grain distances. Upon decreasing the distance the positions move from the open circles to the filled circles.

## 4.3 Ligand-stabilized clusters

### 4.3.1 Introduction

In the measurements on small particles presented above the size of the grains was always typically  $\approx 100$  Å which implies that the density of electronic states inside the particles could appropriately be assumed continuous. For smaller particles this need no longer be justified, certainly not when the particles are in some way

symmetric so that degeneracy increases the level splitting

Candidates possibly meeting these requirements can be found in the class of organometallic clusters, that can nowadays be synthesized by advanced chemical methods [15]. In general, these clusters have a metallic core consisting of a center atom enclosed in one or more shells of atoms. Every  $n^{\text{th}}$  shell contains  $10n^2 + 2$  atoms. Only full shells can be stabilized, so that possible cores consist of the following "magic" numbers of atoms: 13, 55, 147, 309, 561. In this series the clusters represent a gradual evolution from the molecular to the bulk solid state regime. Most clusters are not stable in their naked form. The surface energy is therefore reduced by covering the cluster with organic ligands.

In our group mainly two ligand-stabilized cluster types are investigated using STM and STS. These clusters are  $\text{Au}_{55}(\text{PPh}_3)_{12}\text{Cl}_6$ , which has a core of 55 gold atoms stabilized by  $\text{P}(\text{C}_6\text{H}_5)_3$  molecules and individual Cl atoms, and the somewhat larger  $\text{Pd}_{561}(\text{phen})_{38\pm 2}\text{O}_{\approx 200}$ , which consists of 561 palladium atoms surrounded by a ligand shell of phenanthroline ( $\text{C}_{12}\text{H}_8\text{N}_2 \bullet \text{H}_2\text{O}$ ) and  $\text{O}_2$  molecules. Some results are presented in Ref. [16]. Here I will concentrate on the  $\text{Pd}_{561}$  cluster only.

X-ray diffraction measurements [15] show that the core atoms of the  $\text{Pd}_{561}$  cluster form a face centered cubic lattice, corresponding to a close packed structure. From the width of the diffraction peaks the diameter of the cluster is inferred to be  $24.2 \text{ \AA}$ . Modelling the cluster according to this information one immediately sees that the core is not spherical. In fact it has an icosahedral shape. The surface consists of six square faces connected by eight triangular faces. Viewed in the direction perpendicular to a square face the cluster has a square cross section of about  $22 \times 22 \text{ \AA}^2$ , while looked upon perpendicularly to the triangular face the cross section is octagonal with a diameter of about  $27 \text{ \AA}$ . The phenanthroline ligands are thought to be bound to the face edges in a regular pattern, with the plane of the molecule standing perpendicular to the surface in a crest-like manner.

For STM-purposes the clusters can be deposited from solution on conducting substrates such as graphite, gold facets, or epitaxial gold terraces on mica. The clusters are extremely interesting for spectroscopic STM-measurements, as their small size is expected to result in a discrete density of electronic states in the core. Moreover, the particles have a well defined size and shape, which certainly is not the case for alternatives such as e.g. evaporated metal grains of the same dimensions. The order of magnitude of the level splitting can be estimated using the particle in a box model.

The density of states for a particle in a rectangular box with volume  $V$  is easily calculated to be  $D(E) = (V/2\pi^2)(2m/\hbar^2)E^{1/2}$ , including spin degeneracy. The Fermi energy of such a system filled with  $N$  particles equals  $E_F = (\hbar^2/2m)(3\pi^2 N/V)^{2/3}$ . Combining these two expressions one finds  $D(E_F) = 3N/2E_F$ . The average level spacing is inversely proportional to the density of states and thus equals  $\langle \Delta E \rangle = 4E_F/3N$ . This formula also gives a fairly good estimate for the level spacing in an arbitrarily shaped (i.e. with no symmetry induced degeneracy) metal grain containing  $N$  electrons in a volume  $V$ . Every single Pd atom supplies 10 conduction electrons to the core from its completely filled 4d level. Thus, taking  $E_F = 7$

eV [17] and  $N = 5610$  for our  $\text{Pd}_{561}$  clusters we find a lower bound for the energy spacing equal to approximately 1.7 meV, or 20 K in equivalent temperature units. This estimate is in perfect agreement with the value of about 2 states/eV/atom calculated in Ref. [17] for the bulk density of states of Pd.

The highly symmetric shape of the particle may cause level degeneracies, increasing the level spacing. For the moment, however, I will keep the above value as a guide line, as there are a number of poorly understood effects which can influence the spacing in both ways. Not much is known of the influence of the ligand bonds on the effective number of electrons in the core or on the shape of the potential at the core boundary. From Mössbauer [18] and heat conductivity [19] experiments there are e.g. indications that the outer core shell is bound stronger to the ligands than to the core, and that it is not taking part in the conductance. Also deformation due to the attractive force between cluster and substrate has influence on the spacing, as it will tend to lift the symmetry induced degeneracy.

For the above estimated level splitting to be observable, the clusters have to be properly isolated, so that the internal states essentially remain unperturbed. For point-contact tunnel experiments this means that a relatively opaque tunnel barrier is needed between the cluster and the substrate. Too much overlap between the cluster and substrate states would simply enforce a continuous density of states on the cluster. STM measurements up to now have given no decisive clue regarding the conduction properties of the ligands, so that it is unsure whether these are able to provide the required barrier. This problem can be circumvented by depositing the clusters on an oxidized substrate, but this would severely hinder topographic operation of the STM, making location and identification of the clusters difficult.

In STM-tunneling to a cluster which is isolated from its substrate by a tunnel barrier we essentially recover the double junction system, as described by the theory of section 2.3. The characteristic charging energy of a cluster can be estimated by  $E_c \approx e^2/4\pi\epsilon_0\epsilon_r R$  with  $R$  the radius of the cluster. The capacitance will thus be of order  $4\pi\epsilon_0\epsilon_r R \approx 1 \times 10^{-18}$  F. The discrete density of states can be taken into account through the tunnel rates as defined by Eq. 2.17. Figure 4.10 shows some examples of the expected  $I(V)$  characteristics evaluated with the help of the analytical expression derived in Ref. [10], where we have assumed equidistant energy levels in the cluster core. If the level spacing is smaller than the charging energy of the cluster we essentially find a Coulomb staircase with fine-structure on the step edges. When both energies become of comparable magnitude the staircase gets thwarted and we observe an irregular step structure in which the width and the height of the individual steps is determined by a delicate interplay between the Fermi energies of all three electrodes and the discrete density of states of the cluster. In the model of Ref. [10] the tunneling probability is taken constant. Tunneling through the small particle is thus the result of two sequential tunnel events, and contributions from resonant tunneling are implicitly excluded.

Averin and Korotkov [20] have analyzed the influence of the particle's energy relaxation rate  $\tau_\epsilon^{-1}$  on the observability of the Coulomb staircase and the fine structure due to the discrete density of states. They find that "overheating" due

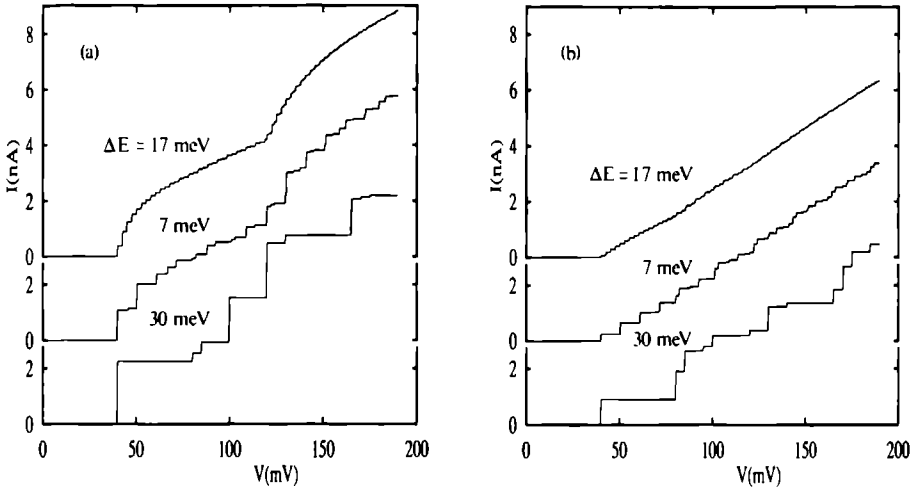


**Figure 4.10** Calculated  $I(V)$  characteristics for tunneling between two bulk metal electrodes through a particle with a discrete density of states. From upper to lower the curves correspond to level spacings equal to 1.7, 7, and 30 mV respectively. In all cases (a) we have  $C_1 = 1 \times 10^{-18}$  F,  $R_1 = 2$  M $\Omega$ ,  $C_2 = 2 \times 10^{-18}$  F,  $R_2 = 14$  M $\Omega$ ,  $Q_0 = 0$ ,  $T = 1.2$  K. In all cases (b) we have  $C_1 = 1 \times 10^{-18}$  F,  $R_1 = 2$  M $\Omega$ ,  $C_2 = 2 \times 10^{-18}$  F,  $R_2 = 14$  M $\Omega$ ,  $Q_0 = 0$ ,  $T = 1.2$  K.

to a small relaxation rate will lead to a suppression of Coulomb correlations and a smoothing of the Coulomb staircase. In contrast, a large relaxation rate leads to life-time broadening of the discrete states, thus smearing out the fine structure on the  $I(V)$  characteristic. Based on an estimate of the upper bound of  $\tau_\epsilon^{-1}$  they however conclude that for all realistic cases the fine structure should be quite clearly visible on the edge of the first step of the Coulomb staircase, provided the step is not too steep. This condition can be fulfilled by arranging the proper capacitance and resistance ratios (see section 2.3).

### 4.3.2 Preliminary results

STS-measurements have been carried out with our new low temperature STM on Pd<sub>561</sub> clusters deposited on gold terraces, which can be epitaxially grown on a mica substrate. These have not yielded any reliable results up to this moment, mainly due to problems with sample preparation and contamination of the surface during cool-down. I have, however, also made some more crude attempts to meet the double junction requirement by depositing Pd<sub>561</sub> clusters on an oxidized aluminum film (thickness 1000 Å). Using the same set-up as in the experiments of the previous sections mechanically touching point contacts were established with a tungsten tip. The concentration of the solution from which the clusters were deposited, was known

from room-temperature STM measurements to give a medium dense coverage, characterized by regions with aggregates of larger numbers of clusters variegated with regions on which individual free lying clusters can be found

Contacts were generally very unstable Nevertheless Coulomb staircases have been observed on some spots during two different measurement sessions, both times on freshly prepared samples Figure 4 11 shows some examples Unfortunately no firm conclusions can be drawn from this as there is no way to really tell whether or not the above traces are the result of tunneling through an individual cluster There are however some features in the experimental results that give indications for the interpretation that we indeed observed the incremental charging of  $\text{Pd}_{561}$  clusters

First of all the step widths were invariably of the order of 100 mV, implying a capacitance less than  $2 \times 10^{-18}$  F This value is in good agreement with the estimate given in the preceding subsection Such small values are generally not encountered in tunneling to granular films A second indication may be found in the derivative of Fig 4 11(a) The fine structure was not reproducible and thus mostly due to vibrations of the instable contact The extreme sharpness, however, of the peaks associated with the first steps on both sides of the origin can not be explained in the context of the theory of section 2 3 if a continuous density of states is assumed In that case the current onset has a finite slope leading to a peak in the derivative with finite height, slowly falling off beyond the step position As we can see from Fig 4 10, incorporation of a finite density of states gives rise to a truly stepwise onset of the current, resulting in sharp peaks in  $\partial I / \partial V(V)$  In this respect Fig 4 11(a) may give us the first, indirect, indication that the density of states of the  $\text{Pd}_{561}(\text{phen})_{38 \pm 2} \text{O}_{\approx 200}$  is discrete with level sharpness better than approximately 5 mV

## 4.4 Discussion

In Refs [8, 9] Wilkins *et al* report the observation of the Coulomb staircase in junctions between a platinum tip and bulk etched tungsten The staircases were observed on some spots of the sample, while most of the surface yielded almost linear  $I(V)$  characteristics with only a slightly suppressed conductance around zero bias The staircases can be fitted perfectly with the model calculations From the fact that the staircases could be observed on several positions on the sample, they conclude that the oxide of etched tungsten apparently contains inclusions in the form of small conducting particles or other impurities

This conclusion might have severe consequences for the interpretation of the data presented in this chapter, as they are all collected with the use of an etched tungsten tip However, although it is of course not entirely possible to exclude the above effect as being the cause of some individual results, we have several reasons to be convinced that the interpretation as given in the previous sections is on the whole correct

First of all, the size of the conducting particles needed to explain the magnitude of the capacitances, as inferred from our experiments, is of the order of 100 Å

It is hard to envisage particles of this size being included in some natural way in an oxide layer on the tip that will on the average not be thicker than some 20 Å. If, on the other hand, the capacitance is not due to a conducting particle but some other type of impurity constituting localized electron states, then it should be extremely surprising that the model system of section 2.3 gives such accurate fits as it does. In the fits it is explicitly assumed that the density of states in the central electrode is continuous, and that the tunnel matrix element is constant in the energy interval of interest. Furthermore, the central electrode is assumed to be in thermal equilibrium before each tunnel event. These conditions are in principle only met for electrodes with a metallic nature. Violation of the assumptions is expected to give significant deviations.

Secondly, in the measurements on the granular Al sample, the staircase was observed with the same tip on different spots of the sample, yielding significantly different capacitance values. On a majority part of the sample surface no charging effects were visible. In the measurement on the  $\text{YBa}_2\text{Cu}_3\text{O}_{7-\delta}$  single crystal a multitude of sample spots was probed, but the staircase was only observed on one. We would expect this to be the other way around, if the particle responsible for the staircase behaviour would be fixed in the oxide layer of the tip.

In future experiments with a new low temperature STM it will be possible to eliminate the uncertainty about the nature of the probed particle, as that set-up allows the combination of topographic and spectroscopic measurements, which was not present in the set-up as used to obtain the results presented in this chapter.

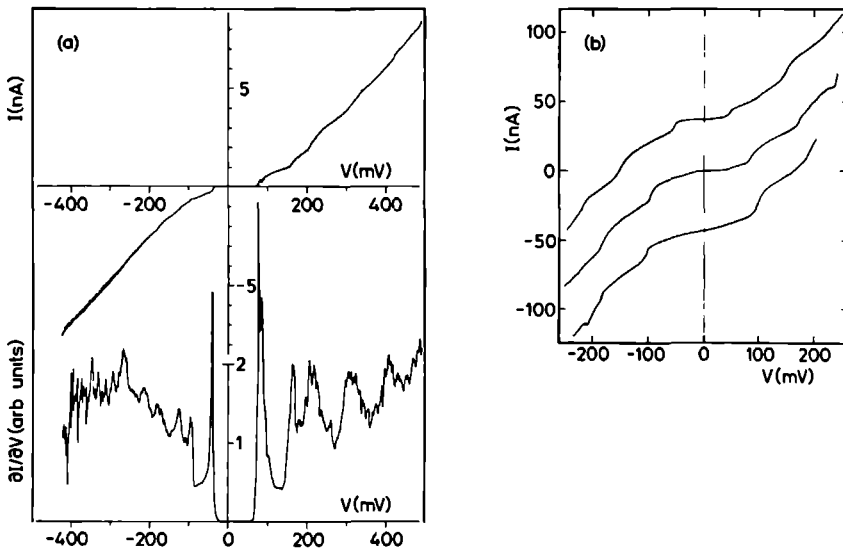


**Figure 4.11** Two examples of Coulomb staircases measured on 1000 thick Å oxidized Al films on which  $\text{Pd}_{561}(\text{phen})_{38\pm 2}\text{O}_{\approx 200}$  clusters were deposited.

## References

1. H.R. Zeller and I. Giaever, Phys. Rev. **181** (1969) 789; I. Giaever and H.R. Zeller, Phys. Rev. Lett. **20** (1968) 1504.
2. J.B. Barner and S.T. Ruggiero, Phys. Rev. Lett. **59** (1987) 807.
3. L.S. Kuzmin and K.K. Likharev, JETP Lett. **45** (1987) 495; Jap. J. Appl. Phys. **26** (1987) 1389.
4. P.J.M. van Bentum, R.T.M. Smokers, and H. van Kempen, Phys. Rev. Lett. **60** (1988) 2543.
5. K.A. McGreer, J.-C. Wan, N. Anand, and A.M. Goldman, Phys. Rev. B **39** (1989) 12260.
6. J.-C. Wan, K.A. McGreer, N. Anand, E. Nowak, and A.M. Goldman, Phys. Rev. B **42** (1990) 5604.
7. R. Wilkins, E. Ben-Jacob, and R.C. Jaklevic, Phys. Rev. Lett. **63** (1989) 1146.
8. R. Wilkins, M. Amman, E. Ben-Jacob, and R.C. Jaklevic, Phys. Rev. B **42** (1990) 8698.
9. R. Wilkins, M. Amman, E. Ben-Jacob, and R.C. Jaklevic, J. Vac. Sci. Technol. B **9** (1991) 996.
10. M. Amman, R. Wilkins, E. Ben-Jacob, P.D. Maker, and R.C. Jaklevic, Phys. Rev. B **43** (1991) 1146.
11. A.E. Hanna and M. Tinkham, Phys. Rev. B **44** (1991) 212.
12. J.G. Bednorz and K.A. Müller, Z. Phys. B **64** (1986) 18.
13. J.B. Barner, K. Mullen, M.J. Honkanen, S.T. Ruggiero, E. Ben-Jacob, and A.R. Pelton, IEEE Trans. Magn. **25** (1989) 2542.
14. K. Mullen, E. Ben-Jacob, and S.T. Ruggiero, Phys. Rev. B **38** (1988) 5150.
15. G. Schmid, Struc. Bonding **62** (1985) 51; Nachr. Chem. Tech. Lab. **35** (1987) 249.
16. L.E.C. van de Leemput, J.W. Gerritsen, P.H.H. Rongen, R.T.M. Smokers, H.A. Wierenga, H. van Kempen, and G. Schmid, J. Vac. Sci. Technol. B **9** (1991) 814.
17. A.M. Begley and W.M. Temmerman, Daresbury Laboratory Report, Warrington U.K., see also: V.L. Moruzzi, J.F. Janak, A.R. Williams, *Calculated Electronic Properties of Metals*, (Pergamon Press, N.Y., 1978).
18. H.H.A. Smit, Ph.D. thesis (1988), University of Leiden, the Netherlands.
19. L.J. de Jongh, private communication.
20. D.V. Averin and A.N. Korotkov, J. Low Temp. Phys. **80** (1990) 173.





## Chapter 5

# Tunneling spectroscopy on high temperature superconductors

## 5.1 Introduction

In 1986 Bednorz and Müller [1] first reported the observation of superconductivity above 30 K in a LaBaCuO system. This discovery initiated a world-wide research effort, aimed at the development of new superconducting materials, and the comprehension of the mechanism behind the unprecedentedly high critical temperatures. By now a whole class of high- $T_c$  superconducting oxides has been discovered, with critical temperatures ranging up to about 125 K. Nevertheless, despite five years of extensive research resulting in some ten thousand articles, still no real consensus has been reached concerning the understanding of the microscopic nature of superconductivity in these materials.

This rather unsatisfactory situation is partly due to the large amount of inconsistent and sometimes even contradicting experimental results, as a consequence of difficulties in reproducible material preparation. The first samples of these complex compounds were brittle sintered ceramics containing a large amount of off-stoichiometric residue. Superconductivity appeared to be very sensitive to the oxygen content of the materials, while sample surfaces tended to degrade in moist atmospheres. Experimental probes which had proven to be successful in the characterization of the classical superconductors, failed to yield unambiguously interpretable results in this case. Nowadays evolved preparation techniques allow the production of small single crystals and oriented thin films, greatly facilitating characterization of the true bulk properties of the materials.

As already mentioned, the main interest is focused on the understanding of the microscopic mechanism underlying the superconductivity in the high- $T_c$  materials. Can it be described within the framework of the existing BCS-theory (see e.g. Refs. [2, 3, 4, 5])? And if not, can we modify or extend BCS to incorporate this new class of materials, or do we need a new theory all together? And even if the materials behave in a BCS-like manner, which attractive interaction is binding the Cooper pairs together, and into what kind of state?

The classical superconductors are all well described by the BCS-theory. A phonon mediated interaction is thought to bind the electrons into Cooper pairs. These Cooper pairs, which are described by a zero momentum s-wave state (i.e.  $(\mathbf{k}\uparrow, -\mathbf{k}\downarrow)$ ), condense into a macroscopic ground state. The energy spectrum for quasi-particle excitations out of this ground state displays a gap of width  $2\Delta$  around the Fermi level (see section 1.3.2. Fig. 1.4).  $2\Delta$  corresponds to the coupling energy of the Cooper pairs. In the weak phonon coupling limit this energy scales with the critical temperature  $T_c$  like  $2\Delta/k_B T_c \approx 3.5$ . Higher values of this ratio, up to approximately 4.7 are encountered in the so-called strong coupling superconductors, of which lead is a well-known example. Also other pair states, such as p- or d-wave, are allowed within the BCS-framework, but these have never been observed so far. For the s-wave pairing the gap is isotropic, and the density of states inside the gap is completely zero. For higher angular momentum states the gap will go to zero on nodal planes or lines in  $k$ -space and the density of states in the gap is not zero. Along the lines of the BCS-theory it is in principle also possible to deal with other

coupling mechanisms than the phonon-mediated one.

From the BCS-theory the coherence length is predicted to scale with the critical temperature like  $\xi_c \approx 0.2\hbar v_F/k_B T_c$ , with  $v_F$  the Fermi velocity. This means that large gap values are likely to fluctuate over small length scales [2, 6].

Good general reviews on the physical properties of the high- $T_c$  superconductors are hard to find. Reference [6] at least gives a good survey of the central questions which have to be addressed in the research on high- $T_c$  material. For a general overview of the present status of the field I refer to the conference proceedings of Refs. [7, 8, 9]. In this chapter I will concentrate mainly on those properties that can be investigated with the help of electron tunneling. As we have seen in chapter 1, tunneling spectroscopy can reveal the quasi-particle density of states of the superconductor. The high- $T_c$  materials are often unfit for application in Giaever-type junctions, but fortunately point-contact tunneling offers a versatile alternative [10]. As a result of the bad surface properties of the materials, however, application of this technique is not as straightforward as one would hope. Many characteristics show only some faint trace of gap structure and most show no gap structure at all. Often other effects, not necessarily related to superconductivity, happen to dominate the current transport in the point contact.

The high- $T_c$  materials are not the only exotic type of superconductors. Other examples of superconducting materials that are extensively studied nowadays are the organic superconductors and the heavy-fermion systems. Most recently, researchers have claimed the observation of superconductivity in crystals of doped  $C_{60}$  Buckminster fullerenes. Although mentioned here for the sake of completeness, these materials will not play a part in the experiments or contemplations presented here.

This chapter is organized on the basis of the various types of characteristics that are repeatedly encountered in point-contact tunneling experiments. In each section measurements on different materials will be shown in order to illustrate the effect under consideration. Following a short summary of the important properties of the high- $T_c$  compounds studied here, sections 5.3 and 5.4 concern gap spectroscopy and Josephson effects, which are both related to the superconducting properties of the materials. Sections 5.5 and 5.6 deal with charging effects and negative differential resistance (NDR) features, effects which are connected with e.g. the granularity and the ill-defined chemical composition of the sample surfaces. The final section 5.7 will be devoted to some general conclusions. Throughout the chapter the emphasis will be on own results. These will be discussed in the context of the results reported by other groups, but in all cases without aiming at completeness.

## 5.2 Material parameters

The most extensively studied high- $T_c$  compound is  $YBa_2Cu_3O_{7-\delta}$ . It has an oxygen deficient orthorhombic perovskite structure with lattice constants:  $a = 3.82$  Å,  $b = 3.89$  Å, and  $c = 11.68$  Å [11]. The critical temperature of about 90 K, depends on the exact oxygen content. The unit cell is shown in Fig. 5.1(a). Each unit cell contains two  $CuO_2$  planes, which actually carry the superconductivity. The co-

herence length shows an anisotropy of a factor of five ( $\xi_c \approx 3-4 \text{ \AA}$  and  $\xi_{ab} \approx 15-25 \text{ \AA}$  [12, 13]). Nevertheless the coupling between the  $\text{CuO}_2$  layers is still strong enough for the superconductivity to be of a three dimensional nature. For the experiments discussed in this chapter both sintered ceramic material and an evaporated film have been used. For details on the preparation of both samples see Refs. [14] and [15] respectively.

Another material studied in this chapter is  $(\text{Pb}_x\text{Bi}_{1-x})_2\text{Sr}_2\text{CaCu}_2\text{O}_8$ . It has a tetragonal perovskite structure. The unit cell, as shown in Fig. 5.1(b), has dimensions  $a = b = 5.39 \text{ \AA}$  and  $c = 30.7 \text{ \AA}$ . Again the superconductivity is attributed to the two  $\text{CuO}_2$  planes in the unit cell. In the  $\text{BiO}$  layers the Bi is partly replaced by Pb resulting in an increase of  $T_c$  compared to the  $x = 0$  phase. The crystalline material used in the experiments presented here is grown in the so-called self-flux method [16]. The critical temperature, as inferred from resistance and magnetization measurements, ranges from 80 to 90 K for different samples. The  $(\text{Pb}_x\text{Bi}_{1-x})_2\text{Sr}_2\text{CaCu}_2\text{O}_8$  crystallizes in the form of thin platelets oriented along the  $ab$ -plane. The layered structure has weak bonds in the  $c$ -direction, so that the small crystals (size a few  $\text{mm}^2$ ) are easily cleavable, producing flat and clean surfaces. The physical properties of  $(\text{Pb}_x\text{Bi}_{1-x})_2\text{Sr}_2\text{CaCu}_2\text{O}_8$  are highly anisotropic. For example, the normal state resistivity in the  $c$ -direction is a factor  $4 \times 10^4$  larger than in the  $ab$ -plane, while the upper critical fields differ by a factor of 40. The coherence lengths in the  $ab$ -plane and along the direction of the  $c$ -axis, as estimated from the upper critical fields, ranged from 18 to 45  $\text{ \AA}$  and from 0.4 to 1.5  $\text{ \AA}$ , respectively, for our crystals. The small coherence length in the  $c$ -direction implies that the superconductivity in these material is of a highly two-dimensional nature. Increasing the number of  $\text{CuO}_2$  planes in the unit cell is found to increase the critical temperature. As an example, the related compound  $(\text{Pb}_x\text{Bi}_{1-x})_2\text{Sr}_2\text{Ca}_2\text{Cu}_3\text{O}_{10}$  has three  $\text{CuO}_2$  planes and a  $T_c$  of the order of 105 K [17].

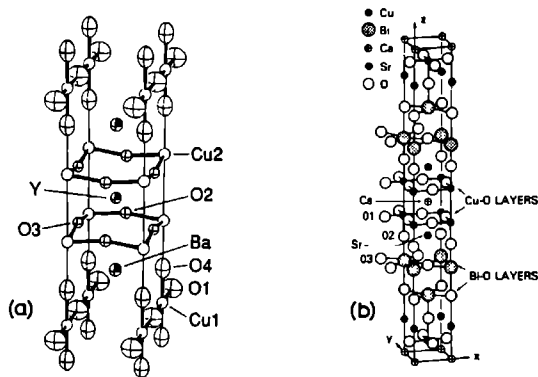


**Figure 5.1** Crystal structures of the high- $T_c$  compounds (a)  $\text{YBa}_2\text{Cu}_3\text{O}_{7-\delta}$  and (b)  $(\text{Pb}_x\text{Bi}_{1-x})_2\text{Sr}_2\text{CaCu}_2\text{O}_8$ .

All results presented in this chapter have been obtained in the experimental set-up described in the appendix of chapter 3.

## 5.3 Gap spectroscopy

### 5.3.1 General considerations

As already mentioned, determination of the quasi-particle density of states is of vital importance for the understanding of the microscopic nature of the superconducting ground state of the high- $T_c$  materials. With Andreev reflection experiments [15] it has been shown that the ground state consists of zero-momentum ( $\mathbf{k}, -\mathbf{k}$ ) pairs. Quasi-particle tunneling can now provide information on the angular momentum and the binding energy of the pair state, as explained in the introduction. The exact shape of the density of states, as inferred from  $\partial I/\partial V(V)$ , may give clues regarding the pairing mechanism.

Figure 3.4 in chapter 3 already showed an example of NIS tunneling between a tungsten tip and a tin film. In Fig. 5.2 I have reproduced two more examples of point-contact tunneling measurements involving classical superconductors.

For the high- $T_c$  superconductors it has in practice proven to be very difficult to obtain gap characteristics that can reliably be considered indicative for the bulk density of states. With respect to this we have to bear in mind that point-contact tunneling is a very sensitive probe of the local density of states (see section 1.4) so that small scale variations of the structure or chemical composition may have large influence on spectroscopic measurements. Especially in compounds like

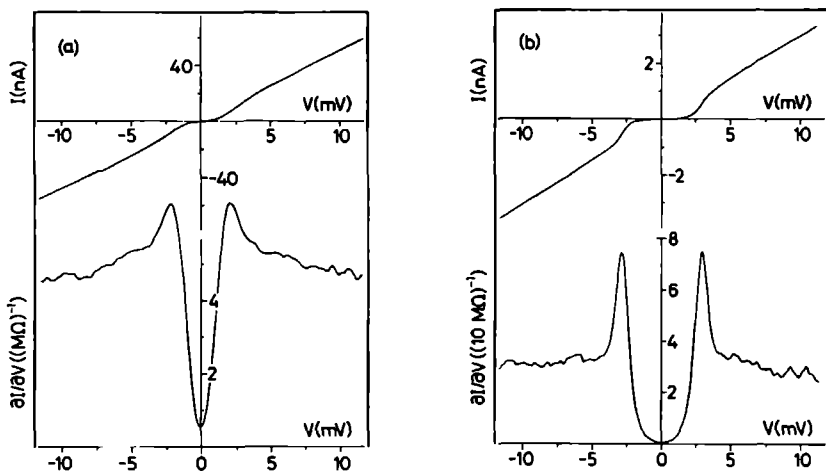


**Figure 5.2** Tunneling characteristics of point-contact junctions between (a) a W tip and a Pb sample, and (b) a NbZr tip and a Pb sample, both measured at  $T = 1.2$  K.

$\text{La}_{1.85}\text{Sr}_{0.15}\text{CuO}_4$  and  $\text{YBa}_2\text{Cu}_3\text{O}_{7-\delta}$  which initially were only available in ceramic form or at best as preferentially oriented thin films, the surface properties may differ drastically from the bulk. Due to the short coherence length in these materials (of the order of the unit cell dimensions, or smaller) the energy gap can vary over small lengthscales under the influence of oxygen deficiency, off-stoichiometric chemical composition, grain boundaries, structural defaults, etcetera. In general the gap will be suppressed at the surface, and the tunneling tip has to be driven deeply into the material in order to probe the superconductivity. In that case the pressure exerted by the tip may in turn change the local superconducting properties. This effect has been established in tunneling experiments on  $\text{La}_{1.85}\text{Sr}_{0.15}\text{CuO}_4$ , but for  $\text{YBa}_2\text{Cu}_3\text{O}_{7-\delta}$  it does not play a role [14].

The ill-defined surfaces constitute non-ideal tunneling barriers. Deformation of the effectively low barrier by the applied potential difference is thought to cause non-linear and asymmetric characteristics [18]. As low barriers imply large transmission probabilities, higher order tunneling processes become possible. These processes are explicitly neglected in the tunneling theory described in section 1.3.2. In this limit the transfer-Hamiltonian approach, assuming well decoupled electrodes, is no longer applicable. Instead, tunneling characteristics should be calculated by proper wave matching of the solutions of the Bogoliubov equations. As calculated in the BTK-theory [19] this can e.g. lead to an enhanced conductance below the gap, as a result of Andreev reflection.

Also the strong anisotropy of the materials influences the gap measurements. On ceramic materials the tip will in general probe an angle averaged gap value. Only in single crystals or oriented films can a reliable distinction be made between the gap values in the  $c$ -direction and in the  $ab$ -plane.

In chapter 4 some  $I(V)$  characteristics have been presented of point-contact tunnel junctions on  $\text{YBa}_2\text{Cu}_3\text{O}_{7-\delta}$  samples, which were dominated by the incremental charging of a small grain on the sample surface. I will shortly come back to these effects in section 5.5. As the low voltage part of the Coulomb staircase strongly resembles the BCS-characteristics for tunneling into superconductors care should be taken not to confuse these two effects. In this section I will only present gap characteristics which can reliably be interpreted as due to NIS or SIS tunneling.

### 5.3.2 Results on $\text{YBa}_2\text{Cu}_3\text{O}_{7-\delta}$

Only a minority of all investigated point-contact tunnel junctions on ceramic samples of  $\text{YBa}_2\text{Cu}_3\text{O}_{7-\delta}$  displayed superconductor-gap-like characteristics. Freshly made contacts mostly exhibit more or less parabolic  $I(V)$  curves, often with extremely low zero-bias conductance. Some examples are depicted in Fig. 5.3(a). Pushing the tip into the sample or further poking around generally resulted in characteristics with more pronounced features, such as gap structure or some of the other effects discussed in the next sections of this chapter. Figure 5.3(b) shows some often encountered, but rarely reported, types of characteristics, which probably have their origin in a complex combination of low-barrier, surface-state, charging and

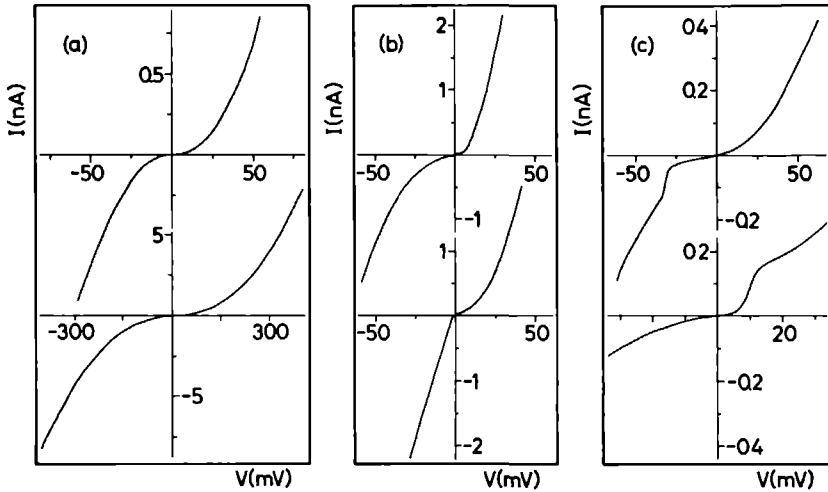


**Figure 5.3**  $I(V)$  curves of junctions between a W tip and ceramic  $\text{YBa}_2\text{Cu}_3\text{O}_{7-\delta}$ : (a) "parabolic" characteristics, (b) and (c) a bestiary of asymmetric features.

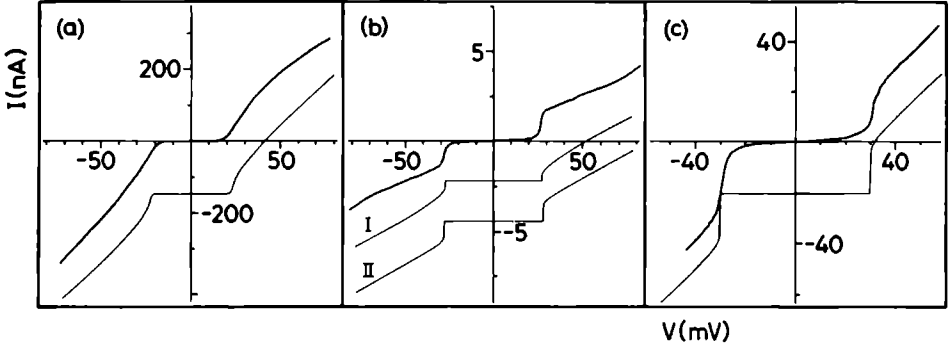
semi-conducting effects.

Figure 5.4 displays a collection of gap characteristics obtained with different tip-sample combinations. A striking quality of all well developed gap characteristics is the absence of a pronounced parabolic background. This indicates that, at least for the  $\text{YBa}_2\text{Cu}_3\text{O}_{7-\delta}$  compound, the linear conductance feature is not a manifestation of bulk properties that might in some way be connected to the mechanism of superconductivity, but is solely to be attributed to surface effects and the resulting inferior quality of the tunnel barrier. Gap values generally varied from contact to contact, and also on the same contact the width of the gap could often be tuned by moving the tip into or out of the sample. Therefore it is senseless to attribute any significance to values inferred from precise fits of individual measurements. The only meaningful results in this case are the statistics of gap values and the overall shape of the  $I(V)$  characteristics. Considering the former, the bulk of our data indicate gap values of the order of  $17 \pm 4$  meV, corresponding to a coupling strength of  $2\Delta/k_B T_c = 4.4 \pm 1.0$ . The measured gap values thus scatter significantly above the weak-coupling BCS-prediction. The  $I(V)$  curves with well developed gap structure strongly resemble the characteristics of NIS and SIS junctions as calculated in section 1.3. The conductance in the gap is usually very low, indicating the absence of bulk quasi-particle states in the gap.

The  $I(V)$  curve of Fig. 5.4(a) can reliably be interpreted as the characteristic of the NIS contact between the tungsten tip and a superconducting grain. From the fit to this curve we obtain  $\Delta \approx 22$  meV, yielding  $2\Delta/k_B T_c \approx 5.6$ .

Curve (b) of Fig. 5.4 is obtained with the use of a NbZr tip. The sharpness of the current onsets confirms the SIS nature of the contact. However, if the observed





**Figure 5.4** Three specimens of gap characteristics measured at  $T = 4.2$  K using: (a) a W tip and ceramic  $\text{YBa}_2\text{Cu}_3\text{O}_{7-\delta}$ , (b) a NbZr tip and ceramic  $\text{YBa}_2\text{Cu}_3\text{O}_{7-\delta}$ , (c) a W tip and an  $\text{YBa}_2\text{Cu}_3\text{O}_{7-\delta}$  film. For interpretations see text. The fits to the curves are offset for clarity.

gap corresponds to the sum gap  $\Delta_{\text{NbZr}} + \Delta_{\text{Ybco}}$ , then this measurement would yield  $\Delta_{\text{Ybco}} = \Delta_{\text{sum}} - 1.5 \text{ meV} \approx 25 \text{ meV}$ , which is relatively large compared to the average value mentioned above. Fit I is made using the above values for  $\Delta_{\text{NbZr}}$  and  $\Delta_{\text{Ybco}}$ . Alternatively one can imagine that in this case the tip makes a low resistance contact with a grain at the surface, and is thus actually probing an SIS junction between two neighbouring grains. In that case the observed gap equals twice the gap of  $\text{YBa}_2\text{Cu}_3\text{O}_{7-\delta}$ , so that we infer  $\Delta_{\text{Ybco}} \approx 13.5 \text{ meV}$ . This interpretation is used for the calculation of fit II. As this fit reproduces the steepness of the current step much better than fit I, we conclude that the characteristics depicted in Fig. 5.4(b) belong to a junction between two  $\text{YBa}_2\text{Cu}_3\text{O}_{7-\delta}$  grains.

In Fig. 5.4(c) a tunnel characteristic is shown of a tungsten tip probing a  $1 \mu\text{m}$  thick  $\text{YBa}_2\text{Cu}_3\text{O}_{7-\delta}$  film deposited on a sapphire substrate. This sample was part of a film that was also used in the Andreev reflection measurements of Ref. [15]. The steepness of the current step again implies SIS nature of the probed junction. As the tip is a normal metal, there can be no doubt that this curve is representing an intergrain junction in the sample. We thus infer  $\Delta_{\text{Ybco}} \approx 15 \text{ meV}$ , which is within the interval as indicated above. In fact this type of intergrain junctions may even be more reliable as they may suffer less from deteriorated surface properties.

From a comparison with the fits it is clear that the  $I(V)$  characteristics are broadened much more severely than is to be expected on the basis of temperature effects alone. This may be attributed to finite lifetime effects [20], but is not necessarily intrinsic to this high- $T_c$  material, as the measurements on classical superconductors presented in Fig. 5.2 also exhibit significant broadening.

## Discussion

From the above examples it is clear that we are able to observe very reasonable BCS-like  $I(V)$  characteristics on ceramic  $\text{YBa}_2\text{Cu}_3\text{O}_{7-\delta}$  samples using point-contact tunneling. The major problems with these measurements concern the strong position dependence of the  $I(V)$  characteristics and the lack of knowledge on the exact sample composition and crystal orientation under the tip. An obvious recommendation for improving reproducibility and control over sample parameters would be to suggest the use of single crystals. For the specific case of  $\text{YBa}_2\text{Cu}_3\text{O}_{7-\delta}$  this however turns out not to be that profitable, as is illustrated by the work of Valles *et al.* [12].

Valles *et al.* have obtained an extensive and systematic collection of tunneling data on evaporated junctions using chemically etched single crystals of  $\text{YBa}_2\text{Cu}_3\text{O}_{7-\delta}$  as a base electrode. Their characteristics only show weak gap structures superimposed on a strong linear conductance background. They in fact observe two distinct gap structures around 4–5 mV and 19 mV. Sub-gap conductances are generally of the order of 50% of the conductance above the gap. Using a Pb counter electrode at  $T = 1$  K they find in the mV-regime high quality NIS behaviour associated with the gap of Pb. The latter proves in my opinion that Valles *et al.* [12], although their tunneling barriers may be quite all right, are not really probing the superconducting density of states of  $\text{YBa}_2\text{Cu}_3\text{O}_{7-\delta}$ . Nevertheless Valles *et al.* claim that both the multiple gap structure and the sub-gap conductance are related to the quasi-particle density of states of  $\text{YBa}_2\text{Cu}_3\text{O}_{7-\delta}$ , and they express their preference for an interpretation in terms of the model by Takahashi and Tachiki [21]. This model calculates the effective quasi-particle density of states of the high- $T_c$  superconductors by assuming a proximity coupling between layers with small and large in-plane gaps.

In establishing our point-contact junctions we did not pay much attention to the preparation of the sample surface, apart from trying different spots on the sample or pushing the tip into it. Nevertheless some junctions produce well developed BCS-like gap characteristics. This simply has to imply that any properly conducted experiment, in which the surface treatment is tackled in a more sophisticated manner, may be expected to do even better. As this is obviously not the case for the careful and systematic experiments presented by Valles *et al.* [12], one just has to conclude that we are dealing with a really difficult material.

The results of Ref. [12] are even more surprising when compared with other experiments by the same group (see Sharifi *et al.* [22]) on a class of high- $T_c$  bismuth-oxides which do not contain copper. On these materials they observe well developed NIS characteristics with low sub-gap conductance and only a slight broadening. A linear conductance background is found which, according to Sharifi *et al.*, is intrinsic to the density of states, as the normalized slope of this background appears to scale with the transition temperature  $T_c$ . Above all they find gap values in perfect accordance with the BCS weak-coupling prediction  $2\Delta/k_B T_c \approx 3.5$ .

In our experiments on  $\text{YBa}_2\text{Cu}_3\text{O}_{7-\delta}$ , the linear conductance background is surely present in characteristics which do not show superconducting features. In the NIS and SIS characteristics however this background is less pronounced, meaning

that it is not straight away justified to attribute this property to the normal state density of states of  $\text{YBa}_2\text{Cu}_3\text{O}_{7-\delta}$ .

The large gap values ( $2\Delta/k_{\text{B}}T_c = 4.4 \pm 1.0$ ) and the broadening of  $I(V)$  characteristics may be explained within the context of the model by Devyatov and Kupriyanov [23], which describes NIS tunneling in a situation where the tunneling process is mediated by resonant tunneling through a distribution of localized states in the barrier. For the reasons already expounded in section 3.2.3 the applicability of the model to our experimental situation is debatable.

Reviews of the wide range of tunneling data on  $\text{YBa}_2\text{Cu}_3\text{O}_{7-\delta}$  that have been published over the last years can be found in Refs. [10, 18]. These references find that the most reliable gap characteristics have a BCS-like behaviour.  $2\Delta/k_{\text{B}}T_c$  values generally range between 3 and 7, indicating that the coupling mechanism may be stronger than the usual phonon coupling in classical superconductors. Due to the large variation in exact shapes of the characteristics no further conclusions can be drawn for the moment with regard to the pair state symmetry or the characteristic energy dependence of the coupling mechanism. A survey of the results of our group can be obtained from Refs. [14, 24, 25, 26, 27].

### 5.3.3 Results on $(\text{Pb}_x\text{Bi}_{1-x})_2\text{Sr}_2\text{CaCu}_2\text{O}_8$

Point-contact tunneling experiments have been performed on small single crystals of  $(\text{Pb}_x\text{Bi}_{1-x})_2\text{Sr}_2\text{CaCu}_2\text{O}_8$  ( $T_c \approx 85$  K). In the first experiments the tip was oriented parallel to the  $c$ -axis of a crystal, which was freshly cleaved just before the measurement. Bringing the tungsten tip gently in contact with the sample we invariably observed more or less parabolic but furthermore featureless  $I(V)$  characteristics. An example is shown in Fig. 5.5(a). Upon pushing the tip further into the material the characteristics would develop varying sequences of kinks as is exemplified in Fig. 5.5(b). These characteristics are highly symmetric, but the positions of the kink pairs depend strongly on the  $z$ -position of the tip. Some pairs move towards the origin, when the tip is pushed into the sample, while others move to higher voltages. In the slow voltage sweep as displayed in Fig. 5.5(b) the kinks manifest themselves as a sudden dip in the conductance, or even as NDR-features. From oscilloscope traces of quick scans, however, it was clear that these kinks actually correspond to a bistability where the junction state at one voltage can be on two distinct  $I(V)$  branches.

Figures 5.6(a) and (b) illustrate what the actual junction configurations might look like in the two situations described above. Due to the weak coupling between the superconducting  $\text{CuO}_2$  planes the superconductivity in the  $c$ -direction is very weak, and likely to be completely suppressed at the crystal surface. When probing the surface only (Fig. 5.6(a)) the tunnel current probably diffuses away from the contact area through surface states in the non-superconducting top layer. Pushing the tip into the sample fractures the crystal planes resulting in a multiple of weak links connecting the junction area to the bulk of the crystal (Fig. 5.6(b)). Exceeding the critical current of such a weak link leads to a reduction of the number of

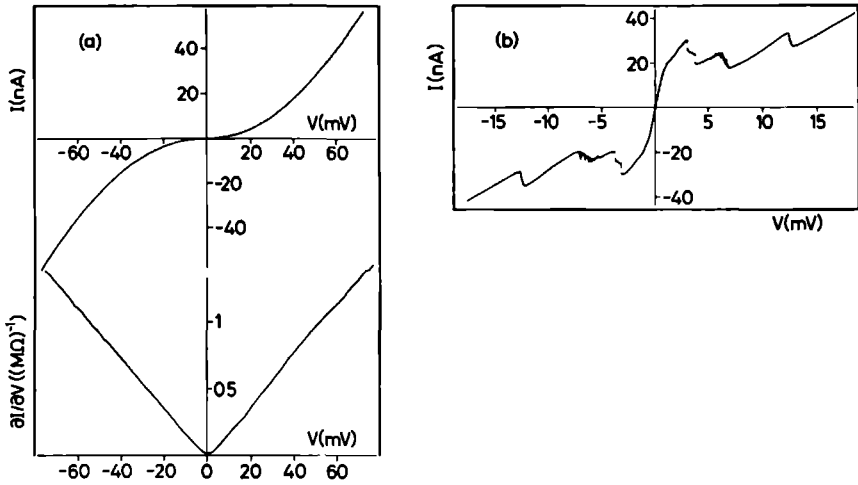


**Figure 5.5** (a)  $I(V)$  and  $\partial I/\partial V(V)$  characteristic for tunneling in the  $c$ -direction on a small single crystal of  $(\text{Pb}_x\text{Bi}_{1-x})_2\text{Sr}_2\text{CaCu}_2\text{O}_8$ , measured with a tungsten tip at  $T = 4.2$  K. (b)  $I(V)$  characteristic of a similar contact, but with the tip pushed deeper into the sample.

paths along which the current can move away from the tunnel area, thus causing an increase of the total junction resistance.

Curves similar to the ones displayed in Fig. 5.6 have been observed in point contacts on ceramic  $(\text{Pb}_x\text{Bi}_{1-x})_2\text{Sr}_2\text{Ca}_2\text{Cu}_3\text{O}_{10}$  ( $T_c = 105$  K). On this material we sometimes observed gap-like characteristics with gap values of the order of a few mV.

In a second set of experiments [28] we employed a small piece of a solidified melt with visible crystal edges reaching out at the surface. Using the melt, instead of extracting the crystal allowed us to keep the crystal in place easily, and to prevent possible distortion of the thin platelets during cooling or touching by the tip. Under

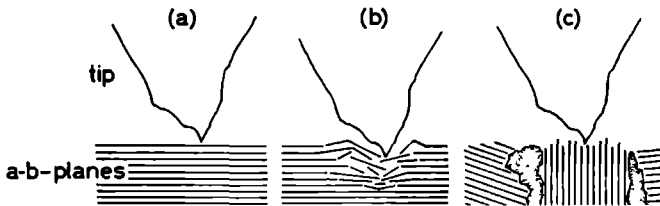


**Figure 5.6** Illustration of three different point-contact configurations with the tunneling direction either parallel to the  $c$ -axis ((a) and (b)), or in the  $ab$ -plane (c).

an optical microscope the tip was prepositioned above a crystalline part of the sample where the  $ab$ -planes were oriented perpendicular to the surface. The tunneling configuration is schematically shown in Fig. 5.6(c). The critical temperature of the melt was established to be about 85 K.

While probing different spots on the sample we also encountered the critical current effects as described above. On several positions, however, we observed clear and reproducible NIS gap spectra, of which two representative examples, measured with a tungsten and a platinum-iridium tip respectively, are depicted in Fig. 5.7(a). The measurements with the tungsten tip display BCS-like characteristics superimposed on a linear background conductance reminiscent of the conductance curves measured parallel to the  $c$ -axis. The gap value inferred from these measurements is  $\Delta \approx 30$  meV, corresponding to  $2\Delta/k_B T_c \approx 8$ . Gap values like this have been reproduced on different spots on the sample.

In the gap characteristics measured with a Pt(10% Ir) tip on the same crystal the linear conductance background was generally less prominent. Measured gap values were somewhat smaller ( $\approx 25$  meV) than in the above case. Double peak structures were repeatedly observed in the  $\partial I/\partial V(V)$  curve on either side of the origin, as illustrated in Fig. 5.7(b).

In a third configuration (see also Ref. [28]) we used two single crystals with their edges crossed to produce a small area tunnel junction in which tunneling takes place primarily perpendicular to the  $c$ -axis. The characteristics shown in Fig. 5.8, recorded at 4.2 and 77 K, clearly indicate that in both cases well defined SIS junctions were obtained. As expected the apparent gap width has doubled in comparison

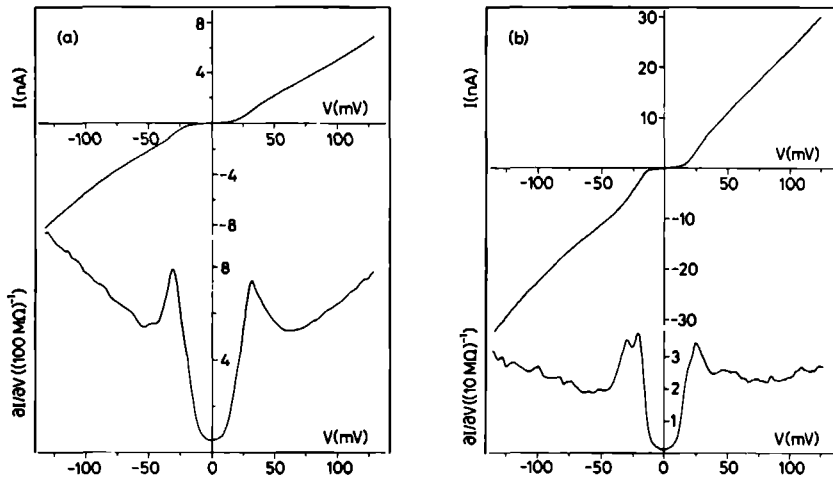


**Figure 5.7**  $I(V)$  and  $\partial I/\partial V(V)$  characteristics of junctions on a  $(\text{Pb}_x\text{Bi}_{1-x})_2\text{Sr}_2\text{CaCu}_2\text{O}_8$  sample using (a) a W tip, and (b) a Pt(10% Ir) tip. In both cases the tip was oriented perpendicular to the  $c$ -axis of the probed crystallite.

to the NIS case of Fig. 5.7, and the peaks in  $\partial I/\partial V(V)$  are sharper and more pronounced. From the differential conductance of the NIS junction of Fig. 5.7(a) we could, after subtraction of the linear background, obtain the conductance of this SIS junction at  $T = 4.2$  K (Fig. 5.8(a)) with an accuracy of a few percent.

The 77 K curve is smeared much stronger than the finite temperature would suggest. However, using the model for finite quasi-particle lifetime as conceived by Dynes *et al.* [20], Fig. 5.8(b) can also be reproduced from the NIS curve of Fig. 5.7(a) within a few percent.

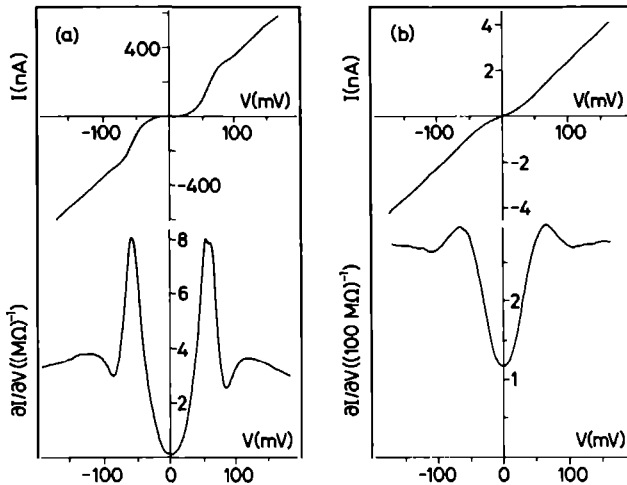


**Figure 5.8**  $I(V)$  and  $\partial I/\partial V(V)$  characteristics of junctions between two small  $(\text{Pb}_x\text{Bi}_{1-x})_2\text{Sr}_2\text{CaCu}_2\text{O}_8$  crystals, measured at  $T = 4.2$  K (a) and 77 K (b).

## Discussion

In contrast to what we have seen in the  $\text{YBa}_2\text{Cu}_3\text{O}_{7-\delta}$  experiments, NIS junctions on  $(\text{Pb}_x\text{Bi}_{1-x})_2\text{Sr}_2\text{CaCu}_2\text{O}_8$  still display a strong linear contribution to the conductance. However, as our SIS junctions exhibit quite linear asymptotes, we again tend to conclude that the strong linear conductance feature is not an intrinsic property of the quasi-particle or normal state density of states. This is in sharp contrast to the conclusions of Refs. [12, 22], which deal with  $\text{YBa}_2\text{Cu}_3\text{O}_{7-\delta}$  and a class of non-cuprate bismuth-oxides.

In his review on tunneling experiments on high- $T_c$  materials Kirtley [18] favours to associate the conductance background with non-ideal barrier properties. In view of the universality of this feature and the not too straightforward energy dependence of the barrier transmission factor, especially in point-contact geometries, this explanation should be considered inappropriate, or at least incomplete.

In Ref. [29] Kirtley *et al.* yet propose another explanation in terms of inelastic electron tunneling from a broad distribution of loss modes in the barrier. The model is compared with measurements on a wide range of junction types, which all to some extent display this linear conductance, and is tested by changing the  $\text{Cr}_2\text{O}_3$  content in barriers between an Al and a Pb electrode. In their opinion the effect is thus connected to barrier properties, though not to an energy dependence of the matrix element. Due to the wrong sign of some predicted asymmetries the value of the model is still questionable.

In the measurements presented above the sub-gap conductance was low but always finite. This may indicate that the gap in  $(\text{Pb}_x\text{Bi}_{1-x})_2\text{Sr}_2\text{CaCu}_2\text{O}_8$  is not fully developed, although contributions from leakage currents or parallel tunneling through e.g. inelastic channels or surface states can not be excluded. The model of proximity coupled layers by Takahashi and Tachiki [21] may apply very well to these highly two-dimensional superconductors. The energy gap is apparently highly anisotropic. The gap value in the *ab*-plane can be determined quite unambiguously. The corresponding ratio  $2\Delta/k_B T_c \approx 8$  implies that the coupling strength in the planes of the  $(\text{Pb}_x\text{Bi}_{1-x})_2\text{Sr}_2\text{CaCu}_2\text{O}_8$  compound is about a factor of two above the BCS weak-coupling prediction. Based on the reproducible  $I(V)$  characteristics and the good correspondence with the SIS measurements, we consider the measurements with W-tips more representative than the ones with Pt(10% Ir) tips, which showed smaller gap values and unexplained double peak structure.

## 5.4 Josephson effects

Together with the Meissner effect, the Josephson effects (see section 1.3.2) provide the proof that a conductor with zero resistance really is a superconductor. Both effects are indissolubly connected to the existence of a macroscopically occupied ground state, which constitutes a superconducting wave function with phase coherence throughout the material. The Josephson effects can be observed in so-called weak links between two superconducting electrodes. Such a weak link can either be a low resistance tunnel junction, or a metallic microbridge. Josephson junctions are resistanceless up to a certain critical current, which generally differs from the critical current associated with the critical current density of the bulk superconductor.

In the ceramic high- $T_c$  materials the macroscopic current is thought to be carried by the random network of intergrain Josephson junctions. This explains the low critical current values in these compounds.

Using low resistance point contacts between two ceramic  $\text{YBa}_2\text{Cu}_3\text{O}_{7-\delta}$  samples de Waele *et al.* [30] first measured the dc-Josephson effect in combination with magnetic field modulation of the quantum interference pattern characteristic of the system of two Josephson junctions coupled in parallel.

Josephson-like behaviour is often encountered in junctions between a normal tip and granular or polycrystalline high- $T_c$  samples. When the tip is making contact with a single grain, which in turn is connected to neighbouring grains by a weak link

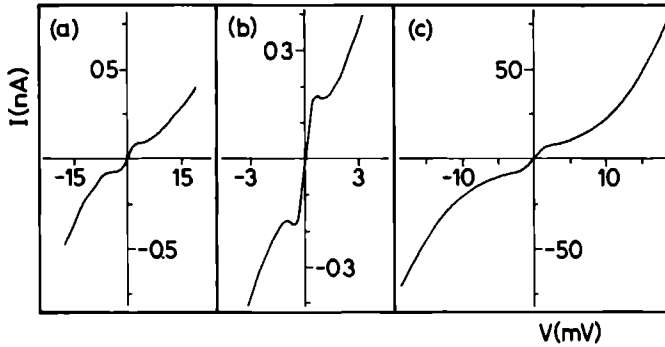


**Figure 5.9**  $I(V)$  curves displaying Josephson-like behaviour for junctions between a tungsten tip and (a) ceramic  $\text{YBa}_2\text{Cu}_3\text{O}_{7-\delta}$ , (b) ceramic  $\text{Bi}_2\text{Sr}_2\text{CaCu}_3\text{O}_x$ , and (c) a ceramic piece of  $(\text{Pb}_x\text{Bi}_{1-x})_2\text{Sr}_2\text{Ca}_2\text{Cu}_3\text{O}_{10}$

we expect to see a resistance increase in the characteristics as soon as the tunnel current surpasses the critical current of the link. In Fig. 5.9 I have drawn some examples, all measured with a tungsten tip, but on various samples. Wilkins *et al.* [35] have reported the same type of characteristics for tunnel junctions between a platinum tip and an oriented but polycrystalline  $\text{YBa}_2\text{Cu}_3\text{O}_{7-\delta}$  film. Below the critical current the junction resistance is not zero, indicating that the tip-grain junction still has a significant resistance. Curves similar to trace (b) are also reported by Walsh *et al.* [31] in tunnel measurements between two thin film segments of  $\text{Bi}_2\text{Sr}_2\text{CaCu}_3\text{O}_x$ .

Using Nb or NbZr tips and ceramic  $\text{YBa}_2\text{Cu}_3\text{O}_{7-\delta}$  samples we have also performed measurements on low resistance SIS point contacts. By digging the tip deep enough into the sample it was possible to routinely obtain well developed Josephson characteristics. Many  $I(V)$  curves displayed complex oscillatory behaviour under the influence of a ramped magnetic field applied perpendicular to the tip axis. This indicates that these junctions actually consisted of several weak links connected in parallel. In the point-contact set-up used in these experiments the temperature could be varied between 1.2 and 4.2 K by pumping the helium bath. For a regular Josephson junction between NbZr and  $\text{YBa}_2\text{Cu}_3\text{O}_{7-\delta}$  one would not expect the critical current to have a strong temperature dependence in this region, as the  $T_c$  of NbZr (10 K) is much higher than 4.2 K (see chapter 1, Eq. 1.29). Nevertheless we observed in a significant number of cases that the critical current dropped more or less linearly with increasing temperature, and sometimes even became zero at 4.2 K. This suggests that the tip was probing areas of the sample with strongly suppressed superconducting properties.

Figure 5.10 shows an  $I(V)$  characteristic which displays, for currents above the critical value, a sequence of stepwise increments of the junction resistance. Each successive jump adds approximately  $2.5 \Omega$  to the differential resistance. All tangents to the linear branches intersect each other at the same point, while each tangent



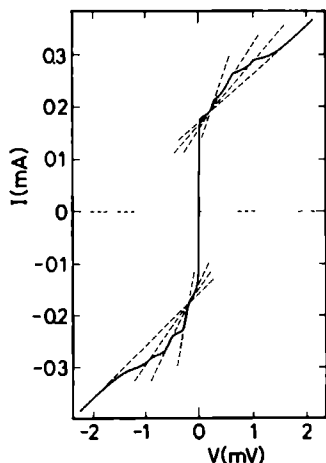


**Figure 5.10**  $I(V)$  curve of a Josephson junction between NbZr and ceramic  $\text{YBa}_2\text{Cu}_3\text{O}_{7-\delta}$ , recorded at  $T = 4.2$  K, probably displaying the nucleation of phase-slip centers.

intersects the current axis far above the origin. The positions of the kinks could be modulated by a magnetic field. The fact that the tangents do not intersect the origin rules out a simple explanation in terms of an array of several (intergrain) weak links connected in series. In that case it would also be surprising that each junction apparently adds the same normal state resistance to the array. The same goes for more-dimensional networks of coupled grains.

A more appealing explanation might be found in the concept of phase-slip centers as developed by Skocpol *et al.* [32]. In their theory, each step in the characteristic corresponds to the nucleation of an additional identical localized resistive center in the weak link. At a critical current, determined by the local effective temperature and the cross-sectional area of the weak link, current induced non-equilibrium effects can lead to a local collapse of the order parameter. The macroscopic phase difference between the two parts of the weak link that are separated by this region will start to slip, resulting in a voltage across the phase-slip center. When the phase difference has reached  $2\pi$ , the order parameter restores itself and the center again becomes superconducting. This process will repeat itself in a cyclic way.

Although the concept may be valid in a wider temperature range, the calculations of Ref. [32] are, strictly speaking, only valid in the limit  $T \approx T_c$ . Considering the bulk critical temperatures of tip and sample, the experiments are certainly not in this limit. The small coherence length in the  $\text{YBa}_2\text{Cu}_3\text{O}_{7-\delta}$  sample, however, does allow large variation of the local order parameter and corresponding local  $T_c$ . In the light also of the above reported anomalous temperature dependence of the critical current in a large number of Josephson junctions, we may conclude that we are either probing sample areas with deteriorated superconducting properties, or that the material on the whole is more sensitive to non-equilibrium effects in a temperature range significantly below  $T_c$ .

## 5.5 Charging effects

The influence of various charging effects, such as the Coulomb blockade in single junctions, and incremental charging in tunneling through small grains, has already been extensively discussed in chapters 3 and 4. Here I will restrict myself to some concluding remarks.

Figure 3.4 of chapter 3 showed possible evidence for the influence of the Coulomb blockade and corresponding voltage fluctuations, on gap spectroscopy measurements. When the tunneling involves e.g. hopping through localized impurity states or surface states with a low group velocity, the small intrinsic capacitance of the point-contact junction may become decoupled from stray capacitances in the junction environment. Tunneling of electrons will then be governed not only by the densities of states and connecting matrix elements, but also by the electrostatic charging energy of the junction capacitor. Spectroscopic features will be shifted by the Coulomb blockade energy  $e^2/2C$ , and voltage oscillations with amplitude of order  $e/2C$  will induce significant broadening (see also the calculations in chapter 2, and Fig. 2.9). The occurrence of the effect will depend heavily on e.g. the surface properties of tip and sample, so that the influence may differ from contact to contact and for different materials.

From this point of view charge fluctuations may provide a possible explanation for the unexpectedly large broadening of gap features measured on high- $T_c$  materials. Figure 5.11 again shows the NIS characteristic between a tungsten tip and a ceramic  $\text{YBa}_2\text{Cu}_3\text{O}_{7-\delta}$  sample already shown in Fig. 5.4(a). The thick line now is a fit, based on the Monte Carlo calculations of section 2.2.3, involving a small capacitance current biased junction with one superconducting electrode. The presumption of perfect current bias is of course not realistic, but, as discussed in chapter 3, the voltage fluctuations can be prominent also in the absence of coherent SET-oscillations. The picture therefore still gives a realistic impression of the possible influence of charging effects. The gap value involved in this fit is closer to the BCS prediction. Furthermore, the incorporation of charging effects naturally accounts for the strong broadening of the gap features.

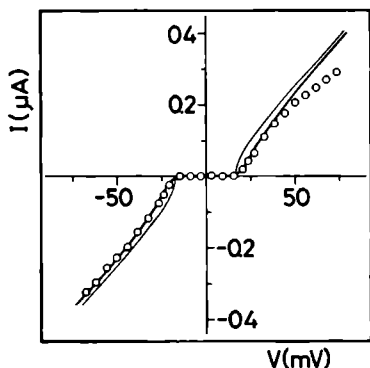


**Figure 5.11**  $I(V)$  curve (dots) of a point-contact junction between W and  $\text{YBa}_2\text{Cu}_3\text{O}_{7-\delta}$  fitted (thick line) with calculations involving charging effects due to a small intrinsic junction capacitance. The relevant parameter values are  $C = 1.6 \times 10^{-17}$  F and  $\Delta = 16$  meV. The thin line shows the BCS ( $T = 0$ ) curve for this value of  $\Delta$ .

The Coulomb staircase, due to incremental charging of small isolated grains, has been observed on a wide range of samples [33], and has also been reported in the literature by several other groups [34, 35]. For more details I refer to chapter 4 of this thesis.

## 5.6 Negative differential resistance

The most curious  $I(V)$  characteristics, observed on a number of  $\text{YBa}_2\text{Cu}_3\text{O}_{7-6}$  samples, were those exhibiting regions of negative differential resistance (NDR). A collection of representative  $I(V)$  curves is shown in Fig. 5.12. The curves are often highly asymmetric and the positions of the peaks are not really fixed, but can shift in response to  $z$ -movement of the tip. Similar characteristics have also been reported by Wilkins *et al.* [35]. In their observations the NDR regions were mostly observed with the sample biased negatively with respect to the tip. In most of our cases the NDR features are also only present on one branch of the  $I(V)$  curve, but with equal probability on either side of the origin (see Fig. 5.12(a)).

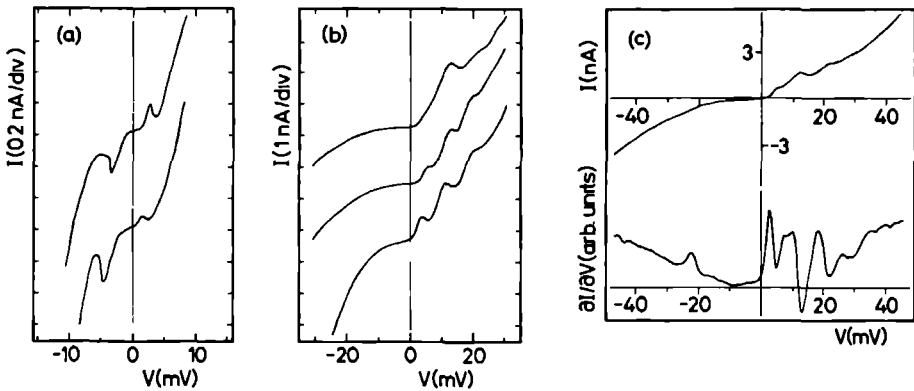


**Figure 5.12** Some examples of the three types of NDR effects that have been observed in tunneling experiments on high temperature superconductors

In measurements on the  $\text{YBa}_2\text{Cu}_3\text{O}_{7-6}$  single crystal, on which we have also observed the Coulomb staircase, we even recorded a set of characteristics in which the effect was seen to switch between the positive and negative side (see Fig. 5.12(b)). Fig. 5.12(c) shows a measurement on a polycrystalline  $\text{YBa}_2\text{Cu}_3\text{O}_{7-6}$  sample in which the NDR effect is present on both sides of the origin. Moving the tip perpendicular to the surface, the current peaks were seen to shift as a pair, the distance between them staying roughly constant. The height of the peak moving away from the origin was seen to increase at the expense of a suppression of the peak approaching the origin. In all cases the effect occurs at voltages of the order of 2–20 mV.

Negative differential resistance is a characteristic effect for double barrier reso-

nant tunneling devices [36] and the Esaki diode [37]. The latter device consists of a junction between two oppositely doped semiconductors. Although the oxide layers in high- $T_c$  material are known to be semiconducting in some cases, it seems a bit far-fetched to assume that in all the above examples the tip is somehow probing a spot on the sample containing two regions with such strongly different impurity dopings. Moreover, the Esaki diode only exhibits NDR in the forward bias direction. Besides this, Ref. [35] reports that similar NDR characteristics were also observed in measurements on samples containing oxidized indium droplets, used to study incremental charging effects. It is not likely that semiconducting properties as sketched above are present in this kind of samples.

The curves of Fig. 5.12 show a striking qualitative resemblance to STS-results by Lyo and Avouris [38]. In room-temperature STM-measurements on boron-doped silicon samples they were able to identify boron-induced defect sites.  $I(V)$  curves recorded with the tip positioned above such sites displayed NDR features on either the positive or the negative side of the origin as well as on both sides simultaneously. The only difference lies in the fact that the positions of the current peaks in the experiments of Ref. [38] are always at voltages of the order of one volt. The results are explained in terms of resonant tunneling through localised defect states, assuming a peaked density of states for both the defect site and the tunneling region of the tip. These defect states can be situated either below or above the Fermi level, resulting in NDR on the negative or positive  $I(V)$  branch.

Despite the different energy scales an explanation along the same lines seems quite appropriate for our situation, especially when keeping in mind the vision on tunneling in this type of point-contact junctions as expounded in section 1.4 and chapter 3 of this thesis. The shifts in peak positions as a result of tip movement may be due to a change of the ratio of the resistances for tunneling from tip to localized state and from localized state to the bulk respectively, and the consequently different potential distribution across both junctions. Charging effects may have a similar effect as they shift the final state energy by an amount inversely proportional to the effective capacitance of the defect state.

## 5.7 Conclusions

General conclusions regarding the energy gap and corresponding coupling strength in high- $T_c$  materials, can only be of decisive significance when a careful evaluation and critical comparison is made of all available tunnel data, together with the results of other techniques that can measure the energy gap, such as far infra-red reflection and Andreev reflection. It may be clear that this goes well beyond the scope of this thesis.

Nevertheless, certainly some reliable conclusions can be drawn from the results presented here. Concerning their apparent coupling strength the three families of high- $T_c$  materials seem to be clearly distinct. The bismuth oxides studied by Sharifi *et al.* [22] display perfect BCS-behaviour with  $2\Delta/k_B T_c \approx 3.5$ , in good correspondence with the weak-coupling limit. The copper oxides containing bis-

ments show reasonable BCS-like tunneling characteristics but the coupling strength ( $2\Delta/k_B T_c \approx 8$ ) exceeds the BCS-prediction by a factor of two. For the most extensively studied high- $T_c$  superconductor,  $\text{YBa}_2\text{Cu}_3\text{O}_{7-\delta}$ , it proves extremely difficult to obtain reproducible tunneling characteristics, and from what is available up to now the coupling strength appears to scatter between 3 and 7, with an average significantly above the weak-coupling factor. For  $\text{YBa}_2\text{Cu}_3\text{O}_{7-\delta}$  the gap anisotropy can not be inferred from our measurements. For the  $(\text{Pb}_x\text{Bi}_{1-x})_2\text{Sr}_2\text{CaCu}_2\text{O}_8$  single crystals however we have quite unambiguously determined the in-plane coupling strength, while superconductivity in the  $c$ -direction appeared too weak to be detectable at the surface.

On the whole we find that well pronounced gap characteristics strongly resemble the BCS-prediction, as calculated in section 1.3. The large scale of non-superconducting effects, that is often seen to completely dominate the  $I(V)$  characteristics, of course raises serious suspicion as to whether well developed gap structures can be considered as due to NIS or SIS quasi-particle tunneling only. Speculations on the detailed shape of the quasi-particle density of states are therefore not opportune.

Many of the questions remaining open in this chapter might be answered to some extent with the help of tunneling experiments employing well characterized single crystals and clean artificial barriers. Although attempts in this direction are reported by several groups (e.g. Refs. [12, 22]), I have not been able to find any clear results in recent literature, that might be considered distinctively more convincing than the point-contact measurements presented here. The problem remains, also in more sophisticated junctions, that tunneling only probes the local density of states just outside the barrier. Due to the short coherence lengths the surface properties may differ significantly from those of the bulk.

## References

1. G. Bednorz and K.A. Müller, *Z. Phys. B* **64** (1986) 189.
2. J. Bardeen, L.N. Cooper, and J.R. Schrieffer, *Phys. Rev.* **108** (1957) 1175.
3. R.D. Parks, ed., *Superconductivity*, Vols. 1 and 2, (Marcel Dekker, N.Y., 1969).
4. M. Tinkham, *Introduction to Superconductivity*, (Krieger Publ. Comp., 1975).
5. J.R. Schrieffer, *Theory of Superconductivity*, (Addison-Wesley, 1964).
6. M. Tinkham and C.J. Lobb, *Solid State Phys.* **42** (1989) 91.
7. *Physica B* **165&166** (1990): proceedings of the 19th International Conference on Low Temperature Physics (LT19), Brighton, U.K. (1990).
8. *Supercond. Sci. Technol.* **4** (1991): proceedings of LT19 Satellite Conference on High- $T_c$  Superconductivity, Cambridge, U.K. (1990).
9. *Physica C* **185-189** (1991): proceedings of the International Conference on Materials and Mechanisms of Superconductivity, Kanazawa, Japan (1991).
10. P.J.M. van Bentum and H. van Kempen, *Scanning Tunneling Microscopy I*, eds. H.-J. Güntherodt and R. Wiesendanger, (Springer-Verlag, Berlin, 1992).
11. M.A. Beno, L. Soderholm, D.W. Capone, D.G. Hunkers, J.D. Jorgensen, J.D. Grace, I.K. Schuller, *Appl. Phys. Lett.* **51** (1987) 57.

12. J.M. Valles Jr., R.C. Dynes, A.M. Cucolo, M. Gurvitch, L.F. Schneemeyer, J.P. Garno, and J.V. Waszczak, *Phys. Rev. B* **44** (1991) 11986; M. Gurvitch, J.M. Valles Jr., A.M. Cucolo, R.C. Dynes, J.P. Garno, L.F. Schneemeyer, and J.V. Waszczak, *Phys. Rev. Lett.* **63** (1989) 1008.
13. B. Batlogg *et al.*, *Physica C* **153-155** (1988) 1062; Y. Matsuda *et al.*, *Solid State Commun.* **68** (1988) 103.
14. P.J.M. van Bentum, L.E.C. van de Leemput, L.W.M. Schreurs, P.A.A. Teunissen, and H. van Kempen, *Phys. Rev. B* **36** (1987) 843.
15. H.F.C. Hoevers, P.J.M. van Bentum, L.E.C. van de Leemput, H. van Kempen, A.J.G. Schellingerhout, and D. van der Marel, *Physica C* **152** (1988) 105; see also H.F.C. Hoevers, Ph.D. thesis (1992), University of Nijmegen, the Netherlands.
16. J.J. Wnuk, L.W.M. Schreurs, Y.S. Wang, P.J.E.M. van der Linden, and P.J.T. Eggenkamp, *Mat. Res. Bull.* **25** (1990) 1121.
17. J.J. Wnuk, L.W.M. Schreurs, P.J.T. Eggenkamp, and P.J.E.M. van der Linden, *Physica B* **165&166** (1990) 1371.
18. J.R. Kirtley, *Int. J. Mod. Phys. B* **4** (1990) 201.
19. G.E. Blonder, M. Tinkham, and T.M. Klapwijk, *Phys. Rev. B* **25** (1982) 4515; see also H.F.C. Hoevers, Ph.D. thesis (1992), University of Nijmegen, the Netherlands.
20. R.C. Dynes, V. Narayanamurti, and P.J. Garno, *Phys. Rev. Lett.* **41** (1978) 1509.
21. S. Takahashi and M. Tachiki, *Physica B* **165&166** (1990) 1067.
22. F.Sharifi, A. Pargellis, and R.C. Dynes, *Phys. Rev. Lett.* **67** (1991) 509; F.Sharifi, A. Pargellis, R.C. Dynes, B. Miller, E.S. Hellman, J. Rosamilia, and E.H. Hartford Jr., *Phys. Rev. B* **44** (1991) 12521.
23. I.A. Devyatov and M.Yu. Kupriyanov, *JETP Lett.* **52** (1990) 311 (*Pis'ma Zh. Eksp. Teor. Fiz.* **52** (1990) 929).
24. P.J.M. van Bentum, H.F.C. Hoevers, L.E.C. van de Leemput, and H. van Kempen, *J. Magn. Magn. Mat.* **76&77** (1988) 561.
25. P.J.M. van Bentum, H.F.C. Hoevers, H. van Kempen, L.E.C. van de Leemput, M.J.M.F. de Nivelte, L.W.M. Schreurs, R.T.M. Smokers, and P.A.A. Teunissen, *Physica C* **153-155** (1988) 1718.
26. P.J.M. van Bentum, H.F.C. Hoevers, L.E.C. van de Leemput, M.J.M.F. de Nivelte, L.W.M. Schreurs, R.T.M. Smokers, P.A.A. Teunissen, and H. van Kempen, *Phys. Scr.* **T25** (1989) 91.
27. H. van Kempen, J.J.A. Wnuk, P.J.M. van Bentum, H.F.C. Hoevers, L.E.C. van de Leemput, L.W.M. Schreurs, and R.T.M. Smokers, *Progress in High Temperature Superconductivity*, Vol. **24** (1989) 147.
28. J.J. Wnuk, R.T.M. Smokers, F.W. Nolden, L.W.M. Schreurs, Y.S. Wang, and H. van Kempen, *Supercond. Sci. Technol.* **4** (1991) S412.
29. J.R. Kirtley, S. Washburn, and D.J. Scalapino, preprint.
30. A.Th.A.M. de Waele, R.T.M. Smokers, R.W. van der Heijden, K. Kadowaki, Y.K. Huang, M. van Sprang, and A.A. Menovsky, *Phys. Rev. B* **35** (1987) 8858.
31. T. Walsh, J. Moreland, R.H. Ono, T.S. Kalkur, *Phys. Rev. Lett.* **66** (1991) 516.
32. W.J. Skocpol, M.R. Beasley, and M. Tinkham, *J. Low Temp. Phys.* **16** (1974) 145.
33. P.J.M. van Bentum, R.T.M. Smokers, and H. van Kempen, *Phys. Rev. Lett.* **60** (1988) 2543.
34. See e.g.: J.R. Kirtley, C.C. Tsuei, S.I. Park, C.C. Chi, J. Rozen, M.W. Shafer, W.J. Gallagher, R.L. Sandstrom, T.R. Dinger, and D.A. Chance, *Jpn. J. Appl. Phys.* **26**

- Suppl. 263 (1987) 998. See also Refs. 64, 86, and 87 of Ref. [18].
35. R. Wilkins, M. Amman, R.E. Soltis, E. Ben-Jacob, and R.C. Jaklevic, Phys. Rev. B **41** (1990) 8904.
  36. See e.g.: B. Ricco and M.Ya. Azbel, Phys. Rev. B **29** (1984) 1970.
  37. L. Esaki, Phys. Rev. **109** (1958) 603.
  38. I.-W. Lyo and Ph. Avouris, Science **245** (1989) 1369.

## Chapter 6

# Quantum resistance and localization in one-dimensional systems



## 6.1 Introduction

The present day status of microfabrication technology allows the manufacturing of metal and semiconductor devices with dimensions smaller than the inelastic scattering length of the materials of which they are made. In these mesoscopic devices conduction is governed by coherent, dissipationless, wave propagation. Any elastic scattering in the system leads to, macroscopically observable, quantum interference effects<sup>1</sup>

An example of these effects are the so-called Universal Conductance Fluctuations (UCF). Resistance measurements on nominally identical mesoscopic devices will display sample to sample fluctuations, which, depending on the dimensions of the samples, may be of the order of the quantum resistance  $R_Q \equiv \pi\hbar/2e^2 \simeq 6.5 \text{ k}\Omega$ . These fluctuations are the result of the markedly different interference patterns of the charge carriers in the devices as a consequence of differences in the positions and distribution of elastic scatter centers (impurities, lattice defects). In fact, the interference is dramatically sensitive to subtle changes in the scatterer configuration, so that migration of impurities or lattice defects will even lead to fluctuations of the resistance of a single device as a function of time.

The resistance of small metallic rings (diameter on the order of  $1 \mu\text{m}$ ) has been shown to oscillate as a function of the magnetic flux applied through the ring, with a period  $h/e$  due to the Aharonov-Bohm effect, and a second period  $h/2e$  as a consequence of "coherent backscattering". In these experiments the magnetic vector potential influences the phases of the electrons going round the loop, and thereby changes the interference pattern. Phase changes of  $2\pi$  are physically indistinguishable, so that the effects are periodic in the flux.

A third effect, occurring in samples with a disordered potential, is localization. Due to the interference as a consequence of multiple scattering extended wave functions tend to become localized. The wave function will have maximum amplitude at a fixed position with, in general, exponentially decaying slopes. The exponential decay constant is associated with a localization length  $\ell$ . If the system is large enough (size  $L > \ell$ ) the electrons will thus become trapped in the disorder.

In this context we have to distinguish between two types of localization. The concept of weak localization applies to systems where the disordered potential is so weak that it can be treated in some perturbation approach. An enhanced backscattering is predicted, as a consequence of the constructive interference of multiple coherent elastic scattering paths of a single conduction electron, resulting in an increased residual resistance of the system.

For strong disordered scattering potentials the theory of strong localization predicts that electrons actually become localized when the dimensions of the sample

---

<sup>1</sup>For extensive reviews on the theoretical and experimental aspects of quantum interference effects the reader is referred to

- S Washburn and R A Webb, *Adv Phys* **35** (1986) 375,
- D J Thouless, "Introduction to disordered systems", in *Critical Phenomena, Random Systems, Gauge Theories*, part II (North-Holland, Amsterdam, 1986), eds K Osterwalder and R Stora

are large compared to the localization length  $\ell$ . This will in principle result in an infinite residual resistance for sufficiently large devices. In practice conduction will remain possible to some extent, due to hopping between localized states.

Localization behaviour will in general only be observable when the inelastic mean free path of the material is larger than the dimensions of the device. Inelastic scattering, e.g. electron-phonon or electron-electron, destroys the phase memory of the electrons, thus killing the interference patterns. Low temperatures and small samples are therefore required. Furthermore a magnetic field suppresses localization, as it breaks the time reversal symmetry, meaning that time reversed paths no longer interfere constructively.

As there is no way for an electron to circumvent a scatterer, the localization behaviour in one-dimensional systems is always of the strong type. As a consequence of the coherent wave propagation, the resistance will scale superlinearly with length. In this chapter we will have a closer look at two fundamentally different one-dimensional systems, a wire of finite length connected to reservoirs, and an isolated ring. Using these examples general concepts of localization are developed and illustrated.

In the theory of tunneling, as described in chapter 1, it is quite natural to ascribe resistance to a tunnel barrier, even though the dissipation, i.e. relaxation of the energy gained by the tunneling electron, only occurs in the electrodes some distance away from the barrier. The electrodes serve as reservoirs, on one side supplying electrons with a thermal equilibrium distribution, and on the other side equilibrating electrons that have gained energy from the potential difference applied over the barrier. The same concept can now be used to model resistance measurements on devices with coherent electron wave propagation. The properties of the device are calculated in a stationary state approach based on the fully coherent interference of multiply scattered wave functions, and expressed in terms of (complex) transmission and reflection probabilities. The device is thought to be connected to thermalizing reservoirs, the chemical potentials of which determine the applied voltage. In the thermalization process inside the reservoirs all phase memory of the electrons is lost, so that the electrons supplied by the reservoirs are fully incoherent.

In section 6.2 we examine the stationary state properties of a one-dimensional wire connected to such reservoirs. The wires contain a random distribution of  $\delta$ -function scatterers, modelling the disordered potential. The scaling behaviour of such a system can be studied by calculating the resistance of several wires connected in series. These calculations require the definition of the intrinsic "quantum" resistance of a coherent scatterer, isolated from thermalizing reservoirs. Such a definition has been given by Landauer for the limit of zero applied voltage. We extend this definition to include averaging effects that follow from adding the interference patterns of electrons with different energies within the window set by the voltage. Using this extended resistance formula the effects of an applied voltage on the Universal Conductance Fluctuations, as well as on the statistical properties of ensembles of wires with equal length but different scatterer distributions, are examined. A scaling "law" is derived, which is confirmed by numerical calculations on

the one-dimensional wire system.

Section 6.3 is the result of a comparison of the properties of the wire system and concepts developed in section 6.2, and the results of calculations by Lenstra and coworkers [1, 2] on the dynamical conduction behaviour of a one-dimensional ring containing a single  $\delta$ -function scatterer. Current through the ring is induced by applying a time-dependent magnetic flux  $\Phi(t)$  through the ring (see Fig. 6.1).  $d\Phi/dt$  is constant, resulting in a constant electromotive potential gradient around the loop. Electron motion is described using the time dependent Hamiltonian of the system. On finite time scales the current is found to saturate, suggesting an intuitive notion of resistance, i.e. constant voltage to current ratio, for the  $\delta$ -function scatterer. The system however contains no reservoirs, and is therefore free of dissipation. An electron circling the loop effectively experiences a potential consisting of a periodic array of scatterers superimposed on a constant potential gradient, which is identical to the potential inside the one-dimensional wire of section 6.1, if the scatterer distribution is taken equidistant. In this analogy the number of roundtrips on the loop can be associated with the length of the wire under consideration. The finite electric field in both systems changes the effective path lengths between scattering events, and the corresponding interference conditions, leading to so-called dynamical phase disorder in the systems.

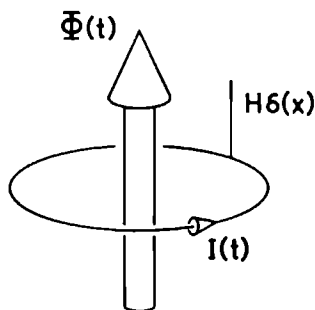


**Figure 6.1** The 1D model system, studied in section 6.3 and Refs. [1, 2], of the loop with one  $\delta$ -function scatterer. The changing flux  $\Phi(t)$ , threading the ring, induces a current  $I(t)$  as a response to the electromotive force  $FL$ .

Using the Landauer resistance of a single  $\delta$ -function scatterer, a connection is now made between the scaling theory of section 6.2 and the dynamical current development in the ring. With the scaling theory we are able to predict the correct average voltage dependence of the saturation current in the loop. This suggests that the Landauer formula of quantum elastic scattering resistance is valid irrespective of the presence of phase randomizing reservoirs, and that elastic scattering alone can be a physical source of resistance, in a concept for which reservoirs and dissipation are not essential ingredients.

## 6.2

# Theory of nonlinear quantum tunneling resistance in one-dimensional disordered systems<sup>1</sup>

Daan Lenstra<sup>2,3</sup> and Richard T M Smokers

### Abstract

A novel generalized Landauer formula is derived and used to study the voltage-dependent resistance in a one-dimensional (1D) disordered system. A finite voltage difference introduces energy integration and gives the system self-averaging behaviour to a certain extent. The quantum resistance of a 1D system generally shows a rich structure in its dependence on applied voltage and length. Resistance fluctuations are shown to decrease with increasing voltage. In spite of the self-averaging, the mean resistance at large voltages turns out to scale superlinearly with length.

---

<sup>1</sup>This section has been published in *Physical Review B* **38** (1988) 6452

<sup>2</sup>Department of Physics, Eindhoven University of Technology, P O Box 513, 5600 MB Eindhoven, the Netherlands

<sup>3</sup>present address Department of Physics and Astronomy, Free University, De Boelelaan 1081, 1081 HV Amsterdam, the Netherlands

### 6.2.1 Introduction

The quantum resistance of a one-dimensional (1D) system with static disorder reflects the coherent wave-propagation nature of electrons at low temperatures [3, 4, 5]. A simple formula which expresses this resistance in terms of the coherent transmission and reflection properties of the structure is Landauer's formula [6]. This formula is valid only for sufficiently small voltages, such that the transmission probability  $T(E)$  can be treated as a constant in the corresponding energy window of width  $\Delta E$  in which the net conduction takes place. Let  $L$  be the system length and  $N(E_F)$  the density of states per unit length at the Fermi energy,  $N(E_F) \simeq (\pi\hbar v_F)^{-1}$ , with  $v_F$  the Fermi velocity. The typical energy scale on which  $T(E)$  will develop large variations is given by  $[LN(E_F)]^{-1}$ . Therefore, the Landauer formula is only applicable as long as  $\Delta E \ll [LN(E_F)]^{-1}$ .

The scaling approach to localization in 1980 by Anderson *et al.* [7] – already anticipated by Landauer [6] in 1969 – is based on the careful investigation of the statistical properties of the elastic scattering segments placed behind each other and leads to the famous exponential scaling law for the resistance, i.e.,

$$\mathcal{R} = (\pi\hbar/e^2)[\exp(L/\ell) - 1],$$

with  $L$  the system length and  $\ell$  the localization length. This result being derived with the use of Landauer's formula is valid in the limit  $V \rightarrow 0$ , where  $V$  is the voltage over the system.

In this article we present the derivation of a new Landauer-type formula for the resistance, which generalizes a formula given by Büttiker *et al.* [8] in the sense that we will not linearize in  $V$ . Our formula is well suited to deal with energy integration associated with substantial differences in chemical potential of two reservoirs (which emit and absorb electrons at both sides of the system) as well as with temperature broadening in the reservoirs. Using this extended resistance formula, we study both the dependence on voltage for a system of given length and the dependence on length (i.e., the scaling behaviour) at given voltage.

The central quantity of interest turns out to be a properly energy-averaged transmission probability  $T$ . In the limit of vanishingly small voltage over the system we recover the exponential scaling regime [7], characterized by  $\langle \ln T \rangle = -L/\ell$ , where  $\langle \dots \rangle$  means ensemble averaging. However, with increasing voltage the scaling properties of  $\bar{T}$  may become such as to induce exponential scaling with a scaling length generally *larger* than the Anderson localization length  $\ell$ . Although the resistance values at zero voltage are heavily dependent on the sample (universal conductance fluctuations [9, 10, 11]), on increasing the voltage difference they were found to converge to a sample-independent value which is significantly smaller than the zero-voltage scale resistance. For a given fixed system with length  $L$ , the resistance turns out to be a very complicated function of voltage with typical fluctuations which for small voltages are in agreement with universal conductance fluctuations, but for larger values of  $V$  tend to decrease. These effects are due to the self-averaging behaviour as a consequence of the conduction taking place in an energy window of

*finite* rather than infinitesimally small width.

Several authors have recognized earlier that the presence of an electric field, such as associated with a finite voltage difference, may be relevant for localization behaviour [12, 13, 14] as well as for transport properties [1,4,15-22]. References [1, 17, 18, 19, 21] treat the quantum dynamics of electrons under the influence of an electric field. The present work of Refs. [12, 13, 14] and [20] is more in the spirit of the present stationary approach, but the energy integration associated with the finite voltage difference over the system was disregarded by these authors.

In section 6.2.2 we will set up the model and derive our central formula. Systems of variable length are numerically analyzed in section 6.2.3 using a Kronig-Penney-type of random potential simulating the presence of scattering centers. The scaling predictions based on the resistance formula are derived in section 6.2.4 leading to a novel exponential scaling law for the mean resistance, in which the scale length is directly related to the fluctuations (on energy averaging) of the transmittivity. In section 6.2.5 the main results are summarized and discussed in relation to existing theory.

## 6.2.2 Derivation of the resistance formula

The configuration to be considered here is sketched in Fig. 6.2. It is the same configuration studied in Ref. [8], but our derivation will be different in that the potential difference over the system will not be assumed to be infinitesimally small. The two reservoirs in Fig. 6.2 are held at fixed chemical potentials  $\mu_l$  and  $\mu_r$ . The crucial point first elucidated by Landauer [6] is that the voltage difference over the system is smaller than  $|\mu_l - \mu_r|/e$  by an amount to be determined from self-consistency requirements.

Let the respective distributions in the left- and right-hand reservoir be given

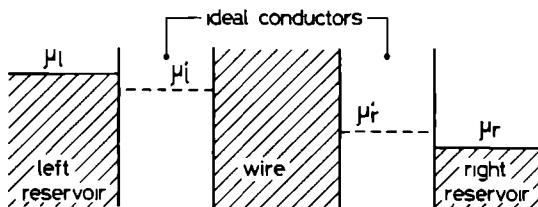


**Figure 6.2** One-dimensional model for the determination of the quantum resistance of a scattering segment ("wire") connected through ideally conducting "contacts" to two reservoirs which are at different chemical potentials  $\mu_l$  and  $\mu_r$ . Due to redistribution of charge, the actual voltage difference over the wire is related to the chemical potentials at both ends of the wire,  $\mu_l'$  and  $\mu_r'$ , which have to be determined in a self-consistent way.

by the Fermi-Dirac distribution functions

$$f_j(E) = \frac{1}{1 + \exp[(E - \mu_j)/k_B T_j]} \quad (j = r, l), \quad (6.1)$$

where it is noted that the temperature of the reservoirs,  $T_r$  and  $T_l$ , may be different and  $k_B$  is Boltzmann's constant. It is assumed that the electrons propagate fully coherently both in the *ideal* conductors (see Fig. 6.2) and in the wire between them. The role of temperature is restricted to dictating the precise shape of the two distribution functions. All scattering processes present in the wire are assumed to be coherent processes, i.e., the electrons are scattered by a time-independent rigid potential (no phonon creation or annihilation; no electron-electron interactions).

In order to obtain the net current through the wire we will need the transmission and reflection probabilities for an electron at given energy  $E$ . These quantities are completely determined by the full scattering structure of the system which in turn is self-consistently related to the charge distribution in the wire and the leads. In an exact procedure one would have to use an iterative method for integrating Schrödinger's equation subject to the given boundary conditions associated with the prescribed incoming fluxes at both reservoir-contact boundaries. Fortunately, a first-order solution to this complicated self-consistency problem can be obtained by relatively simple means [6, 7, 8]. In this method, one introduces the local chemical potentials  $\mu'_l$  and  $\mu'_r$  and identifies the voltage difference over the wire as  $V = |\mu'_l - \mu'_r|/e$ .

For convenience, we will assume in Fig. 6.2 the symmetric situation with  $\mu_l - \mu'_l = \mu_r - \mu'_r$ . It will be shown below that this is a very reasonable assumption indeed, fully consistent with the approximation made. The potential felt by an electron is sketched in Fig. 6.3. Drops in potential occur when an electron moves from inside a reservoir to the point of entering the wire ( $0 < x < L$ ). In the left reservoir ( $x < x_l$ ) the potential is  $\Delta\mu$ . In the ideal conductor ( $x_l < x < 0$ ) the potential has dropped by an amount  $\frac{1}{2}(\Delta\mu - eV)$ , where  $V$  is the voltage over the wire. In the wire we put the total potential equal to  $U(x) - (eVx/L) + \frac{1}{2}(\Delta\mu + eV)$ , where  $U(x)$  is the static-disorder potential. In the other ideal conductor ( $L < x < x_r$ ) the potential is again at a constant, given by  $\frac{1}{2}(\Delta\mu - eV)$ , while the right reservoir ( $x > x_r$ ) the potential is zero. All ingredients necessary for solving the transmission and reflection problem have now been given.

The probability of emitting an electron at energy  $E$  by the left-hand reservoir is  $f_l(E)$ . When this electron is incident on the wire, its wave number equals

$$k'_l = [(2m/\hbar^2)(E - \frac{1}{2}\Delta\mu - \frac{1}{2}eV)]^{1/2}.$$

after transmission the electron will leave the wire with wave number

$$k'_r = [(2m/\hbar^2)(E - \frac{1}{2}\Delta\mu + \frac{1}{2}eV)]^{1/2}.$$

The current contribution due to electrons emitted from the left is

$$I_l = \frac{e}{\pi} \int_0^\infty dk f_l(E) v(k) T(E), \quad (6.2)$$

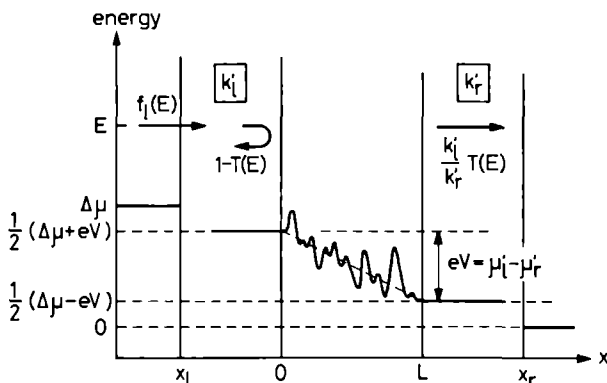


**Figure 6.3** Potential felt by an electron in the configuration of Fig. 6.2. An electron emitted at energy  $E$  by the left reservoir [probability  $f_l(E)$  given by Eq. 6.1] has wave number  $k_l' = [(2m/\hbar^2)(E - \frac{1}{2}\Delta\mu - eV)]^{1/2}$  when incident on the wire [reflectivity  $1 - T(E)$ ] and has wave number  $k_r' = [(2m/\hbar^2)(E - \frac{1}{2}\Delta\mu - eV)]^{1/2}$  when transmitted [transmittivity  $k_l'T(E)/k_r'$ ], as indicated in the upper part of the figure.

where  $k$  is the wave number in the left reservoir,

$$k = [(2m/\hbar^2)(E - \Delta\mu)]^{1/2},$$

$v(k) = \hbar k/m$ , and  $T(E)$  is the transmission probability for an electron with energy  $E$ . As a matter of course  $T(E)$  will strongly depend on  $V$ . A precise definition and treatment of the quantity  $T(E)$  will be postponed to section 6.2.4. We mentioned already that one has to be careful in introducing  $T$  because of the wave numbers being different at both ends of the scattering system.

The right-hand side of Eq. 6.2 is converted into an integral over energy, using the density of states (with positive  $k$ ) per unit length,  $[\pi\hbar v(k)]^{-1}$ ,

$$I_l = \frac{e}{\pi\hbar} \int dE f_l(E) T(E). \quad (6.3)$$

A similar expression can be written down for the current contribution due to electrons emitted from the right-hand reservoir. In this expression, the transmission probability is equal to the one in Eq. 6.3, as will be shown in section 6.2.4. Subtracting this current from Eq. 6.3, we arrive at the net current through the wire

$$I = \frac{e}{\pi\hbar} \int dE [f_l(E) - f_r(E)] T(E). \quad (6.4)$$

Next, we must determine the voltage  $V$  that stands over the wire by relating it to the local chemical potentials  $\mu_l'$  and  $\mu_r'$  in the ideally conducting contacts at both sides of the wire. First, we notice from Eq. 6.4 that the net current is carried only by electrons in a narrow interval (width  $\approx \Delta\mu$ ) around the Fermi energy  $E_F =$



$\frac{1}{2}(\mu_l + \mu_r)$ . Directly associated with the current there is a difference between the densities of electrons in the reservoir and in its perfectly conducting connector to the wire. To a good approximation the density difference is given by

$$\Delta\rho_l = \frac{1}{\pi\hbar v_F} \int dE [f_l(E) - f_r(E)] T(E) = I/(ev_F), \quad (6.5)$$

where the velocity  $v_F$  is assumed to be a constant on the relevant energy interval around  $E_F$ . It was assumed, in deriving Eq. 6.5, that the density of states in the ideal conductor is given by the *incoherent* sum of densities due to electrons incident from the left and right reservoir, respectively. A justification for this might be given in terms of the randomizing dynamical nature of the reservoirs leading to temporal averaging of phase relations, but strictly speaking we are faced here with a basic difficulty which confronts us with an inconsistency of the stationary-state approach.

The chemical potential difference corresponding to  $\Delta\rho_l$  equals

$$\mu_l - \mu'_l = \Delta\rho_l \frac{\partial E}{\partial \rho} \approx \Delta\rho_l \frac{1}{2} \pi\hbar v_F = \frac{\pi\hbar}{2e} I. \quad (6.6)$$

Similarly, we find in this approximation, at the right-hand side

$$\mu'_r - \mu_r = \frac{\pi\hbar}{2e} I. \quad (6.7)$$

From Eqs. 6.6 and 6.7 we obtain

$$V = \Delta\mu/e - \frac{\pi\hbar}{e^2} I, \quad (6.8)$$

which is the same relation as found for infinitesimally small voltages.

The resistance can be written, using Eqs. 6.4 and 6.8,

$$\mathcal{R} = V/I = \frac{\pi\hbar}{e^2} \left[ \frac{1}{\bar{T}} - 1 \right], \quad (6.9)$$

where  $\bar{T}$  is the energy-averaged transmission probability

$$\bar{T} = \int dE W(E) T(E), \quad (6.10)$$

with the energy weight function

$$W(E) = \frac{f_l(E) - f_r(E)}{\Delta\mu}. \quad (6.11)$$

Note that  $W(E)$  is to a good approximation normalized to unity, but not necessarily a non-negative function. At zero temperature,  $W(E)$  is equal to the uniform distribution on the interval  $[\mu_r, \mu_l]$ . If both reservoirs are at equal finite temperature, then  $W(E)$  will be a non-negative distribution.  $W(E)$  will assume negative values as well when the reservoirs are at different temperatures.

Our formula Eq. 6.9 is fully compatible with the results derived by Hu [22] (see Eqs. 8 and 9 in this reference and let the chemical potential difference be much smaller than the Fermi energy). Hu's result is derived with application to larger potential differences in mind. In view of our scope with  $\Delta\mu \ll E_F$ , we prefer to deal with the more suggestive formula Eq. 6.9. Sinkkonen [15] and Eränen and Sinkkonen [16] use linearized Boltzmann expressions for the distribution functions in the connectors at both sides of the wire. Our approach is different in that these connectors are ideally conducting, i.e., scatterer-free regions separating the wire from the reservoirs. Both our Eq. 6.9 and Hu's result [22] are not directly derivable from the results in Refs. [15, 16], presumably because the linearized Boltzmann approximation to the distribution function in the connectors is inconsistent with nonlinear current response.

Equation 6.9 is a surprisingly simple result which takes into account self-averaging effects on the transmission probability through the energy integration in Eq. 6.10. Note that Eq. 6.9 is not an exact result, but nevertheless an extension of existing Landauer formulas. The latter are valid for sufficiently small potentials only, that is, as long as  $|eV| \ll [LN(E_F)]^{-1}$ , where the right-hand side is just the energy scale on which  $T(E)$  will show large fluctuations. Our extension Eq. 6.9 is valid as long as  $|eV| \ll E_F$ . It is easily seen that for  $\mu_l - \mu_r \rightarrow 0$  and  $T_l, T_r \rightarrow 0$  the expression Eq. 6.9 coincides with usual Landauer formula, since in that case we have  $T \rightarrow T(E_F)$ . It will be shown in the next sections that both the statistical and scaling properties of the resistance given by Eq. 6.9 will drastically change with increasing voltage.

### 6.2.3 Numerical results for a Kronig-Penney-type potential

The model system that we will numerically explore in this section, and to which we shall refer as 1D wire, is depicted in Fig. 6.4. The wire has length  $L$  and consists of a chain of  $N$   $\delta$ -functions with equal weights  $H$  placed at irregular positions  $x_j$  along the wire. A constant electric field  $F = V/L$  is assumed to be present inside the wire, where  $V$  is the voltage difference over the wire. In a fully self-consistent treatment charges would pile up in between the  $\delta$ -function scatterers in the presence of a dc current, leading to a much more complicated background potential than the one corresponding to the constant electric field. However, our model must be considered as a first attack of the self-consistency problem in terms of a first-order self-consistent approximation to the potential. Throughout this paper, the emphasis is put on physical principles rather than accurate numbers.

The stationary Schrödinger equation for an electron in the wire ( $0 \leq x \leq L$ ) is

$$\left[ -\frac{\hbar^2}{2m} \frac{\partial^2}{\partial x^2} + \sum_{j=1}^N H\delta(x - x_j) + E_0 + eF(L - x) \right] \psi(x) = E\psi(x), \quad (6.12)$$

where  $E_0 = \frac{1}{2}(\Delta\mu - eV)$ . Solutions to this equation will be obtained by using the transmission-reflection formalism. In this formalism there corresponds to each given energy  $E$  a  $2 \times 2$  complex scattering matrix  $\mathcal{M}$ , which relates the plane-wave

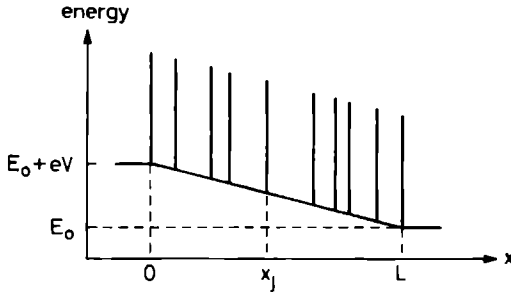


**Figure 6.4** Potential energy of an electron in the model wire used in the numerical calculations. The vertical bars denote  $\delta$ -function potentials  $H\delta(x - x_j)$ , where the positions  $x_j$  are random. The energy  $E_0$  equals  $\frac{1}{2}(\Delta\mu - eV)$  and is chosen such that the potential in the right-hand reservoir equals zero.

amplitudes on one side of the wire to those on the other side (Fig. 6.5)

$$\begin{bmatrix} A_r \\ B_r \end{bmatrix} = \mathcal{M} \begin{bmatrix} A_l \\ B_l \end{bmatrix}, \quad (6.13)$$

where it is noted that the wave numbers  $k_r$  and  $k_l$  are different according to the potential difference  $eV$ .

Quite generally,  $\mathcal{M}$  can be obtained as an ordered product of matrices  $\mathcal{M}_j$  of the individual  $\delta$ -function scatterers and matrices  $\mathcal{T}_j$  which account for variations in amplitude and phase in the areas of constant electric field between the scatterers,

$$\mathcal{M} = \mathcal{M}_N \mathcal{T}_{N-1} \mathcal{M}_{N-1} \cdots \mathcal{M}_2 \mathcal{T}_1 \mathcal{M}_1. \quad (6.14)$$

The scattering matrix for a  $\delta$ -function of weight  $H_j$  and local wave number

$$k_j = [(2m/\hbar^2)(E - \frac{1}{2}\Delta\mu - \frac{1}{2}eV + eFx_j)]^{1/2},$$

where  $x_j$  is the position of the scatterers ( $x_1 = 0$ ;  $x_N = L$ ), can be written as

$$\mathcal{M}_j = \begin{bmatrix} 1 - i\beta_j & -i\beta_j \\ i\beta_j & 1 + i\beta_j \end{bmatrix} \quad (j = 1, \dots, N) \quad (6.15)$$

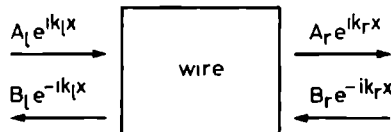


**Figure 6.5** Illustrating the model wire of Fig. 6.4 in the reflection-transmission formalism. The wave vectors are given by  $k_l = [(2m/\hbar^2)(E - E_0 - eV)]^{1/2}$  and  $k_r = [(2m/\hbar^2)(E - E_0)]^{1/2}$ , where  $E_0$  is denoted in Fig. 6.4.

with

$$\beta_j = mH_j/(\hbar^2 k_j). \quad (6.16)$$

The matrix for the translation from  $x_j$  to  $x_{j+1}$  in a constant electric field  $F$  has been derived in a Wentzel-Kramers-Brillouin (WKB) approximation [23],

$$T_j = \begin{bmatrix} \exp(i\phi_{j,j+1}) & 0 \\ 0 & \exp(-i\phi_{j,j+1}) \end{bmatrix}, \quad (6.17)$$

where

$$\phi_{j,j+1} = \frac{2mE_1}{\hbar^2} \left[ L_j + \frac{eF}{4E_1} L_j^2 \right] \quad (L_j = x_{j+1} - x_j), \quad (6.18)$$

and  $E_1 = E - \frac{1}{2}\Delta\mu - \frac{1}{2}eV$ . For the present purpose of giving a qualitative analysis with emphasis on principles, the Wentzel-Kramers-Brillouin approximation of Eq. 6.18 is satisfactory since it adequately accounts for the change in effective path length due to the electric field. Once the matrix  $\mathcal{M}$  has been obtained, the transmission probability  $T$  can easily be determined by [see also section 6.2.4, Eqs. 6.22 and 6.24]

$$T^{-1} = \frac{k_r}{k_l} |\mathcal{M}_{11}|^2. \quad (6.19)$$

The calculational procedure is now as follows. For a wire of given length and given positions of  $\delta$ -functions, we calculate  $T$  using the zeroth-order approximation to the self-consistent voltage  $V = V_0 = \Delta\mu/e$ . Then we calculate the first-order approximation to the voltage difference by using Eq. 6.8, and repeat the scheme until satisfactory convergence for  $V$  is reached. In our calculations it was never necessary to do more than two iterations. With the self-consistent  $V$  we can now calculate the resistance by performing the energy integration in Eq. 6.10 and substitution of the result in Eq. 6.9.

Figure 6.6 shows for a given wire with 10 scattering centers the transmission probability  $T$  versus wave number  $k = (2mE/\hbar^2)^{1/2}$ , where the energy  $E$  varies in a small region. In Fig. 6.6(a) no voltage is applied across the wire whereas in Fig. 6.6(b) the voltage corresponds to 2.5% of the Fermi energy ( $E_F = 2.7$  eV). Both characteristics are for the same geometry of scatterers; the field present in Fig. 6.6(b) has changed all effective lengths, thus leading to a similar, but markedly different  $T$  versus  $E$  characteristics.

The calculated effect of voltage on the resistance at zero temperature is depicted in Fig. 6.7 for three different wires of equal length, equal scatterer density, and equal scatterers but different random positions. Note that the horizontal (logarithmic) scale gives the applied chemical potential difference  $\Delta\mu$  between the reservoirs. The actual voltage difference over the wire is simply related to  $\Delta\mu$  by  $eV = \Delta\mu/(1 + \pi\hbar/e^2\mathcal{R})$ , as follows from Eq. 6.8 after substitution of  $I = V/\mathcal{R}$ . All numerical results on resistance to be presented pertain to the situation with both reservoirs having zero temperature. Hence, the energy weight function  $W(E)$  defined in Eq. 6.11 is just the normalized uniform distribution on  $[\mu_r, \mu_l]$ .

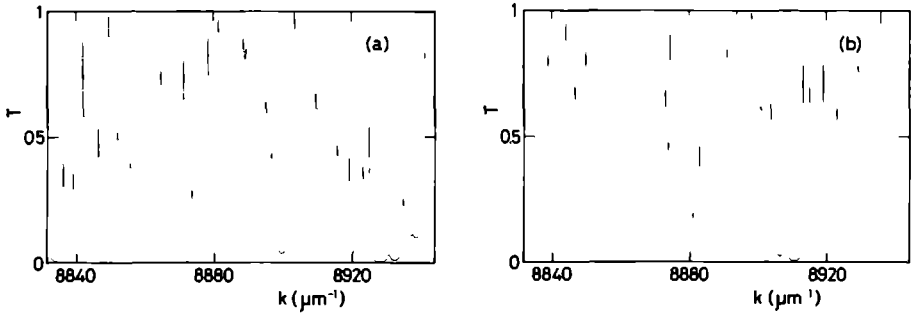


**Figure 6.6** Transmission probability  $T$  vs wave number  $k = (2mE/\hbar^2)^{1/2}$ , where  $E$  is the energy. The wire has length  $L = 1 \mu\text{m}$  and contains 10  $\delta$ -functions at random positions and equal weight  $H = 2.7 \text{ eV}\text{\AA}$ . (a) No voltage difference over the wire. (b) The voltage difference equals 67.5 mV. Due to the electric field present in (b), all effective lengths have changed, resulting in a different  $T$ - $E$  characteristic.

At small voltage values the three resistances differ by as much as an order of magnitude. This phenomenon, i.e., the strong dependence of the resistance at  $V = 0$  on the actual configuration of scattering centers, is a manifestation of the universal conductance fluctuation phenomena [9, 10, 11]. For values of  $\Delta\mu$  well below 1 meV, the resistance is independent of voltage. This is in agreement with the expectation that self-averaging effects should develop when  $\Delta\mu$  becomes of the order of  $[LN(E_F)]^{-1}$ , where the latter is equal to 1.6 meV. For sufficiently large voltage the resistance values tend to approach each other and become less dependent on

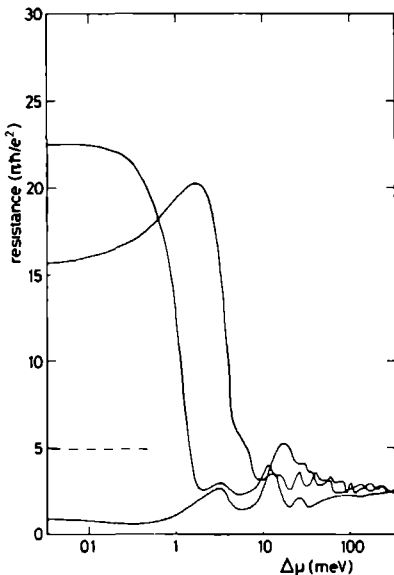


**Figure 6.7** Resistance  $\mathcal{R}$  (in units  $\pi\hbar/e^2$ ) vs applied chemical potential difference for three wires of equal length  $1 \mu\text{m}$ , equal scatterer density ( $10^7 \text{ m}^{-1}$ ), equal scatterers ( $H = 2.7 \text{ eV}\text{\AA}$ ), equal Fermi energy  $E_F = 2.7 \text{ eV}$ , but different random scatterer positions. The dashed line indicates the scale-resistance value equal to 4.95 (in units  $\pi\hbar/e^2$ ) obtained from the ensemble average of  $\ln(1/T)$  at zero voltage.

voltage. In fact, the voltage-induced averaging over energy dramatically improves the statistical distribution of resistance values over ensemble members, that is, the width of the distribution decreases with increasing voltage.

Also indicated in Fig. 6.7 is the scale resistance (dashed line) obtained at zero voltage from averaging  $\ln(1/T)$  over 2000 ensemble members, i.e., the resistance introduced by Anderson *et al.* [7]. The corresponding value of 4.95 (in units of  $\pi\hbar/e^2$ ) is significantly larger than the mean resistance value (2.7 in these units) at large voltage. We conclude that proper inclusion of transmission channel broadening due to finite voltage difference leads to a substantial decrease of the quantum resistance in a disordered system.

#### 6.2.4 Scaling behaviour of the resistance

The scaling analysis of the resistance by Anderson *et al.* [7] is based on the Landauer formula for infinitesimal voltage, i.e., Eq. 6.9 with  $\bar{T}$  equal to  $T(E_F)$ . The resistance values obtained with this formula are known to be highly sensitive to the precise position of the Fermi energy  $E_F$ . This is related to the statistical distribution of  $\mathcal{R}$  values over an ensemble of similar wires not being a regular, but rather a singular one. In fact, it was shown by the authors of Ref. [7] that the ensemble distribution of  $\ln(1 + e^2\mathcal{R}/\pi\hbar) = -\ln T(E_F)$  behaves much more regularly with its mean scaling linearly with length and its variance scaling no worse than linearly.

As far as we know, there exists as yet no quantum-resistance scaling theory which includes the effects of a finite potential difference. The idea, however, of a finite voltage influencing the scaling and other statistical properties of the resistance is most interesting, as it may extend our understanding or alter our view on the relevance of localization in disordered systems.

In the first instance, one might expect that due to self-averaging at larger voltages the resistance would exhibit linear scaling behaviour, in which case we would have a simple Drude formula

$$\mathcal{R} = (\pi\hbar/e^2)L/l_e, \quad (6.20)$$

with  $l_e$  the elastic mean free path, not to be identified with the localization length  $\ell$ . In fact, it is noted in Ref. [7] (see Eq. 19 of this reference) that the result of averaging  $T(E_F)$  may lead to perfect additivity, i.e., linear scaling, of the resistance. However, we will show that linear scaling will not occur when the electrons propagate coherently. The coherence is not destroyed by the field-induced averaging process, nor by having the reservoirs at finite temperature. The coherence can only be destroyed by introducing inelastic scattering events inside the wire.

In order to establish the scaling theory that is valid for sufficiently large potential differences, we first consider a wire segment of length  $L$  as illustrated in Fig. 6.8. The presence of a voltage difference over the system implies different wave numbers  $k_1$  and  $k_2$  at both sides. Therefore, we represent the wave function in region  $j$  ( $j = 1, 2$ ) as

$$A_j \exp(ik_j x) + B_j \exp(-ik_j x).$$

The relation between  $(A_2, B_2)$  and  $(A_1, B_1)$  can be expressed as

$$\begin{bmatrix} A_2 \\ B_2 \end{bmatrix} = \mathcal{M} \begin{bmatrix} A_1 \\ B_1 \end{bmatrix}, \quad (6.21)$$

where  $\mathcal{M}$  denotes a  $2 \times 2$  matrix which summarizes all scattering properties at a given energy. The most general expression of  $\mathcal{M}$  (assuming time-reversal symmetry, i.e., no magnetic scattering centers) is

$$\mathcal{M} = \begin{bmatrix} 1/t & r/t \\ r^*/t^* & 1/t^* \end{bmatrix}, \quad (6.22)$$

where  $t$  and  $r$  are complex-valued quantities which satisfy the current-conservation condition

$$k_1 |t|^2 = k_2 (1 - |r|^2). \quad (6.23)$$

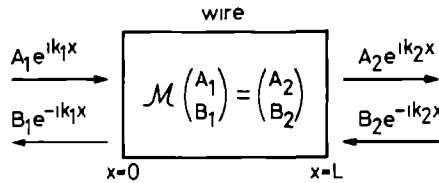


**Figure 6.8** Illustrating the transmission matrix  $\mathcal{M}$ .

In terms of  $r$  and  $t$  the transmission and reflection probabilities are given by

$$\begin{aligned} T_{21} &= |t|^2 = (k_2/k_1)T && \text{(transmission from 2 to 1),} \\ R &= R_1 = R_2 = |r|^2 = 1 - T && \text{(reflection),} \\ T_{12} &= (k_1/k_2)^2 T_{21} = (k_1/k_2)T && \text{(transmission from 1 to 2).} \end{aligned} \quad (6.24)$$

Note that the relationships are a little more complicated than usual due to the occurrence of different wave numbers  $k_1$  and  $k_2$ . In absence of a potential difference we have  $k_1 = k_2$ , and this implies the usual transmission symmetry  $T = T_{21} = T_{12}$ .

Let us now add to the right-hand side of our wire a segment of length  $\Delta L$ , which is sufficiently short for the corresponding transmission probability  $T(\Delta L)$  to be independent of energy in the integration interval in Eq. 6.10 and such that

$$T(\Delta L) = 1 - \Delta R, \quad (6.25)$$

with  $\Delta R \ll 1$ . The transmission probability  $T(L + \Delta L)$  for the total segment with length  $L + \Delta L$  can be written as (see also Ref. [7])

$$T(L + \Delta L) = \frac{T(L)(1 - \Delta R)}{1 + [1 - T(L)]\Delta R + 2\{[1 - T(L)]\Delta R\}^{1/2} \cos \psi}, \quad (6.26)$$

where the angle  $\psi$  expresses phase information collected in the segment of length  $L$ .

Let us consider the  $E$  dependence of the right-hand side of Eq. 6.26. As a consequence of random positions of the scatterers,  $\cos \psi$  will be a heavily fluctuating, more or less random, function of the energy  $E$  in the intergration interval, at least when  $\Delta\mu \gg [LN(E)]^{-1}$ . Moreover, if we assume that the distribution of  $\cos \psi$  values over energy can be considered as uncorrelated to the distribution of  $T(L)$  values over energy, then we can perform two independent averaging procedures in order to arrive at an expression for  $T(L + \Delta L)$  in terms of  $\overline{T(L)}$  and  $\Delta R$ . Assuming that any  $\psi$ -value on the interval  $[0, 2\pi]$  is equally probable, the  $\psi$ -averaging yields

$$\overline{T(L + \Delta L)}^\psi = \frac{T(L)[1 - \Delta R]}{1 - [1 - \overline{T(L)}]\Delta R} \quad (6.27)$$

Performing the energy averaging, i.e., the  $E$  intergration of Eq. 6.27, we can express the result in the lowest order of  $\Delta R$  as

$$T(L + \Delta L) = T(\overline{L}) - T(L)^2 \Delta \overline{R}$$

from which we find that  $1/\overline{T} - 1$  obeys the scaling relation

$$\frac{1}{\overline{T(L + \Delta L)}} - 1 = \frac{1}{\overline{T(L)}} - 1 + \Delta R + \frac{\overline{T(L)^2} - \overline{T(L)}^2}{\overline{T(L)}^2} \Delta R. \quad (6.28)$$

This result is most convenient as it expresses the amount by which the scaling is superlinear in terms of the variance of the  $T(L)$  distribution. Hence, the only possibility for arriving at linear scaling, i.e., classical additivity, is when the variance vanishes. This would imply  $T(L)$  to be fully independent of energy, which is impossible in the context of the model discussed here.

We have not yet been able to find *general* properties for the variance of  $T(L)$ , i.e.,

$$\text{var } T(L) = \overline{T(L)^2} - \overline{T(L)}^2$$

where we recall that the averaging is in fact energy integration according to Eq. 6.10. However, we have deduced properties which the variance should have in order to lead to simple scaling behaviour. To be precise, if the quantity  $f$  defined by

$$f = \frac{\overline{T(L)^2} - \overline{T(L)}^2}{\overline{T(L)}[1 - \overline{T(L)}]} \quad (6.29)$$

would (for some reason not yet understood) be independent of length  $L$ , then Eq. 6.28 can be written as

$$\rho(L + \Delta L) - \rho(L) = [1 + f\rho(L)]\Delta R(L), \quad (6.30)$$

where  $\rho(L) = 1/\overline{T(L)} - 1$ . Transforming Eq. 6.30 into a differential equation, we obtain

$$\frac{d\rho}{dL} = [1 + f\rho(L)]\alpha(L), \quad (6.31)$$



with

$$\alpha(x) = \lim_{\Delta L \rightarrow 0} \frac{\Delta R(x)}{\Delta L}. \quad (6.32)$$

The solution to Eq. 6.31 is given by

$$\rho(L) = \frac{1}{f} (e^{f \int_0^L dx \alpha(x)} - 1). \quad (6.33)$$

The interesting thing about this result is that it can be related to the Anderson localization length  $\ell$  by writing

$$\int_0^L dx \alpha(x) \approx L \langle \alpha \rangle = \lim_{x \rightarrow 0^+} \frac{L}{x} \langle \Delta R \rangle = - \lim_{x \rightarrow 0^+} \frac{L}{x} \langle \ln T(x) \rangle = L/\ell.$$

Hence, we may write Eq. 6.33 as

$$\rho = \frac{1}{f} (e^{fL/\ell} - 1). \quad (6.34)$$

Equation 6.34 is a very interesting scaling relation, since it unifies three different scaling laws into one form. The scaling due to Landauer [6, 7] is obtained by putting  $f = 2$  in Eq. 6.34, while the scale resistance derived by Anderson *et al.* [7] corresponds to  $f = 1$ . In the case here studied we always have  $0 < f < 1$ , as can easily be shown from Eq. 6.29, by using  $0 \leq T(L) \leq 1$ . Of course, the unification aspect of Eq. 6.34 is only of formal significance.

Let us recall that Eq. 6.34 is based on the assumption that  $f$  defined by Eq. 6.29 is independent of length. We were not able to find a general proof for this property, but numerical calculations on model systems of variable length with randomly placed  $\delta$ -function potentials in the presence of a voltage difference indeed indicate that  $f$  is a constant, independent of  $L$ . Moreover, consistent with the above-given theory, the resistance scaling law Eq. 6.34 was numerically confirmed for the model systems.

In Fig. 6.9 the average resistance and standard deviations (six members each) are plotted versus the quantity  $f^{-1}[\exp(fL/\ell) - 1]$ , for the  $L$  values indicated. Here  $\ell = 0.56 \mu\text{m}$  while  $f$  was determined directly from transmission data for each length separately using Eq. 6.29, whereafter all  $f$  values thus obtained were averaged again, yielding  $f = 0.37$ . The data depicted in Fig. 6.9 reveal the remarkably good agreement between the numerical results obtained straightforwardly using Eq. 6.9 and the theoretical scaling prediction Eq. 6.34. It should be mentioned, however, that we have not found the reason why the scaling indicator  $f$ , defined by Eq. 6.29, is a characteristic quantity not depending on length.

### 6.2.5 Summary and conclusions

With the purpose of studying the voltage-dependent resistance of a one-dimensional disordered system, we have derived a straightforward extension of the Landauer resistance formula. In a model system with  $\delta$ -function scattering centers and

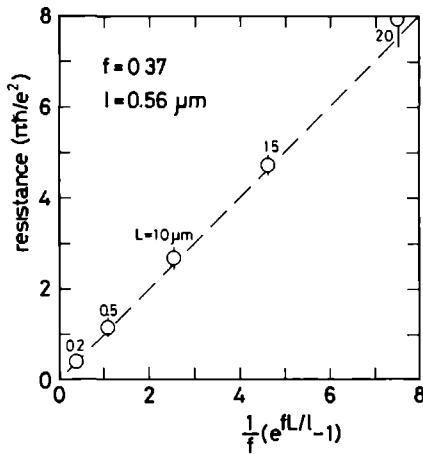


**Figure 6.9** Comparison between calculated resistance values (vertical axis) and the predictions based on the high-voltage scaling law (Eq. 6.34) (horizontal axis), for systems of several different lengths ranging from 0.2 to 2  $\mu\text{m}$  as indicated. The scatterer density is  $10^7 \text{ m}^{-1}$  in all cases. The scaling indicator  $f$  was determined numerically (see text) at  $f = 0.37$ .

a constant electric field we have found significant dependences of the resistance on increasing voltage, ranging from decreasing resistance fluctuations to an appreciable decrease of the scale resistance. A finite voltage difference introduces self-averaging over energy and, therefore, may lead to a sharply peaked and well-behaving resistance distribution over ensemble members. Exponential scaling of the mean resistance with system length at large voltage difference has been obtained while the corresponding scale length is markedly larger than the zero-field scale length, i.e., the localization length. A scaling theory has been presented which is valid in the large voltage regime where sufficient self-averaging occurs, i.e.  $eVN(E_F)L \gg 1$ . A simple universal scaling formula is derived which combines the existing exponential scaling laws and the one here obtained in one formal expression.

Let us discuss how our findings compare with reported results on electric-field-induced effects in the stationary state [12, 13, 14, 20]. In none of these works the aspect of intergration over a finite energy interval was considered; all references discuss the influence of an electric field on the localization of wave functions. They agree that an increasing electric field induces a crossover from exponential localization at zero field to power-law localization at large fields. Refs. [13, 20] have also dealt with the field-dependent resistance which they evaluated, however, using the zero-field Landauer formula. It is not surprising then that the scaling of the resistance thus obtained strongly resembles the above cross-over from exponential scaling at zero field to power-law at large fields.

The reported field-induced effects in the transmittivity typically are  $eV/E_F$  effects, that is, one needs to consider rather large fields in order to see anything happen. In our view, the discussion of the influence of these effects on the resistance suffers from incompleteness so long as the intrinsic energy averaging associated with a finite voltage is not included. That is what we have done here and we have shown that the averaging leads to substantial effects on the resistance which typically go with  $eVN(E_F)L$ , where  $N(E_F)$  is the density of levels per unit length at the Fermi energy. Hence, since  $N(E_F)L \gg E_F^{-1}$ , the voltage-averaging effects and the resis-

tance saturation predicted by us will have developed long before a power-law scaling will become manifest. The approach followed by us is closely related both to the work by Sinkkonen [15] and Eränen and Sinkkonen [16] and the work by Hu [22]. However, these authors seem to have had other applications in mind as they do not mention the self-averaging in a disordered system due to a finite voltage difference.

Finally, let us attempt to extrapolate our findings to real, i.e., 3D systems. One has to be careful in doing so, because 1D systems are very special in view of their discrete properties. As compared to 1D systems, 2D and 3D systems already have intrinsic self-averaging behaviour, which is due to the naturally available energy degeneracy, even for small voltage. This is the main reason for strong localization in a random potential in 2D or 3D being hard if not impossible to realize. One aspect of electronic coherence which is nevertheless present in real samples is the occurrence of universal conductance fluctuations, i.e., the conductances in real, macroscopically identical, samples show large variations from one sample to the other in a universal manner. We may expect from our findings for 1D systems that these sample-to-sample variations will diminish and gradually disappear due to the energy averaging on increasing the voltage difference. This is not to say that the conduction will become diffusive, since there will be a quantum-interference contribution to resistance which cannot be accounted for in a classical Drude-like approach in which subsequent scatterings are uncorrelated events.

### **Acknowledgement**

The authors would like to thank Professor W. van Haeringen for fruitful discussions on the research presented here and for reading the manuscript.

## 6.3

# Carrier dynamics in a ring, Landauer resistance and localization in a periodic system<sup>1</sup>

Daan Lenstra<sup>2,3</sup>, Willem van Haeringen<sup>2</sup>, and Richard T.M. Smokers

### Abstract

We lay the connection between the carrier dynamics in a small 1D loop driven by a time-dependent flux and stationary quantum tunneling through a 1D periodic structure between two reservoirs. It is explicitly shown that the phenomenon of dynamical quasi-randomization of phases in the loop, which leads, among other things, to current saturation behaviour, is physically equivalent to the phenomenon of field-induced quasi-disorder in the periodic structure between reservoirs. In both cases the respective types of disorder lead to apparent localization effects on the resistance. A new and independent confirmation of Landauer's  $R/T$  formula is obtained.

---

<sup>1</sup>This section has been published in *Physica A* **182** (1990) 405.

<sup>2</sup>Department of Physics, Eindhoven University of Technology, P.O. Box 513, 5600 MB Eindhoven, the Netherlands.

<sup>3</sup>present address: Department of Physics and Astronomy, Free University, De Boelelaan 1081, 1081 HV Amsterdam, the Netherlands.

In this paper we will point out the physical connection between flux-induced dynamical current effects in small 1D loops [1, 2, 21, 24, 25, 26] and the Landauer theory of electrical conductance based on quantum mechanical tunneling through a 1D system between two reservoirs held at different chemical potentials [4, 6, 7, 8, 27, 28]. The ring is a very attractive system from the theoretical point of view, enabling us to study electrical conductance at  $T = 0$  K in a Hamiltonian quantum system without the necessity of introducing randomizing reservoirs with complicated and basically unknown temporal behaviour. On the other hand, very important developments of ideas and concepts concerning electrical conduction at low temperatures in mesoscopic systems are based on stationary considerations which make essential use of reservoirs. Among these developments we mention Landauer's theory of quantum resistance [6] and the scaling theory of localization [7]. In view of this there is an obvious need for unification of the seemingly different approaches.

It will be shown that it is indeed possible to lay the – unifying – connection between the current behaviour in the two kinds of systems, and we will elucidate the new and essential ingredients in their comparison.

The essential ingredients of the model for the closed ring are given in Refs [1, 2, 17]. We will consider the 1D ring with the circumference  $L$  enclosing a magnetic flux which for  $t \geq 0$  linearly increases in time, thus producing a constant electromotive force  $FL$ , where  $F$  is the electric field strength. The electrons in the ring are free except for the presence of one single delta-function potential  $U\delta(x)$  of weak strength such that the miniband structure [1, 17] is characterized by identical gaps  $E_g$ , which are small compared to the average spacing of levels near the Fermi energy.

If  $F$  is large enough to have Zener tunneling through the minigaps with probability almost equal to unity, the time evolution of the carriers on a time scale including many Zener tunneling events shows similarities to the evolution in the case the elastic collision events would be uncorrelated to each other. Numerical current calculations [1, 2] show the occurrence of current saturation on a mean value proportional to the applied electromotive force. The current saturation is shown to be strongly correlated with the occurrence of quasi-phase randomization in the wave functions of the electrons carrying the current. The work of Blatter and Browne [25] and Gefen and Thouless [26] indicates that after time intervals much longer than considered by Refs [1, 2], i.e. a few times the inverse Zener-tunneling backscatter rate, the mean current clearly tends to relax back to zero, an effect that has been related to localization in energy (or time) [25, 26].

The quasi-randomization of phases which occurs in the time-dependent wave functions [1, 2] has, to a certain content, the effect of decorrelating subsequent scattering events and thus seems to imply a kind of "Stosszahlansatz". Therefore, we expect the time-dependent 1D Boltzmann equation to give an adequate description of the electrical current development in the ring, at least during time scales short enough to stay away from dynamical localization [25, 26]. In the Boltzmann approach, extensively discussed in Ref [29], the current appears to saturate at the

time-independent value

$$I_{sat} = \frac{e^2 FN}{2mLW}, \quad (6.35)$$

where  $N$  is the total number of electrons and  $W$  is the backscatter rate. For not too small values of  $F$ , i.e.  $F \gg \pi E_g^2/4e\hbar v_F$ , where  $v_F$  is the Fermi velocity,  $W$  is given by [1, 17, 18]

$$W = \frac{E_g^2 L}{4\hbar^2 v_F}. \quad (6.36)$$

The saturation level (Eq. 6.35) is reached in a few times  $W^{-1}$ .

In Fig. 6.10 the various saturated current levels as obtained by the method described in Refs. [1, 2] for a case in which all Zener probabilities are equal, are compared with the corresponding Boltzmann predictions (Eq. 6.35). The numerically obtained values scatter somewhat, but significantly below the Boltzmann predictions. As we will show below, the deviation between Eq. 6.35 and the field dependent saturation level as obtained by the method described in Refs. [1, 2] can be attributed to the onset of *dynamical localization* which takes place on longer time scales [25, 26] and which is principally missed in the Boltzmann approach. The quantitative analysis of this multiple-scattering localization correction will be delayed, however, until we have made the full connection with quantum mechanical tunneling through a chain of scattering centers. At this point it is useful to refer to a discussion in Ref. [21] in which Landauer argues that it would be misleading to assign the word *resistance* to the ratio of  $FL$  and a dynamically obtained saturation current since "an obviously Hamiltonian system has no dissipation". However, in our opinion it is justified to use the notion of resistance in the present context since current saturation in our model system goes hand in hand with the phenomenon of *phase randomization* [2]. This leads us to suggest that in our ring system – in which external reservoirs are obviously missing – the role of reservoirs is taken over by the ring itself by means of a process in which phases are dissipated.

The resistance value predicted by the above mentioned Boltzmann approach is given by

$$\mathcal{R}_B = \frac{FL}{I_{sat}} = \frac{\pi\hbar m^2 |U|^2}{e^2 \hbar^4 k_F^2}, \quad (6.37)$$

where we have used Eq. 6.36 with  $v_F = \hbar k_F/m$  and  $E_g = 2|U|/L$ . The result (Eq. 6.37) coincides with the Landauer resistance  $(\pi\hbar/e^2)(1-T)/T$ , where  $T$  is the transmission probability for tunneling through the  $\delta$ -function potential at the Fermi level, as can easily be verified from elementary considerations. Therefore, apart from the localization corrections to be discussed in detail later on and which can be related to multiple transmissions, the current calculations of Refs. [1, 2] yield a resistance value for one localized scatterer in a ring which is in agreement with Landauer's formula. In this connection, confusion may arise about whether the resistance is given by  $1/T - 1$  (also written  $R/T$ ), or by  $1/T$ . The latter result is obtained in experiments, notably by van Wees *et al.* [30], but refers to situations in which the conductor has lower dimension than the reservoirs (one and two dimensional in Ref.

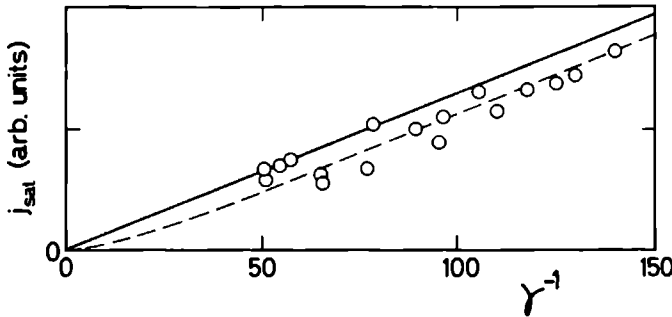


**Figure 6.10** Electrical current saturation level  $j_{sat}$  vs. normalized electromotive force ( $\gamma^{-1}$ ) in a small 1D ring with one localized scatterer. For a ring with  $1 \mu\text{m}$  circumference, 100 horizontal scale units would correspond to approximately 20 mV. Circles represent the result of numerical current calculations as described in Refs. [1, 2]. The straight solid line is based on the Boltzmann result (Eq. 6.37). The dashed line is obtained from the scaling analysis to be discussed further on.

[30]). In such cases, disregarding the feedback of current on the effective chemical potential difference at both sides of the conductor does not lead to incorrect results. On the other hand, if both the reservoirs and the conductor are one-dimensional, as is assumed throughout this paper, it is essential to follow Landauer and properly take into account the self-consistent feedback effect, leading to  $1/T - 1$ .

Recently, Gefen and Thouless [26] have shown, by using a Fourier-transformation technique, that the dynamics of electrons in the ring can be mapped onto that of stationary wave transmission through a disordered chain. Here we will elucidate the physics involved. We will consider a one-dimensional periodic chain consisting of  $M$  identical  $\delta$ -function scatterers at distances  $L$  apart and connect this periodic structure (the repeating unfolded ring) at both sides to reservoirs. These reservoirs are assumed to be at chemical potentials of such magnitudes that the voltage equals  $MLF$ , where  $F$  is the field strength applied in the ring situation. The resistance of the periodic structure can be obtained using the recently derived [27, 28] generalized Landauer formula in which the energy-averaged transmission probability around the Fermi level is the relevant quantity.

Apart from the energy averaging which leads to interesting effects by itself [27, 28], the following more subtle effect will now play a crucial role: due to the finiteness of  $F$ , the periodicity of the chain has been removed in a noticeable way. Except for very special values of the electric field, to be discussed below, the electrons will essentially experience a quasi-random system. This can be shown by considering the total phase accumulated between scatterers  $j$  and  $j + 1$  (Fig. 6.11), i.e.

$$\phi_i = \int_{jL}^{(j+1)L} dx \left[ \frac{2m}{\hbar^2} (E + eFx) \right]^{1/2}$$

$$\simeq \left(\frac{2mE}{\hbar^2}\right)^{1/2} \left[1 + \frac{eFL}{4E}(2j + 1)\right]L, \tag{6.38}$$

where it is noted that  $E \simeq E_F$  and  $eFL \ll E_F$ . Hence, the field-induced extra phase on the  $j$ th interval can be written  $\Delta\phi_j = eFL^2(2j + 1)/2\hbar v_F$ . Once the voltage drop per scatterer,  $FL$ , becomes of the order  $\pi\hbar v_F/eL$  or larger, the  $\Delta\phi_j$  values ( $j = 0, \dots, M - 1$ ) will form, after reduction to the interval  $[0, 2\pi]$ , a quasi-random set, *as if the scatterers were at random positions*. This spatial phase randomization effect has now to be compared with the dynamical randomization effect in the ring system [1, 2].

In order to make this comparison, let us first discuss the above-mentioned exceptional electric field values for which the system does not lead to random phases. If we express  $F$  as

$$F = \frac{2\pi\hbar v_F}{eL^2} \tau, \tag{6.39}$$

with  $\tau$  a dimensionless number, we have  $\Delta\phi_j = (2j + 1)\pi\tau$  and this implies that for integer or simple rational values of  $\tau$  in Eq. 6.39, such as  $\tau = \frac{1}{4}, \frac{1}{3}, \frac{1}{2}, 1, 2, 3, \dots$ , electrons near the Fermi level experience the system as periodic. The striking feature is that these special field values coincide with the values for which the dynamical current evolution in the ring shows no saturation [1, 2], where the latter is attributed to the *lack of dynamical* phase randomization! Indeed, from Eq. 2 of Ref. [2], in which  $n$  assumes integer values around  $N = (2/\pi)k_FL$ , we find that the  $F$ -value of Eq. 6.39 leads in good approximation to the dynamical phase angles  $2\pi s/r$  with  $s = 0, 1, 2, 3, \dots$ . Again, for fixed integer or simple rational value of  $\tau$  this set contains, after reduction to the interval  $[0, 2\pi]$ , a restricted number of equidistant

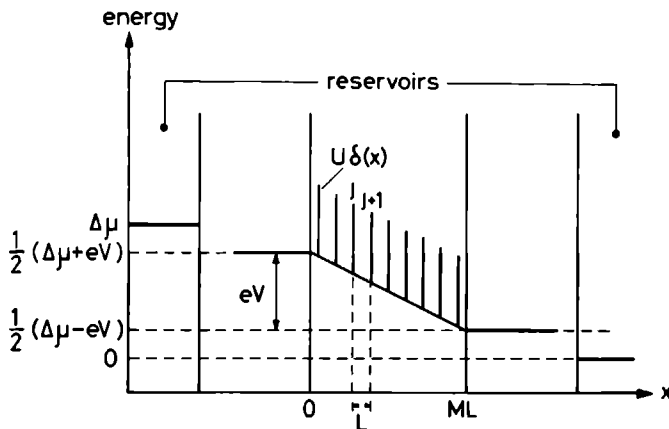


**Figure 6.11** Potential felt by an electron in the configuration consisting of the model wire, to be identified with the repeatedly unfolded ring, and the two reservoirs at chemical potentials differing by  $\Delta\mu$ . The vertical bars denote  $\delta$ -function potentials  $U\delta(x - x_i)$  where the positions  $x_i$  are periodic.



angles. For other values of  $\tau$ , however, the dynamical phase angles form a quasi-random distribution on  $[0, 2\pi]$ .

When actually calculating the quantum resistance  $\mathcal{R}$  of the 1D system sketched in Fig. 6.11 in the case of a finite voltage difference it has been shown in Refs. [27, 28] that  $\mathcal{R} = (\pi\hbar/e^2)(1/\bar{T} - 1)$ , where  $\bar{T}$  is the energy-averaged transmission probability being equal to  $\bar{T} = (1/\Delta\mu) \int_{E_F - \Delta\mu}^{E_F} T(E) dE$ . Fig. 6.12 shows a number of plots for resistance vs. chemical potential difference. The curves in Fig. 6.12a pertain to disordered systems and are taken from Ref. [28]. The curve in Fig. 6.12b concerns the periodic system. For small voltages the resistance value is low, for  $\Delta\mu \geq \pi\hbar v_F/L$  ( $\simeq 20$  mV in Fig. 6.12) the resistance of the periodic system approaches the two other resistances, but shows sharp minima at discrete voltages. These latter correspond to the special field values for which the corresponding  $\tau$ -values in Eq. 6.39 are indicated in the figure.

We will now proceed towards a *quantitative* connection between the dynamical effects in the ring and the above mentioned resistance effect in a periodic system. The calculations of Fig. 6.10 for the saturated current levels were performed for typical time intervals of  $100t_p$  where  $t_p = \pi\hbar/eFL$ . The round-trip time for an electron at the Fermi level equals  $L/v_F$  and it can easily be shown for the data of Fig. 6.10 that the number of round-trips  $N_t$  during the relevant time interval  $100t_p$  equals  $N_t = 10^6\gamma/\pi$ , where  $\gamma$ , defined in Refs. [1, 2], is a dimensionless measure for the inverse field strength. In Fig. 6.10 the  $\gamma$ -values range from  $6 \times 10^{-3}$  to  $10^{-1}$  and this implies that electrons near the Fermi level have made  $2 \times 10^3$  to  $3 \times 10^4$  round-trips. The transmission probability for the  $\delta$ -function potential of Fig. 6.10

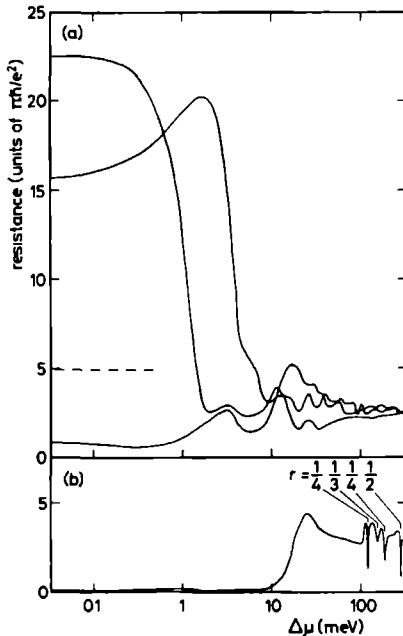


**Figure 6.12**

Resistance vs. chemical potential difference for three different wires of equal length ( $1 \mu\text{m}$ ), equal number of scatterers (10), equal scatterers  $U = 2.7 \text{ eV}\text{\AA}$ , equal Fermi energy ( $E_F = 2.7 \text{ eV}$ ), but different scatterer positions. The curves in (a) are for disordered configurations and are taken from Ref. [28]. The curve in (b) is for the periodic system.

can be shown to be equal to  $T = (1 + \beta)^{-1}$ , with  $\beta = (\pi^2/4) \times 10^{-4}$ . We will compare this with the current behaviour in a chain with reservoirs of length  $N_t L$  with  $N_t$   $\delta$ -function scatterers. According to the scaling theory developed in Ref. [28] the resistance in such a system can be written as

$$\mathcal{R}(N_t L) = \frac{\pi \hbar}{e^2} \frac{1}{f} (T^{-f N_t} - 1), \quad (6.40)$$

where the scaling factor  $f$  has a value between 0 and 1, but is, apart from this, an as yet unknown quantity [28] which depends on the type of backscatterer but not on the total system length. Eq. 6.40 gives rise to a ring resistance  $\mathcal{R} = \mathcal{R}(N_t L)/N_t$  and this implies that the electrical current in the ring can be written as

$$I = \frac{f N_t \beta}{(1 + \beta)^{f N_t} - 1} \frac{FL}{\mathcal{R}_L}, \quad (6.41)$$

where  $\mathcal{R}_L$  is the Landauer resistance for the single  $\delta$ -function scattering potential,  $\mathcal{R}_L = \pi \hbar \beta / e^2$ . The factor in front of  $FL/\mathcal{R}_L$  in Eq. 6.41 is exclusively due to the localization effect, its value depends on  $F$  through the number of round-trips  $N_t$ .

The dashed curve in Fig. 6.10 is obtained from Eq. 6.41 by assuming for  $f$  the value 0.2. In the limit of vanishingly small  $F$  we have  $N_t \rightarrow \infty$ , implying the prefactor in Eq. 6.41 to vanish. In fact, if Eq. 6.41 is taken seriously in the limit  $F \rightarrow 0$  all derivatives of  $I$  become zero at  $F = 0$ . This is related to the general property of the linear-response conductivity in any disordered 1D system to vanish or to be at least ill defined [18], no matter how weak the disorder. For larger fields it can easily be verified that, as long as  $f N_t \gg 1$ , Eq. 6.41 gives rise, in very good approximation, to a linear relation  $I$  vs  $F$  which is, however, shifted downwards by a constant amount with respect to the original Boltzmann result.

In conclusion, by having argued that Eq. 6.41 is valid not only for a chain between two reservoirs but also for a Hamiltonian ring system driven by a field, we have laid a connection between two seemingly different theoretical approaches to quantum elastic scattering resistance in a simple system. The essential and new element needed to bridge the gap between the two different descriptions is the concept of phase disorder in a *periodic* system when a finite voltage stands over both ends of the system. This implies quantum resistance, localization and scaling effects similar to nonperiodic systems subject to a finite voltage. A closely related effect occurs in the ring, where the electrons circling around the loop, while being accelerated, feel a nonperiodic array of scatterers. This causes dynamical phase randomization and leads to saturation of the time-dependent expectation value of the current. Apart from the localization correction, the 1D Boltzmann equation gives an adequate, though smoothed, description of the current development. From the number of round-trips needed to reach saturation, the localization correction has been estimated and this was shown to explain the difference between the Boltzmann prediction and the results of quantum dynamical calculations.

It is important to realize that the model system studied here is very special and extremely simple. On the one hand one may have severe doubts as to whether

conclusions based on such a model make any sense with regard to real systems; on the other hand, the richness of the structure which emerges in the dynamical and/or stationary transport behaviour forces us to believe that the significance of our simple system is much greater than just leading to solvable dynamics. In this paper, we have not attempted to deal with more general scattering potentials. Keeping the model simple as we did enabled us to communicate our points as clear as possible, we think. Our main conclusion will not drastically depend upon the particular shape of the scattering potential for the following reason: Our considerations involve finite time scales (in case of the ring) or finite lengths (in case of the tilted lattice). This implies that the detailed structure of the scatterers will not be fully exploited. Therefore, a delta function is a good model for a scattering potential whose dimension is small with respect to the particle wavelength involved.

Some further interesting conclusions can be drawn from the analysis here presented. Firstly, we have given a new and independent derivation of the Landauer formula for the resistance of a single scatterer and obtained first evidence for its significance in situations without reservoirs, where the conductance is *not* a consequence of the incident carrier flux [6, 31]. We therefore claim that the dynamics of the system is such as to give it reservoir properties to a certain extent, as a result of chaotic dynamics. Of course, the time intervals during which this makes sense are short, but nevertheless they are identifiably longer than the elastic collision time [1, 2]; on longer time scales persisting correlations lead to localization effects here discussed. Secondly, we have shown that elastic scattering *alone* can be a physical *source of resistance* for which reservoirs and energy dissipation are *not* essential ingredients. This may be of helpful use towards the full understanding of quantum-mechanical resistance in submicron systems.

### Acknowledgement

We thank Mr. Bart Somers for carrying out the calculations in Fig. 6.10.

## References

1. D. Lenstra, H. Ottevanger, W. van Haeringen, and A.G. Tjihuis, *Phys. Scr.* **34** (1986) 438.
2. D. Lenstra and W. van Haeringen, *Phys. Rev. Lett.* **57** (1986) 1623.
3. D.J. Thouless, *Phys. Rep. C* **13** (1974) 93.
4. P. Erdöss and R.C. Herndon, *Adv. Phys.* **31** (1982) 65.
5. J. Hertz, *Phys. Scr.* **T10** (1985) 1.
6. R. Landauer, *Phylos. Mag.* **21** (1970) 863.
7. P.W. Anderson, D.J. Thouless, E. Abrahams, and D.S. Fisher, *Phys. Rev. B* **22** (1980) 3519.
8. M. Büttiker, Y. Imry, R. Landauer, and S. Pinhas, *Phys. Rev. B* **31** (1985) 6207.
9. B.L. Al'tshuler and D.E. Khmel'nitskii, *Pis'ma Zh. Eksp. Teor. Fiz.* **42** (1985) 291, [*JETP Lett.* **42** (1985) 359].
10. Y. Imry, *Europhys. Lett.* **1** (1986) 249.
11. P.A. Lee, A. Douglas Stone, and H. Fukuyama, *Phys. Rev. B* **35** (1987) 1039.
12. C.M. Soukoulis, J.V. José, E.N. Economou, and P. Sheng, *Phys. Rev. Lett.* **50** (1983) 764.
13. F. Delyon, B. Simon, and B. Souillard, *Phys. Rev. Lett.* **52** (1984) 2187.
14. A. Brezini, M. Sebbani, and F. Behilil, *Phys. Status Solidi B* **138** (1986) K137.
15. J. Sinkkonen, in: *Physical Problems in Microelectronics*, ed. J. Kassabov, (World-Scientific, Singapore, 1985), 380.
16. S. Eränen and J. Sinkkonen, *Phys. Rev. B* **35** (1987) 2222.
17. D. Lenstra and W. van Haeringen, *J. Phys. C* **14**, (1981) 5293.
18. D. Lenstra and W. van Haeringen, *Physica B* **128** (1985) 26.
19. R. Landauer, *Phys. Rev. B* **33** (1986) 6497.
20. G.V. Vijayagovindan, A.M. Yanyannavar, and N. Kumar, *Phys. Rev. B* **35** (1987) 2029.
21. R. Landauer, *Phys. Rev. Lett.* **58** (1987) 2150; D. Lenstra and W. van Haeringen, *Phys. Rev. Lett.* **58** (1987) 2151.
22. P. Hu, *Phys. Rev. B* **35** (1987) 4078.
23. E. Merzbacher, *Quantum Mechanics* (Wiley, New York, 1961), chapter 7.
24. Y. Gefen, E. Ben-Jacob and A.O. Caldeira, *Phys. Rev. B* **36** (1987) 2770.
25. G. Blatter and D.A. Browne, *Phys. Rev. B* **37** (1988) 3856.
26. Y. Gefen and D.J. Thouless, *Phys. Rev. Lett.* **59** (1987) 1752.
27. D. Lenstra and R.T.M. Smokers, *Physica B* **151** (1988) 503.
28. D. Lenstra and R.T.M. Smokers, *Phys. Rev. B* **38** (1988) 6452.
29. D. Lenstra and W. van Haeringen, *J. Phys. C: Solid State Phys.* **14** (1981) L819.
30. B.J. van Wees, H. van Houten, C.W.J. Beenakker, J.G. Williamson, L.P. Kouwenhoven, D. van der Marel, and C.T. Foxon, *Phys. Rev. Lett.* **60** (1988) 848.
31. R. Landauer, in: *Localization, Interaction and Transport Phenomena*, eds. B. Kramer, G. Bergmann, and Y. Bruynserade, (Springer, Heidelberg, 1985), p. 38.



## Summary

This thesis deals with a number of effects associated with electron tunneling in solid-state geometries. Tunneling can be used as a tool to study e.g. the density of states of superconductors, but is also an interesting object of study in its own right, especially in mesoscopic systems where single-electron charging effects and quantum interference may come into play.

Chapter 1 elucidates the basic concepts of tunneling and discusses several approaches to the theoretical description of electron tunneling in junctions with normal-metal or superconducting electrodes. It is emphasized that the two methods, which are widely applied to the planar evaporated-junction geometry, may have serious shortcomings when applied to the point-contact geometry employed in the experimental work presented in chapters 3, 4 and 5 of this thesis. Exact wave matching can be applied to effectively one-dimensional systems, and is able to deal with arbitrary barriers. The transfer-Hamiltonian method is a first order perturbation approach, applicable to three-dimensional systems including many-particle effects. It is however restricted to barriers with a small transmission coefficient and to low applied voltages. The circumstances encountered in point-contact tunnel geometries, especially in the case of the Scanning Tunneling Microscope (STM), can go beyond the limits of validity of the above mentioned theories. Recent developments towards a general theory of STM-tunneling are discussed. Formal approaches using Green's function techniques, such as the Keldysh formalism, seem most promising.

In ultrasmall tunnel junctions the intrinsic junction capacitance  $C$  can become so small that, at low enough temperatures, the tunneling is completely dominated by the electrostatic charging energy  $e^2/2C$ . As a result, tunneling of a single electron may have a significant effect on the junction voltage and on the probability of subsequent tunnel events. Chapter 2 is devoted to the theoretical description of these single-electron charging effects, with the emphasis on junctions between normal metals.

A major consequence of the small junction capacitance is the occurrence of a so-called Coulomb blockade, which manifests itself in the current-voltage characteristics as a combination of offset linear asymptotes and a suppressed current at low voltages. This Coulomb blockade is only visible if the junction is properly decoupled from stray capacitances in the environment. This can be achieved either by series connection with a large impedance close to the junction, or by incorporating the junction in a network of other small tunnel junctions.

For the case of connection to a series impedance three regimes can be distinguished. In the ideal case, where the series resistance is much larger than the tunnel resistance, the junction is current biased and for small current levels almost coherent oscillations (so-called Single-Electron Tunneling or SET-oscillations) of the junction

voltage are predicted. This regime is described by the so-called "orthodox" theory of Averin and Likharev. The ideal case as well as the intermediate regime, where the series and junction resistances are comparable, can be analyzed with the aid of semi-classical Monte Carlo simulations of the time-development of the junction charge. The intermediate regime is characterized by incoherent fluctuations of the junction voltage. In the third regime, where the series resistance is much smaller than the tunnel resistance, quantum fluctuations and the interaction of a tunneling electron with the electromagnetic modes of the environment have to be taken into account. If the series resistance is larger than the resistance quantum  $\pi\hbar/2e^2$  this regime also displays a Coulomb blockade which is however conceptually different from the one in the ideal current biased limit.

The simplest non-trivial network is a series connection of two small tunnel junctions called the double junction system. In this case the central electrode connecting both junctions is an isolated island, which can only be charged by integer multiples of the elementary charge  $e$ . Depending on the ratios of capacitances and resistances of the two junctions this system is predicted to exhibit a current-voltage characteristic with a regular array of steps and kinks commonly denoted as the Coulomb staircase. The positions of these steps and kinks can be tuned by the voltage on some capacitive coupling to the central electrode (Single-Electron Transistor) or by the presence of localized charges in the neighbourhood of the island.

Chapter 2 also gives a short survey of the present experimental status of the field as far as nanolithographically defined systems are concerned.

The experimental aspects of charging effects in single junctions established with point-contact techniques are presented in chapter 3. Taking the observation of offset asymptotes and current suppression near the origin of the current-voltage characteristics as a working definition for the possible presence of a Coulomb blockade, we find strong indications for charging effects in point-contact tunnel junctions on a wide variety of sample materials. As decoupling mechanisms of the sort discussed in chapter 2 are not present in these junctions, we propose a novel decoupling mechanism, involving hopping conductance through localized surface or impurity states at the tip or sample surface. This hypothesis is tested in measurements with point-contact tunnel junctions on arsenic-doped silicon samples in which charge transport at low temperatures is completely governed by hopping. These junctions indeed exhibit Coulomb blockade features, which can be influenced by surface treatment, but are independent of the series resistance seen by the junction. We also have experimental indications that the ideal current biased situation can be realized by tunneling into metallic islands deposited on top of the doped silicon.

The double junction system is experimentally studied in chapter 4. Point-contact junctions on various samples containing isolated grains clearly display the Coulomb staircase, including the predicted influence of localized charges in the environment of the central electrode. In most cases the particle constituting the central electrode is still so large that the density of states can be assumed constant. Some speculations are presented concerning future measurements on extremely small organometallic clusters in which we do expect to see the effects of a discrete elec-

tronic structure.

In chapter 5 results are presented of spectroscopic measurements on high- $T_c$  superconductors using point-contact tunneling. The aim of these measurements is to resolve the superconducting density of states of these materials. For both  $\text{YBa}_2\text{Cu}_3\text{O}_{7-\delta}$  and  $(\text{Pb}_x\text{Bi}_{1-x})_2\text{Sr}_2\text{CaCu}_2\text{O}_8$  reasonable BCS-like characteristics are observed in normal metal-superconductor as well as in superconductor-superconductor junctions, albeit with unexpected and as yet unexplained broadening. In the case of ceramic and polycrystalline  $\text{YBa}_2\text{Cu}_3\text{O}_{7-\delta}$  the inferred gap values are all in the interval  $2\Delta/k_B T_c \approx 3-7$ , and scatter significantly above the BCS weak-coupling prediction of 3.5. For tunneling into the  $ab$ -plane of  $(\text{Pb}_x\text{Bi}_{1-x})_2\text{Sr}_2\text{CaCu}_2\text{O}_8$  single crystals we find an unambiguous value of  $2\Delta/k_B T_c \approx 8$ . Apart from these gap-characteristics we have also observed critical current and Josephson-effects, charging effects, and negative differential resistance features. The occurrence of the latter two effects is associated with the poorly defined surface properties of the materials.

Chapter 6 contains a theoretical study of quantum resistance and localization in one-dimensional disordered mesoscopic systems. In these systems, where the inelastic scattering length exceeds the sample dimensions, conductance is fully determined by coherent wave propagation and quantum interference. Transmission and reflection coefficients are calculated using the wave-matching procedure mentioned above. In the first part of this chapter a novel generalized Landauer formula is derived and used to study the voltage dependent resistance in a one-dimensional wire with disordered potential. A finite voltage difference is shown to introduce energy integration and self-averaging behaviour. Resistance fluctuations as a function of voltage and wire length are seen to decrease with increasing voltage. In spite of the self-averaging, the mean resistance at large voltages turns out to scale superlinearly with length. The second part of chapter 6 lays a connection between the carrier dynamics in a small one-dimensional loop driven by a time dependent magnetic flux and stationary quantum tunneling through a one-dimensional wire with periodic potential between two reservoirs. It is shown that the phenomenon of dynamical quasi-randomization of phases in the loop, which leads, among other things, to current saturation behaviour, is physically equivalent to the phenomenon of field-induced quasi-disorder in the periodic structure between two reservoirs. In both cases the respective types of disorder lead to apparent localization effects on the resistance. Furthermore a new and independent confirmation of Landauer's  $R/T$  formula is obtained, which is not depending on the presence of reservoirs.





## Samenvatting

Dit proefschrift behandelt een aantal effecten die alle te maken hebben met het tunnelen van electronen in vaste-stofgeometrieën. Het tunnel effect kan worden gebruikt als een instrument om bijvoorbeeld de toestandsdichtheid van supergeleiders te bestuderen, maar is ook een interessant studie-object van zichzelf, vooral in mesoscopische systemen waar één-electron oplaadeffecten en quantum-interferentie een rol kunnen gaan spelen.

Hoofdstuk 1 beschrijft de conceptuele basis van het tunnелеffect en bespreekt een aantal alternatieven voor de theoretische beschrijving van electron-tunnelen in juncties met normaal-metalen of supergeleidende elektroden. Benadrukt wordt dat de twee methoden, die algemeen worden toegepast in de beschrijving van tunnelen in vlakke opgedampte juncties, een aantal serieuze tekortkomingen kunnen hebben wanneer ze worden toegepast op de Scanning Tunnel Microscoop (STM) en puntcontact geometrieën, zoals die gebruikt zijn in het experimentele werk dat gepresenteerd wordt in de hoofdstukken 3, 4 en 5 van dit proefschrift. Exacte golfaanpassing kan worden toegepast op effectief één-dimensionale systemen met tunnelbarrières van willekeurige hoedanigheid. De transfer-Hamiltoniaan methode is een eerste-orde storingstheorie, toepasbaar op drie-dimensionale systemen met inachtneming van veel-deeltjes effecten. De toepasbaarheid is echter beperkt tot barrières met een lage transmissiecoëfficiënt en tot kleine waarden van de aangelegde spanning. De omstandigheden, zoals we die tegenkomen in puntcontactgeometrieën, in het bijzonder in het geval van de STM, overschrijden mogelijk de geldigheidsgrenzen van bovenstaande theorieën. Recente ontwikkelingen in de richting van een algemene theorie van STM-tunnelen worden besproken. Formele methoden, gebruikmakend van Green's functie technieken zoals het Keldysh formalisme, lijken het meest veelbelovend.

In ultrakleine tunneljuncties kan de intrinsieke capaciteit  $C$  van de junctie zo klein worden dat het tunnelgedrag bij lage temperaturen volledig wordt gedomineerd door de electrostatische oplaadenergie  $e^2/2C$ . Dientengevolge kan het tunnelen van één enkel electron significante gevolgen hebben voor de spanning over de junctie en de waarschijnlijkheid van volgende tunnelgebeurtenissen. Hoofdstuk 2 is gewijd aan de theoretische beschrijving van deze één-electron oplaadeffecten, met de nadruk op juncties tussen normale metalen.

Een belangrijk gevolg van deze oplaadeffecten is het optreden van een zogenaamde Coulomb blokkade, die zichzelf manifesteert in de stroom-spanning karakteristiek als een combinatie van verschoven asymptoten en een onderdrukte geleiding bij lage spanningen. Deze Coulomb blokkade is alleen zichtbaar wanneer de junctie afdoende is ontkoppeld van parasitaire capaciteiten in de omgeving. Dit kan worden bereikt door een grote impedantie in serie met de junctie te schakelen, of door de

junction op te nemen in een netwerk van andere kleine tunneljunctions

In het geval van een serie-impedantie kunnen drie regimes worden onderscheiden. In het ideale geval, wanneer de serieweerstand veel groter is dan de tunnelweerstand, is de junctie stroomgestuurd, en verwacht men het optreden van bijna coherente oscillaties (SET-oscillaties) in de spanning over de junctie. Dit regime wordt beschreven door de theorie van Averin en Likharev ("orthodoxe theorie"). Zowel dit ideale als het tussen-regime, waar de serie- en tunnelweerstand vergelijkbare grootte hebben, kunnen worden bestudeerd met behulp van semi klassieke Monte-Carlo simulaties van de tijdsontwikkeling van de lading op de junctie. Het tussen-regime wordt gekarakteriseerd door sterke maar incoherente, tunnelgeïnduceerde fluctuaties van de spanning. In het derde regime, waar de serieweerstand veel kleiner is dan de tunnelweerstand, moet de invloed van quantumfluctuaties en de interactie tussen het tunnelend electron en de electromagnetische modes in de omgeving worden meegenomen. Voor serie-impedanties groter dan de quantumweerstand  $\pi\hbar/2e^2$  is ook in dit regime een Coulomb blokkade zichtbaar, die echter conceptueel verschilt van die in de ideale stroomgestuurde situatie.

Het eenvoudigste niet-triviale netwerk is een serieschakeling van twee kleine junctions, het dubbele-junctiesysteem genaamd. In dit geval is de middelste electrode die beide junctions verbindt een geïsoleerd eiland dat alleen kan worden opgeladen met gehele veelvouden van de elementaire lading  $e$ . De stroom-spanning karakteristiek zal een regelmatige serie stappen en knikken vertonen (Coulomb ladder) waarvan de vorm en positie afhangt van de verhoudingen der capaciteiten en weerstanden van de twee junctions. De posities van stappen en knikken kunnen bovendien beïnvloed worden door de potentiaal van een of andere capacatieve koppeling naar de centrale electrode (Single-Electron Transistor) of door de aanwezigheid van gelocaliseerde ladingen in de buurt van het eiland.

Hoofdstuk 2 geeft bovendien een beknopt overzicht van de huidige experimentele status van dit vakgebied, voor zover betrekking hebbend op nanolithografisch gedefinieerde systemen.

De experimentele aspecten van oplaadefecten in enkele junctions gemaakt met puntcontact-technieken worden gepresenteerd in hoofdstuk 3. Wanneer we de observatie van verschoven asymptoten in combinatie met een onderdrukte geleiding rond de oorsprong van de stroom-spanning karakteristiek aannemen als werkdefinitie voor de mogelijke aanwezigheid van een Coulomb blokkade, vinden we sterke aanwijzingen voor oplaadefecten in puntcontact-tunneljunctions op een veelheid aan sample-materialen. Aangezien ontkoppelingsmechanismen van het soort beschreven in hoofdstuk 2 hier niet aanwezig zijn, stellen wij een nieuw mechanisme voor, dat gebaseerd is op de mogelijkheid van hoppinggeleiding door gelocaliseerde oppervlakte- of onzuiverheidstoestanden op de tip of het sample-oppervlak. Deze hypothese is getest in metingen met puntcontact-tunneljunctions op arseen-gedoteerde silicium samples waarin het ladingstransport bij lage temperaturen volledig wordt gedomineerd door hoppinggeleiding. Deze junctions vertonen inderdaad Coulomb blokkade effecten, die wel beïnvloed kunnen worden door oppervlakte-behandeling, maar overigens onafhankelijk zijn van de serieweerstand die de junctie ziet. Daar-

naast hebben we experimentele aanwijzingen dat de ideale stroomgestuurde situatie gerealiseerd kan worden wanneer getunneld wordt door metallische eilandjes die op het gedoteerde silicium zijn aangebracht

Het dubbele-junctiesysteem wordt experimenteel bestudeerd in hoofdstuk 4 Puntkontakt juncties op verscheidene samples, die geïsoleerde eilandjes bevatten, vertonen Coulomb-ladders Ook de invloed van gelocaliseerde ladingen in de buurt van de centrale electrode is duidelijk zichtbaar In de meeste gevallen is het deeltje dat de centrale electrode vormt nog zo groot dat de toestandsdichtheid als continu kan worden beschouwd Enige verwachtingen worden uiteengezet t a v toekomstige experimenten aan ultrakleine organometallische clusters waarin we weldegelijk de effecten van een discrete elektronische structuur verwachten te zien

Hoofdstuk 5 presenteert resultaten van spectroscopische experimenten aan hoge- $T_c$  supergeleiders m b v puntkontakt-tunnellen Het doel van deze experimenten is het meten van de supergeleidende toestandsdichtheid van deze materialen Voor  $\text{YBa}_2\text{Cu}_3\text{O}_{7-\delta}$  en  $(\text{Pb}_x\text{Bi}_{1-x})_2\text{Sr}_2\text{CaCu}_2\text{O}_8$  worden redelijke BCS-achtige karakteristieken gemeten aan zowel normaal-metaal-supergeleider als supergeleider-supergeleider juncties, hoewel met een onverwacht grote en vooralsnog onverklaarde verbreding In het geval van keramisch en polykristallijn  $\text{YBa}_2\text{Cu}_3\text{O}_{7-\delta}$  liggen de gevonden gapwaarden in het interval  $2\Delta/k_B T_c \approx 3 - 7$ , met een gemiddelde significant boven de door de BCS-theorie voorspelde waarde van 3.5 voor het geval van zwakke koppeling Tunnelend in het  $ab$ -vlak van  $(\text{Pb}_x\text{Bi}_{1-x})_2\text{Sr}_2\text{CaCu}_2\text{O}_8$  vinden we een eenduidige waarde  $2\Delta/k_B T_c \approx 8$  Naast deze gapkarakteristieken zijn ook kritische stroom en Josephson effecten, oplaadeffecten, en negatieve differentiele weerstandsverschijnselen waargenomen Het optreden van deze laatste twee effecten houdt verband met de slecht gedefinieerde oppervlakte-eigenschappen van de materialen

Hoofdstuk 6 betreft een theoretische studie van quantumweerstand en localisatie in ééndimensionale wanordelijke mesoscopische systemen In deze systemen, waar de inelastische verstrooiingslengte de sample-dimensies overschrijdt, wordt de geleiding volledig gedomineerd door coherente golfvoortplanting en quantuminterferentie Transmissie- en reflectiecoëfficiënten worden berekend met de hierbovengenoemde golfaanpassingsprocedure In het eerste deel van dit hoofdstuk wordt een nieuwe gegeneraliseerde Landauer formule afgeleid en gebruikt om de spanningsafhankelijke weerstand van een ééndimensionale draad met wanordelijke potentiaal te bestuderen Er wordt aangetoond dat een eindig potentiaalverschil energie-integratie en zelf-middelend gedrag introduceert Weerstandsfluctuaties als functie van spanning of draadlengte blijken af te nemen met toenemende spanning Ondanks de zelf-middeling, blijkt de gemiddelde weerstand bij hoge spanningen sterker dan lineair te schalen met de lengte Het tweede deel van hoofdstuk 6 legt een verband tussen de ladingsdragersdynamica in een kleine ééndimensionale ring aangedreven door een tijdafhankelijke magnetische flux en de stationaire beschrijving van quantum-tunnellen door een ééndimensionale draad met periodieke potentiaal tussen twee reservoirs Aangetoond wordt dat het verschijnsel van dynamische quasi-randomisatie van de fases in de ring, dat onder meer leidt tot verzadiging van

de stroom, fysisch equivalent is met het verschijnsel van veld-geïnduceerde quasi-wanorde in de periodieke structuur tussen reservoirs. In beide gevallen leiden de respectievelijke types van wanorde tot aantoonbare localisatie-effecten in de weerstand. Bovendien wordt een nieuwe en onafhankelijke bevestiging verkregen van Landauers  $R/T$  formule, die niet afhankelijk blijkt van de aanwezigheid van reservoirs.

## List of publications

### Superconductivity

- *Macroscopic quantum phenomena in high- $T_c$  superconducting material*,  
A Th A M de Waele, R T M Smokers, R W van der Heijden, K Kadowaki,  
Y K Huang, M van Sprang, and A A Menovsky, *Phys Rev B* **35** (1987)  
8858
- *Determination of the energy gap in  $YBa_2Cu_3O_{7-\delta}$  by tunneling, far infrared reflection and Andreev reflection*,  
P J M van Bentum, H F C Hoevers, H van Kempen, L E C van de Leemput,  
M J M F de Nivelte, L W M Schreurs, R T M Smokers, and P A A Teunissen,  
*Physica C* **153-155** (1988) 1718
- *The energy gap of  $YBa_2Cu_3O_{7-\delta}$  tunneling, far infrared reflection and Andreev reflection*,  
H van Kempen, P J M van Bentum, H F C Hoevers, L E C van de Leemput,  
L W M Schreurs, R T M Smokers, and P A A Teunissen, *Progress in High Temperature Superconductivity* **9** (1988) 175
- *Comparison of three methods to determine the energy gap of  $YBa_2Cu_3O_{7-\delta}$* ,  
P J M van Bentum, H F C Hoevers, L E C van de Leemput, M J M F de Nivelte,  
L W M Schreurs, R T M Smokers, P A A Teunissen, and H van Kempen,  
*Phys Scr* **T25** (1989) 91
- *The energy gap of high- $T_c$  superconductors*,  
H van Kempen, J J A Wnuk, P J M van Bentum, H F C Hoevers, L E C van de Leemput,  
L W M Schreurs, and R T M Smokers *Progress in High Temperature Superconductivity* **24** (1989) 147
- *Tunneling spectroscopy in  $(Pb_xBi_{1-x})_2Sr_2CaCu_2O_8$  crystals*,  
J J Wnuk, R T M Smokers, F W Nolden, L W M Schreurs, Y S Wang, and  
H van Kempen, *Supercond Sci Technol* **4** (1991) S412

### Charging effects

- *Incremental charging of single small particles*,  
P J M van Bentum, R T M Smokers, and H van Kempen, *Phys Rev Lett* **60** (1988) 2543
- *Single-electron effects observed with a low-temperature STM*,  
P J M van Bentum, L E C van de Leemput, R T M Smokers, and H van Kempen,  
*J Microscopy* **152** (1988) 11

- *Single-electron effects in low capacitance point-contact tunnel junctions*, P.J.M. van Bentum, L.F.C. van de Leemput, R.T.M. Smokers, and H. van Kempen, Phys. Scr. **T25** (1989) 122.
- *Single-electron tunneling in point-contact tunnel junctions*, R.T.M. Smokers, P.J.M. van Bentum, and H. van Kempen, Physica B **165&166** (1990) 63.
- *The Coulomb blockade in STM-type tunnel junctions*, H. van Kempen, R.T.M. Smokers, and P.J.M. van Bentum, in: *Scanned Probe Microscopy*, ed. H. Kumar Wickramasinghe, AIP conf. proc. **241** (1991) 101.
- *Study of single-electron tunneling in point-contact tunnel junctions at low temperatures*, R.T.M. Smokers, P.J.M. van Bentum, and H. van Kempen, in: *Granular Nanoelectronics*, eds. D.K. Ferry, J.R. Barker, and C. Jacoboni, (Plenum, N.Y.,1991), proceedings of NATO Advanced Study Institute, 1990, Il Ciocco, Italy.
- *Coulomb blockade effects in STM-type tunnel junctions*, H. van Kempen, P.J.M. van Bentum and R.T.M. Smokers, (1992), to appear in Phys. Scr..

## Clusters

- *Scanning tunneling microscopy observations of metallic clusters Pd<sub>561</sub> and Au<sub>55</sub> and the implications of their use as a well defined tip*, L.E.C. van de Leemput, J.W. Gerritsen, P.H.H. Rongen, R.T.M. Smokers, H.A. Wierenga, H. van Kempen, and G. Schmid, J. Vac. Sci. Technol. B **9** (1991) 814.

## Quantum resistance and localization

- *Voltage-dependent scaling of the quantum resistance in 1D disordered systems*, D. Lenstra and R.T.M. Smokers, Physica B **151** (1988) 503.
- *Theory of nonlinear quantum tunneling resistance in one-dimensional disordered systems*, D. Lenstra and R.T.M. Smokers, Phys. Rev. B **38** (1988) 6452.
- *Carrier dynamics in a ring, Landauer resistance and localization in a periodic system*, D. Lenstra, W. van Haeringen, and R.T.M. Smokers, Physica A **162** (1990) 405.

## Curriculum Vitae

Richard Smokers

geboren op 22 september 1964 te Eindhoven.

- 1976–1982 : Gymnasium  $\beta$ , aan het Eindhovens Protestants Lyceum te Eindhoven.
- 1982–1987 : Studie technische natuurkunde, aan de Technische Universiteit te Eindhoven, met de volgende stages:
- *Productie, detectie en looptijden van metastabiele helium-moleculen in vloeibaar helium bij  $T \approx 1.7$  K en  $T = 4.2$  K*, o.l.v. Dr. R.W. van der Heijden en Dr. A.Th.A.M. de Waele (vakgroep Lage Temperaturen);
  - *De moleculaire chaos aanname voor Bose-Einstein gecondenseerde systemen*, o.l.v. Prof. Dr. B.J. Verhaar (vakgroep Theoretische Natuurkunde), en afstudeerstage:
  - *Electronic quantum interference in solids*, o.l.v. Dr. A.Th.A.M. de Waele (vakgroep Lage Temperaturen) en Dr. D. Lenstra (vakgroep Theoretische Natuurkunde).
- 1987–1991 : In dienst van de stichting voor Fundamenteel Onderzoek der Materie (FOM). Promotie-onderzoek op de afdeling Experimentele Vaste Stof Fysica 2 van de K.U.N., onder leiding van Prof. Dr. H. van Kempen en Dr. P.J.M. van Bentum.
- maart 1992 : Vervulling vervangende dienstplicht bij de business unit Energiestudies van het E.C.N. in Petten.







